Gravity and Magnetic Investigations Along the Peruvian Continental Margin

Dissertation

zur Erlangung des Doktorgrades
der Naturwissenschaften im Fachbereich
Geowissenschaften
der Universität Hamburg

vorgelegt von

Raffaela Esther Heinbockel

aus
Hamburg

Hamburg
2002

Als Dissertation angenommen vom Fachbereich Geowissenschaften
der Universität Hamburg
auf Grund der Gutachten von Prof. Dr. Dirk Gajewski
und Dr. Gholam Ali Dehghani

Hamburg, den 24.01.2003

Prof. Dr. U. Bismayer
Dekan
des Fachbereichs Geowissenschaften

Contents

1 Abstract

This work presents the first three-dimensional gravity and magnetic investigation along the convergent Peruvian margin. Three-dimensional magnetic modelling is still a relatively untried and challenging technique. The gravity and magnetic models image nearly the whole margin which has been only partly resolved with geophysical methods up to now. The gravity and magnetic models are constructed for three areas between 7.25°S and 16.75°S and are based on the available wide-angle seismic velocity models (Hampel et al., 2002a; Broser et al., 2002). The continental margin is characterised by positive free-air anomalies of varying amplitudes, indicating that the margin has been shaped by the subduction of different features on the Nazca Plate. A comparison of the shipboard gravity measurements with the satellite data ensures that the data compiled from different marine surveys are compatible. In the Yaquina Area (7.25°S to 11°S) gravity anomalies caused by the Trujillo Trough and the Mendaña Fracture Zone are successfully modelled with remarkable undulations in the layer geometry of the oceanic crust. Along the continental margin, especially in the Lima Area (10.50°S to 14.40°S), strong undulations of the lower continental crust influence the upper sedimentary layers and support the development of basins along the Peruvian margin.

The theory stating that the Peruvian margin is uplifted by the subducting Nazca Ridge (Kulm et al., 1988; Hagen & Moberly, 1994) is supported by gravity modelling. Consequently the buoyant Nazca Ridge is, at least partly, responsible for the extended region of flat subduction. The thickened and slightly asymmetrical crust of the Nazca Ridge is envisaged in gravity modelling. In the Nazca Ridge Area (14.25°S to 16.75°S) no accretionary prism is modelled. I conclude that the ridge is eroding the continental margin; furthermore the subduction of eroded sediments is probable. Gravity modelling suggests that the Nazca Ridge has fractured the continental margin. North of the ridge, in the Lima Area, a rather uniform accretionary complex is observed. This indicates that, after the margin was eroded by the southwards moving Nazca Ridge, the prism rapidly reached its stable size. In the Yaquina Area an accretionary prism is modelled in the whole research area but local variations of its location and structure indicate the former erosive influence on the continental margin of subducting features on the Nazca Plate. The layers of the oceanic crust show increasing densities implying they possess an originally high degree of porosity before actually subducting.

The lineations 13 to 18 are traced from the southern part of the studied region as far north as the Mendaña Fracture Zone. Their orientation indicates that the Nazca Plate has not significantly changed its convergence direction between 12°S and 17.5°S in the past 33 Ma. In the Nazca Ridge Area a different anomaly pattern compared to the surrounding areas is observed. I conclude that the ridge is younger than the respective Nazca Plate and that it was formed on the already existing Nazca Plate and obliterated the original magnetic anomalies. In all models the basaltic layer sheeted dykes is considerably weaker magnetised than the upper pillow lavas and the lower gabbros. Generally the rocks of the continental margin possess a weak magnetisation. The Königsberg ratio is small for all layers of the oceanic crust, i.e. the induced magnetisation is partly higher than the remanent magnetisation. When it has subducted to a minimum depth of 25 km the magnetised oceanic crust exerts almost no influence on the observed total intensity field.

2 Introduction

The Peruvian margin is an active continental margin, where the oceanic Nazca Plate is subducting underneath the continental South American Plate. The prominent plate boundary is subject to intense crustal deformation caused by plate subduction. This study constitutes the first three-dimensional gravity and magnetic investigation of the Peruvian subduction zone. Extensive three-dimensional magnetic modelling is a very demanding and still largely unexplored method to interpret magnetic anomalies. A major motivation of this study is to gain more information on the concept of three-dimensional potential field modelling. Prior to this investigation only very few two-dimensional gravity and magnetic profiles have been acquired in this research area. Other geophysical investigations have provided information on the subduction zone which may be supported and expanded or eventually negated by the gravity and magnetic investigations.

For about 11.2 Ma the southward moving Nazca Ridge has been subducting obliquely beneath South America (Hampel, 2002). The subduction of the Nazca Ridge caused tectonic uplift of the forearc area which was followed by subsidence (Kulm et al., 1988; Hagen & Moberly, 1994). While Hampel et al. (2002a) did not resolve an accretionary prism with wide-angle seismic and bathymetric measurements in the present area of the Nazca Ridge, Hagen & Moberly (1994) observed an accretionary complex with swath mapping. North of the ridge reflection seismic measurements image an accretionary prism (von Huene et al., 1996). Gutscher et al. (1999) proposed that the buoyant Nazca Ridge is responsible for an extended area of flat subduction. Two wide-angle seismic profiles indicate that in the area of the Nazca Ridge the oceanic crust is considerably thickened (Hampel et al. 2002a). Hagen & Moberly (1994) observed with swath mapping that intrusive and extrusive volcanism occurred on the Nazca Plate after it had moved away from the spreading ridge.

In the studied region Couch et al. (1981) carried out gravity measurements along four profiles and observed that the oceanic crust is 5 km thick both north and south of the Nazca Ridge. Consequently, they did not resolve the thickened oceanic crust of the ridge. According to Hayes (1966) the Nazca Ridge is essentially isostatically compensated. Hayes (1966) did not yet recognize the presence of a subduction zone. Hayes (1966) also conducted magnetic measurements and found that magnetic anomalies cannot be correlated over large distances. Huchon & Bourgois, 1990 carried out magnetic measurements in the area of the Mendaña Fracture Zone at 11°S. Based on the observed lineations they concluded that this fracture zone has been actively rifting for 3.5 Ma. Along the whole Peruvian margin only very few magnetic lineations have been recognized up to now.

The investigations described in the following are two of the very few works of three-dimensional magnetic modelling documented in literature. Off Costa Rica Barckhausen et al. (1998) found that explicit magnetic anomalies may be correlated with not yet subducted seamounts. Barckhausen et al. (1998) noted that the observable anomalies get smoother and weaker with increasing subduction of the oceanic plate. Schreckenberger (1998) constructed a three-dimensional model for an area off central Chile. According to Schreckenberger (1998) the magnetic source layers are being disintegrated mechanically just landward of the trench.

There is still some debate on how strongly the different layers of the oceanic crust are magnetised. The rocks of the oceanic crust exposed in fracture zones and ophiolites are subject to alteration and consequently possess a non-conclusive, varying magnetisation. Based on borehole measurements in the southwest Indian Ocean, Pariso & Johnson (1993) observed that the lower gabbros significantly contribute to the observed magnetic anomalies. Worm et al. (1996) studied drill holes off Costa Rica and found that the observable magnetic anomalies are caused primarily by pillow basalts and, thereafter, by sheeted dykes. Contrary to Pariso & Johnson (1993) they conclude that gabbros are unlikely to contribute to the observable anomalies. According to Roeser (2000) sediments normally do not contribute noticeably to the observable anomalies.

In this study I provide a regional integrated model of the gravity and magnetic features observed along the Peruvian continental margin. Considering the only sparse previous gravity and magnetic investigations, this study is overdue. New gravity and magnetic data were acquired during the GEOPECO (GEOphysical experiments along the PEruvian COntinental margin) expedition from March till May 2000 using research vessel SONNE, cruise number 146. Between 83°W to 74°W and 6°S to 17°S a total length of 12500 km gravity profiles and 3577 km magnetic profiles were collected. The multi-disciplinary expedition GEOPECO comprised refraction and reflection seismics, a bathymetric survey, a seismological investigation, sampling and video observations of the ocean floor, heatflow measurements as well as gravity and magnetic investigations. The high-quality wide-angle seismic profiles generated by Hampel et al. (2002a) and Broser et al. (2002) provide the necessary constraints for gravity and magnetic modelling. The gravity and magnetic data recorded during the GEOPECO project are a very good supplementation of the existing data sets from the GEODAS data base (GEOphysical DAta System, provided by NOAA and NGDC). Combined three-dimensional gravity and magnetic models of the continental margin are constructed for the Nazca Ridge Area (14.25°S to 16.75°S), the Lima Area (10.50°S to 14.40°S) and the Yaquina Area (7.25°S to 11°S).

The examination of the free-air and Bouguer anomalies as well as the residual free-air and Bouguer anomalies clarifies the anticipated substantial influence of the subduction zone on the gravity fields. From studying the free-air anomalies it is possible to conclude on the state of isostatic compensation. Based on the free-air anomalies, I intend to investigate whether the influence of the long-term subduction zone on the appearance of the margin has been uniform. In my opinion a combined modelling of the gravity and magnetic fields allows a detailed investigation of the development of basins along the Peruvian margin.

Three-dimensional gravity modelling will quantify the past and present effect of the subducting Nazca Ridge on the overriding forearc. The influence of the subducting Nazca Ridge on the continental margin is observable in the densities of the seaward continental block. The investigation of the structural features of the oceanic Nazca Plate in correlation with the uplift and deformation of the overriding continental plate improves the understanding of the processes occurring during the subduction of a submarine ridge. The thicker and therefore the more buoyant the subducting crust is, the greater are the forces required for its subduction. During the subduction of thickened crust the initial angle of subduction gets shallower. I mean to investigate whether the theory, stating that the Peruvian margin is uplifted by the subducting Nazca Ridge (Cross & Pilger, 1982), is supported by gravity modelling. Constrained by the seismic lines the three-dimensional gravity model covers an extended area and images the overall crustal structure of the subducting Nazca Ridge.

I present an approach to assess the density distribution within the subducting and within the overriding crust. If the layers of the oceanic crust show increasing densities when actually subducting I can conclude that they originally possessed a high degree of porosity. The densities modelled for the upper layer of the subducting slab will determine whether eroded sediments from the continental margin subduct together with the oceanic crust. It is possible to estimate the amount of accreted and subducted material. If no accretionary prism is present the quantity of subducted material has to be at least like the amount of incoming sediments on the Nazca Plate.

Three-dimensional gravity modelling constitutes a powerful means of studying the presence or absence of an accretionary complex. Along the Peruvian margin this effective method has not been employed before. The transition from the continental South American crust to an accretionary complex can be modelled successfully. In my opinion it is possible to conclude that, if an accretionary prism is missing, the continental margin has been eroded. More precisely, the absence of an accretionary prism indicates that the Nazca Ridge is eroding the continental margin. If a uniform accretionary complex is observed north of the Nazca Ridge, this is supporting the theory that, after the subducting Nazca Ridge has moved further southwards, an accretionary prism developed and rapidly reached its stable size (von Huene et al., 1996). As most parts of the Yaquina Area have not been influenced by the subducting Nazca Ridge (Hampel, 2002) other features of the convergent margin must be responsible for the appearance of the continental margin. In my opinion it is possible to determine whether the margin has been shaped by subducting features, e.g. seamounts on the Nazca Plate in the past. If high-density layers are exposed the continental margin must have been eroded. It is possible to simulate erosion by a varying thickness of the upper sediment layer.

The main objective of magnetic modelling is to learn more about the lineation pattern of the oceanic Nazca Plate. The orientation of these lineations will allow a determination of the paleo convergence direction of the Nazca Plate. The observed lineations can be identified by means of the geomagnetic polarity time scale published by Cande & Kent (1995). Modelling of the Königsberg ratio, i.e. the ratio of the remanent to the induced magnetisation, will signify whether the induced or the remanent magnetisation is the dominating component. In all three models I will investigate which layers of the oceanic crust possess the highest magnetisation.

I will show that even an irregular magnetic anomaly pattern leads to valuable conclusions. Different explanations for heterogeneous magnetic anomalies are possible. On the one hand the available magnetic data may not be sufficing to render a clear anomaly pattern or the data may not be sufficiently compatible due to the influence of magnetic variations. On the other hand the Nazca Plate may have experienced extensive volcanism after its creation at the spreading centre as observed by Hagen & Moberly (1994).

Three-dimensional magnetic modelling provides the possibility to investigate whether the subducting oceanic crust is still significantly magnetic after it has subducted to a certain depth. It is possible to determine whether the magnetised oceanic crust still exerts an influence on the observable total magnetic field.

Gravity and magnetic modelling is very sensitive to the thickness of the oceanic crust. I am positive that in the Yaquina Area the tectonic features Trujillo Trough and Mendaña Fracture Zone, which are not definitely constrained by seismic profiles, will be resolved in three-dimensional modelling of the oceanic layers.

The potential field data alone do not provide definite models of the geological structures. In addition to the gravity and magnetic data, the results of reflection seismics, geological investigations, seismological data and information from satellite altimetry play a major role in generating the models. The combined and simultaneous three-dimensional modelling of the gravity and magnetic data provides further constraints on the imaged structures. The seismic models, generated by Hampel et al. (2002a) and Broser et al. (2002), are used to constrain layer geometry and thickness and to provide initial estimates of the layer densities. Gravity modelling will assert whether the layer geometries and densities, required to reproduce the observed anomalies, mostly agree with the seismic velocity models.

The following agenda gives an overview of the structure of this thesis. I will start with an introduction to the main geological characteristics of the Peruvian margin. Here, I will show that the Peruvian continental margin exhibits variable and complex structures. The variation of age and temperature of the oceanic plate, the angle of subduction, the depth of the trench axis and the different rock types lead to different gravity and magnetic field structures. The next chapter is concerned with a detailed description of the three areas of three-dimensional modelling.

In the following section the gravity and magnetic survey is portrayed and the data are presented. The recently acquired potential field data are compiled with all the already available gravity and magnetic data. The dense distribution of gravity and magnetic measurements constitutes a sound condition for three-dimensional modelling. Modelling is conducted in the areas with the highest data coverage. High resolution free-air and Bouguer gravity maps are presented for the entire Peruvian margin. Special attention is paid to different representations of the potential fields which enhance particular aspects. To ensure that the marine gravity data compiled from different marine surveys are compatible they are compared with the satellite data of the Peruvian continental margin.

In the course of this study I will provide a detailed discussion of the difficulties connected with magnetic modelling. Magnetic modelling includes significantly more variable and interdependent parameters than gravity modelling. The only variable parameters in gravity modelling are density and model geometry. In contrast the mapped magnetic anomalies are simulated in three-dimensional modelling by a variation of the magnetisation values, the magnetic susceptibilities, inclination and declination values, the Königsberg ratio and, of course, the model geometry. The possible error sources are manifold. Consequently, the three-dimensional magnetic models render mostly qualitative results. The identified magnetic lineations are imaged along the whole Peruvian margin and, in greater detail, in the three study areas.

In the following the three-dimensional models are presented. The models show a variability in crustal structure, density, susceptibility and layer thickness between the northern and southern research areas. They consist of numerous parallel, vertical planes which are oriented perpendicular to the main structural trends. Each of the vertical planes comprises part of the oceanic plate, the Peru trench and the continental shelf. As the structures of the Peruvian margin are three-dimensional, the gravity and magnetic anomalies have to be modelled in three dimensions. Finally, I will discuss the results of the gravity and magnetic investigations and name the conclusions.

3 Geology

The Peruvian continental margin is characterized by the subduction of the oceanic Nazca Plate underneath the continental South American Plate. In the course of this subduction the Andean mountain chain has developed. The Andes extend about 8000 km along the western continental margin of South America. They are the longest land mountain chain of the world and extend from Central America to southern Patagonia. The Andes are up to 6500 m high and 600 km wide. The subduction system has developed since the Late Cretaceous. The Western Cordillera describes the active volcanic arc. In the central Andes, the highest and widest part of the mountain chain, the Eastern and Western Cordilleras enclose a 200 km wide central plateau, the Altiplano, at an average altitude of 4000 m. The Central Andes possess a crustal root of up to 65 to 70 km (Couch et al., 1981; Schmitz et al., 1999). In Figure 1 the studied Peruvian margin is enclosed by a white box.

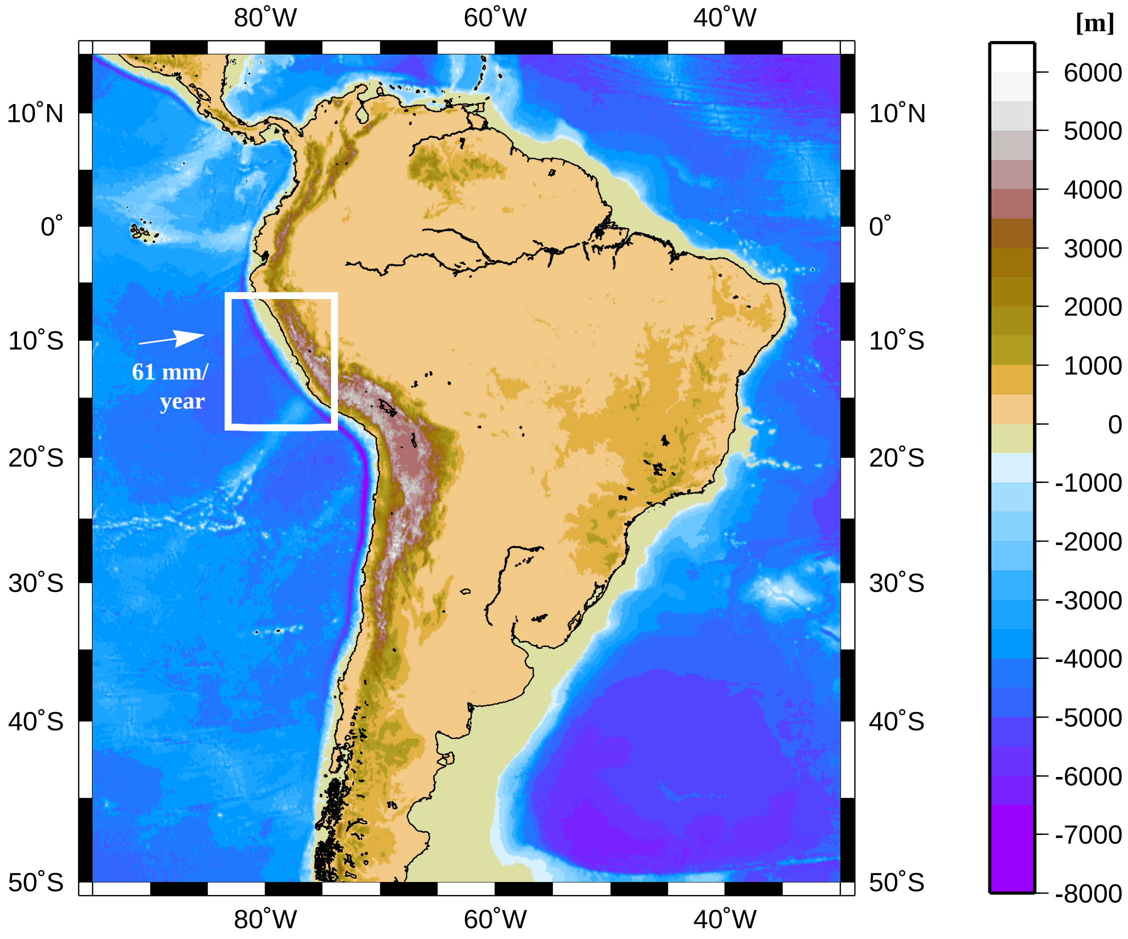

Figure 1: The South American Convergent Margin
The bathymetric and topographic data were obtained from Sandwell et al. (1997).

The convergence rate of the Nazca Plate is varying along the South American margin. Along the Peruvian margin, at 12°S, the relative convergence rate is 61 ± 3 mm/year (Norabuena et al., 1999; Angermann et al., 1999). According to DeMets et al. (1990) the active plate convergence is in a roughly east-west direction at approximately 85 mm/year in the central Andes. Off northern Chile plate convergence takes place at a rate of 95 mm/year oriented 20˚ from normal to the trench (von Huene et al., 1999). Further to the south, at 33˚10’S off Valparaiso in Chile, the convergence rate is approximately 80 mm/year (Flueh et al., 1998). In the north the spreading rate of the Cocos-Nazca spreading centre is 31 mm/year (Meschede & Barckhausen, 2001). According to DeMets et al. (1990) the spreading rate off Ecuador is 60 to 70 mm/year and the subduction rate of the Carnegie Ridge is 70 mm/year.

The Peru-Chile Trench is a product of the subduction zone and is generally shallower than the island arc trenches in the western Pacific. Off Peru and southern Chile the trench shows a maximum depth of 6.5 km, off northern Chile it is up to 8 km deep. In the area of the Nazca Ridge the trench is less than 5 km deep.

The Peruvian margin was greatly influenced by the subduction of the Nazca Ridge. The Nazca Ridge moved down the coast from the north at a rate of about 72 km/Ma (Hampel, 2002). The geologic record along the coast gives evidence of this movement. Changing episodes of uplift and subsidence (von Huene et al., 1988) can be observed. The ridge migrates south along the margin because plate convergence is almost normal to the continental margin but at 45˚ to the strike of the ridge. The Peruvian coast shows a trend of 315˚.

3.1 Segmentation of the Peruvian Margin

The Andean subduction zone can be subdivided into regions of flat and normal subduction (see Figure 2). In the areas of normal subduction in Ecuador, southern Peru, northern Chile and southern Chile active volcanism is taking place. Between 0˚ and 35˚S four tectonic segments alternating between normal and flat subduction (Cahill & Isacks, 1992). The angle of subduction and the related location of the volcanic front has changed often in the evolution of the Andean subduction system (Beck, 1998). Near 15˚S and near 27˚S to 28˚S the wide and volcanically active plateau is changing to a narrow and non-volcanic cordillera (Cahill & Isacks, 1992).

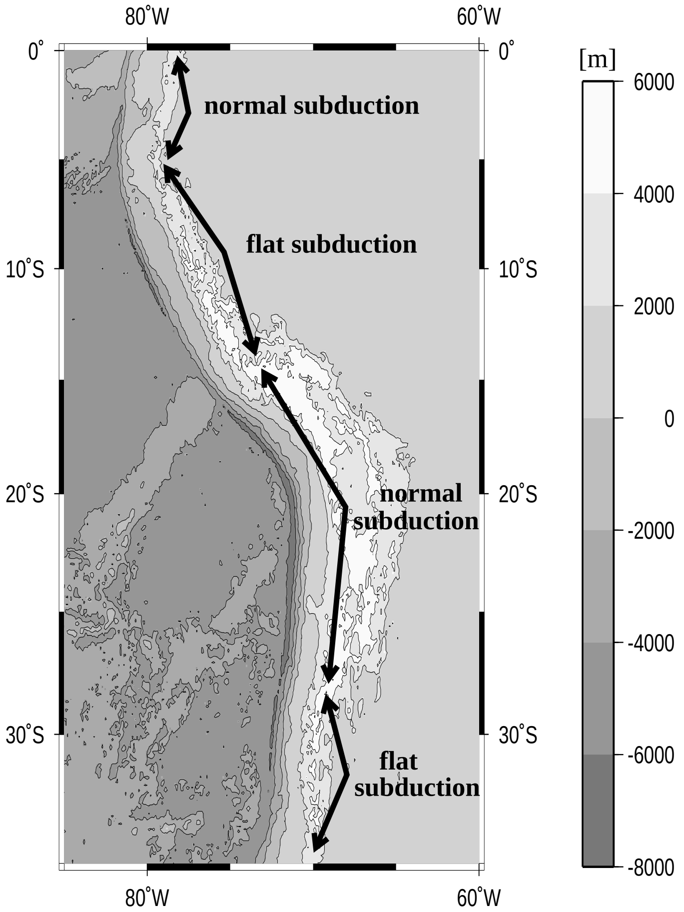

Figure 2: Regions of flat and normal subduction along the South American margin. The bathymetric and topographic data were obtained from Sandwell et al. (1997).

3.1.1 Flat Subduction

In the areas of flat subduction in northern and central Peru as well as in central Chile no active volcanism is taking place. These areas form the most shallow dipping of all modern subduction zones (Jarrard, 1986). The largest zone of flat subduction in the world is located between 5˚S and 15˚S along the Peruvian continental margin. Plate subduction starts at an initial angle of 8° to 15° until a depth of 20 to 40 km is reached (Spence et al., 1999). From then on the oceanic plate is subducting at approximately 30˚ to a depth of about 100 km. The slab is then moving horizontally along the lower surface of the South American lithosphere for hundreds of kilometres before dipping steeply into the upper mantle (Hasegawa & Sacks, 1981). The reason for this unusual behaviour most probably is the subduction of buoyant aseismic ridges and plateaus (Cross & Pilger, 1982). Other explanations for the flat subduction are (1) the young age of the oceanic plate, (2) the high convergence rate, (3) interplate hydrostatic suction (Jischke, 1975), (4) a northward kink in the subducted extension of the Nazca Ridge (Pilger, 1981), and (6) the flexure into a concave-up form of the subducting plate beneath the convex-seaward sections of the continental margin (Cahill & Isacks, 1992).

Flat subduction is the result of slab buoyancy assuming that the basaltic crust of the descending slab has a density of about 2.8 to 2.9 g/cm^3. Another explanation for the flat subduction could be a delay in the basalt to eclogite phase change for young (<70 Ma), but cool (<600°C) oceanic lithosphere (Sacks, 1983). The transformation of basalt to the high-density eclogite in the descending oceanic crust is usually occurring at 80 km depth. When this process is delayed the plate can remain buoyant for long periods of time (Sacks, 1983). A retardation of the basalt-eclogite transition is possible when the slab temperatures are less than 600˚C (Fukao et al., 1983).

The areas of low-angle subduction are characterised by the absence of active volcanism and the non-existence of plateau in the Andes. As no asthenospheric material lies in between the subducting oceanic and the overriding continental plate the partial melting necessary for the formation of a volcanic arc does not take place (Gutscher et al., 1999a). Therefore the onset of horizontal subduction beneath central Peru is related to a cessation of volcanic activity in the region (Noble & McKee, 1977). Volcanism along northern and central Peru ended gradually 5 Ma ago in the Early Pliocene after a strong pulse of magmatic and volcanic activity (Noble & McKee, 1977). The non-volcanic zones show heat flow values of about 30 mW/m^2. This heat flow is low in comparison with a heat flow of between 80 and more than 100 mW/m^2 measured along the northern and southern South American margin.

The subducting Carnegie Ridge at 2°S also supports a local area of flat slab subduction (Gutscher et al., 1999a). Consequently, there is a volcanic gap between the Carnegie Ridge at 2°S and the Mendaña Fracture Zone at 10.5°S (Okal & Newman, 2001). According to Gutscher et al. (1999b) the different subducting ridges can each support a 500-km-long zone of flat subduction. The buoyancy of the Nazca Ridge alone cannot support a 1500 km long section of the Nazca Plate. The Nazca Ridge and the Inca Plateau together possess a buoyancy which would support a 1500 km long segment of flat subduction. The Juan Fernandez Ridge within the Nazca Plate is also supporting a flatly subducting segment of the Nazca Plate (Barazangi & Isacks, 1979).

3.1.2 Normal Subduction

Characteristic features of the normal and therefore steeper subduction zones in Ecuador, southern Peru, northern and southern Chile are an active volcanic arc bordering a broad plateau and a thin-skinned foreland thrust belt along the eastern margin of the plateau (Jordan et al., 1983). These characteristics may be attributed to the combined effects of rapid plate convergence, overriding of the trench by the South American Plate and the relative youth of the subducting Nazca Plate (Cross & Pilger, 1982). The volcanic arc in southern Peru and northern Chile forms the western border of an extensive plateau between 15˚S and 27˚S, the Altiplano-Puna, where a series of young volcanoes is observed (Isacks, 1988). According to Isacks (1988) this plateau is an indicator of the thermal processes acting at depth. The heat flow values measured in regions of normal subduction typically reach 60 mW/m^2 (Henry & Pollack, 1988) and regionally increase to more than 100 mW/m2 (Hamza & Muñoz, 1996). The distribution and nature of magmatic activity in the overriding South American Plate is directly linked to the geometry of the subducting slab (Pilger, 1984). The geometry of subduction zones is defined by four inter-dependent variables (Cross & Pilger, 1982; Jarrard, 1986): (1) the relative convergence rate of the lithospheric plates, (2) the direction and rate of absolute upper plate motion, (3) the age of the subducting plate and (4) the subduction of aseismic ridges, oceanic plateaus or intraplate island and seamount chains.

3.2 Features of the Western South American Margin

Along the Peruvian and northern Chilean margin several tectonic features can be observed. The most prominent features imaged in the bathymetric map (see Figure 3) are being introduced in the following.

The most prominent feature of the Peruvian margin is the Nazca Ridge which subducts between 15°S and 16°S. A detailed description of the Nazca Ridge is provided in relation with the research areas in Chapter 4.3.

The Mendaña Fracture Zone intersects the Peru Trench between 9°40’S and 10°35’S. In the Mendaña Fracture Zone intraplate deformation and exceptional morphological features were observed (Huchon & Bourgois, 1990). The fracture zone is characterized by north-eastward trending ridges with intervening troughs (Warsi et al., 1983). The fracture zone can be regarded as a seaward propagating rift. This rift is forming as a reaction to the extensional stresses in the Nazca Plate which are related to the subduction process (Warsi et al., 1983). The Mendaña Fracture Zone is getting wider towards the subduction zone. The subduction of the Mendaña Fracture Zone under the area of Chimbote leads to significant intraplate deformation and a disruption of the morphology of the subducting oceanic crust.

The spreading fabric differs by 10° north and south of the Mendaña Fracture Zone. The fracture zone divides oceanic crust of different ages. North of the fracture zone the Nazca Plate is about 28 Ma old, in the south the oceanic plate is approximately 38 Ma old. An average heat flow of 40 mW/m^2 was observed (Yamano & Uyeda, 1990). This value is lower than 65.5 mW/m^2 which would be expected for the 38 Ma age of the subducting

Nazca Plate in the Lima Area (Kukowski & Pecher, 1999). The lowest heat flow was measured where the Mendaña Fracture Zone is subducting. The low heat flow is explained by advection in the fractured areas. As can be expected the heat flow increases towards the continental margin (Yamano & Uyeda, 1990).

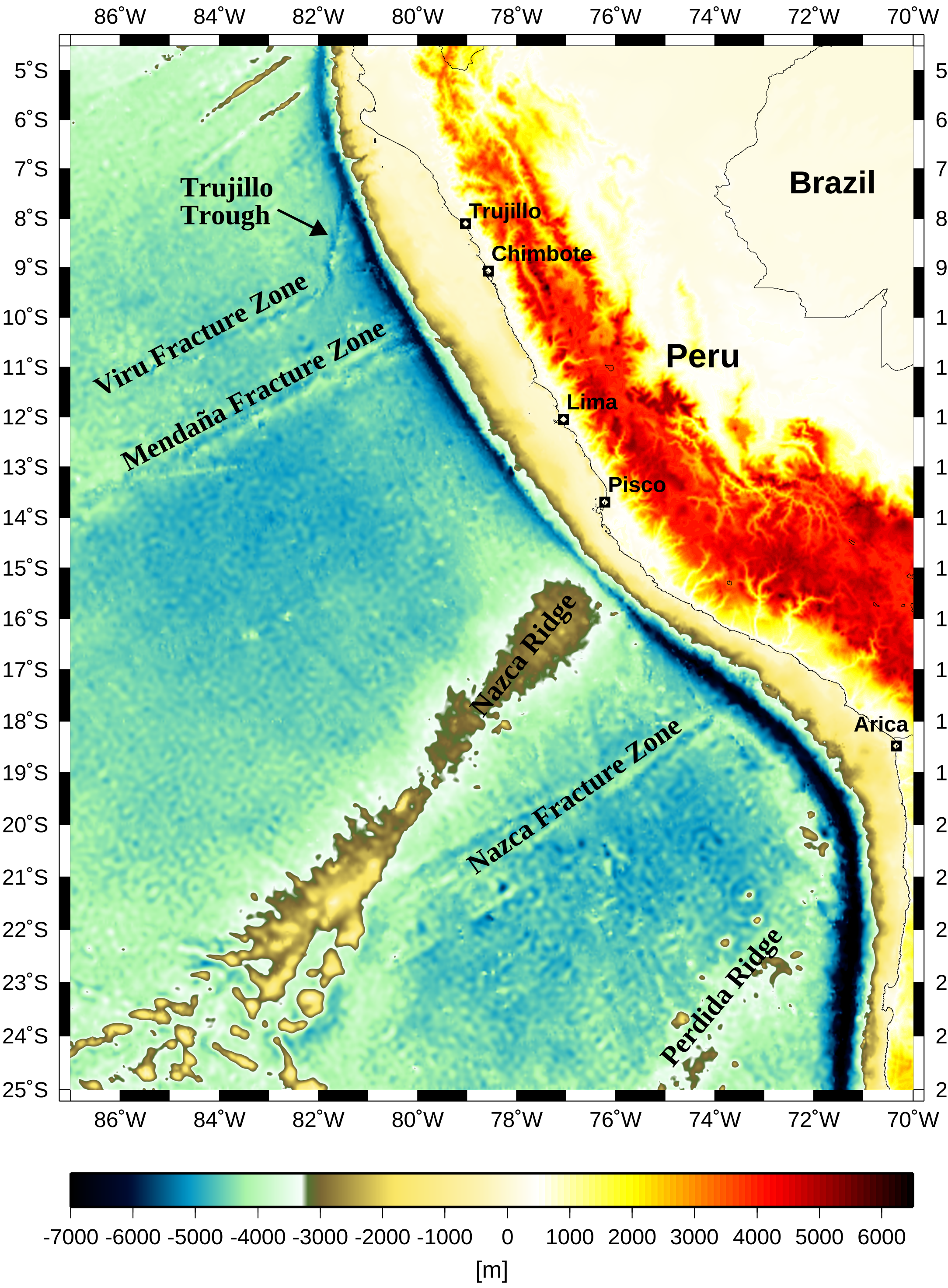

Figure 3: Features of the Peruvian Margin
The bathymetric and topographic data were obtained from Sandwell et al. (2000, pers. commun.).

The 270-km-long Trujillo Trough is presently subducting at 7.5˚S. Here, transpression and left-lateral strike-slip motion have been observed (Huchon & Bourgois, 1990). In accordance with these observations the Trujillo Trough is probably related to the Mendaña Fracture Zone in the south. The seafloor morphology and the tectonic structures of this area are very complex (Huchon & Bourgois, 1990). The Trujillo Trough connects the Viru Fracture Zone with the Peru Trench. The Viru Fracture Zone is located about 100 km north of the Mendaña Fracture Zone (Warsi et al., 1983). A further description of these features is supplied in Chapter 4.1.

The Perdida Ridge is subducting at 22.5˚S, in a zone of steep subduction. According to Cahill & Isacks (1992) this ridge possesses a more substantial structure than the Juan Fernandez Ridge located further in the south of the examined area at 33°S. The Carnegie Ridge is presently subducting under South America at 2°S. It originated from the Galapagos Hotspot which formed approximately 20 to 22 Ma ago (Hey, 1977).

The Nazca Fracture Zone is located south of the Nazca Ridge. Like the Mendaña Fracture Zone this fault separates parts of the Nazca Plate possessing different ages. South of this fracture zone the oceanic crust is about 6 Ma older (Rosa & Molnar, 1988).

3.3 Seismicity

The South American subduction zone possesses one of the highest seismicities on earth (see Figures 4 and 5). This high seismic potential is a motivation to better understand the structure of the continental margin. The distribution of earthquake epicentres defines the generally shallow-dipping Wadati-Benioff zone beneath central Peru and the more steeply subducting Nazca Plate beneath southern Peru and northern Chile (Barazangi & Isacks, 1979). The seismic events near the coast are located in elongated clusters.

Usually a seismic gap is observed when an oceanic plateau, a ridge or a seamount is subducting at a convergent margin. Accordingly a segmentation of the seismicity along the Andean margin can be observed (Gutscher et al., 1999a). Many large earthquakes occurred north and south of the Nazca Ridge in the past centuries. Just north of the Nazca Ridge a seismic gap is observed indicating that the stress caused by the subducting ridge is concentrated on the leading southern side (Spence et al., 1999).

In Figure 4 the earthquakes which occurred along the Peruvian margin between 1973 and 2001 are illustrated with regard to their depths. The data were obtained from USGS. For most of the earthquakes the magnitude is available as well. In Figure 5 the earthquakes are illustrated with respect to their magnitudes. The earthquakes with a minimum magnitude of 7.0 are marked with a star. The three black boxes mark the areas of three-dimensional gravity and magnetic modelling.

Almost the entire length of the Peruvian margin has ruptured during large earthquakes in the past centuries (Swenson & Beck, 1999). The deep earthquakes are concentrated in a narrow region. The flat subduction causes a high level of coupling between the subducting and the overriding plate.

The Chimbote earthquake in 1996, featuring a magnitude of M_w=7.5, was located where the Mendaña Fracture Zone subducts under the South American Plate (Spence et al., 1999). In 1960 an earthquake, possessing a magnitude of M_w= 6.8, occurred at 7.5°S where the Trujillo Trough is subducting (Okal & Newman, 2001; USGS: http://neic.usgs.gov/neis/epic/epic_rect.html). Both earthquakes generated tsunamis. A local area of slowness was found where both the 1996 and 1960 tsunami earthquakes occurred (Okal & Newman, 2001). Tsunami earthquakes took place where major tectonic features on the Nazca Plate are subducting, e.g. the Mendaña Fracture Zone and the Trujillo trough. A slow rupture is thought to be responsible for tsunami earthquakes. This slow rupture may be due to the presence of sediments involved in the subduction process. As sediments possess weak mechanical properties they can lubricate the fault (Satake & Tanioka, 1999). Since 1940 the largest earthquakes have occurred where the amount of subducted sediments is the least (von Huene et al., 1996). Gravity modelling may contribute to a better estimate of the amount of subducted sediments.

Several small events were observed during the GEOPECO expedition. The high seismicity can be explained with a large taper and a high basal friction at the plate interface of the subducting Nazca Plate and the overlying South American Plate (Bialas et al., 2000).

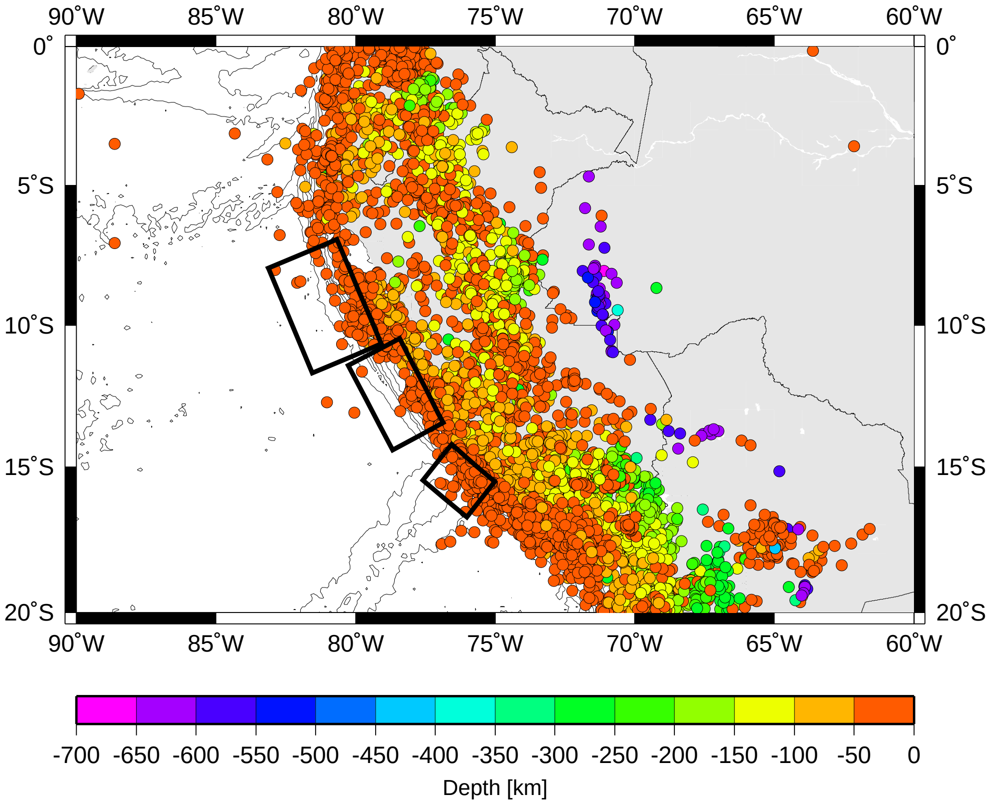

Figure 4: Depth of Seismicity for 1973 to 2001
The black boxes mark the areas of three-dimensional modelling.
(Seismic Data obtained from USGS: http://neic.usgs.gov/neis/epic/epic_rect.html)

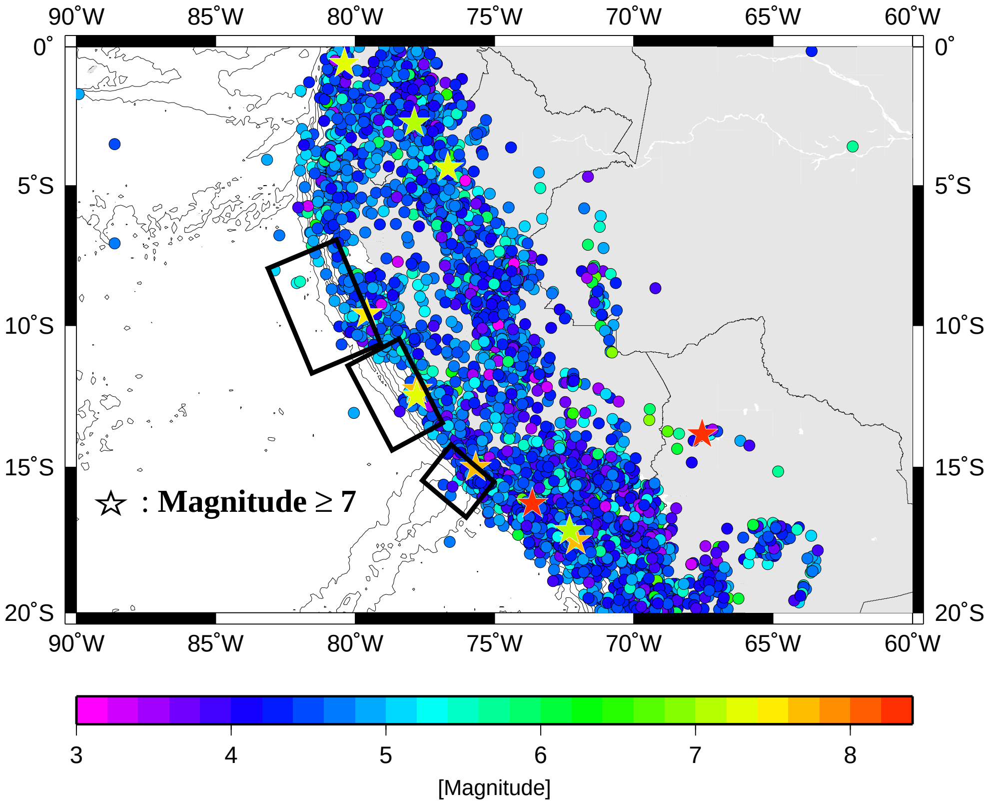

Figure 5: Magnitude of Seismicity for 1973 to 2001
The black boxes mark the areas of three-dimensional modelling.
(Seismic Data obtained from USGS: http://neic.usgs.gov/neis/epic/epic_rect.html)

3.4 The Continental Margin

The Andes do not exhibit a uniform structure. Along northern Peru and throughout most parts of Chile a single mountain range lies between the trench and the Precambrian rocks of central South America. In southern Peru the Andes are composed of two cordilleras. The western Cordillera consists of sedimentary and volcanic sequences of the Mesozoic and Tertiary (Cobbing, 1985). The eastern Cordillera, lying close to the Brazilian shield, is built of folded lower Paleozoic metamorphic rocks (Cobbing and Pitcher, 1972). The Altiplano molasse is located between the two cordilleras. The active surface deformation is concentrated along the eastern margin of the Andes in the thin-skinned Sub-Andean fold-and-thrust belt (Dewey & Lamb, 1992). There is an abrupt change in the trend of the mountain belt in Bolivia, from approximately northwest-southeast north of the bend to about north-south further south (Isacks, 1988).

Extensive linear batholith belts run parallel to the South American continental margin. The largest batholith is the coastal batholith of Peru. It is 60 km wide, over 1600 km long and comprises more than 1000 plutons which were emplaced between 100 and 37 Ma ago (Wilson, 1989). They were created during the Mesozoic and the Tertiary when a major plutonic phase of magmatism in Peru took place (Haederle & Atherton, 2002). According to Cobbing & Pitcher (1983) most batholiths are located within 3 to 4 km of the surface and were emplaced by permissive subsidence. The batholiths are composed mostly of tonalites and granodiorites which are linked to basaltic andesite dykes. The batholiths usually follow a linear trend over most of their lengths. A deep structural lineament is thought to have channelled the magmas on their way upwards. Along the whole western continental margin of South and North America similar granite batholith belts are exposed. All of these batholiths are intruded and surrounded by volcanic rocks related to the subduction process.

Many of the batholiths are situated in regions of thickened Precambrian crust (Haederle & Atherton, 2002). The Precambrian Arequipa massif in southern Peru consists mainly of gneisses and of pegmatites (Ocola et al., 1995). Underneath the batholith old high-grade metamorphic rocks of the Brazilian shield are located which crop out on the Pacific coast. In regions of thickened continental crust the magmas pass through more than 50 km of high-grade Precambrian gneiss before reaching the magma chambers. Along the northern Chilean coast Paleozoic and Mesozoic metamorphic rocks are exposed (Scheuber et al., 1994) and were recovered off shore (Kudrass et al., 1995). Along the Peruvian margin metamorphic continental crust has been recovered in several places offshore (Sosson et al., 1994; Kulm et al., 1988).

Along reverse faults block uplifting of the crystalline basement can be observed between 28˚S and 33˚S (Jordan et al., 1983). This is the dominant foreland deformation above the flat slab. The foreland deformation above the steeper slab between 15˚S and 27˚S is part of an eastwards moving thin-skinned fold and thrust belt (Jordan et al., 1983).

According to Cobbing (1985) the rocks of the western cordillera consist of intermingled Mesozoic and Tertiary sedimentary and volcanic sequences. The eastern cordillera is composed of folded lower Paleozoic slates and quartzites. The altiplano molasse is located between the two cordilleras.

According to magma types the active volcanism within the Andes can be divided into three zones (Thorpe et al., 1982). The northern volcanic zone is extending from 5°N in Colombia to 2°S in Ecuador. Here, lavas are mostly andesites and basaltic andesites. The composition of minerals and major elements is similar to island-arc magmas. Mesozoic and Cenozoic crust is underlying the northern volcanic zone. The central volcanic zone is extending from 16°S to 28°S in southern Peru, northern Chile, Bolivia and Argentina. In this zone the lavas are typically intermediate to acid in composition (Wilson, 1989).

The central volcanic zone is underlain by Precambrian basement and therefore the lavas carry a strong imprint of continental crust contamination. The southern volcanic zone is located in southern Chile and Argentina. In this area lavas are similar to those of the northern volcanic zone but slightly more basic. The most common rocks are high-alumina basalts and basaltic andesites. As in the northern zone young Mesozoic and Cenozoic crust is lying beneath this volcanic zone. In each of these regions volcanism has taken place episodically since the Mesozoic. The intense final period of active volcanism in central Peru took place between 11 and 8 Ma ago (Noble & McKee, 1977).

	Northern Volcanic Zone (5°N-2°S)	**Central Volcanic Zone (18°S-26°S)**	**Southern Volcanic Zone (33°S-45°S)**
dip of seismic zone	ca. 20°-30°	ca. 25°-30°	<25°
depth to seismic zone	ca. 140 km	ca. 140 km	ca. 90 km
maximum crustal elevation	4000-6000 m	5000-7000 m	2000-4000 m
crustal thickness	40 km	50-70 km	30-35 km
crustal age	Cretaceous - Cenozoic	Precambrian - Paleozoic	Mesozoic - Cenozoic
composition of the volcanic rocks	basaltic andesite to andesite	andesite-dacite with dacite-rhyolite ignimbrites	basalt with minor andesite and dacite

Table 1: The different volcanic zones (modified from Harmon et al., 1984)

The magmas originating from the mantle are interacting with the crustal rocks. Some of the more acid magmas may even be crustal remelts. The magmas contain information about the composition and thickness of the crustal rocks (Leeman, 1983). Complex processes of partial melting and fractional crystallization are to be expected within the crust. The intrusive rocks are gabbro, diorite, tonalite, granodiorite and granite (Uyeda, 1982). This range in rock composition is similar to that of the volcanic rocks implying that intrusive and extrusive rocks are genetically related. According to Uyeda (1982) the plutonic rocks are the root zones of former active volcanoes. The intermediate to acid intrusives are granitoids.

3.5 Faulting on the Nazca Plate and Along the Peruvian Margin

The Nazca Plate is being fractured by cooling stress as it moves away from the mid-oceanic ridge. Small volcanoes, sills and lava flows were observed on the oceanic crust. This intrusive and extrusive volcanism took place after the seafloor was created at the spreading centre (Hagen & Moberly, 1994). Seismic reflection and side-scan sonar profiles show examples of these sills and intrusions and demonstrate that some sediment was deposited before the sills were emplaced. The analysis of dredged samples from one of these volcanoes revealed basaltic glass with a chemistry unrelated to mid-oceanic ridge basalts (Hagen & Moberly, 1994). A reason for this volcanism may have been a broad thermal anomaly. This period of volcanism ended before the seafloor entered the zone of subduction-induced faulting at the outer slope of the trench (Hagen & Moberly, 1994).

Seaward of the Peru Trench an extensive region of sediment thinning and rough basement topography can be observed (Erlandson et al., 1981; Warsi et al., 1983). Caused by the bending of the Nazca Plate prior to subduction trench-parallel faults form grabens which are 3 to 5 km wide, about 200 m deep and up to 100 km long (Warsi et al., 1983). The faults on the subducting Nazca plate are oriented mostly parallel to the trench axis which trends about 315˚. The faults have not been developed by a reactivation of the already existing seafloor spreading fabric trending at about 335˚ (Hilde & Warsi, 1984). However, where the seafloor spreading fabric on the oceanic lithosphere differs from the strike of the dipping slab by less than 30˚ the faults are parallel to this fabric (Masson, 1991).

There is tectonic segmentation of the upper plate. The South American subduction zone shows an along-strike change in structural features (Allmendinger et al., 1983). This could be caused by the presence or absence of deep Paleozoic and Mesozoic basins. Downdip extension dominates in the subducting slab above 350 km, at greater depth downdip compression is dominating (Cahill & Isacks, 1992).

3.6 Bending of the South American Plate

Near Arica in northern Chile, at about 18˚S, a distinct bend of the South American Plate and a change in topographic and tectonic trends can be observed. Here, the counter-clockwise rotation in the north changes to a clockwise rotation in the south (Beck, 1998). In the Late Miocene the deformation tectonics in the Sub-Andean zone were most active. Since the Late Miocene the Andes, south of the bend, have rotated regionally in a clockwise direction by up to 30˚ relative to stable South America (McFadden et al., 1990). This rotation is proved by paleomagnetic data. According to McFadden et al. (1990) and Macedo-Sanchez et al. (1992) and also based on paleomagnetic data a regional anti-clockwise rotation around a vertical axis of up to 20˚ has taken place since the Middle Miocene.

The bending of the Andean mountain and the extend of Andean foreland shortening is controlled by regional variations in flexural rigidity (Watts et al., 1995). This explains the along-strike shortening gradients in the Sub-Andean zone which have been observed. According to Cahill & Isacks (1992) the continental plate has experienced considerable more shortening in the area of steep subduction between 15˚S and 27˚S. Shortening increases towards the bend region to about 100 to 150 km (Roeder, 1988; Sheffels, 1990). Deformation is more complex north and south of the bend in the Sub-Andean zones of Peru and northwestern Argentina (Allmendinger et al., 1983). Here, intense crustal seismicity in depths of some tens of kilometres is observed (Watts et al., 1995). The lithosphere shows variations in its flexural strength. This is a pre-Cainozoic feature of the South American Plate. As a consequence only thin-skinned deformation occurred where the lithosphere is flexurally strong (Watts et al., 1995).

3.7 Accretion along the Peruvian Margin

In the Andean subduction zone only a small accretionary complex has developed. The observable accretionary prism is associated with the steep lower continental slope (Kulm et al., 1985; Hussong & Wipperman, 1981). The accretionary morphology along parts of the Peruvian continental margin has been identified with swath mapping and with seismic surveys (von Huene et al., 1985) and consists of mostly pelagic and slope sediments (von Huene & Pecher, 1999).

The leading flank of the Nazca Ridge eroded the foot of the margin during subduction and therefore the time of ridge crest subduction defines a maximum age of the accretionary prism. This is supported by the results from drilling. During the subduction of the Nazca Ridge underneath the South American Plate the margin was tectonically eroded and a backstop was exposed by tectonical erosion (von Huene et al., 1996; von Huene & Pecher, 1999). The front of the Mesozoic margin is missing (Rutland, 1971; Scholl et al., 1970). After the subducting Nazca Ridge moved further southwards, a 10 to 15 km wide accretionary complex developed against this backstop (von Huene et al., 1996). On the wide-angle seismic profiles of the GEOPECO cruise a 20 to 30 km wide and 4 to 5 km thick accretionary prism was observed at 8°S, 11.5°S and 13.5°S (Broser et al., 2002). The accretionary prism therefore developed rapidly after the subducting Nazca Ridge had passed. It stopped growing when it reached its stable size (von Huene et al., 1996).

According to von Huene et al. (1996) the frontal 15 to 20 km of the continental margin comprise the accretionary prism and show a moderately steep slope angle between 6˚ and 9.5˚. Warsi et al. (1983) observed that sediments accrete only temporarily and are eventually subducted after slumping into the grabens on the Nazca Plate. The Peru prism probably grows adjacent to the trench and is basally eroded at the same time. Shepherd & Moberly (1981) proposed that, because a substantial accretionary wedge is missing, all material derived from the continent has either been subducted or removed laterally.

The backstop presumably consists of metamorphic rocks, similar to rocks sampled from the lower slope (Kulm et al., 1988). A stabilized backstop height prevents further seaward growth of the prism. When this stage is reached sediments are more easily subducted than accreted (von Huene & Pecher, 1999). Von Huene & Scholl (1991) have observed material being subducted beneath the active backstop. However, the backstop cannot be clearly determined from most seismic records (von Huene et al., 1996). The knowledge of the backstop's edges allows mass balance estimates.

When sediment accretion initiated, the taper increased to its maximum relatively fast. The taper stability field of the Peruvian margin is higher than that defined for typical accretionary wedges by Lallemand et al. (1994). With increasing age tapers trend toward a stable taper field. This stability field is determined by the coefficient of internal friction and cohesion as well as by basal friction which is influenced by pore fluid pressure (Dahlen et al., 1984). Convergence rate, taper and basal friction are large off Peru (Kukowski & Pecher, 1999). Strong sediments and a low pore pressure produce a relatively high basal friction. The critical taper, where continuous accretion occurs, lies at the lower boundary of the taper stability field (Davis et al., 1983). In northern Chile the margin shows a large taper as well, indicating a high basal friction where the subducting plate gets in contact with the strong continental crust (von Huene et al., 1999). The frontal part of the upper plate is thought to induce only a small basal friction because it consists of weak material. The coastal uplift caused by the subduction process invokes an unstable slope and accordingly gravitational sliding leads to a debris fill in the trench (von Huene et al., 1999).

The taper is different at 9˚S and at 12˚S due to other material properties. Compared to the prism at 12° at 9°S only very little was added to its volume after about 3 Ma of further plate convergence. The prism is composed of stronger material than the typical accretionary wedge. According to von Huene & Pecher (1999) the Miocene to Quaternary pelagic sediment accreted in the Yaquina Area might be stiffer than average turbidites.

According to Suess et al. (1988) diatomaceous sediment from upwelling along the shelf may be part of the turbidites because the sediment recovered in cores from the shelf and slope is particularly strong. Since the Miocene not much tectonic thickening of the sediment covering the back stop occurred at 9°S, as indicated by ODP cores. The material flux of the Peruvian margin was imitated with sandbox modelling (Kukowski et al., 2002).

The material flux along the central Peruvian margin was not constant during the subduction of the Nazca Ridge. The rate of turbidite sedimentation in the trench axis is changing. During the Pleistocene the rates of turbidite sedimentation increased (Suess et al., 1988). According to von Huene & Scholl (1991) the rate of sedimentation before 2.5 Ma ago was only 50%. The sediments in the trench axis vary from only very thin pelagic sediment to pelagic and turbidite sediment of 1 km thickness (Kulm et al., 1996). Turbidites followed the axial gradient and moved northwards where the trench gets deeper (von Huene & Pecher, 1999). Underneath the turbidites and on top of the igneous oceanic crust a layer of hemipelagic and pelagic sediment was observed. The rough seafloor topography is attenuated by the overlying debris and sediments. An unresolved question is how much continentally derived detritus is currently being subducted beneath the Andes.

The Nazca Ridge is forming a barrier for further sediment flow. North of the Nazca Ridge sediment is ponded. The same phenomenon was observed off Valparaiso in Chile where a thick sediment layer was imaged only south of the Juan Fernandez Ridge (Flueh et al., 1998). North of the ridge there is only little sediment infill and the trench shows a greater depth.

As can be seen in the swath bathymetry data of the GEOPECO expedition the roughness of the oceanic plate increases from the southern Nazca Ridge Area to the northern Yaquina Area (Kukowski at al., 2002). This is going to influence the accretionary behaviour of the margin in future.

A detailed description of the presence or absence of an accretionary prism in the areas of three-dimensional modelling is given in Chapter 4.

3.8 The History of the Peruvian Margin

Subduction beneath the western margin of South America began between the Late Devonian and the Late Triassic or Early Jurassic (Ocola et al., 1995). During the Jurassic period, about 150 Ma ago, South America was still joined to Africa, forming the subcontinent of West Gondwanaland (see Figure 6). In the Cretaceous, about 100 Ma ago, South America separated from Africa and drifted westwards. During the Early Tertiary, about 50 Ma ago, the Andean mountain chain was considerably uplifted.

In the Late Oligocene, a major reorganization of plate motions took place. At 22.8 Ma, the Farallon Plate split into the Cocos Plate and the Nazca Plate (Silver et al., 1998; Barckhausen et al., 2001). According to Gutscher et al. (1999a) the Grijalva Fracture Zone divides the old Farallon crust from the oceanic crust formed at the Cocos-Nazca spreading centre. The Grijalva Fracture Zone is currently subducting under the South American

Plate at 3°S, just north of the studied Peruvian margin. This dating is based on the identification of the oldest magnetic anomaly, 6B, which belongs to the initial Cocos-Nazca spreading ridge. The observation of discordant and distinct magnetic anomalies denotes abrupt changes in the spreading direction (Meschede & Barckhausen, 2001).

During most of the Eocene plate convergence took place at moderate rates in a north-oblique direction in northern Chile (Pilger, 1984; Pardo-Casas & Molnar, 1987). In the Oligocene slow and almost normal convergence has happened most of the time and from the Miocene to the present again a rapid and north-oblique convergence is occurring (Beck, 1998). The plate interaction in the Mesozoic is still not clearly understood because the magnetic lineations giving evidence about plate motions only date to the Latest Cretaceous (Beck, 1998). Between 8 and 5 Ma plate convergence occurred at an accelerated rate (Cande, 1985). At about 5.8 Ma a re-organisation of the tectonic plates in the circum pacific zone took place (Bird et al., 1998).

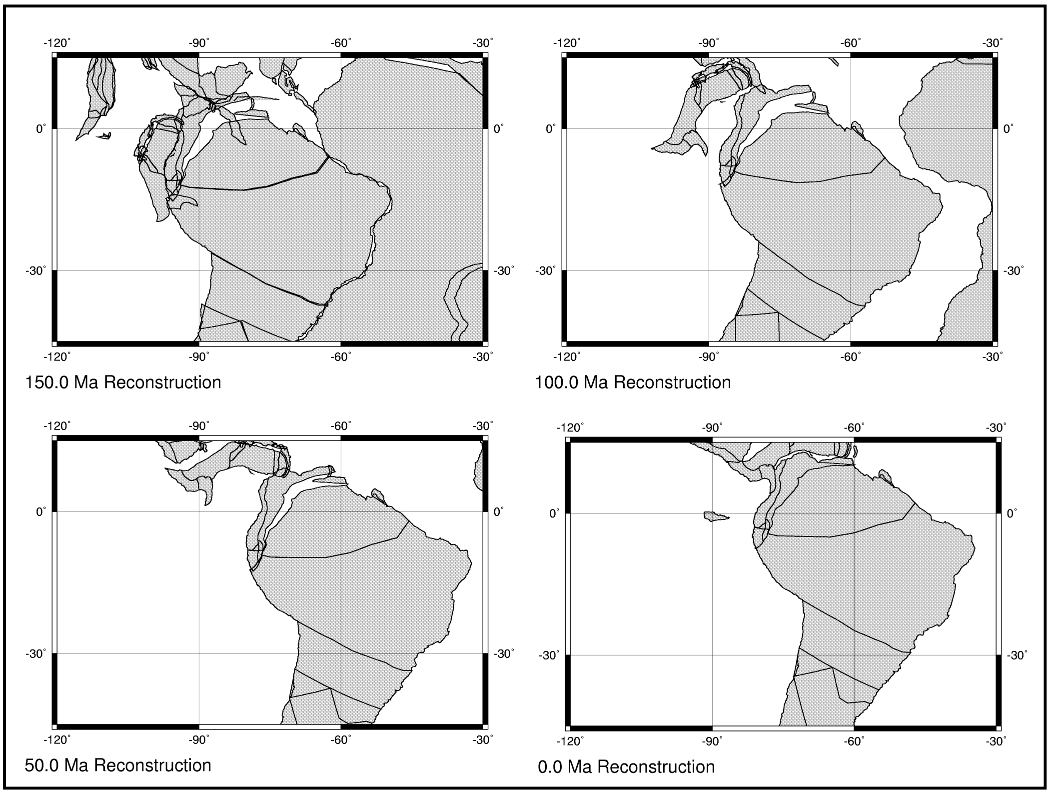

150.0 Ma Reconstruction

100.0 Ma Reconstruction

50.0 Ma Reconstruction

0.0 Ma Reconstruction

Figure 6: A Reconstruction of Plate Movement.
These reconstructions are based on paleomagnetic data and were obtained from: http://www.odsn.de

According to Gutscher et al. (1999b) an oceanic plateau, the Inca Plateau, has subducted beneath northern Peru 10 to 12 Ma ago. Kinematic reconstructions require this conjugate part of the Marquesas Plateau. The generation of the various plateaus and ridges found on the Nazca Plate is thought to be related to the mantle upwelling of the South Pacific Superswell (Gutscher et al., 1999b; McNutt, 1998).

A volcanic arc developed in the late Triassic or early Jurassic (Dalziel, 1986). Neogene volcanism along northern and central Peru ended gradually 5 Ma ago (Noble & McKee,

1977) after a strong pulse of magmatic and volcanic activity at 9.5 Ma. In the Pliocene the Nazca Plate started to subduct horizontally beneath central Peru. This change into horizontal movement is related to the termination of volcanic activity in the region (Noble & McKee, 1977).

A re-evaluation of the migration history of the Nazca Ridge shows that the ridge started subduction about 11.2 Ma ago at 11°S (Hampel, 2002). According to earlier reconstructions, 8 Ma ago the Nazca Ridge started to subduct at 8°S (Cande, 1985; Nur & Ben-Avraham, 1981). The Nazca Plate currently being subducted along southern Peru and northern Chile is at least 36 Ma old (Handschumacher, 1976). This area shows magnetic lineations which were created at the spreading centre in a northnorthwest-southsoutheast direction.

3.9 Gas Hydrates

The gravity and magnetic properties of the sediment layer are influenced by the occurrence of gas hydrates. Gas hydrates are ice-like, crystalline solids which are composed of water molecules surrounding a gas molecule, usually methane. Free methane gas is often trapped beneath the hydrate-bearing sediments. The hydrate-bearing sediments possess a higher density and a higher seismic velocity compared to the underlying low-velocity gas-filled sediments. A Bottom Simulating Reflector (BSR) is the base of a zone in which gas hydrates are stable. Due to the high impedance contrast the BSR is a strong seismic negative polarity reflector which is parallelling the seafloor. BSRs are observed in the upper few hundred meters of ocean bottom sediments. They are found on and adjacent to many continental margins, most often in accretionary sediment prisms at convergent continental margins.

As the gas hydrate stability depends on temperature the BSR describes local isotherms. Depending on the thermal gradient, marine gas hydrates can be stable down to a few hundred meters below the sea floor. The formation of gas hydrates naturally depends on the amount of available methane. The chemical bond of methane gas and its liberation is important for global climate models and the methane gas trapped within and beneath hydrates may eventually be economically important. The presence or absence of BSRs along the Peruvian continental margin is linked to vertical tectonism, sedimentation rates and the carbon content of the sediments (von Huene & Pecher, 1999). The methane concentrations necessary to exceed the methanes solubility at ocean bottom pressures are not easily achieved by a local biogenic degeneration of organic material. Methane could originate from upwelling of free or dissolved methane generated at depth or, alternatively, thermal perturbations such as those caused by continued sedimentation, which cause the base of the zone of hydrate stability to rise through the sediment column. The velocity increase in relation to the amount of hydrate in the pore space and the velocity decrease due to the presence of free gas is difficult to calculate and as a consequence, uncertainties in the determination of the seismic velocity remain. According to Housen & Musgrave (1996) an increased diagenesis of magnetic minerals takes place in zones of hydrate stability.

3.10 Seismic information along the South American convergent margin

The seismic information directly concerning the three research area is described in detail in Chapter 4. The only seismic profiles resolving the deeper structures of the studied Peruvian margin were acquired during the GEOPECO expedition.

At 33˚10’, off Valparaiso in Chile, a normal oceanic crust of 6 km thickness was observed with seismic wide-angle measurements (Flueh et al., 1998). Here, layer 2, with velocities increasing from 4.5 to 6.0 km/s, and layer 3, showing velocities grading from 6.4 to 6.8 km/s, were clearly resolved. For the mantle a velocity of 8 km/s was determined. Seaward of the trench the sediment layer is only 200 m thin. Its thickness increases to 3.5 km in the trench, southwards of the Juan Fernandez Ridge. A low-velocity layer has been attributed to underplated sediments. An accretionary wedge was observed which is thought to have developed in the last several million years.

At a depth of 100 to 150 km the slab velocities are very high with about 8.6 km/s. The seismic velocity contrasts between slab and the surrounding mantle are very high with 4 to 12% (Helffrich & Stein, 1993). As the subducting slab is subject to stress normal to the trench, this may lead to anisotropy aligned parallel to the maximum stress direction. There is a shear wave mantle anisotropy beneath central Peru. Parallel to the trench a fast polarisation direction for s-waves is observed. According to Russo & Silver (1994) the mantle shows the greatest anisotropy. Several different explanations were given for these high velocities. One is a thermal anomaly. If a thermal anomly is the reason for the high seismic velocities then the temperature would have to be as low as 400˚C. This low temperature contradicts the thermal models which predict 500˚C for the coldest 30 or 35 km of the slab interior. Another explanation for the high seismic velocities can be seen in anisotropic behaviour of the structures which are subject to shear stresses (Babuska & Cara, 1991).

3.11 Results from Earlier Gravity and Magnetic Investigations

Along the Peruvian batholith a positive Bouguer anomaly was measured indicating the presence of dense material at depth (Haederle & Atherton, 2002). The Bouguer anomalies are parallel to the coast and the axis of the batholith. The Bouguer anomaly field shows steep gradients of -4 to -5 mGal/km from the coast to 90 km inland. In total a drop of 400 mGal is observed (Haederle & Atherton, 2002). The batholith consists mostly of tonalite with a density of 2.66 g/cm^3. According to Watts et al. (1995) the Bouguer anomaly shows values of -400 mGal and is up to 1000 km wide in the region of the Altiplano in the central Andes. Positive anomalies are caused by local mass distributions.

Between 19˚S and 28˚S the observed gravity values correspond to a 65 to 70 km thick crust (Kirchner, 1997). Kirchner (1997) created a density model for the Chilean continental margin between 20˚S and 29˚S. The gravity highs in the Coastal Cordillera are caused by the contribution of the subducting, dense oceanic slab and a high-density zone in mid-crustal layers. In the region of the Coastal Cordillera und Eastern Cordillera the density model is isostatically undercompensated, i.e. a mass surplus is observed. In the region of the Altiplano-Puna the model shows an isostatic equilibrium to a slight overcompensation. At 22˚S negative Bouguer anomalies of up to -450 mGal were observed in the area of the recent volcanic arc (Götze & Kirchner, 1997). In the Jurassic forearc near the coast positive Bouguer anomalies of 100 mGal were measured.

Results of gravity modelling by Couch et al. (1981) at 17°S show that the oceanic crust is 5 km thick 500 km west of the coast and only 3 km thick near the trench. The depth of the Mohorovicic discontinuity could be determined to lie 60 km below sea level at 100 km inland. As a maximum the Mohorovicic discontinuity is located more than 70 km below sea level.

At 13.5°S Couch et al. (1981) found a two-layer oceanic crust of about 5 km thickness. The continental slope and the shelf are composed of two blocks with a relatively high density contrast. The upper block consists of sediments with an average density of 2.0 g/cm^3. The lower block is composed of crystalline rock with an average density of 2.75 g/cm^3. The crystalline block extends seawards to the toe of the continental slope. This crystalline rock crops out just east of the coast. A block of lower crustal material with a density of 3.0 g/cm^3 is intruding into a layer with a density of 2.75 g/cm^3 beneath the coast. The free-air anomaly requires a high density block of 3.0 g/cm^3 at a relatively shallow depth beneath the coastal gravity high.

At 12˚S a layer of basal oceanic crust with a density of 3.22 g/cm^3 was modelled (Couch et al., 1981). The toe of the continental slope is formed by several layers of low density sediments. It is situated between the trench and a formation of high density rocks, probably of the continental crust. A block with the high density of 2.9 g/cm^3 on top of another block with a density of 3.04 g/cm^3 was modelled in the upper crust.

At 9˚ high density rocks with a density of 3.0 g/cm^3 were modelled at shallow depth near and seaward of the coast (Couch et al., 1981). The shallow, high density rocks widen and shoal towards the north. The formation is centred near the coast at 14˚S and is located predominantly offshore at 9˚S. According to the interpretation of Couch et al. (1981) the high velocity rocks may be metamorphic rocks but are probably part of the gabbro or mafic rocks which are a major part of the crystalline continental block of western Peru.

In all areas thin crust was modelled close to the trench. The crust is bowed up and fractured seaward of the trench. Hayes (1966) determined from gravity modelling of the Peru trench that the oceanic crust is thinnest beneath and just seaward of the trench.

According to Couch et al. (1981) the structure of the continental margin is distinctly different on both sides of the Nazca Ridge.

Magnetic measurements were carried out in the area of the Mendaña Fracture Zone at 11°S (Huchon & Bourgois, 1990). Here, the magnetic lineations 1 (0 to 1.07 Ma) and 2A (2.58 to 3.58 Ma) were identified (Hilde & Warsi, 1982; Cande & Kent, 1995). These lineations are oriented approximately parallel to the fracture zone and about normal to the Peru Trench.

Hayes (1966) found that the magnetic anomalies measured along the South american margin cannot be correlated over large distances. According to Hayes (1966) the anomalies are caused by a remanent magnetisation of magnitudes many times larger than the predicted induced magnetisation and in a direction opposite to the earth’s present field.

Hayes (1966) observed that the magnetic signature is smoother over the shoreward flank of the trench than on the landward side.

Further magnetic investigations were carried out in other parts of the South American convergent margin. These are two of the very few works of three-dimensional magnetic modelling found in literature. Off Costa Rica Barckhausen et al. (1998) could explain magnetic anomalies by already subducted seamounts where seismics did not provide the necessary resolution. Explicit magnetic anomalies can be correlated with not yet subducted seamounts. With three-dimensional magnetic modelling it was attempted to explain the observed anomalies with already subducted seamounts. The principle characteristics of the observed anomalies could be reproduced by the modelled subducted seamounts. Barckhausen et al. (1998) noted that the observable anomalies get smoother and weaker with increasing subduction of the oceanic plate.

Near the Mejillones peninsula, off Antofagasta in northern Chile the magnetic lineations 20 to 22 were recognized (Roeser, 2000). Accordingly the oceanic lithosphere is 46 to 52 Ma old in this area. Here, the magnetic anomalies show a strike of about 135˚ and form an angle of 50˚ with the trench. Schreckenberger (1998) constructed a three-dimensional model for an area close to the Mejillones Peninsula. This model includes Chron 21 and consists of two stripes of oceanic crust magnetised normally and one stripe with reversed magnetisation. The magnetisation intensity applied is 5 A/m. A rock unit on the Nazca Plate off Antofagasta in northern Chile shows local variations of magnetisation. Schreckenberger (1998) postulates that the magnetic source layers are disintegrated mechanically just landward of the trench.

Off Valparaiso in Chile, at 33˚10’S, the now subducting oceanic crust is of Eocene age (Yañez et al., 2001). Here, at the edge of the middle slope, the observed magnetic anomalies are no longer caused by the northwest oriented stripes of the oceanic crust, but are trending east-westwards due to magnetic bodies in the continental crust (Yañez et al., 2001).

4 The Research Areas

The three areas of three-dimensional modelling are enclosed by the white boxes in Figure 7. The bathymetric characteristics of the Yaquina Area, the Lima Area and the Nazca Ridge Area are illustrated.

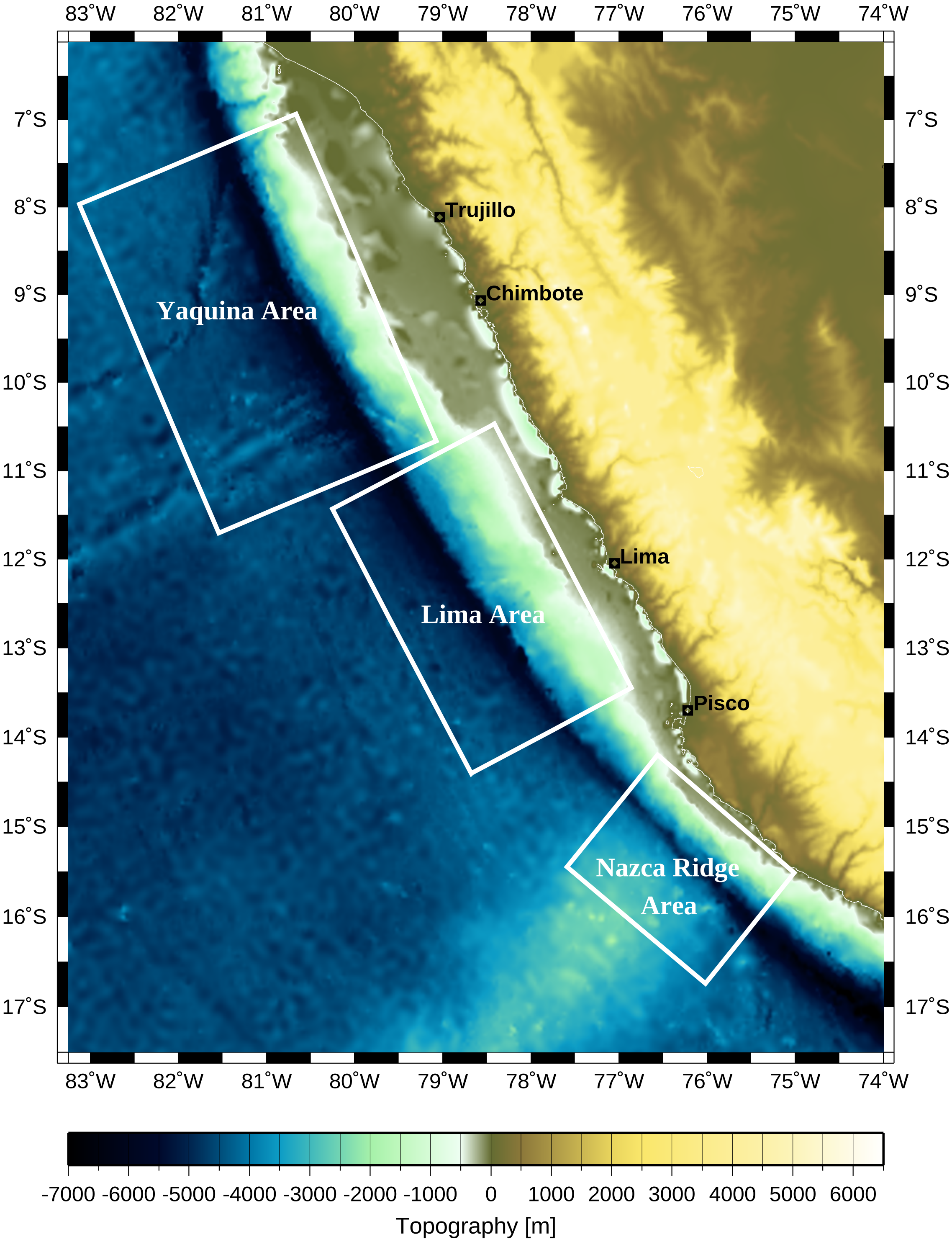

Figure 7: Location of the Research Areas. The bathymetric and topographic data were obtained from Sandwell et al. (2000, pers. commun.).

The study regions Lima Area and Yaquina Area enclose the Lima Basin and, respectively, the Yaquina Basin, the continental slope, the Peru Trench and part of the oceanic lithosphere.

The Peruvian Forearc can be subdivided into a lower forearc, a middle forearc, an upper forearc and the forearc shelf (Bourgois et al., 1988). During the subduction of the Nazca Plate beneath the South American Plate different forearc basins have developed. This series of elongated basins is located on the shelf and on the upper slope off Peru. The terraces and slope basins of the Peruvian forearc are common features of forearcs in general (Dickinson & Seely, 1979). They have developed by periodical thrusting caused by discrete pulses in accretion of material to the forearc (Johnson & Ness, 1981). Along the margin these terraces and slope basins are situated at a relatively constant depth parallel to the structural boundaries.

The Sechura Basin, the Salaverry Basin and the East Pisco Basin are located on the continental shelf. The basins are bounded by a margin-parallel outer-shelf structural high. A block-faulted Paleozoic or Precambrian metamorphic basement has been observed in these basins (Kulm et al., 1988). The Lima Basin, the Trujillo Basin and the West Pisco Basin are situated on the upper continental slope. The basins are bounded by an upper-slope ridge. There are no upper slope basins opposite the Nazca Ridge (Kulm et al., 1981).

The forearc basins are subject to vertical tectonic movement. Subsidence has not been a uniform process along the entire margin. The sedimentation in the forearc basins reflects these vertical displacements of the margin basement. The diagenetic processes in the forearc basins were controlled by the tectonic development of the continental margin. The terrigenous material is mixed with biogenic matter from coastal upwelling. Diagenesis is influenced by the range of chemical and sedimentological conditions. In the forearc basins diagenetic dolomitization of the sediments has been observed (Suess et al., 1987).

Several drill holes are located on the Nazca Plate along the Peruvian margin. The Ocean Drilling Project (ODP) sites 679 to 688 were cored during Leg 112 in 1986. They are situated seaward of two industry drill holes Delfin and Ballena, and landward of two DSDP (Deep Sea Drilling Project) sites 320 and 321 which were cored in 1974 (see Figure 9). They were cored to render constrains for geophysical and geological investigations. The results of drilling on the wide north-central continental shelf and the slope describe typical morphologies of the Andean margin. The drilling sites record the sedimentary history of the margin and provide reliable age constraints for the oceanic crust.

During the GEOPECO project 6 wide-angle seismic profiles were recorded and velocity models were created (Bialas et al., 2002). The 6 refraction seismic profiles are illustrated in Figure 8. The grey boxes mark the three research areas. Up to 14 ocean-bottom-hydrophones and -seismometers as well as a 24 channel streamer recorded signals generated by three 32 l BOLT airguns.

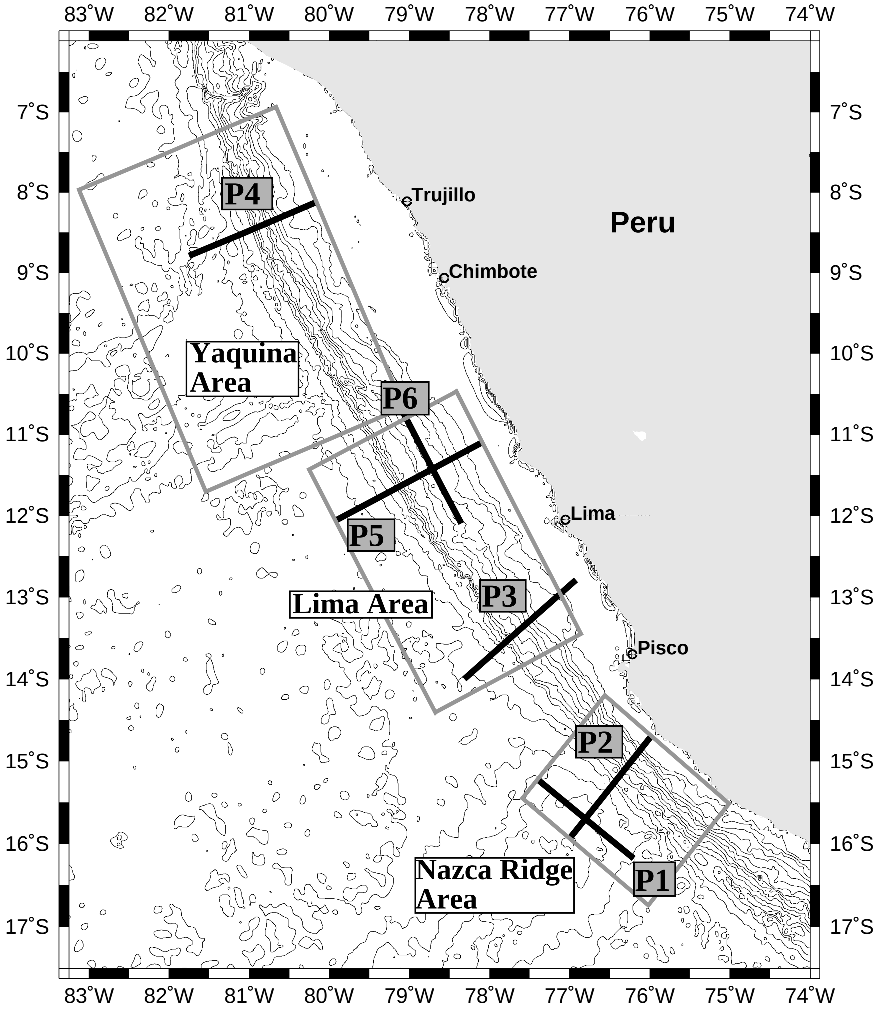

Figure 8: The Wide-Angle Seismic Profiles of the GEOPECO Expedition

4.1 The Yaquina Area

The Yaquina Area is located between 6.94°S and 11.71°S. It includes the Yaquina Basin which is situated between 8˚S and 10˚S on the midslope part of the Peruvian margin. Landward of the Yaquina Basin, in the northeastern part of the research area, the Trujillo Basin is located. The Yaquina Basin is separated from the upper-slope Trujillo Basin by a low basement high which has been described as the upper-slope ridge (Thornburg & Kulm, 1981). The outer slope high and the upper slope ridge are found in the major forearc basins of north-central Peru. The Yaquina Basin is located subparallel to the Andean structural orientation at water depths of 3000 to 4000 m (Suess et al., 1988). At 8˚S, where the refraction seismic profile P4 of the GEOPECO expedition is located, the Yaquina Basin is about 20 km wide and 2 km deep (Bialas et al., 2000). The Yaquina Area is crossed by the Mendaña Fracture Zone. North of the fracture zone the oceanic crust of the Nazca Plate is, with an age of 28 Ma, 10 Ma younger than the crust in the southern research areas.

Nearly normal to the trench a basement high separates the Yaquina and Trujillo basins from the Lima Basin in the south. This structure, accompanied by fractures and fault scars, was observed in swath mapping images by Hussong et al. (1988). Seaward of the trench a 700 to 800 m high and about 40 km long ridge, located subparallel to the trench axis, is currently being subducted (Bourgois et al., 1988). At 9°S a seismic line crosses this large subducting ridge which is offset by a transverse fault (Prince & Kulm, 1975). The structure of the trench axis and the deformation front are being distorted by the subducting ridge.

Where the wide-angle seismic profile P4 is located an only small accretionary prism with a width of 20 to 30 km and a thickness of 4 to 5 km is observed (Broser et al., 2002). The midslope terrace represents a structural boundary between this accretionary complex and the continental crust. The tectonic features on both sides of the terrace suggest that a large segment of transitional crust is missing (Suess et al., 1988). Low amplitude and irregular reflections dip landward seawards of the terrace and can be interpreted as accreted beds, upturned continental crust, or slope deposits. According to von Huene et al. (1985) the accretionary complex is part of the lower slope. Accreted sediment including turbidites were observed at 9°S. Here the subduction of an up to 1 km thick turbidite layer was observed (von Huene & Pecher, 1999). The prism landward boundary is described as a young morphology, without canyons and not very modified by slope sediment (von Huene et al., 1996).

In the seismic velocity models the young oceanic crust north of the Mendaña Fracture Zone is only 7 km thick, 3 km thinner than along the southern profiles (Bialas et al., 2000). The velocity model of profile P4 consist of the layers Pillow Lava, Sheeted Dykes and Gabbros, covered by sediments. Due to the rough seafloor topography the sediment layer is varying in thickness. The subduction angle and the lower slope angle are smaller than on the southern profiles. The oceanic plate subducts with a dip angle of 8˚. The resulting taper is 16° indicating high basal friction and a now non-accretionary subduction (Broser et al., 2002).

At 7°S in the Chiclayo Canyon which is oriented east-northeastwards, perpendicular to the trench axis, an accretionary prism has been observed. Here, a Paleozoic metamorphic basement, Eocene, Lower to Middle Miocene and younger rocks were recovered (Sosson et al., 1994). The sediment layer is of Early Pliocene age, i.e. it is 5.3 to 5.6 Ma old. Here, the margin subsided in the course of the subduction process. An older accretionary prism was completely eroded.

The Yaquina Basin was subject to uplift and subsidence of up to 1000 m (Kulm et al., 1988; von Huene & Pecher, 1999). The unconformity at the base of the Eocene used to be subaerial (Suess et al., 1988). According to Sosson et al. (1994) the subsidence of the Peruvian margin is explained by undercrustal subduction-erosion.

Highly sheared and recrystallized rocks were dredged from the lower slope (Kulm et al., 1988). This could be a sign of a seaward extension of the continental block or it could be part of an accretionary complex. The recovered conglomerates carrying quartzite and andesite pebbles are more clearly continental in origin. A significantly thick overburden must have been removed to expose these low-grade metamorphic rocks along the trench-slope border (Kulm et al., 1988). On the structural high which forms the seaward edge of the Trujillo Basin crystalline rocks of the continental lithosphere have been dredged (Kulm et al., 1988). At 7°S Paleozoic metamorphic basement of the continental margin was found to crop out along the middle and upper slope (Sosson et al., 1994). At 9°S Kulm et al. (1988) observed a high-grade metamorphic basement along the upper-slope ridge consisting of quartz-biotite gneiss and schist. Therefore the continental massif is extending beneath and seaward of the Trujillo Basin. Metamorphic basement, i.e. Paleozoic gneiss and schist, was found in two industry bore holes (Kulm et al., 1985). Pre-Andean, Paleozoic and Precambrian, continental metamorphic rocks were recovered from the outer slope high in industry drill holes at 9˚S and as island exposures at 12˚S. Shallow-water conglomerate located on top of the upper slope ridge was recovered. A turbidite layer of 300 to 600 m thickness was observed (von Huene & Pecher, 1999). The observed BSR indicates a source of organic-rich sediment which may originate from an area of coastal upwelling. According to Hübscher et al. (2001) BSRs are present in the Yaquina Basin and according to von Huene & Pecher (1999) strong BSRs are found in the accretionary prism of the Yaquina Area at 9˚S. Here, the accretionary prism remained undisturbed in the Quaternary providing stability for a developing BSR. On the lower slope terrace von Huene & Pecher (1999) found no BSR.

The slope shows a cover of reflections paralleling the slope on top of landward-dipping reflections. Underneath these dipping reflections subhorizontal layers are observed. The top of the crystalline crust can be followed across the upper slope. Horst-like basement structures and several normal faults on the landward flank have been observed (von Huene et al., 1985; Hussong et al., 1985). In this area the strata are strongly deformed. Faulting mainly took place in the Neogene.

The sediment thickness is variable in the Yaquina Area. On the Nazca Plate large scale horst and graben structures thinly filled with sediments were observed. These structures were not observed on the lines south of Mendaña fracture zone. At the base of the upper slope the upper sediments are very thin. The subducting oceanic crust shows local sediment-filled topographic lows. Subducted trench sediment has been observed as thick stratiform sequences in seismic records by Kulm et al. (1981) and von Huene et al. (1985). In the Yaquina Area the sedimentary sequence is known from different drill holes (see Figure 9). Underneath Quaternary-Pliocene sediments, Middle Miocene rocks are located on top of the Eocene.

ODP site 683 is situated at the edge of the Yaquina Basin (see Figure 9). The recovered sediment was deposited before the Neogene. It displays the continental sequence of a lithostratigraphy and geochemistry not usually found in ocean basins. This is a verification that continental crust extends this far seaward. Considerable subsidence has taken place. Here, rocks of Eocene age were also recovered. An unconformity between middle and upper Miocene sediment was found at Site 683. Here, Eocene and younger sediment lies unconformably on top of the basement.

Site 684 is located at the edge of the shelf. Middle Miocene sediment was recovered which provides a stratigraphic connection to the industry holes of Delfin and Ballena in the Trujillo Basin. The drill hole 684 reveals a stratigraphic history for the north-central Peruvian margin since Eocene time.

Site 685 is situated just below the midslope terrace. The cored rocks are of Eocene age and are clasts of a sedimentary breccia. These rocks are a sign for accretion and they determine the time when accretion started.

The DSDP hole 321 of leg 34 is located further seawards on the oceanic plate. Here, the basaltic basement of the oceanic crust was reached at 124 m. The oldest sediment recovered is of upper Eocene age.

The Eocene sediments can be followed from Site 683 landward across the upper slope to the basement ridge separating the Yaquina and Trujillo basins. This layer is thick in the Delfin drill hole, but was not found on the basement ridge penetrated at the Ballena hole. The distribution of the Eocene sediments was controlled by the subaerial basement topography with sediment transport from the east, trapping of the coarse fraction in the Trujillo Basin and the restricted outlet over a sill along the seaward basin flank. The drill holes of Leg 112 show consistent images of vertical tectonism. The benthic foraminifera in the ODP cores (Resig, 1990) show a pattern of subsidence as the subducting ridge migrated south causing water depths to increase across benthic foraminiferal depth zones. The depocentres in the Yaquina Basin moved northward.

The Ballena and Delfin exploration drill holes are situated in the Trujillo Basin, located on the shelf edge. Here, many small faults with limited offset can be observed (Thornburg, 1985). The drill holes revealed Eocene to upper Miocene continental shelf sediments on top of an erosional surface on Paleozoic metamorphic basement (Kulm et al., 1985).

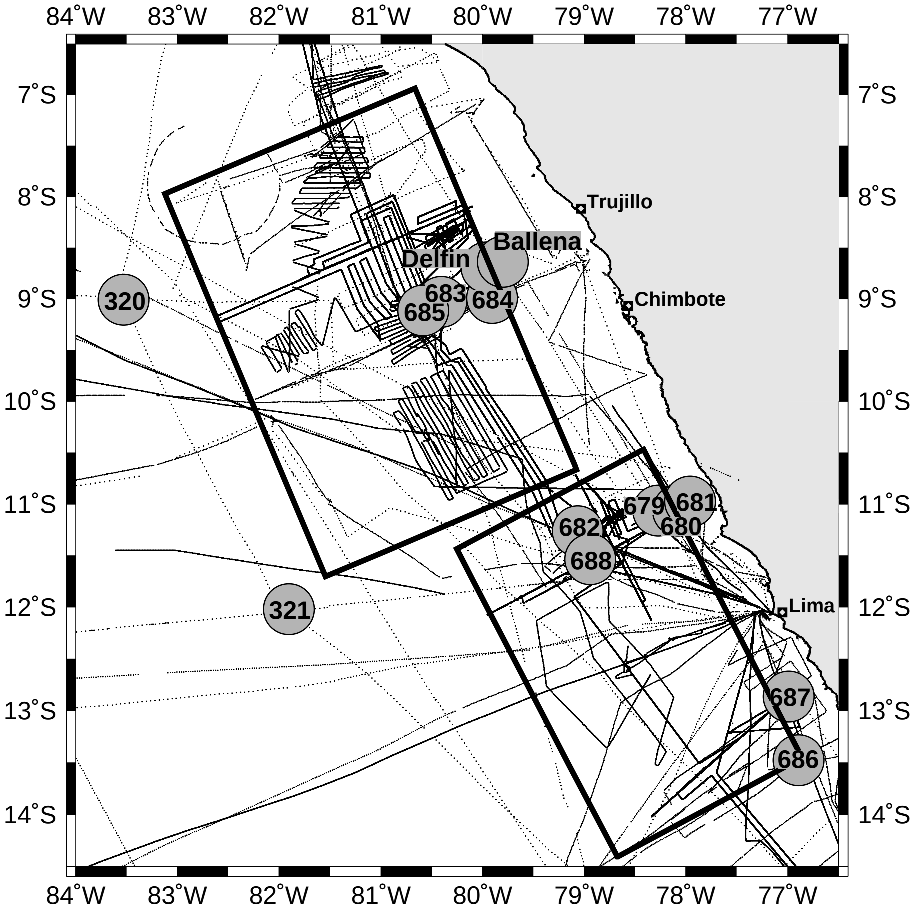

Figure 9: Drill Sites Along the Peruvian Margin Additionally, the gravity stations and profiles are imaged.

The Mendaña Fracture Zone, oriented N70°E, is crossing the Yaquina Area in its southern part. The fracture zone developed 3.5 to 4 Ma ago (Huchon & Bourgois, 1990). As a consequence to the ongoing rifting along the Mendaña Fracture Zone a left-lateral transpressive strike-slip fault characterises the Trujillo Trough to the north. The Trujillo Trough is trending N30°E. The Viru Fracture Zone features nearly pure thrusting

(Huchon & Bourgois, 1990). The opening of the Mendaña Fracture Zone is supposed to be similar to the formation of the rift which split the Farallon Plate into the Cocos and Nazca Plates at 23 Ma (Huchon & Bourgois, 1990). The Mendaña Fracture Zone is propagating westwards at a velocity of about 2 cm/year with respect to the Peru Trench. The fracture zone is about 100 km wide where it intersects the trench; 400 km seawards the fracture zone is only about 50 km wide. On average the sea floor lies at a depth of 5000 m south of the Mendaña Fracture zone and at 4500 m in the north. The changing depth of the Nazca Plate is consistent with the 10 Ma age difference (Huchon & Bourgois, 1990). A series of parallel ridges and troughs, oriented N65°E, is located within the Mendaña Fracture Zone.

4.2 The Lima Area

The Lima Area is situated between 10.47°S and 14.41°S. This research area comprises the Lima Basin which is located between 10˚S and 13˚S on the upper slope of the Peruvian continental margin. At 13˚S, where the basin is crossed by the refraction seismic profile P3, it is located at a water depth of 2500, is 5 km wide and 500 m deep. It is approximately 1 km deep at a water depth of 2000 m at 11.5°S, where profile P5 is located (Bialas et al., 2000). The Lima Basin is about 150 km wide and is separated from the Salaverry Basin on the continental shelf by a positive basement feature described as the outer-shelf high (Thornburg & Kulm, 1981). The stratigraphic sequences are mostly elongated, parallel to the trench and usually broad and undeformed. Here, the lower slope is 13 to 18 km wide and relatively steep (von Huene et al., 1996). As in the Yaquina Area high-grade metamorphic rocks, quartz-biotite, gneiss and schist, were dredged (Kulm et al., 1988).

At 13°, where P3 is located, the Nazca Ridge subducted 6 Ma ago whereas at 11.5°S, where P5 is situated, the Nazca Ridge passed 9.5 Ma ago (Hampel, 2002). According to von Huene & Lallemand (1990) the trench has retreated by about 2.5 km/Ma since the subduction of the Nazca Ridge.

On the refraction seismic profiles P3 and P5 of the GEOPECO expedition the observed accretionary wedge is very similar to that found in the Yaquina Area. Again the wedge is 20 to 30 km wide and 4 to 5 km thick (Broser et al., 2002). This accretionary prism has developed within only 2 to 4 Ma after the oblique subduction of the Nazca Ridge. The slope angle is 6° and the initial dip angle of the subducting plate is 8° on profile P3 at 13.5°S. On profile P5 at 11.5°S these angles are 9° and 6° respectively.

According to Miller et al. (1991) a 15-km-wide accretionary prism is located adjacent to the eroded margin. The prism landward boundary is described as a young morphology, without canyons and not very modified by slope sediment (von Huene et al., 1996). A local variability of the prism width has been observed with swath mapping and seismic investigations (von Huene et al., 1996). As in the Yaquina Area a 10 to 15 km wide accretionary complex developed of mostly pelagic and slope sediments (von Huene & Pecher, 1999). Landward, a 17 km wide terrace is observed showing a sediment sequence lying irregularly on high velocity rocks (Hussong & Wipperman, 1981). This wedge of high velocity rocks possesses only little internal reflective structure. The wedge, sediments and underlying oceanic basement can be observed across the middle slope to the terrace formed by the seaward flank of the Lima Basin. According to Hussong et al.

(1985) and von Huene & Miller (1988) there is a profound unconformity beneath the Lima Basin which truncates steeply dipping layers. A lower terrace is located along the upper edge of the lower forearc at a depth of about 3800 m (Hussong et al., 1988). As known from multichannel seismic reflection profiles this terrace lies above the boundary between the narrow wedge of accreted material and older accreted material or thinned crust (Moore & Taylor, 1988; von Huene & Miller, 1988). On the lower slope terrace von Huene & Pecher (1999) observed a strong BSR in the Lima Area. In contrast no BSRs were found in the accretionary prism of the Lima Area at 12˚S (Moore & Taylor, 1988; Ballesteros et al., 1988; von Huene & Pecher, 1999). Miller et al. (1991) also found the BSR to be laterally discontinuous in the Lima Basin.

Swath mapping images of the Lima Area show the absence of canyons although the slope is, with an inclination of 10˚, relatively steep (Hussong et al., 1988). A 100-m-high ridge at the top of the lower slope is bounding the edge of the lower slope terrace. It formed by tectonic uplift above the basement wedge. This ridge is an indicator of the landward boundary of the backstop. The backstop is marked by landward dipping reflectors (von Huene et al., 1996). At 12˚S a relatively small wedge built against this tilted continental backstop was observed (von Huene et al., 1996). A thick layer of younger sediments is located on the seaward side of the backstop. Seismic data show a varying, up to 300 m thick sediment cover on the subducting oceanic plate (von Huene et al., 1996). In extended areas a sediment cover is even missing. The bathymetric and the seismic data prove that at 8˚S the Peruvian continental margin is subject to tectonic erosion. Here, only little, if any, sediment was observed. As a substantial sediment cover is missing and since the topography is very rough tectonic erosion of the Nazca Plate is possible.

The wide-angle profiles P5 and P6 of the GEOPECO cruise show that the top of the basement is located at a depth of 5 km underneath the Lima Basin. Where the profiles cross each other the subducting Nazca Plate is seen at 15 km depth, the upper continental crust is 10 km thick (Bialas et al., 2002).

In the late Miocene and early Pliocene the Nazca Ridge subducted at 12°S and the Lima Basin was probably uplifted to sea level. After the crest of the Nazca Ridge subducted, the Lima Basin subsided to a depth of 2775 m and is still in the final stage of subsidence. The average subsidence rate in the past 3 to 6 Ma was between 300 and 900 m/Ma (von Huene & Pecher, 1999). The subsidence history of the Lima Basin can be seen in the benthic foraminifer assemblages and the coastal upwelling facies. The reconstruction of the sea-level position at 6 Ma, the median age of the hiatus at Site 679, describes a subsidence rate of 490 m/Ma. There are significant local variations in the subsidence rate (Kulm et al., 1988). Especially the changing subsidence rates in the Miocene determined the depositional processes in the Lima Basin. The area was uplifted between the middle and the late Miocene forming an insular platform. It was subject to erosion between 7 and 11 Ma and then subsided rapidly after approximately 5 Ma (Suess et al., 1988). In the middle and upper Miocene a lot of material from erosion of the insular platform was transported and reworked as indicated by Sites 682 and 688. At ODP Site 688 gas hydrate was recovered. In the upper Miocene, at the latest, a change from tectonic erosion to accretion occurred as indicated by the age of the accreted sediment drilled at Site 688. Today the former insular platform forms a buried ridge separating the upper- and middle-slope terraces.

Site 680 is located at the central position of the Salaverry Basin. Here, no more than 100 m of subsidence took place (Suess et al., 1988). The Lima Basin shows a landward and a southward movement. This movement can partly be explained with the relative subsidence of the landward part of the basin (Suess et al., 1988).

The tectonical and depositional processes in the Lima and in the Yaquina Basin occurred at different times and in different grades. In the Neogene deposition and structural development were significantly different in both basins (Ballesteros et al., 1988). The Lima Basin and the Yaquina Basin show remarkable variations in the shape and nature of their sequences. The factors controlling the sedimentation processes are closely linked with tectonics and are different in the Lima and Yaquina Basins. During the GEOPECO cruise landslides were observed between the Yaquina and the Lima basins (Wagner et al., 2001).

Three refraction seismic profiles of the GEOPECO cruise are located in the Lima Area. Profile P3 is situated at 13.5°S, normal to the trench. Profile P5 is also perpendicular to the trench at 11.5°S, profile P6 crosses profile P5 and is oriented parallel to the Peruvian margin (see Figure 8). The sediment cover of the oceanic crust is only thin. A large taper was observed in all lines. In profiles P3 and P5 the continental crust landward of the wedge is modelled with an obvious raising of the 4.0 to 4.5 km/s velocity isoline which may form the backstop for sediment accretion (Bialas et al., 2000). At 13˚ S, about 40 km seaward of the trench, the depth of the oceanic basement is varying by about several hundred meters (Bialas et al., 2000).

4.3 The Nazca Ridge Area

The Nazca Ridge Area is located between 14.20°S and 16.74°S and comprises the currently subducting Nazca Ridge. The ridge is a large, linear and aseismic submarine basement high. It is oriented northeast-southwestwards and is 100 to 200 km wide. The ridge enters the trench at about 15˚S and subducts obliquely beneath southern Peru. Here the trench is less than 5 km deep. The ridge extends for more than 1100 km to the southwest where it intersects the Easter Seamount Chain. Another 900 km of the Nazca Ridge have already been subducted (Hampel, 2002). The Nazca Ridge rises to an average depth of 3 km, partially 4 km, above the surrounding seafloor. According to Pilger & Handschumacher (1981) the Ridge possesses the same age as the adjacent seafloor. 8 Ma ago the ridge started to subduct beneath South America (Cande, 1985). As plate convergence takes place at 45˚ to the strike of the Nazca Ridge and almost normal to the continental margin the subduction zone of the Nazca Ridge continually moved southwards with 72 mm/year (Hampel, 2002). According to Hampel (2002) the subduction of the Nazca Ridge started about 11.2 Ma ago at 11°S. The Nazca Ridge subduction history was reconstructed. The geometry of the plates and the convergence rates determine a time when the Nazca Ridge subducted at any point along the margin (von Huene et al., 1996; Hampel, 2002).

Former seismic refraction and gravity measurements implied that the crust beneath the ridge is at least twice as thick as the surrounding seafloor (Couch & Whitsett, 1981). Where the Nazca Ridge subducts the continental slope is narrow and the shelf is nearly absent. The steepened lowermost slope is about 5 km wide (von Huene et al., 1996).

The subduction of seamounts locally increases the normal stress across the subduction interface and the structure of the overriding plate is affected (Dominguez et al., 1998). The subduction of the buoyant Nazca Ridge caused first uplift and then subsidence of the margin and is thought to be the reason for the especially shallow dipping angle of the subducting oceanic Nazca Plate beneath Peru (see Chapter 3.1.1) (Cross & Pilger, 1982; Gutscher et al., 1999b). The Nazca Ridge is able to slide beneath the forearc because it possesses slope angles of only 1˚ to 2˚ (Hagen & Moberly, 1994). Firstly the seamount indents the base of the trench slope by causing tectonic erosion. The ridge is causing uplift but only little compressional deformation of the forearc. Most other subducting ridges and seamounts are smaller in size and possess steeper slopes which cause not only uplift but also significant compressional lateral deformation as they are being subducted. Still, the subduction of the Nazca Ridge has had a great impact on the morphological characteristics of the Peruvian continental margin. An uplift of the forearc by as much as 1500 m can be observed in the northern part of the Nazca Ridge Area (Hagen & Moberly, 1994). It is the dominant response to the subduction of the Nazca Ridge. The uplift creates steeper and unstable slopes which are subject to erosion. Uplift is seen in the varied depths of two forearc terraces opposite the subducting ridge. The upper and lower terraces vary in depth, to the southeast they are more than 1500 m deeper. In the southern part of the Nazca Ridge subduction the Peruvian coast is rising at a rate of about 0.5 m/1000 years (Hsu, 1992). Further to the south the coast is uplifted by only 0.2 m/1000 years. During the southeastward movement of the Nazca Ridge the zone of forearc uplift is migrating southwards. In the area of the Nazca Ridge the outer shelf high, known from the central Peruvian forearc and composed of Paleozoic and Mesozoic igneous and metamorphic rocks, has been uplifted and forms the approximately 500-m-high, northeast-southwest oriented Cordillera de la Costa (Hsu, 1992).

In the Nazca Ridge Area the lower forearc is 10 to 15 km wide and consists of small trench-parallel ridges and ledges. In other parts of the Peruvian forearc these features have been interpreted as accreted sediment packets (Hussong et al., 1988). The boundary of the trench-parallel ridges and ledges is generally linear. Southwards, the steep lower slope is narrowing (Johnson & Ness, 1981). In the Nazca Ridge Area two levels of terraces varying in shape are situated on the forearc. The terraces are usually 5 to 10 km wide. One terrace is situated on the upper part of the lower forearc at about 3200 m depth in the north and 5000 m depth in the south, the other terrace is located at the base of the upper forearc slope. According to Hussong et al. (1988) these terraces are about half as wide as those observed in the Lima Area. The structural boundaries of the middle and upper forearc are not as distinct as those of the lower forearc and the structures are mostly not parallel to the trench axis (Moore & Taylor, 1988; von Huene & Miller, 1988). Higher backscatter indicates that consolidated material is exposed on the sea floor of the upper forearc (Hagen & Moberly, 1994). The upper forearc extends from the upper terrace to the edge of the forearc shelf at a depth of about 500 m. The forearc shelf is smooth and covered with sediment. There are a large number of small canyons and gullies in the northern part of the Nazca Ridge Area which might be due to erosion.

The current trench axis sediment thickness indicates axial sediment transport. The axial sediment transport is thought to occur over thousands of kilometres. North of the Nazca Ridge the trench contains small amounts of ponded turbidites which were transported from the north. The Nazca Ridge is a barrier for sediments moving southwards. Directly south of the Nazca Ridge almost no sediments were observed in the trench (Schweller et al., 1981).

The subduction of pelagic sediment on the ridge crest is favoured by the presence of a tectonized area which rises pore-fluid pressure. This is consistent with the erosive processes related to the Nazca Ridge subduction (Johnson & Ness, 1981).

In the Nazca Ridge Area subduction induced faults with offsets of up to 500 m can be observed. Normal faulting is dominant in this area. The faults start approximately 50 km seaward of the trench axis and become more frequent and show greater offsets towards the trench (Hagen & Moberly, 1994). In the deepest part of the trench reverse faults at narrow angles to the trench axis can be found. The oblique compressional stresses caused by the colliding Nazca Ridge may lead to structural lineations on the middle and upper forearc. On the middle and upper forearc there are lineations which are not trench-parallel, but show trends of 305°. There are trench-parallel lineations on the upper forearc in the southern part of the Nazca Ridge Area. Across the middle forearc and towards the trench the lineations change their trend to about 300° (Hagen & Moberly, 1994).

Trench parallel striking lineaments can be observed where the Nazca Ridge is reaching into the trench. These faults are the result of extension tectonics related to the bending of the Nazca Plate before starting subduction. Fractures were caused by the uplift of the forearc. The oblique subduction of the Nazca Ridge causes trench-parallel faults and possibly strike-slip fractures on the forearc (Hagen & Moberly, 1994). These faults show an only small offset. In the Nazca Ridge Area the faults are more trench parallel than parallel to the spreading fabric because, according to Hagen & Moberly (1994) the thick crust of the Nazca Ridge probably has no spreading fabric to provide preferred zones of weakness.

During the GEOPECO project a 1° by 0.7° (i.e. 111 km by 78 km) large area at the southeastern side of the Nazca Ridge was investigated by swath mapping. This area is bounded by the wide angle profiles P1 and P2 as well as the Peru Trench. Here, the Nazca Plate is slightly dipping northeast and southeastwards. Several seamounts and linear structures of up to several hundred meters height and probably of a volcanic origin were observed (Hampel et al., 2002a). A prominent seamount near the centre of the mapped area shows a typical volcanic appearance. This seamount has a height of approximately 600 to 700 m and a diameter of about 20 km. The seamount seems to be subject to erosion because only little roughness was observed. Another seamount is located in the western part of the Nazca Ridge Area. This seamount possesses a caldera and also shows a smooth topography. Close to it various small cone shaped peaks of about 200 m height were observed. Ridge-shaped linear structures trending approximately north can be observed. According to (Hampel et al., 2002a) the existence of the seamounts can be explained with very late stages of active volcanism. The mountains in the southeastern part are higher than these seamounts and show a notable sediment cover. The gentle topography in the southern part may be due to a sediment cover or erosional debris fill. At the crest of the Nazca Ridge approximately 300 m of pelagic sediments were observed. In the deepest part of the trench as much as 800 m of turbidites were found. The southeastern flank of the ridge shows a rather smooth topography and different volcanic structures. Trench parallel normal faults are seen close to the trench (Hampel et al., 2002a).

The rough surface of the trench possesses little to no sediment fill. Seismic data show that the actual sediment input along the margin varies, but never exceeds a thickness of about 300 m (Kukowski & Bialas, 2000). The linear structures causing a very rough relief have a southsouthwest-northnortheast strike in the northern part of the surveyed area, and strike almost north-southwards in its southern part. Therefore, they are oriented obliquely to the direction of convergence and to the strike of the trench. This implies that they are inherited structures and that they are not caused by the bending of the Nazca Plate at the beginning of subduction. About 80 km west of the trench an only thin sediment coverage and a smoother seafloor are observed indicating that the sediment supply is varying along the Peruvian margin.

The structure and the velocity field of the Nazca Ridge were determined from refraction and reflection seismic measurements during the GEOPECO expedition. Profile P2 is situated along the axis of the Nazca Ridge. It covers part of the oceanic plate seawards of the Peru Trench, the trench itself and reaches onto the continental shelf. Here, the Peru Trench possesses a maximum depth of about 5000 m. On profile P2 10 OBHs (Ocean Bottom Hydrophones) and 4 OBSs (Ocean Bottom Seismographs) were deployed. Clear signals were received over the entire length of 177 km but at least to a distance of about 100 km and partly up to 140 km. Unfortunately three OBHs failed to record any data at all. Accordingly an observational gap of 37 km lies between OBS 5 and OBH 1. Angle reflections from the Mohorovicic discontinuity were registered by most stations. On the continental shelf, however, the deployed stations recorded only poor PmP and Pn phases. Consequently there is only very little constraint over the northeastward extension of the crust-mantle boundary at greater depth. The Nazca plate can be traced to a depth of about 28 km (Hampel et al., 2002a). Profile P2 intersects with profile P1 at a right angle at 15°41.59’S, 76°47.59’W. Perpendicular to the ridge axis the refraction and wide-angle seismic profile P1 was recorded. Along this 98-nm-long profile 9 instruments were deployed. To correlate the data one OBS was located both in the middle of profile P1 and at the western end of profile P2. Unfortunately only the hydrophone of this instrument recorded data.

The seismic model of the Nazca Ridge consists of six layers with seismic velocities corresponding to the velocities of typical oceanic crust (Hampel et al., 2002a). The sediments show variations in thickness between 0.4 km to 0.6 km in the trench area with slight increases from 1.2 to 1.5 km in small sedimentary basins towards the continental shelf. Beneath the ridge axis, layer B (pillow lava) is thickened. This corresponds to the outcrop of rocks differing from the surrounding sediments as seen in reflection seismics. Layer C (sheeted dykes) shows a velocity increase and the top of the basement, layer D, lies at a depth of 7 km. This gabbro layer shows a lower velocity than the standard model of the oceanic crust. The Mohorovicic discontinuity increases in depth from 16 km in the north to 17 km beneath the ridge crest. At the southern end of the profile the Mohorovicic discontinuity lies at a depth of 14 km (Hampel et al., 2002a). The upper part of the Nazca Ridge shows a nearly symmetrical structure but an asymmetric root. The southeastern flank of the root is steeper than the northwestern side. The corresponding thickness of the oceanic crust is about 12.5 km in the north and 11.5 km in the south. The continental margin was modelled with velocities between 4.8 and 6.0 km/s (Hampel et al., 2002a).

Ocola et al. (1995) studied the coastal region of southern Peru with refraction and wide-angle reflection seismics and found a 0 to 7 km thick upper crustal layer with velocities of 5.4. Furthermore they found a 3 to 7 km thick layer with velocities of 6.0 km/s, a thicker layer with a velocity of 6.5 km/s and a relatively thick layer with the unusually high velocity of 7.3 km/s. Ocola et al. (1995) also observed a mantle velocity of 8 km/s. The first upper layers are interpreted as surficial deposits, metamorphosed sediments and granitic material of the coastal batholith overlaying the more basic rocks of the cratonic Arequipa massif. According to Ocola et al. (1995) a buoyant effect of the Nazca Ridge underneath the South American Plate does not disturb the crustal structure of the continent. In the studied area between Lima and the Peru-Chile border the refractor interfaces dip uniformly at about 5˚ northeastwards underneath the Arequipa Massif.

The refraction seismic profiles of the GEOPECO expedition show that the Nazca Ridge is covered by only some hundred meters of sediment. The profile perpendicular to the continental slope shows thickening of the incoming sediments towards the trench. No accretionary wedge was observed and therefore the sediments have to be completely subducted (Hampel et al., 2002a).

Near the crest of the Nazca Ridge the lower slope angle lies between 10˚ and 15˚. Together with the subduction angle of 12˚ the opening angle is 21˚ pointing at a high basal friction. A comparison with the GEOPECO profiles in the north shows that this may be interpreted as a consequence of the subduction of the Nazca Ridge and the erosion of a formerly present prism (Bialas et al., 2002). The Nazca plate subducts at an angle of about 9˚. The lower continental slope shows a steep topography with an angle of 8˚ and indications for erosion. The Mohorovicic discontinuity is gently dipping north-eastwards at about 11.7° beneath the continental plate, where its confirmed depth on this reaches 27 km.

In reflection seismics a streamer and a BOLT-Gun were deployed during the GEOPECO cruise. On profile P1, perpendicular to the ridge axis, a sediment thickness of approximately 300 m was observed. Near the centre of the line the basement crops out on the seafloor. On both sides of the outcrop strong reflections, interpreted as sill layers, are intercalated with the pelagic cover. Calderas or an abandoned spreading axis can be observed. According to the results of reflection seismics the Nazca Ridge is underlain by a magma chamber which has partly collapsed. Four different basement highs, up to 700 ms TWT high, were observed. At a depth of 2200 m a triangular basin is located. On the shelf several normal faults underneath a layer of parallel reflectors were observed (Hübscher et al., 2000).

The GEOPECO parasound data from the Nazca Ridge Area indicate that hemi-pelagic deposits, probably carbonated sediments, cover the basement. Several blocks which are tilted away from the depression axis, may be interpreted as a caldera or an ancient spreading centre (Hübscher, 2000).

4.3.1 Origin of the Nazca Ridge

The origin of the Nazca Ridge is explained by the interaction of the Easter Island hotspot at 109.45°W, 27.12°S with the spreading mid-ocean ridge (Pilger & Handschumacher, 1981). Another example of such an interaction is the formation of Iceland by the Iceland hotspot and the Mid-Atlantic Ridge spreading centre. The Nazca Ridge possesses a mirror image, the Tuamotu Ridge. The results from drilling, dredging and kinematic reconstructions support the theory that the Nazca Ridge and the Tuamotu Ridge are conjugate structures which are between 25 and 50 Ma old. The already subducted part of the Nazca Ridge under the South American Plate can be estimated by comparison with the shape of the Tuamotu Ridge (Pilger, 1981). Today the Tuamotu Ridge is located near Tahiti (see Figure 10).

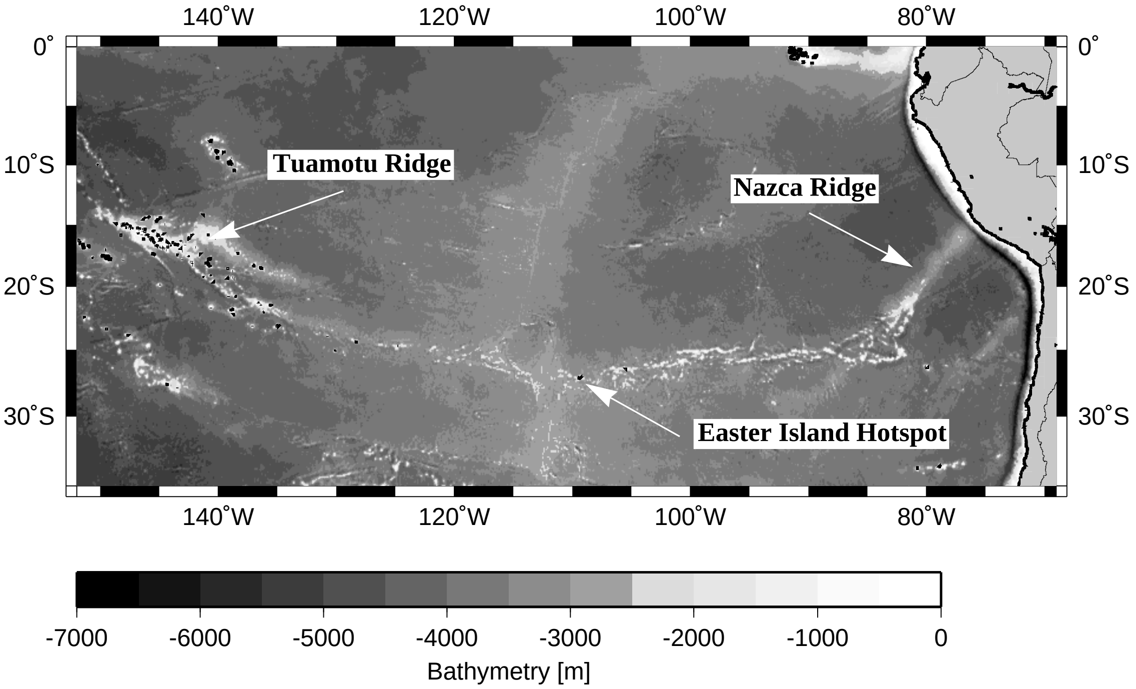

Figure 10: The Conjugate Structures Nazca Ridge and Tuamotu Ridge The bathymetric data were obtained from Sandwell et al. (1997).

5 Gravity Investigations

The aim of most gravity investigations is to model the earth's crust and upper mantle. The inhomogeneities of the mass distribution in the earth's crust and upper mantle are being determined. These density anomalies can be correlated with geological structures and tectonic processes. Gravity measurements are used to determine the geoid and help to understand the structure of the earth's crust and mantle. Furthermore the state of isostatic equilibrium can be determined by employing the gravity data.

Gravity anomalies describe differences between the measured gravity field and the theoretical and calculated field. A gravity anomaly is a sign of a surplus or a lack of mass. Gravity investigations are based on potential field calculations. Gravity models do not constitute unique models of the underground structures. An observed gravity anomaly can be caused by an unlimited number of mass distributions. The results from other geophysical and geological investigations are used to obtain the necessary constraints of the gravity models. The gravity measurements contain contributions from bodies at shallow depth, i.e. the residual gravity field, and from sources at greater depth, namely the regional gravity field. The deeper lying bodies produce long wavelength anomalies, the shallower bodies generate anomalies of sharper and shorter wavelength.

5.1 The Navigation Data of the GEOPECO Expedition

The navigation data were recorded every 10 seconds using the navigation system of RV SONNE. The navigation data were determined using the following independent facilities: x- and s-band ARPA-Radar, VHF radio-direction finder, a satellite navigation system consisting of one DGPS and two GPS receivers, two gyrocompasses, two autopilots, course and rudder angle recorders, rate of turn, Doppler log and Em-log. The results of these different methods are weighted with respect to their accuracy. The highest priority is given to the Global Positioning System. The bathymetric data were measured continuously using HydroSweep.

5.2 The Gravity Data and the Gravity Meter

The gravity data were collected using the air-sea gravity meter KSS 30/31, No. 15, Bodenseewerke Geosystem GmbH. The gravity values, together with the navigation data, were recorded continuously every 10 seconds during the whole cruise. The newly acquired data were compiled with all the available data from the GEODAS data base (GEOphysical DAta System, provided by NOAA and NGDC) after applying the necessary corrections. In Figure 11 the GEOPECO gravity data are displayed in black, the GEODAS gravity data are presented in grey.

The data processing consists of the following steps. Firstly, the data set is checked for erroneous values. After considering the frequency spectrum the recorded data are processed with a Gaussian, weighted average filter. Speed, heading and course are filtered before calculating the gravity anomalies.

A sea gravity meter measures relative gravity differences. The air-sea gravity meter KSS 30/31 consists of a gyro-stabilized platform, the gravity sensor KSS 30 and the data handling and control system KSS 31. The sensor contains a non-astasied spring-mass assembly (see Figure 12). The gyro-stabilized platform performs the stabilisation of the gravity sensor. With marine gravity measurements strong disturbing accelerations occur due to the sea state. These are short-periodic and can be eliminated by filtering. To minimize the influence of the sea condition the gravity meter is installed in the ship's meta centre. The remaining disturbing accelerations are counterbalanced by the gyro-stabilized platform. The sensor can still be stabilized at 30° for roll and 25° for pitch. The gyro is

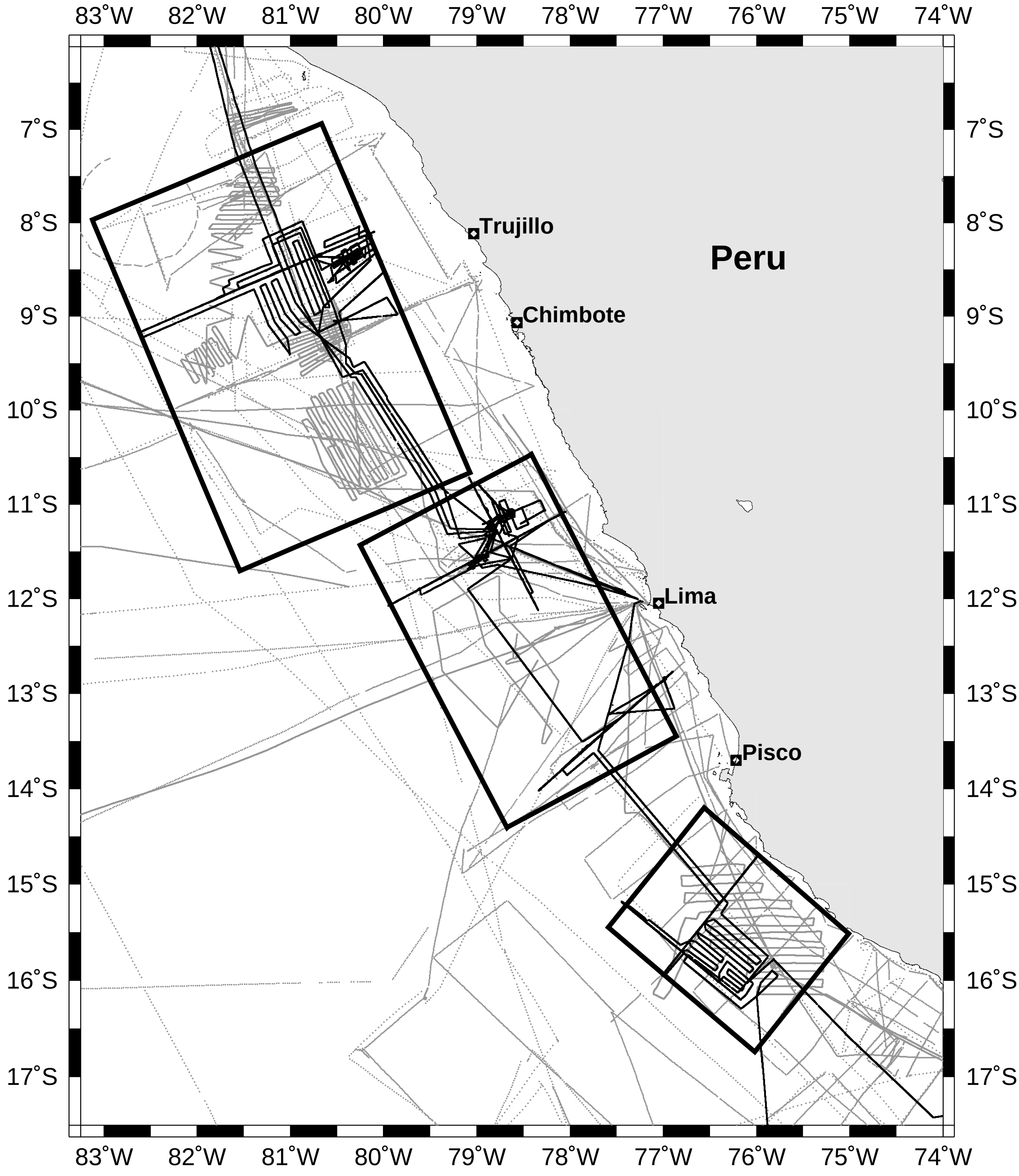

Figure 11: Overview of the Gravity Stations and Profiles
The gravity data acquired during the GEOPECO expedition are displayed in black, the gravity data obtained from the GEODAS data base are painted grey

gimballed and the position of the gyro axis in relation to the gyro box is continuously measured. The gyro box is subject to the same movements as the platform. The amplified electric signals direct two motors which turn the platform around two axes parallel to the Cardan axes. The platform has to be balanced horizontally. The mass can move exclusively in the z-direction and therefore only the z-component of gravity is measured. The method is completely insensitive to horizontal accelerations (see Figure 12). Changes in the spring’s length caused by gravity anomalies are transformed into a proportional amperage. The electric current causes magnetic forces on the solenoid, moving in a permanent magnet, to shift the spring back into its zero position. The coil’s amperage is an indicator of a change in gravity. To suppress the influence of the sea state the system is attenuated by digital filters.

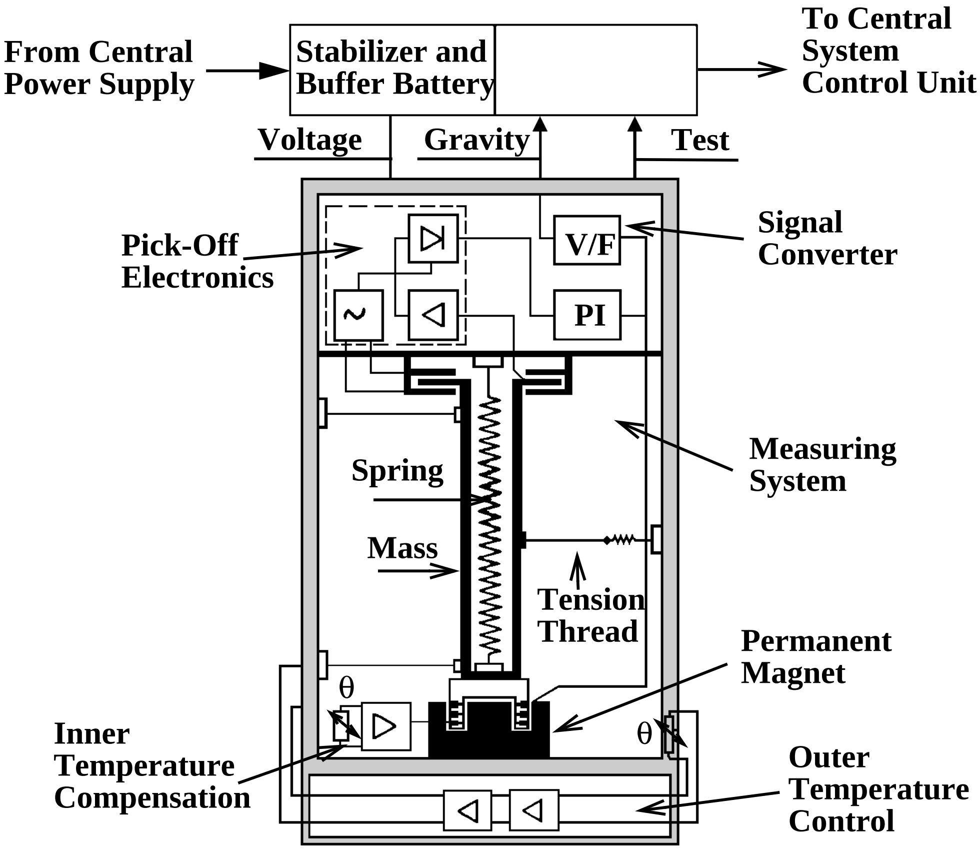

Figure 12: The Gravity Sensor GSS 30 (modified from Bodenseewerke Geosystems, 1981)

The relative gravity data measured on board RV Sonne were adjusted to the international absolute gravity net IGSN 71 on land by land tie measurements in the harbours of Arica (Chile), Callao (Peru) and Talcahuano (Chile). The land measurements were carried out using a LaCoste & Romberg gravity meter, model G, No. 260. The drift of the sea gravity meter was corrected by these land tie gravity measurements at port before and after both legs of the cruise. As given by the manufacturer a drift of less than 3 mGal per month can be expected. For the 63 days of the cruise a drift of only 0.68 mGal was determined. The drift is calculated by comparing the gravity measurements of the sea gravity meter and the land gravity meter in the beginning and in the end of the expedition. Taking into account the different sources of error an accuracy of measurement of better than 1 mGal was achieved. Figure 13 shows a histogram of the gravity differences at the crossing points of all considered profiles. Crossing points are defined as those areas where two profiles lie at a maximum distance of 22 m. The gravity differences show a Gaussian curve for a total of 232 cross-over points.

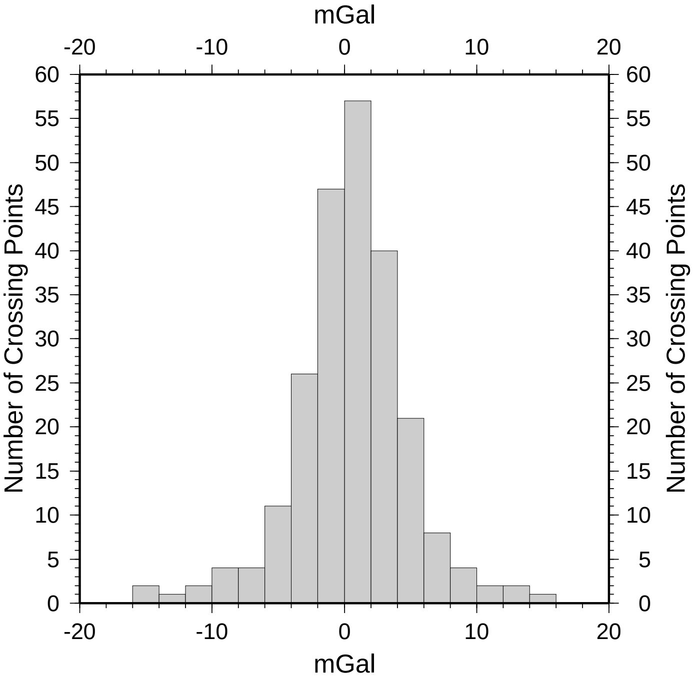

Figure 13: Histogram of the gravity differences at crossing points of profiles from the GEOPECO cruise and the GEODAS data base

5.3 Latitude Dependency

The geoid is the equipotential surface of the earth which is approximated by the average calm sea surface. The figure of the earth can be approximated with the geoid. The geoid is an equipotential surface of the gravity field. Positive gravity anomalies result in an uplifted geoid. The reference ellipsoid is approximating the complex figure of the geoid. It is a mathematically simpler reference surface for the gravity field of the earth. The reference ellipsoid is determined by geodetic, astronomical and gravity measurements. The results from satellite altimetry are most important in calculating the reference ellipsoid.

Before interpreting gravity data from a survey area the data have to be transferred to a reference level. The gravity field of the earth is depending on the geographic latitude. The gravity field of the earth is decreasing from the poles to the equator. This dependency is corrected when applying the international gravity formula. This equation gives the corresponding gravity value on the reference ellipsoid dependent on the latitude. The 1980 International Gravity Formula was applied to the measured gravity data:

$$g_0 = 978.0327(1 + 0.0053024 \cdot (\sin\varphi)^2 - 0.0000058 \cdot (\sin 2\varphi)^2) \qquad [mGal]$$

with φ = geographic latitude.

This International gravity Formula is a Chebychev approximation with a maximum error of 0.004 mGal.

5.4 The Eötvös Correction

The Eötvös Correction is the most important reduction for marine gravity measurements. The Eötvös effect describes the vertical component of the Coriolis acceleration which is occurring when the ship is moving. At sea the main error in gravity investigations results from incorrect navigation data. The determination of the velocity over ground is most difficult. Consequently the accuracy of gravity measurements at sea is dependent on the correct determination of the Eötvös correction. The Eötvös effect is described by:

$$\Delta g_E = 7.503 \cdot v \cdot \cos\varphi \cdot \sin\alpha + 0.004154 \cdot v^2 \qquad [mGal]$$

with v = velocity [kn], φ = latitude [°] and α = course [°].

As the east component of the ship's velocity lies in the same direction as the velocity vector of the earth's rotation the centrifugal force is increased. This leads to a reduction of the gravity value. Therefore, the largest error in calculating the Eötvös correction is caused by a wrong determination of the ship's velocity while on east-west course. The efficiency of the Eötvös-correction is dependent on the quality of the navigation data, especially the ship's velocity. By substracting the normal gravity field the latitude dependent gravity of a reference ellipsoid is taken as a reference for the gravity anomalies. After applying all corrections the measured data only contain the impacts of the anomalous mass distribution. The Eötvös corrections were applied and the 1980 theoretical reference gravity field was removed from the raw gravity values to produce the free-air anomaly map.

5.5 The Free-Air Gravity Field

The free-air reduction concerns the fact that gravity is decreasing with increasing distance to the reference height. As marine gravity measurements are carried out at the reference level no extra height correction factor has to be applied. In calculating the free-air anomaly only the normal gravity is being substracted from the observed values:

$$\Delta g = g - g_0$$

The gravity anomaly maps were compiled from a set of different surveys. The data collected during the GEOPECO cruise were merged with the available data of the GEODAS data base. The data set was edited to remove unreliable and spurious data points acquired while turning or accelerating quickly. The data were also checked and corrected for cross-over errors. The data acquired during the numerous cruises form an irregular network of profiles along the Peruvian continental margin. By interpolation of the original gravity data a regular grid was obtained. The gravity data were gridded at a spacing of 0.005°, i.e. 18” or 0.555 km, using GMT (Wessel & Smith, 2001). Based on these grids contour maps were constructed. According to the accuracy of the gravity data a contour interval of 5 mGal is still allowed. In order to obtain a clear image of the free-air anomalies a contour interval of 20 mGal is chosen in Figure 14. Naturally the pictured anomalies are only real where they are proved by shipboard measurements.

Figure 14 shows the free-air anomaly map of the Peruvian margin. A comparison between the bathymetric map (Figure 7) and the free-air anomaly map reveals many similarities. The main features of the free-air anomaly are related to topography. Offshore the free-air anomalies are caused mainly by the topography of the oceanic Nazca Plate. Most anomalies reflect bathymetric structures. The gravity lows coincide with the bathymetric lows most remarkably along the Peru Trench.

The gravity map contains information on tectonic features at both a regional and a local scale. All tectonic structures showing density differences will contribute to the gravity anomalies. Small but shallow formations can hide the effects of deeper bodies. The free-air anomaly describes the state of isostatic equilibrium of a large-scale structure like a sedimentary basin. It is very small if a region is totally compensated. The structure has to be at least ten times wider than the compensation depth. The free-air anomaly is positive if the structure is only partially compensated or not compensated at all. It is negative if the structure is over-compensated. By regarding the orientation of the free-air anomalies it is possible to roughly conclude on the isostatic anomalies.

In Figure 14 the negative anomalies reflect the Peruvian trench with values as low as -180 mGal. Between 9.4°S and 11.5°S this minimum is especially pronounced. South of 14°S the gravity values continually decrease until a minimum of -240 is reached at 17°S. Between 13°S and 14°S just a small negative anomaly of merely -120 mGal is observed although the trench is only about 200 m less deep than north of 12°S where the seafloor lies at a depth of 6.3 km. Remarkable, in comparison, is the strong negative anomaly in the area of the Nazca Ridge where the Peru Trench shoals to a depth of less than 5 km. The negative anomalies related to the Peru Trench show a relative maximum in the southern part of the Lima Area. The free-air gravity minimum is expanded towards the South American continent between 10°S and 13°S. In the northernmost part of the displayed region and between 8°S and 9.5°S an expanded maximum, showing gravity values ranging between 20 and 120 mGal, is located adjacent to the South American continent.

The expression of the Nazca Ridge in the free-air anomaly map is an expanded maximum with gravity values ranging between 20 and 40 mGal including one peak with values up to 60 mGal. The surrounding seafloor exhibits free-air gravity values of 0 to 10 mGal. The gravity maximum is entering the seaward part of the Nazca Ridge Area, indicated by the southern black box.

The Trujillo trough is envisaged as a free-air minimum oriented northnortheast-southsouthwestwards. It is located between 7.8°S and 9°S and shows gravity values ranging between -20 and -40 mGal. A series of local maxima and minima is located along the southern seaward side of the Peru Trench in the Yaquina Area. The Mendaña Fracture Zone is most probably the cause of these anomalies.

The oceanic Nazca Plate is dominated by short- and medium-wavelength features pointing at a varying basement topography and at a varying thickness of the sedimentary cover. Seawards of the Peru Trench the Nazca Plate shows free-air gravity values around 0 mGal. This region is isostatically compensated. In the area surrounding the Nazca Ridge the free-air gravity values are slightly higher than further north-westwards.

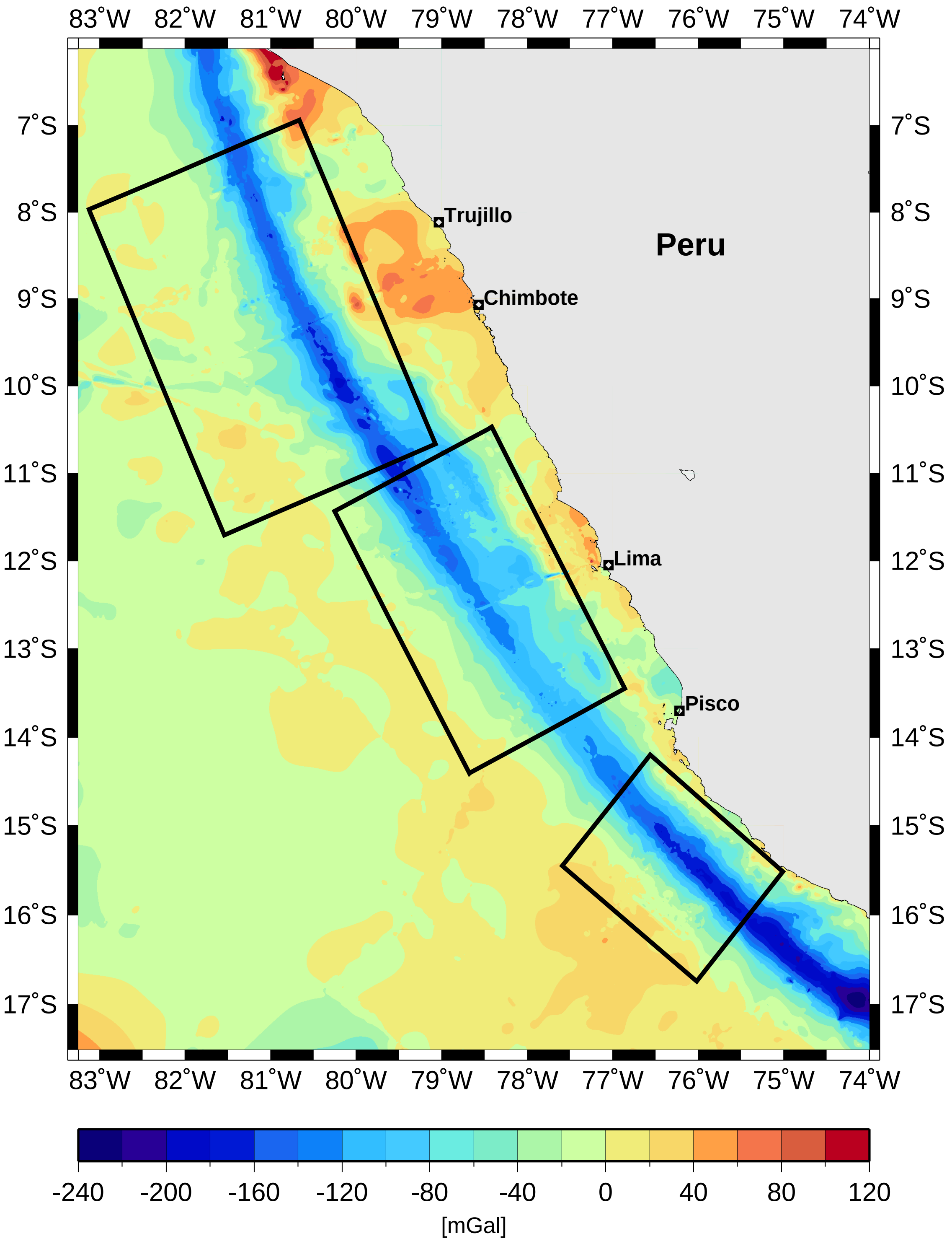

Figure 14: The Free-Air Anomaly Map

5.6 The Regional Free-Air Gravity Field

In order to isolate the gravity field caused by upper crustal sources, a residual free-air anomaly map was produced (see Figure 16). This residual map was created using polynomial trend surfaces and wavelength filtering. Wavelength filtering helps in determining the depth of the different anomalous bodies. The regional-residual separation of the gravity field is non-unique, not all the regional trends may be excluded and not all the local anomalies are retained in the residual fields. Therefore, these maps may only be used for a qualitative interpretation.

The regional – residual gravity field separation is presented in the following. The regional trend was calculated as a third order polynomial surface. A polynomial surface possessing the order 3 provides the best approximation to the observable gravity field. The data were gridded and smoothed using the inverse distance method. The low-order polynomial trend was fitted to the two-dimensional gridded data by a weighted least-squares method provided by GMT (Wessel & Smith, 2001). The trend surface is defined by:

$$m_1 + m_2x + m_3y + m_4xy + m_5x^2 + m_6y^2 + m_7x^3 + m_8x^2y + m_9xy^2 + m_{10}y^3$$

The data were iteratively reweighted based on a robust scale estimate, in order to converge to a solution insensitive to outliers. Thus, the planar trend of the regional field was separated from the observed gravity field.

The regional free-air anomaly map shows a linear trend (see Figure 15). The gravity values increase from -60 mGal close to the South American continent to 60 mGal in the southwestern part of the studied region.

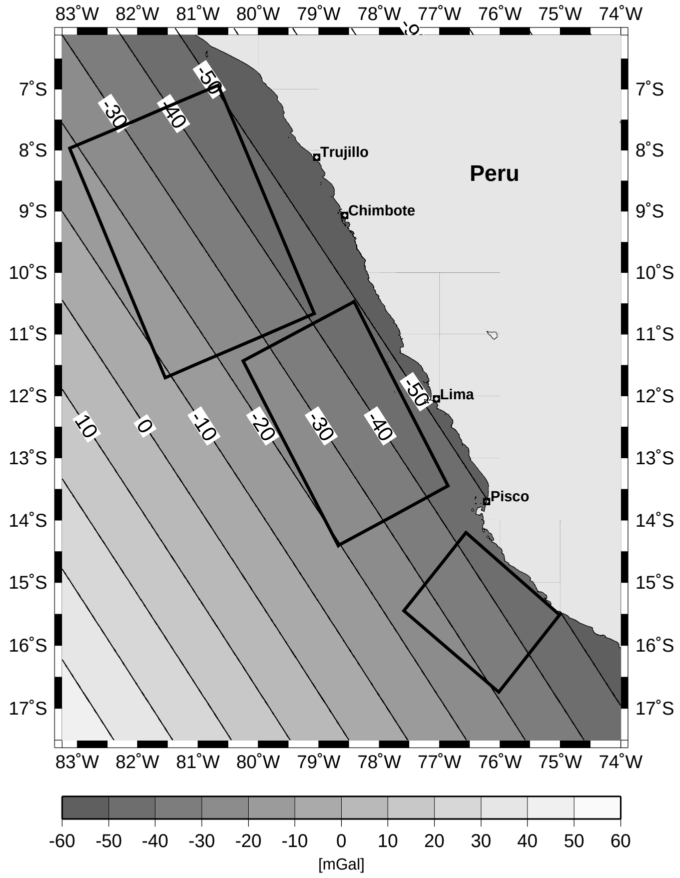

Figure 15: The Regional Free-Air Anomaly Map

5.7 The Residual Free-Air Gravity Field

The residual gravity map has been compiled by removing the regional trend and therefore by applying a high-pass filter. Especially in the area of the Nazca Ridge and close to the South American continent the residual free-air anomaly map shows more positive values than the normal free-air anomly map. The gravity anomalies mostly range around 100 mGal close to the South American continent and are as negative as -200 mGal in the southern Peru trench. The oceanic plate now shows a considerable negative anomaly of -60 mGal. The general characteristics of the free-air anomaly map can still be observed in the residual free-air gravity.

A large wavelength anomaly describes the change of gravity values from the seaward side of the imaged area to the Peru Trench. The residual gravity values increase from -60 mGal in the southwest to 40 mGal just seawards of the trench. The gravity maximum of up to 80 mGal caused by the Nazca Ridge forms an exception to this pattern.

In the Yaquina Area short wavelength anomalies are predominant. These anomalies indicate a rough topography of the ocean floor. Landward of the Yaquina Area, close to the Peruvian cities of Trujillo and Chimbote, a high maximum of up to 140 mGal is located. A comparison with the bathymetric map shows that this maximum is partly caused by the relatively shallow water depth. As a comparable maximum is not found in other parts of the margin, where the sea floor lies at a similar depth, an especially dense material can be expected landward of the Yaquina Area. The Mohorovicic discontinuity may be located at shallow depth.

A more detailed description of the free-air anomalies in the areas of three-dimensional modelling is given in Chapter 7.

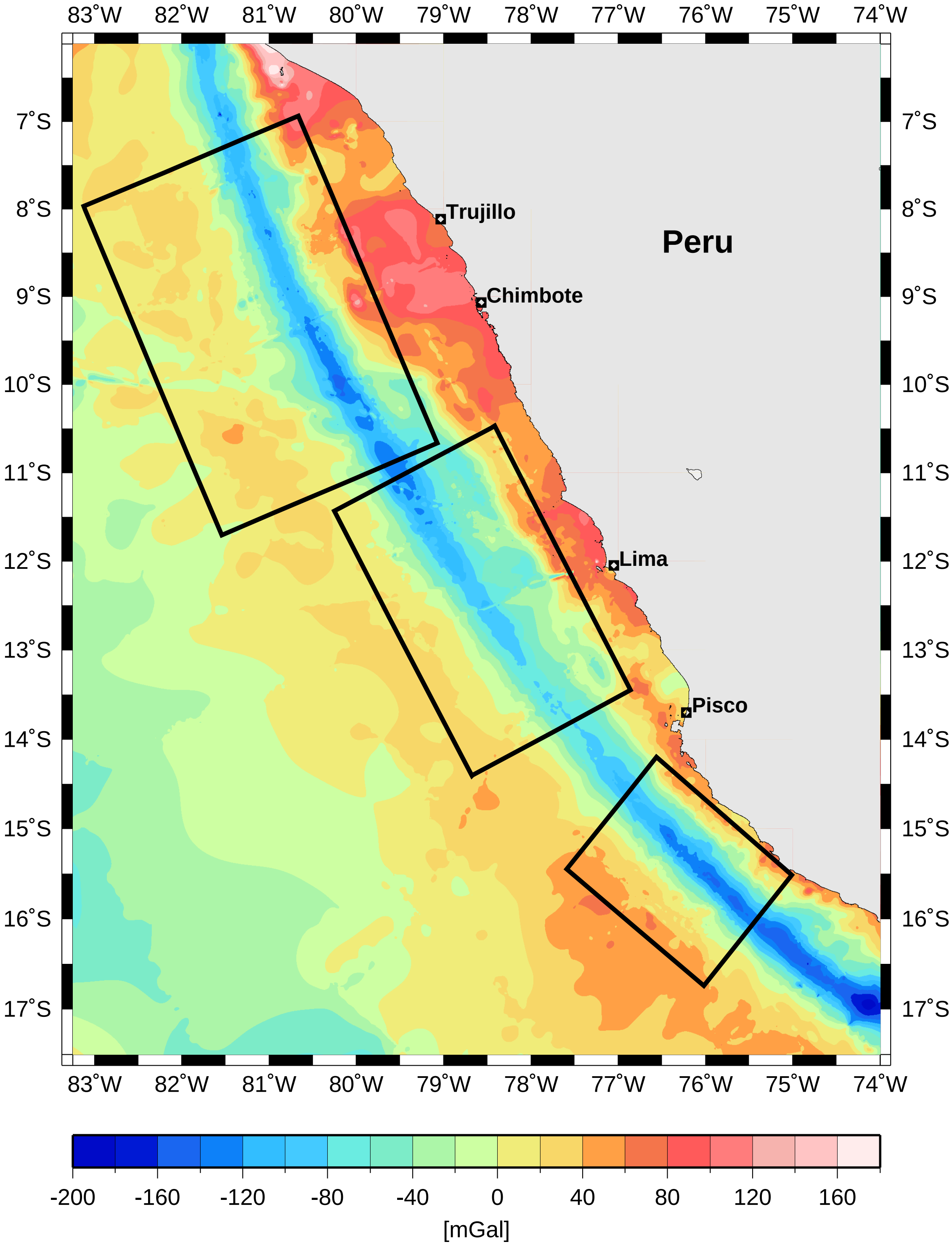

Figure 16: The Residual Free-Air Anomaly Map

5.8 The Bouguer Gravity Field

When applying the Bouguer correction to marine gravity measurements the water body is substituted with a homogeneous material possessing the average crustal density. In this work a Bouguer reduction density of 2.67 mg/cm^3 was used. Accordingly the Bouguer correction is:

$$\delta g_{Bouguer} = 2 \cdot \pi \cdot f \cdot \rho \cdot h = 0.11873 \cdot h \qquad [mGal]$$

with f = gravitation constant, ρ = density, h = depth of the ocean floor

The Bouguer gravity Δg_B is obtained by substacting the free-air correction δg_F, the Bouguer correction δg_B and the normal gravity γ_0 from the measured gravity value g.

$$\Delta g_B = g - \delta g_F - \delta g_B - \gamma_0$$

In Figure 17 the Bouguer anomaly map along the Peruvian margin is displayed. Where the water depth is high the Bouguer anomaly usually shows comparatively strong anomalies of approximately 300 mGal. The increasing Bouguer gravity observed offshore is due to the thinning of the continental crust. These anomalies are caused by the dense upper mantle which is located relatively close to the sea floor. The deeper a body causing a gravity anomaly is placed the longer the wavelength and the smaller the amplitude of the anomaly.

The Bouguer anomaly is negative for a totally or partially compensated structure, an excess of less dense material beneath the measurement station. It is zero for a non-compensated structure. The Bouguer anomaly is positive when an excess of especially dense material is present. The absence of a large Bouguer anomaly associated with the extreme relief indicates that the area is, as could be expected, not isostatically compensated by local variations in the crustal or mantle structure. If the area is not completely isostatically compensated by local variations in the crust or mantle an additional dynamic compensation mechanism must be considered.

The Peru Trench is characterised by Bouguer anomalies of 260 to 500 mGal. Where the Nazca Ridge is currently subducting the anomaly decreases to 160 mGal. South of the Nazca Ridge the residual Bouguer gravity is highest with 520 mGal. A sharp boundary depicts the seaward extend of the continental margin. A strong transition-effect at the change from oceanic to continental crust can be observed. Residual Bouguer gravity values of about 140 to 200 mGal describe the beginning of the continental margin. Further landward another sharp boundary exists with gravity values of 40 to -20 showing minima of -80 mGal.

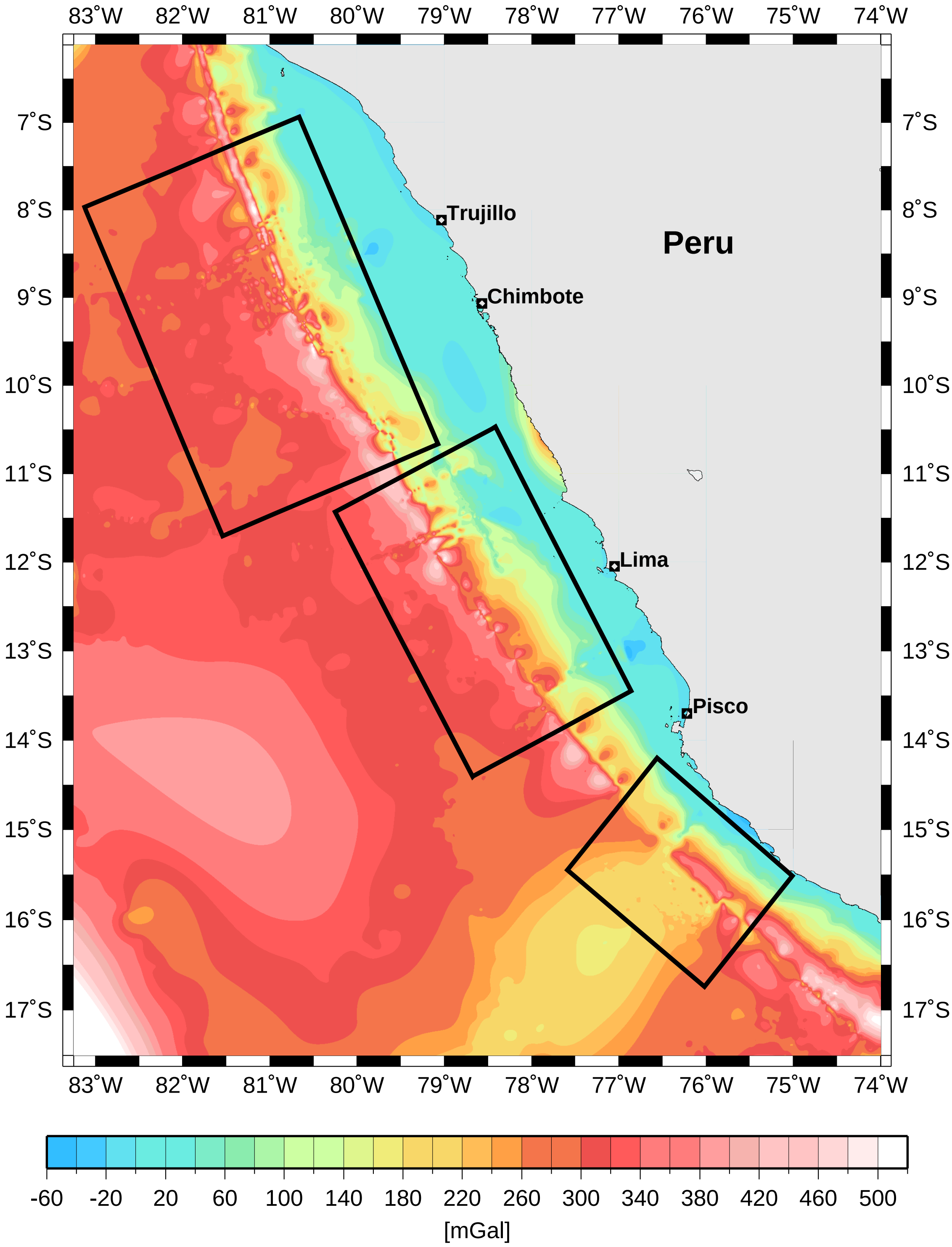

Figure 17: The Bouguer Anomaly Map

5.9 The Regional Bouguer Gravity Field

The long wavelength components of the Bouguer gravity field can be attributed to major crustal density variations or undulations of the crust-mantle boundary. Similar to the regional free-air gravity the regional Bouguer gravity exhibits a linear orientation parallel to the continental margin (see Figure 18). The regional Bouguer gravity values range from 0 mGal close to the margin to 600 mGal in the southwestern part of the studied area. As the data density is low in the southwestern part of the examined region, the high gravity value of 600 mGal may be explained by extrapolation.

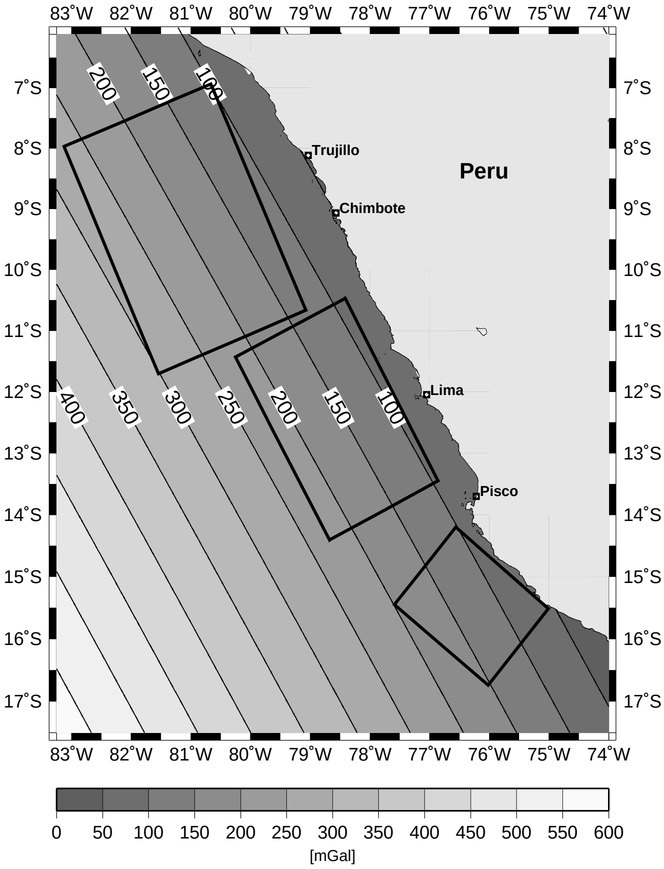

Figure 18: The Regional Bouguer Anomaly Map

5.10 The Residual Bouguer Gravity Field

The residual Bouguer gravity field is the difference field obtained by substracting the regional Bouguer gravity field from the observed Bouguer gravity field. The shorter wavelength components remain in the residual field. In Figure 19, displaying the residual Bouguer gravity map, the same colour scale was chosen as in the normal Bouguer anomaly map.

Along the Peru Trench the anomalies mostly range between 180 and 260 mGal. Where the Nazca Ridge is currently subducting the anomaly decreases to 20 mGal. South of the Nazca Ridge the residual Bouguer gravity is highest with 420 mGal. The continental margin shows negative values of about -100 mGal. Seaward of the subduction zone an expanded area with values between 60 and 80 mGal is observed. Further seawards the Nazca Plate shows a decreasing residual Bouguer gravity. Due to the insufficient number of gravity profiles, the anomalies are rather unreliable in the southwestern part of the research area.

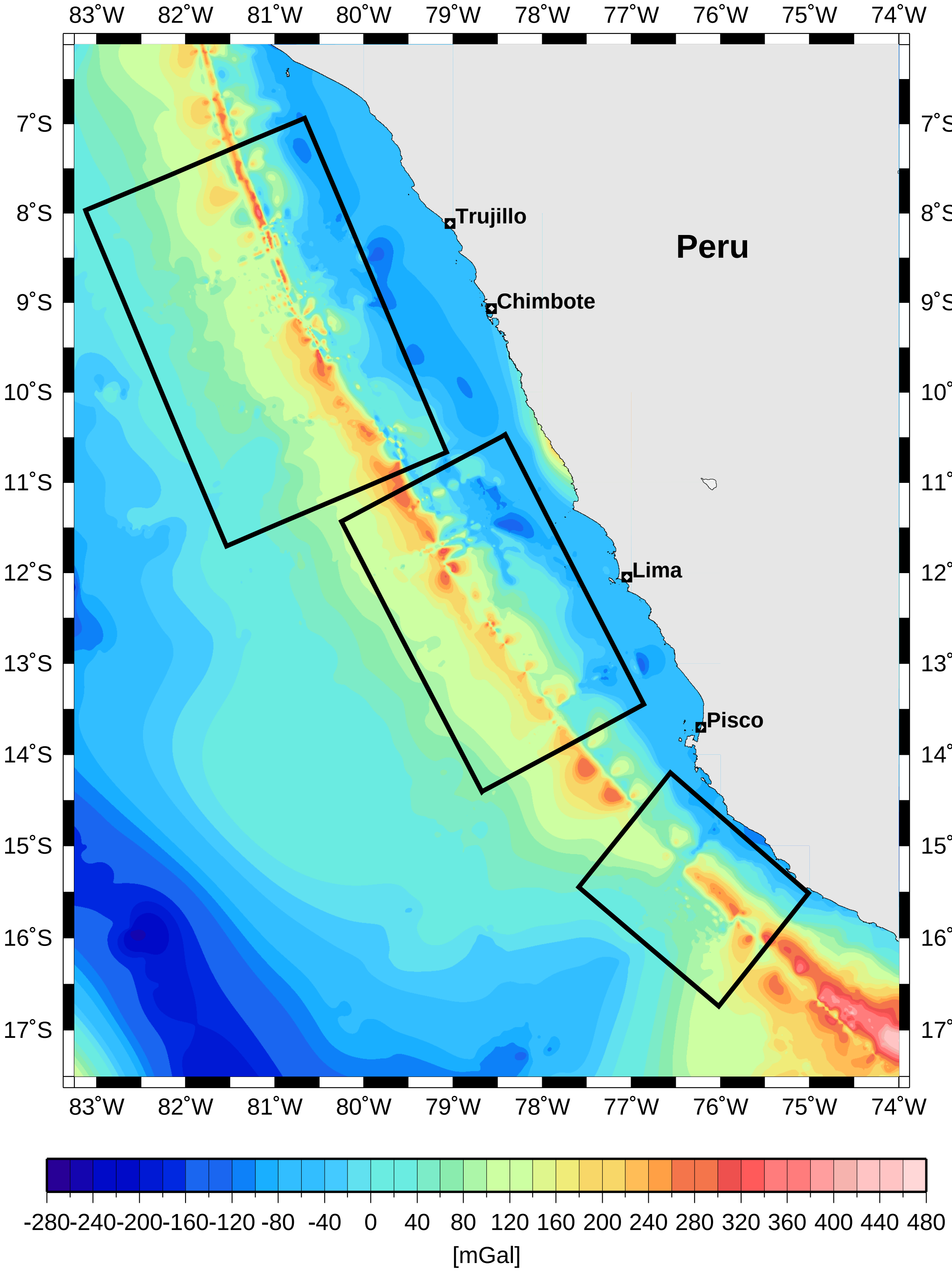

Figure 19: The Residual Bouguer Anomaly Map

5.11 Satellite Gravity

The shipboard gravity data were compared with the gravity data derived from satellite altimetry. Figure 20 shows the gravity map based on satellite data and in Figure 21 the residual of shipboard and satellite data is presented. In general the differences between the satellite and the shipboard data are small. This comparison is a means to prevent that some of the shipboard data is significantly erroneous. In comparison with processed marine gravity data the resolution of satellite gravity data still seems to be limited. According to Sandwell (1992) the major limitation of the satellite altimetry data is not precision but poor data coverage. The marine gravity field derived from satellite altimetry shows wavelengths of 10 to 15 km (Sandwell & Smith, 1997a, 1997b). In comparison with the marine free-air gravity anomaly data the satellite data show a deviation of about 5 mGal (Sandwell & Smith, 1997b), but, as is obvious when studying Figure 20, the partially still strong differences between satellite and shipboard measurements underline the need of high-precision shipboard gravity investigations.

The difference of the shipboard data and the satellite data shows that most of the larger discrepancies occur near land although there are several strong deviations in the ocean (see Figure 20). The extrema near the continent can be explained by an edge-effect amplified by the Fourier transform of the vertical deflection grids. The remaining outliers in the deep water are still unexplained.

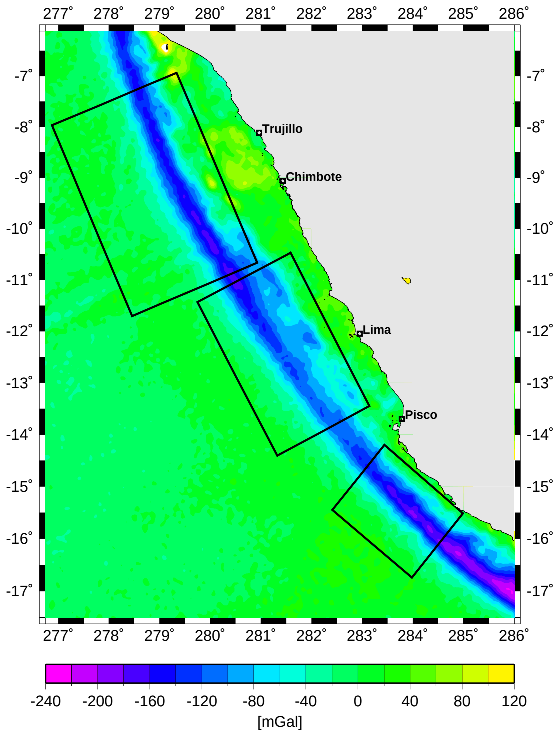

Figure 20: Map of the Satellite Data (data obtained from: Sandwell et al., 1997)

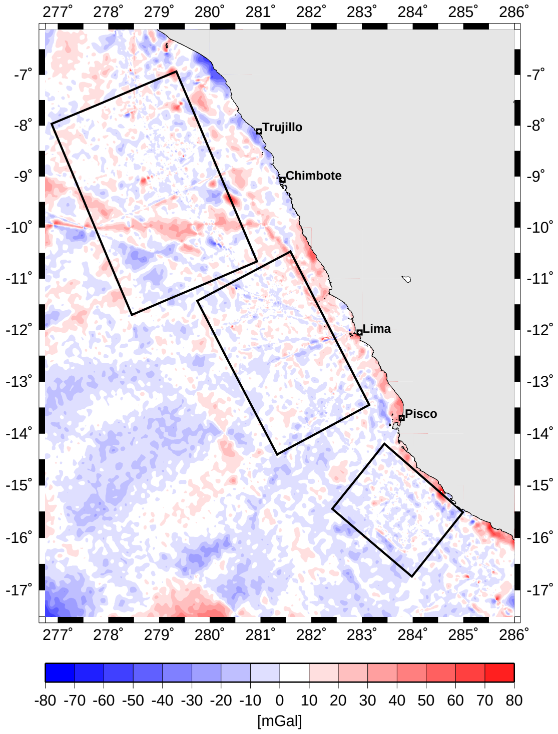

Figure 21: The differences between the Satellite Data and the Shipboard Data (satellite data obtained from: Sandwell et al., 1997)

Different gravity signatures can be observed. This proves to be a challenge for structural interpretation. The gravity anomalies show differences in frequency. The short- and medium-wavelength features point to a varying basement topography and a varying thickness of sedimentary cover as well as low water depth. A high-frequency signature of the oceanic crust and a strong edge-effect at the transition from oceanic to continental crust can be observed.

These characteristics are analysed in three-dimensional modelling. The gravity models of the Yaquina Area, the Lima Area and the Nazca Ridge Area are constrained by the available seismic velocity models of the GEOPECO expedition, developed by Hampel et al. (2002a) and Broser et al. (2002). In incorporating the seismic information into the gravity models the seismic p-wave velocities have to be converted to densities.

5.12 The Different Velocity-Density Relationships

Various relationships between the seismic p-wave velocity and the density of rocks have been developed. Here those relations are discussed which can be applied to the Peruvian convergent margin, i.e. to the oceanic crust and to the continental margin. For the three-dimensional gravity models the following relations have been employed.

5.12.1 The Density Model of Nafe & Drake

Nafe and Drake (1957) developed an empirical relationship between seismic velocities and densities. This relationship was originally based on marine shelf and deep sea sediments but was extended for a wider range of rocks with higher velocities. In Figure 22 this relation is illustrated. The mean values are plotted as black dots, the possible minimum and maximum values are illustrated by error bars.

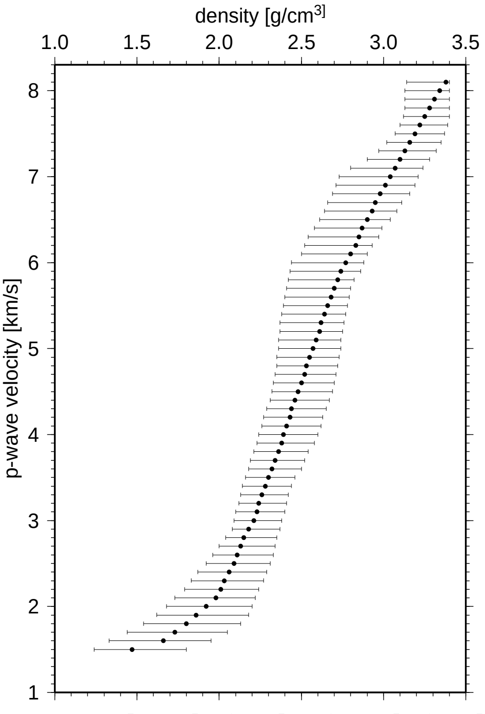

Figure 22: The velocity-density relationship according to Nafe & Drake (1957). (The mean and average values were adopted from Barton, 1986.)

According to Ludwig et al. (1970) the velocity-density relation grades into a relation for mainly metamorphic and igneous rocks approximately starting at a velocity of 5.8 km/s to higher velocities.

A range of densities can be attributed to each seismic velocity. According to Barton (1986) the uncertainties in the calculated gravity anomalies using the Nafe & Drake (1957) relationship can exceed the amplitude of the observed anomalies. When a modelled body has a thickness of more than a few kilometres the uncertainty in the velocity-density transformation becomes significant. As Barton (1986) points out it is improbable that all the velocity-density values lie at one extreme of the distribution.

5.12.2 The Density Model of Birch

Birch (1960, 1961) developed an empirical linear relationship between the velocity and the density variations for magmatites. The following equation is valid for magmatic rocks with an average atomic weight less than 24.

$$\rho = \frac{v_p + 0.98}{2.76}$$

By way of trial this velocity-density relation was used for the rocks of the continental crust in three-dimensional modelling. As metamorphic rocks have been sampled along the Peruvian margin it is sensible to assume that the continental margin consists of metamorphic rocks. Consequently the velocity-density relation, developed for magmatites, renders illogically low densities.

5.12.3 The Density Model of Carlson & Raskin

Carlson & Raskin (1984) have generated a velocity-density relationship based on the investigation of igneous rocks of the oceanic crust. In their model the porosity of the oceanic layer 2 is taken into account. The results are consistent with downhole logging in igneous basement and with the inferred variations of physical properties with increasing depth in the oceanic crust (Carlson & Herrick, 1990). For velocities <6.65 km/s the following equation is used:

$$\rho = (3.5 \pm 0.2) - \frac{(3.79 \pm 0.1)}{v_p}$$

For velocities >6.65 km/s the subsequent, modified equation is applied:

$$\rho = (3.81 \pm 0.02) - \frac{(5.99 \pm 0.11)}{v_p}$$

In Table 2 the average densities and thickness for the different layers of the Pacific oceanic crust are listed. According to Carlson & Raskin (1984) the mean density of the pacific oceanic crust is 2.89±0.03 g/cm^3.

Layer	Thickness [km]	Velocity [km/s]	Lithology	Density [g/cm3]
2A	0.4±0.1	3.47±0.35	Metabasalt, basalt and spilite	2.41±0.11
2B	0.8±0.1	5.28±0.39	Metabasalt, basalt, spilite, diabase and metadiabase	2.78±0.05

Table 2: The Velocity-Density Model of Carlson & Raskin for the Pacific Oceanic Crust (based on: Carlson & Raskin, 1984)

Layer	Thickness [km]	Velocity [km/s]	Lithology	Density [g/cm3]
2C	0.9±0.4	6.12±0.18	diabase and metadiabase	2.88±0.02
3	4.97±1.25*	6.90±0.17	metagabbro, gabbro and olivine gabbro	2.94±0.03
Mean				2.89±0.03
* Christensen & Salisbury, 1975				

Table 2: The Velocity-Density Model of Carlson & Raskin for the Pacific Oceanic Crust (based on: Carlson & Raskin, 1984)

As far as the oceanic crust was concerned the initial gravity model was constructed by converting the average p-wave velocities into densities using the relationships by Nafe & Drake (1957) and by Carlson & Raskin (1984).

Tables of the velocity-density conversions applied in the different three-dimensional models are presented in the appendix (see Tables 7 to 9).

5.13 Characteristics of the Oceanic Crust

In general the oceanic crust is 6 to 7 km thick and lies beneath a typical water depth of 4.5 km. (Kearey & Vine, 1990). The oceanic crust shows a structure of different layers. This layered structure is a consequence of the different compositions of source magma and of the different cooling processes depending on depth.

The different layers which are included in the three-dimensional models are described in the following. The magnetic properties of the oceanic crust are described in Chapter 6.6.

Layer 1
Layer 1 corresponds to sediments and has been extensively studied by coring, dredging and drilling. On average layer 1 is 0.4 km thick. The sediment layer is progressively thickening away from the ocean ridges. The sediments consist of pelagic deposits such as brown zeolite clays, calcareous and silicic oozes and manganese nodules. Terrigeneous sediments are carried into the deep oceans by turbidity currents. The unconsolidated deep sea sediments are often being redistributed by bottom currents or contour currents, caused by thermal and haline anomalies.

Layer 2
Layer 2 consists of extrusive basalts. It is variable in its thickness, varying from 1.0 to 2.5 km. Due to its volcanic nature layer 2 shows a considerably more rugged surface than layer 1. The seismic velocity of layer 2 ranges from 3.4 km/s to 6.2 km/s. By direct sampling and dredging the sediment-free crests basalts and olivine tholeiites have been recovered. Three subdivisions of layer 2 have been recognized:

Sublayer 2A
Sublayer 2A ranges in thickness from 0 to 1 km. It is the uppermost portion of the

crystalline crust and is comprised of extrusive pillow lavas.

Sublayer 2B

Sublayer 2B, also consisting of pillow basalts, is approximately 1 km thick. It shows a lower porosity and therefore a higher seismic p-wave velocity than layer 2A, ranging from 4.8 to 5.5 km/s. By the filling of pores layer 2A is slowly being converted into layer 2B. The pores may be filled by secondary minerals such as calcite, quartz and zeolites.

Sublayer 2C

This layer is about 1 km thick and consist of intrusive and basic rocks vertical sheeted dikes. The seismic velocities range between 5.8 and 6.2 km/s. This layer grades downwards into layer 3.

Layer 3

Layer 3 consists of gabbros and is approximately 5 km thick. Gabbros are intrusive plutonic rocks and constitute the main component of the oceanic crust.

Sublayer 3A

Sublayer 3A shows a seismic velocity range from 6.5 to 6.8 km/s. Layer 3A is composed of isotropic and rather foliated gabbros.

Sublayer 3B

Sublayer 3B possesses a higher velocity, ranging between 7.0 and 7.7 km/s. Sublayer 3B consists of cumulate gabbro and ultrabasic rocks and formed by crystal settling of a shallow magma chamber.

5.14 Gravity Characteristics of the Continental Margin

A continental margin typically consists of sedimentary layers and an underlying crystalline basement. Based on the recoveries of dredging and drilling the crystalline backstop of the Peruvian margin is presumed to consist of metamorphic rocks.

The metamorphic rocks of the continental margin remarkably increase the rocks' densities. The higher the degree of metamorphism the denser the rocks have recrystallized and the less pore spaces remain.

6 Marine Magnetic Measurements

In Figure 23 the magnetic data are presented. The data recovered during the GEOPECO project are displayed in black, the data from the GEODAS data base (GEOphysical DAta System, provided by NOAA and NGDC) are pictured in grey. The total intensity of the geomagnetic field was recorded along some of the gravity profiles.

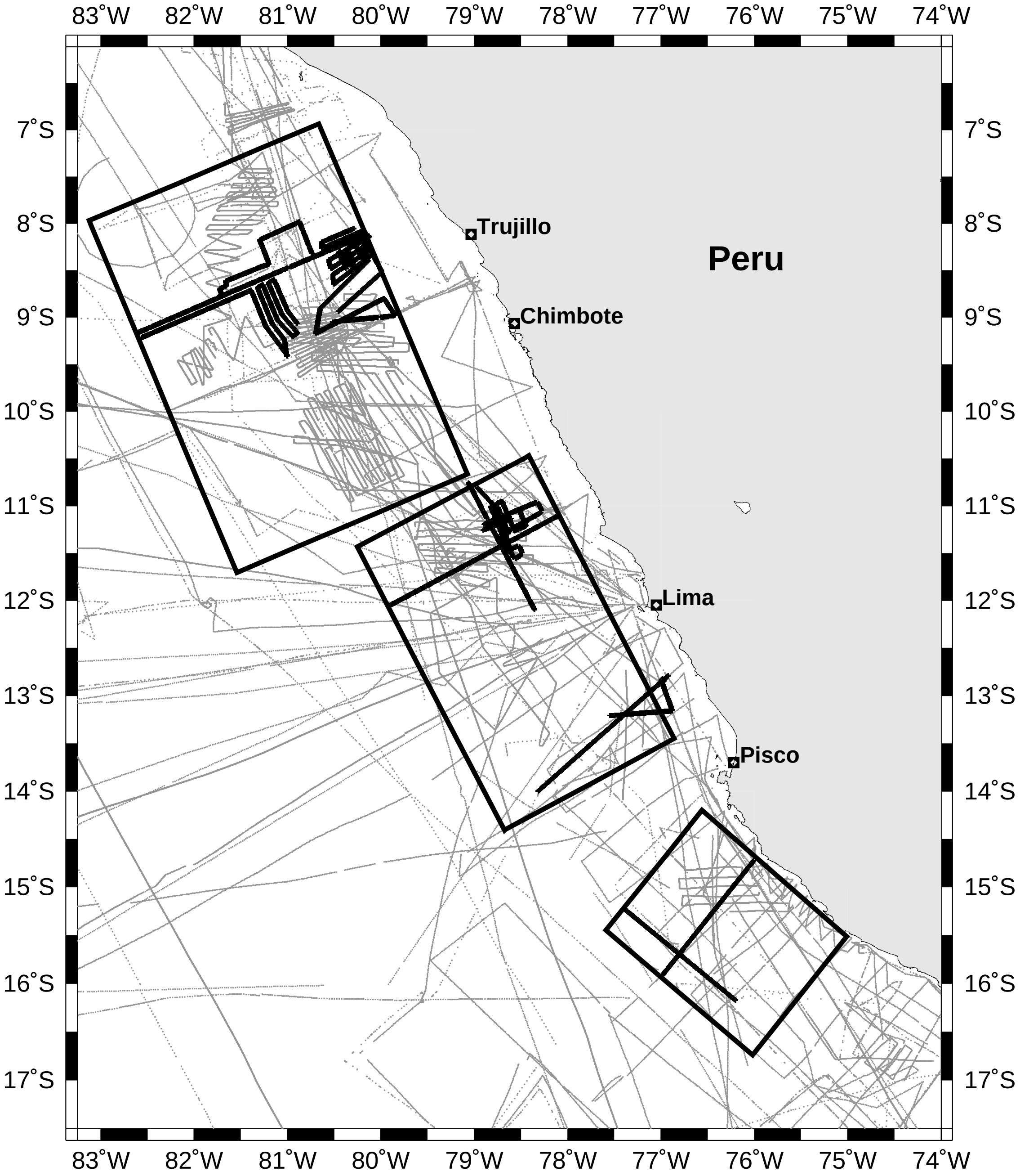

Figure 23: Overview of the Magnetic Stations and Profiles
The magnetic data acquired during the GEOPECO expedition are displayed in black, the magnetic data obtained from the GEODAS data base are painted grey

6.1 The Magnetic Data

The magnetic measurements were carried out with a protone precession Gradiometer, type GEOMETRICS G-801G. A different protone precession magnetometer, type GEOMETRICS G-811/G-813 was used on one profile as well but the acquired data did not show the expected quality. With a protone magnetometer the intensity of the total magnetic field is measured. The components of the geomagnetic field are displayed in Figure 24. The inclination angle is defined as I, the declination angle is described as D. The total magnetic field *T* can be split into the horizontal component *H* and the vertical component *Z*.

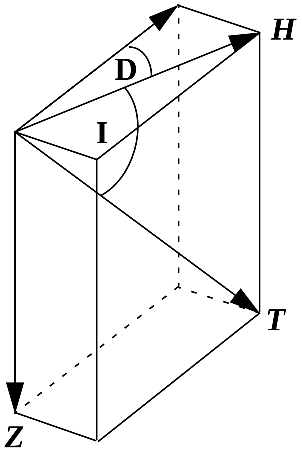

Figure 24: The components of the magnetic field

Digital and analogue recordings of the magnetic data were acquired. The magnetic intensity values were recorded every 10 seconds and merged with the navigation data. An especially dense distribution of collected data was reached in the Lima Area, the Yaquina Area and in the Nazca Ridge Area (see Figure 23). The magnetic anomalies, respectively the residual magnetic data, were calculated using the current International Geomagnetic Reference Field model (IGRF 2000, see Chapter 6.2). The daily variations of the magnetic field were considered and the navigation related errors were corrected. All the available magnetic data from the GEODAS data base were integrated (see Figure 23).

Magnetic investigations on land include reference stations which help in determining and reducing the temporal variations of the earth’s magnetic field. If variation data of a reference station are available these are used for the correction of the magnetic anomalies. Usually there are no such reference stations for marine magnetic measurements. Permanently operating magnetic observatories were too far from our study areas to be used for a sensible reduction of the measurements. To obtain magnetic data without variations a gradiometer was used. The two protone magnetometers belonging to the gradiometer, described as master and slave, were towed 250 m behind the ship. The distance between the two sensors was 10 m. The omnidirectional sensors may be towed behind the ship with a long non-magnetic floatable cable. Because the sensors are towed on a long cable behind the ship the magnetic influence of the ship need not be considered. A further source of error is the unknown position of the sensors in relation to the profile. The sensors measure the total intensity of the earth’s magnetic field simultaneously and therefore the difference between these two values does not contain temporal variations. The gradient of the magnetic field along the profiles can be calculated and by integrating the gradient curve, the variation-free magnetic anomaly can be reconstructed. Variations of the shorter periods can be eliminated successfully using a gradiometer. Unfortunately only the master sensor measured reliable data during the GEOPECO expedition.

The interior of one gradiometer sensor is displayed in Figure 25. The sensor is filled with decane, i.e. liquid paraffin, which is very rich in protons. A strong polarisation current is applied and a uniform magnetic field is created. After turning of the current the spin of the protons causes them to precess in phase in the direction of the geomagnetic field. The protons precess at a rate proportional to the total magnetic intensity. The signal of the precessing protons is induced in the same coil array which was used for producing the initial strong magnetic field. The protone magnetometer measures the precession frequency of the protone, ν_p:

$$\nu_p = \frac{\gamma_p T}{2\pi}$$

with: γ_p = gyromagnetic ratio of the electron, T = total magnetic field

$$T = 23.4874 \cdot \nu_p$$

As indicated by the manufacturer GEOMETRICS, a signal-to-noise ratio of 100:1 can be expected at a rate of one measurement of the magnetic intensity every ten seconds.

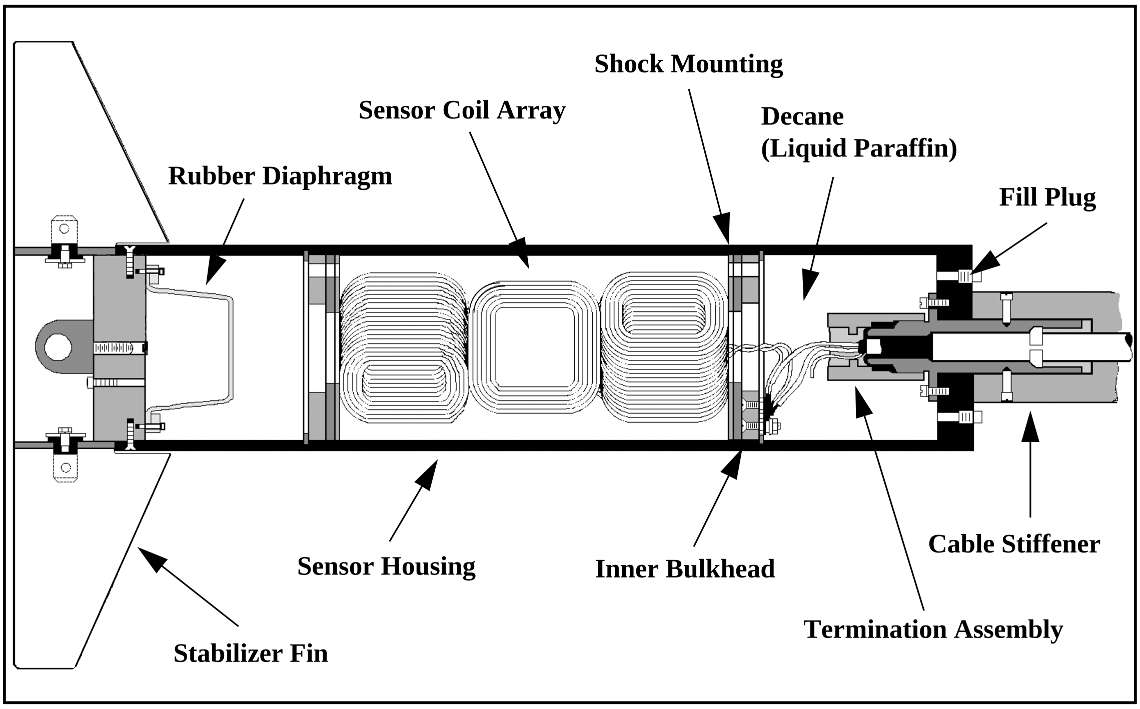

Figure 25: Sensor of the gradiometer (modified from GEOMETRICS, 1975)

The intensity of the magnetic field decreases according to the shape of the magnetised body with increasing distance r with $1/r^3$ (Breiner, 1973). Only the magnetostatic parts of local magnetic bodies which are projected in the direction of the main field are seen in intensity measurements.

6.2 The IGRF

The International Geomagnetic Reference Field (IGRF) and the Definitive Geomagnetic Reference Field (DGRF) are based on a spherical harmonic expansion. The maximal degree and order of the core’s field is 10, for the secular terms the degree and order is 8 (Mandea, 2001). A linear development is adopted for the secular variations in the 5-year

IGRF model. The earths dipole moment possesses a standard deviation of 42% over the past 5 million years (McFadden & McElhinny, 1982). The IGRF is the most widely used mathematical model for fitting the main magnetic field of the earth at a given time. It is used to objectively remove long wavelength components from survey data to obtain the anomalous magnetic field, which contains the shorter wavelength components of interest. To isolate the anomalies from the measured values the following three parts have to be separated: the main earth magnetic field, the magnetic field of the measuring system, especially the magnetic field of the ship, and the temporal variations of the magnetic field. The main part of the magnetic field of the earth is the long-periodic part and is caused by currents in the fluid outer core of the earth. The first step in data processing is to substract the International Geomagnetic Reference field (IGRF). In this project the IGRF 2000 was used. The model consists of spherical harmonic coefficients for the earth's magnetic field in the year 2000 and the corresponding coefficients for the expected changes of the field in the following five years. The spherical harmonic coefficients are derived from observatory and satellite data. After substracting this field from the total intensity values the anomalies of the magnetic field are obtained. Now they can still be disturbed by temporal variations.

6.3 Susceptibility

The total magnetisation M of a rock has two components: the remanent magnetisation M_r and the magnetisation induced by the present-day dipole field M_i:

$$\vec{M} = \overrightarrow{M_r} + \overrightarrow{M_i}$$

A rock placed in a magnetic field acquires a magnetisation M which, if small, is proportional to the field H:

$$\vec{M} = k \cdot \vec{H}$$

The proportionality factor k is the susceptibility of the rock. For most natural materials the susceptibility is very small. The susceptibility is a measure of the degree to which a

Type	Susceptibility (Range)	Susceptibility (Average)
Sediments	0.0-0.018	0.0009
Metamorphic rocks	0.0-0.07	0.0042
Igneous rocks acidic: basic:	 0.0-0.08 0.0005-0.097	 0.008 0.025
Basalt	0.0002-0.175	0.07
Gabbro	0.001-0.09	0.07
Peridotite	0.09-0.2	0.15
Granite	0.0-0.05	0.0025

Table 3: Magnetic Susceptibilities (based on Telford et al., 1990)

Type	Susceptibility (Range)	Susceptibility (Average)
Rhyolite	0.0002-0.035	
Diorite	0.0006-0.12	0.085

Table 3: Magnetic Susceptibilities (based on Telford et al., 1990)

substance may be magnetised. It is the ratio of the intensity of magnetisation I to the magnetic field *H*. The susceptibility has been shown to be proportional to the volume percentage of magnetite contained in a rock. A susceptibility contrast is the susceptibility difference between two rocks or geologic bodies.

The observable magnetic anomalies are caused by a small number of substances which are ferro- or ferri-magnetic. In these rocks the molecular magnets are held parallel by strong intermolecular forces. Maghemite, pyrrhotite and especially magnetite are the only three important naturally occurring magnetic minerals. They possess Curie temperatures of about 600°C. The magnetic properties of a rock usually depend on its magnetite content. The carriers of magnetisation are predominantly ferri-magnetic titanomagnetites, but other magnetic minerals, especially sulphides, are also causing significant magnetic anomalies. Sediments and acid igneous rocks show small susceptibilities. Rocks with high susceptibilities are basalts, dolerites, gabbros and serpentinites. A selection of magnetic susceptibilities is listed in Table 3. Figure 26 shows the susceptibility ranges of several rock types.

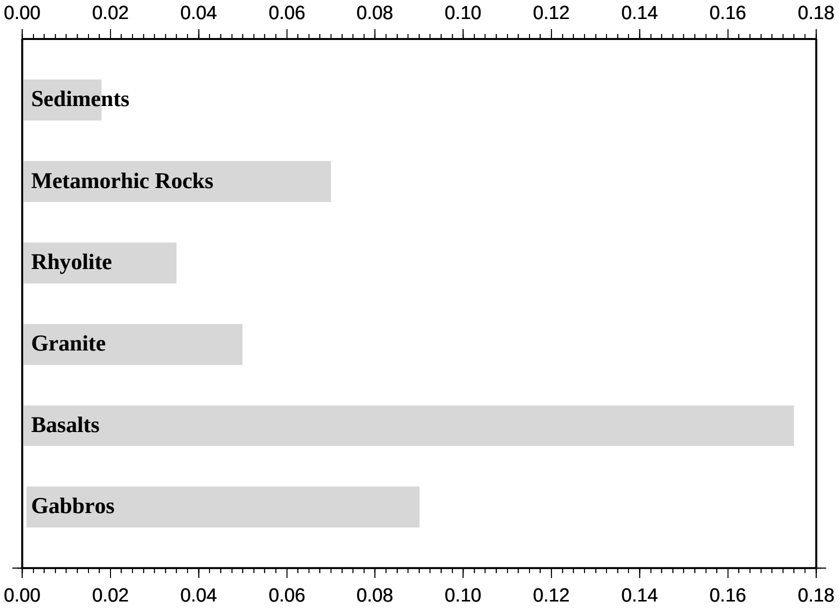

Figure 26: Susceptibility ranges of different rock types (based on Telford et al., 1990)

The magnetic properties of a rock depend strongly on the grain size (Gee & Kent, 1999). Then many of the magnetic elements include only one Weiss domain and the remanent magnetisation of rocks is more stable. The fine-grained ferri-magnetic titanomagnetites found in submarine lavas are regarded as the dominant source for magnetic anomalies. According to Gee & Kent (1998) up to two thirds of the magnetic variations in mid-oceanic ridge basalts of comparable age may be caused by differences in geochemistry.

The upper layers of the uprising magma at a spreading ridge are especially quickly cooled when in they come in contact with the sea water and therefore they are especially fine-grained. Caused by this thermal shock cracks are appearing in the rocks, enabling the sea water to penetrate into deeper layers and cool them as well. According to (Pariso & Johnson, 1993a) the seawater can intrude some kilometres in depth. At the sea floor it flows into the cold sea water and the minerals fall out. Cooling happens more slowly at greater depth, the crystals can grow undisturbed for a longer time, and the magnetisation is less intense in spite of the same chemical composition.

Magnetic anomalies are caused by magnetic bodies in the crust and eventually in the upper mantle. The anomalies possess wavelengths between only a few meters and several hundred meters. Magnetic anomalies of the lower and of the upper crust are investigated. The oceanic crust is highly magnetic due to its high basalt content.

6.4 Remanence and Königsberg Ratio

Ferro- and ferri-magnetic materials show permanent as well as induced magnetic moments. The resulting magnetisation is not necessarily oriented in the direction of the earth’s field. The remanent magnetisation is acquired when the rocks are cooled below the Curie-temperature.

The Königsberg ratio is the ratio of the remanent to the induced magnetisation in a standard magnetic field of 50,000 nT. Using the Königsberg ratio the magnitudes of induced and remanent moments can be compared. The Königsberg ratio is generally large in highly magnetic rocks and small in weakly magnetic rocks. Haematite occasionally shows an extraordinary high (>10,000) Königsberg ratio which can be entirely due to remanence. Ocean basalts often show a high Königsberg ratio, typically 1 to 160. Here the intensity of remanent magnetisation is often significantly larger than the induced. Its value depends on two main factors, i.e. the type of rock and the paleointensity of the earth's magnetic field. The thermoremanent magnetisation of the oceanic crust reflects the variability in the earth’s dipole field. It is difficult to gain detailed information on intensity changes from sea surface magnetic measurements alone.

Larger, multidomain magnetic grains have a smaller magnetisation per volume than smaller grains and are less able to overcome mechanical resistance from the surrounding matrix and align along the magnetic field (Williams et al., 2002). A sediment containing predominantly large ferri-magnetic grains will have a smaller remanence than one containing smaller grains. The Königsberg ratio should also be smaller for coarser-grained rocks. The ratio depends on the paleointensity as an increased intensity of the earth's field leads to better alignment of magnetic grains along it and therefore an increased remanent magnetisation. The ratio cannot be calculated absolutely from core measurements, as a large overprint and subsequent demagnetisation has often occurred.

6.5 Magnetic Properties of the Oceanic Lithosphere

The magnetic anomalies are caused by magnetic rocks in the crust and possibly in the upper mantle. Except for layer 2 the magnetic properties of the oceanic layers are only indirectly deduced from magnetic anomalies or from alterated xenolithes. The same rocks can have completely different magnetic features in different circumstances.

Layer 1

The sediment layer normally shows an only small induced and remanent magnetisation (Roeser, 2000). The magnetic anomaly measured at sea level is only rarely influenced by this layer. Sediments are less strongly magnetised than basalts.

Layer 2

Layer 2A, composed of extrusive pillow lavas, is highly magnetic and responsible for the main part of the magnetic anomalies. According to Schreckenberger (1998) pillow basalts possess a magnetisation of 5 A/m. According to Worm et al. (1996) the observable magnetic anomalies are caused primarily by pillow basalts and, thereafter, by sheeted dykes, i.e. layer 2B. Layer 2B probably possesses an only weak magnetisation and adds little to the observable magnetic lineations. According to Schreckenberger (1998) sheeted dykes show a magnetisation of 1.5 A/m. Pariso & Johnson (1993a) found that the average magnetisation of basalts, which are older than 2 Ma, is 3.5 A/m.

Layer 3

A high magnetisation of layer 3 was found at ODP Site 735B in the southwest Indian Ocean (Pariso & Johnson, 1993b). The gabbros show a magnetisation of 2.5 A/m. It is difficult to determine the magnetisation of the upper mantle although strongly magnetic serpentinized peridotites have been cored in the Hess Deep. According to today’s knowledge the mantle possesses only little magnetisation. The magnetisation of rocks recovered by drilling, though, requires a distinctive magnetisation to greater depth to explain the observed anomaly strength. At ODP site 735B lineated anomalies are present although the upper layers have been completely removed and the gabbro layer is exposed. Therefore the deeper gabbro layer has to contribute significantly to the observable magnetic anomalies. The contribution of layer 3 to the magnetic anomalies leads to a skewness of the observed anomalies. Layer 3 cools slower and later than the upper layers so that the rocks which have passed the Curie temperature at a certain time do not lie directly on top of each other. The deeper lying parts of the oceanic crust therefore lie further away from the spreading ridge than the upper parts which obtained their magnetisation at the same time. The skewness has been integrated into the three-dimensional models.

According to Okubo et al. (1991) demagnetisation of the oceanic crust takes place at a depth of approximately 30 km where the Curie temperature is reached.

6.6 Magnetic Properties of the Continental Margin

The overriding continental crust typically shows a magnetisation of 0.8 A/m (Roeser, 2000). Off Costa Rica a magnetic body of the continental margin was modelled with a magnetization ranging from 0.6 A/m to 1.2 A/m (Barckhausen et al., 1998).

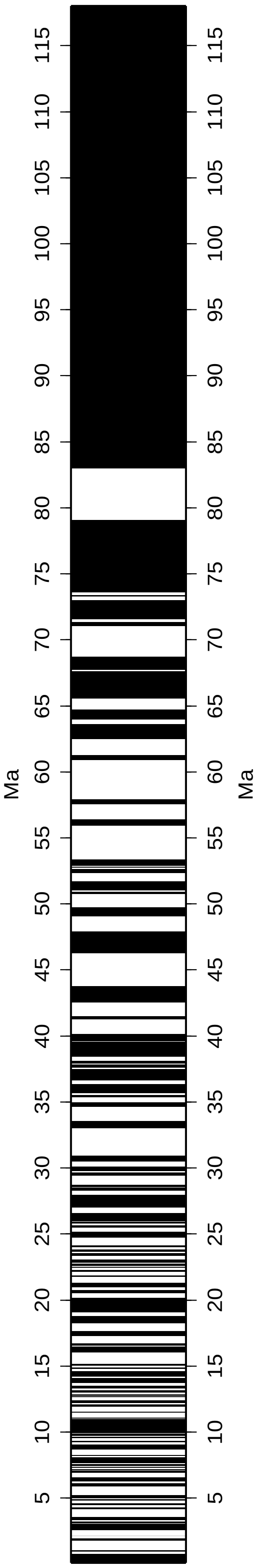

Figure 27: The Magnetic Polarity Time Scale (Cande & Kent, 1995)

6.7 Magnetic Lineations

The magnetic lineations are magnetic anomalies imprinted on the oceanic lithosphere. As the magnetic stripe pattern is caused by field reversals it describes the history of plate motion. They are the most valuable data for reconstructing earlier plate configurations. The magnetic stripes parallel the mid-oceanic ridges and are often fractured by transform faults. The lineations typically show magnitudes of 500 nT and are usually a few tens of kilometres wide.

The shape of a magnetic anomaly is controlled by the orientation of its total magnetisation vector, i.e. the resultant of the remanent and induced components. The shapes of the magnetic lineations are determined by the primary remanent direction. The shape and amplitude of a magnetic anomaly is also affected by the orientation of the spreading ridge. Only that component of the magnetisation vector lying in the vertical plane through the magnetic profile influences the magnetic anomaly. This component is at a maximum when the ridge is oriented east-westwards and the profile north-southwards, and at a minimum for ridges oriented north-southwards. Usually the amplitude of a magnetic anomaly decreases as the latitude lessens and as the strike of the ridge progresses from east-westwards to north-southwards. The Curie temperature of all geologically important magnetic materials is about 550° to 600°C. Beneath the oceans this temperature is reached within the upper mantle.

The marine magnetic anomalies provide a strong record of past geomagnetic polarity reversals. The shorter wavelength variations may provide information on geomagnetic intensity variations within intervals of constant polarity (Gee et al., 1996). The intensity variations of the geomagnetic field strongly influence the magnetisation of the oceanic crust. Part of the high-frequency anomalies is probably due to variations in the magnetic layer thickness, geochemistry or degree of alteration of the magnetic rocks (Gee et al., 1996). How detailed the intensity variations of the geomagnetic field are recorded on the seafloor depends on the spreading rate, i.e. the band pass filter of the mid-oceanic ridge.

The Vine-Matthews hypothesis (Vine & Matthews, 1963) describes the formation of magnetic lineations. New oceanic crust is created by the solidification of magma injected and extruded at the crest of an ocean ridge. With further cooling, the temperature passes through the Curie temperature below which ferro-magnetic behaviour becomes possible. The solidified magma then acquires a magnetisation with the same orientation as the ambient geomagnetic field. The seafloor-spreading anomalies show variations in their amplitude. These variations can be caused by differences in angles between the main field and the direction of strike of the bodies as well as between the geomagnetic latitude at the time of formation of the crust and the latitude today. The anomalies also vary because of differences in the strength of the dipole field as part of the main field. Furthermore the minerals of the oceanic crust are crucial. The magnetisation of the oceanic crust may change due to the alteration of the respective rocks. Tectonic processes and melting may have changed the magnetisation.

Times of constant polarity vary in duration from the 37 Ma period of the Cretaceous Normal Superchron to shorter periods lasting only a few thousand years. Usually a period stays on for a few 100,000 years. At a maximum the polarity reversal takes place in some 1000 years. The polarity reversals can be seen in the easily recognizable lineation pattern. Anomaly variations with a shorter wavelength are also commonly observed. A field-related origin for some of these short-wavelength anomalies can be deduced from the linearity and symmetry with respect to the spreading axis. Paleointensity variations within intervals of constant polarity can be seen as an explanation for the common occurrence of these tiny wiggles (Cande & Kent, 1992). According to Gee et al. (1996) deep sea sediments may provide a representation of geomagnetic variations within the Brunhes era. As the anomaly data and the paleointensity records of sediments rely on different mechanisms they provide independent information on changes in the earth’s magnetic field.

The magnetic pattern ends where the temperature of the subducting plate is approximating the Curie temperature of about 600˚C. At what depth the Curie temperature is reached depends on the subduction angle, the subduction velocity, the surrounding temperature and the content of magnetic minerals of the respective rocks. During the subduction process the oceanic crust is losing its magnetic stripe pattern. The magnetic anomalies of the subduction zone become smoother and weaker with increasing depth of the subducting plate (Roeser, 2000). In what depth and how this happens are still unanswered questions. According to Barckhausen et al. (1998) the seamounts remain magnetically intact for a long time during the subduction process. The geomagnetic polarity time scale will be further refined due to higher precision radiometric and astronomical dating methods (Cande & Kent, 1995). The magnetic reversal time scale of Cande & Kent (1995) is displayed in Figure 27. The black stripes denote periods of normal magnetisation, the white stripes indicate intervals of reversed magnetisation. By studying the magnetic data more information on the subduction process can be gained. Slower spreading ridges preserve only the longer wavelength intensity variations of the magnetic field. The strike of the magnetic anomalies describes the movement of the tectonic plates.

6.8 Temporal Magnetic Variations

The most difficult noise to reduce is caused by temporal variations of the magnetic field. These variations can also spacially be very variable. High-frequency field variations in the range of minutes can cause amplitudes of more than 10 nT (Jacobs, 1970). The longer the wavelength of a variation the bigger is the influenced area. The best way to deal with this problem is to repeat noisy profiles. By summing up the differences of the simultaneously measured data it is possible to calculate a variation-free total intensity. This reduction is only possible with a reference station which should not be farther away than 100 km from the survey area. This requirement could not be met in the GEOPECO project because there are only very few reference stations along the Peruvian margin and because the distances during the survey where by far to big. A direct reduction of the daily variations is only possible in the direct environment of a reference station. With increasing distance to the reference station the measured data have to be more and more lowpass-filtered. A unique relation between the distance to the reference station and the filter length cannot be given because the nature of the currents systems, which are causing the geomagnetic variations, is complex. Fortunately there are other criteria to evaluate the quality of the measured data. The geomagnetic daily variations can be reduced using the geomagnetic indices.

6.9 The Geomagnetic Indices

Daily regular magnetic field variations arise from current systems caused by regular solar radiation changes. These irregular current systems produce magnetic field changes caused by the interaction of the solar wind with the magnetosphere, by the magnetosphere itself, by the interactions between the magnetosphere and the ionosphere as well as by the ionosphere itself. Magnetic activity indices were designed to describe variations in the geomagnetic field caused by these irregular current systems.

6.9.1 The K_p-Index

The planetary 3-hour-range index K_p is designed to measure the solar particle radiation by its magnetic effects. The mean standardized K-index is deducted from 13 geomagnetic observatories between 44 and 60 northern and southern geomagnetic latitude. This index is relative to an assumed quiet-day curve for a single geomagnetic observatory site. The scale is 0 to 9 expressed in thirds of a unit, e.g. 5- is 4 2/3, 5 is 5 and 5+ is 5 1/3. A reduction of the measured magnetic data is only necessary when the variations show strong amplitudes during a long timespan in the range of measuring. K_p helps to decide whether this is the case and describes the extent of the geomagnetic disturbance in the magnetosphere (Bartels, 1949; Rangarajan, 1989). The nominal value for K_p is 1 or 2. During a geomagnetic storm the K_p values range from 5 to 9.

6.9.2 The A_p-Index

The A_p index is a 3-hourly equivalent range index. It is derived from the K_p index in the following way:

K_p	0	0+	1-	1	1+	2-	2	2+	3-	3	3+	4-	4	4+
A_p	0	2	3	4	5	6	7	9	12	15	18	22	27	32
K_p	5-	5o	5+	6-	6o	6+	7-	7o	7+	8-	8o	8+	9-	9o
A_p	39	48	56	67	80	94	111	132	154	179	207	236	300	400

Table 4: The Relation Between the K_p and the A_p Indices (obtained from: ftp://ftp.ngdc.noaa.gov/STP/GEOMAGNETIC_DATA/INDICES/KP_AP/)

The planetary indices for the period of the GEOPECO expedition are plotted in Figures 28 and 29.

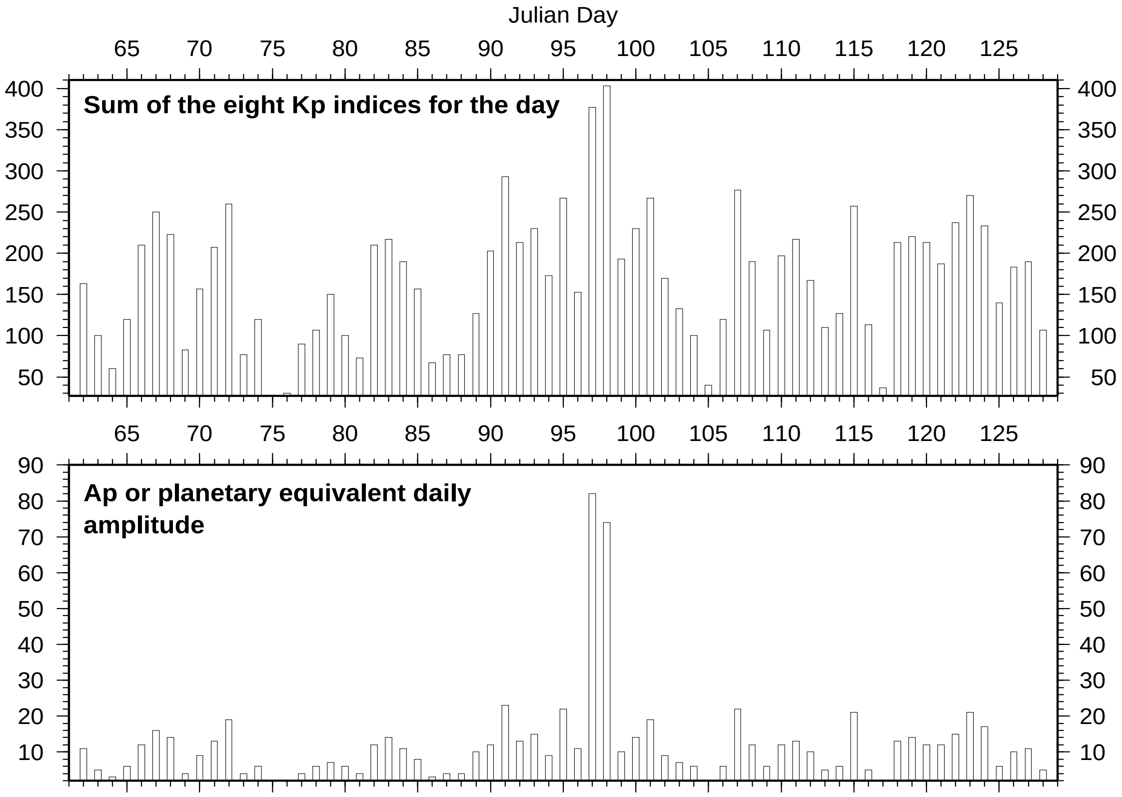

Figure 28: The Planetary Indices K_p and A_p (obtained from: ftp://ftp.ngdc.noaa.gov/STP/GEOMAGNETIC_DATA/INDICES/KP_AP/)

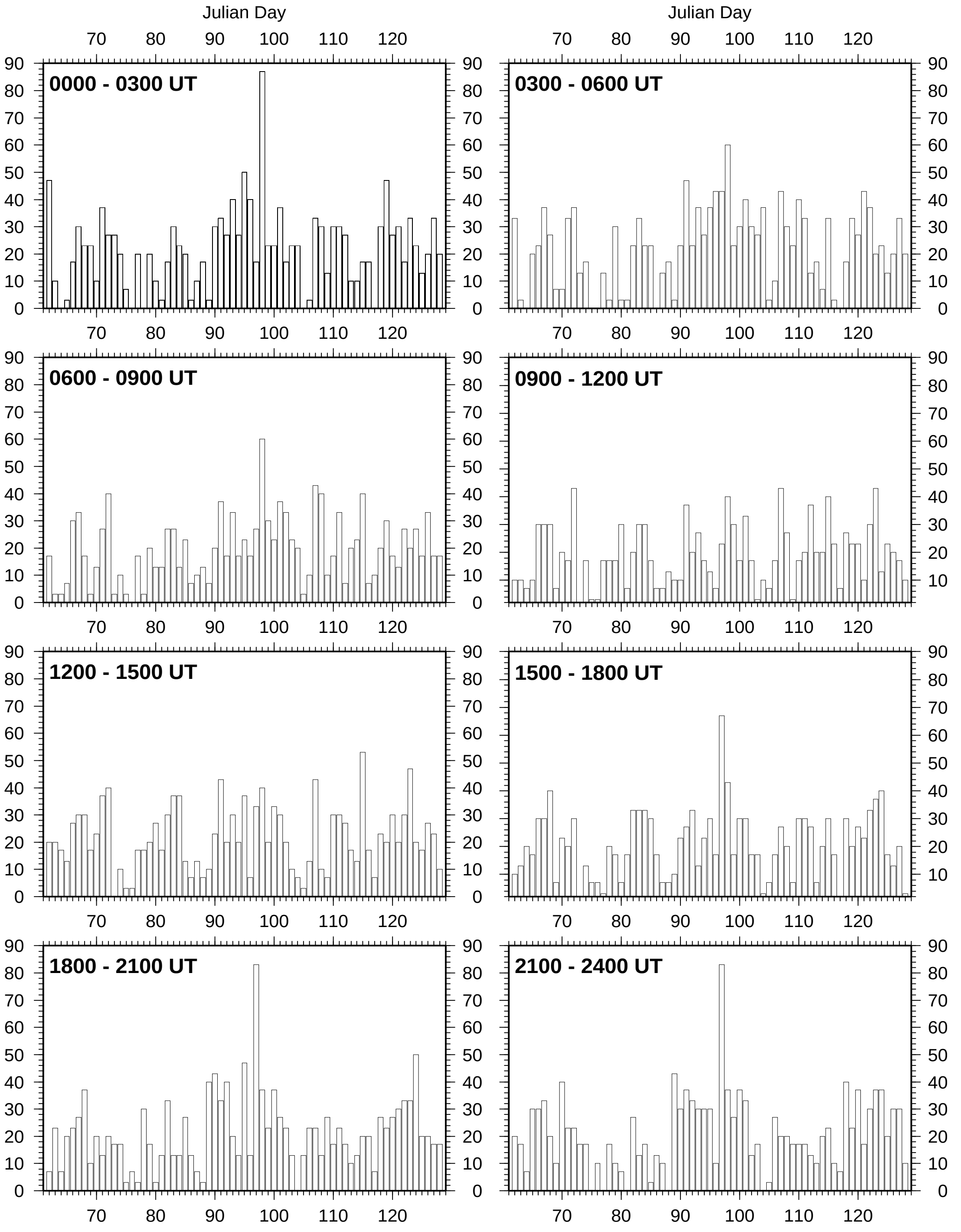

Figure 29: K_p or The Planetary 3-Hour Range Index (obtained from: ftp://ftp.ngdc.noaa.gov/STP/GEOMAGNETIC_DATA/INDICES/KP_AP/)

6.9.3 The Least and the Most Magnetically Disturbed Days of the GEOPECO Expedition

The selection of the quietest days (Q) and most disturbed days (D) of each month is deduced from the K_p indices based on the sum of the eight K_p values, the sum of squares of the eight K_p values and the maximum of the eight K_p values. According to each of these criteria, a relative order number is assigned to each day of the month, the three order numbers are averaged and the days with the lowest and the highest mean order numbers are selected as the five (respectively ten) quietest and the five most disturbed days. These selection criteria give only a relative characterization of the selected days with respect to the other days of the same month. A selected quiet day is considered not really quiet and is marked by the letter A if A_p is greater than 6, or marked by the letter K if A_p is less or equal 6 and either one K_p value is greater than 3 or two K_p values are greater than 2+. A selected disturbed day is considered not really disturbed and marked by an asterisk (*) if A_p is less than 20. The quietest days and the most disturbed days in March to May 2000 are listed in Table 5.

Month	**Quietest Days**										**Most Disturbed Days**				
	Q_1	Q_2	Q_3	Q_4	Q_5	Q_6	Q_7	Q_8	Q_9	Q_{10}	D_1	D_2	D_3	D_4	D_5
March 2000	15	16	26	27	4	21	28	9	17	13	31	1	12*	7*	8*
April 2000	26	14	22	18	25	15	23	13K	12A	11A	7	6	4	16	24
May 2000	8	11	20	7	21	10	4	18A	19A	9A	24	25	17	23	29

Table 5: The least and the most magnetically disturbed days of the GEOPECO cruise (obtained from: http://www.gfz-potsdam.de/pb2/pb23/GeoMag/niemegk/kp_index/quietest/)

6.9.4 Disturbance Storm Index

The Disturbance storm index (Dst index) is a measure of the magnetic perturbation at the Earth’s surface caused by the symmetric ring current in the magnetosphere which is a major feature of a geomagnetic storm. On a magnetically quiet day the daily perturbations caused by ionospheric currents and the very slow variations of the internal dynamo field still have to be considered. The nominal value of the Dst index is 0 nT. During a geomagnetic storm the Dst index ranges between less than -300 nT and -30 nT. The main phase of a magnetic storm lasts for a few hours, the whole storm is measured in days. The Dst-Index for the period of the GEOPECO expedition is displayed in Figure 30.

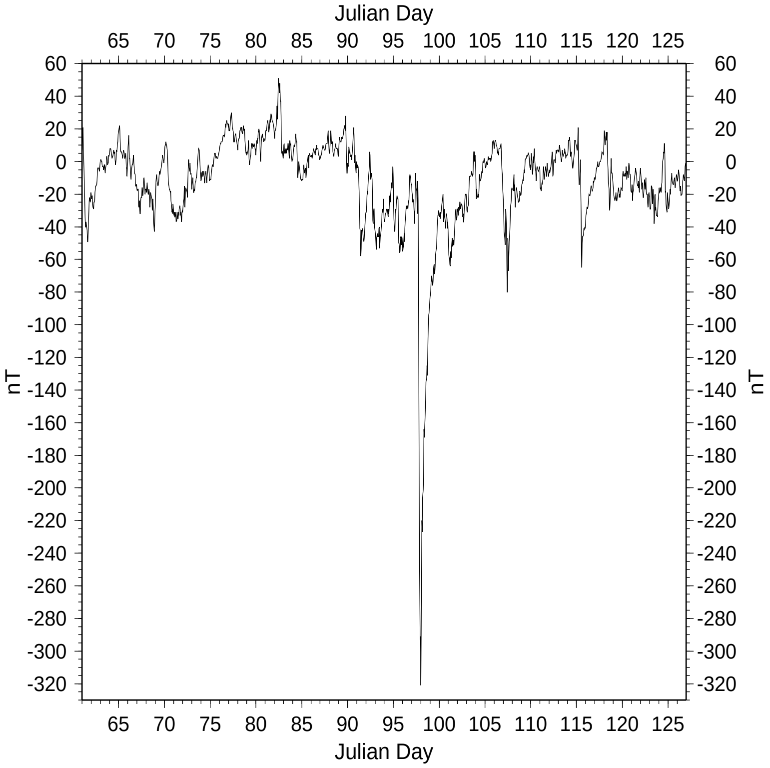

**Figure 30: Disturbance Storm Index March 1st - May 6th (i.e.: Julian Day 61st -127th)
(obtained from: ftp://ftp.ngdc.noaa.gov/STP/ GEOMAGNETIC_DATA/INDICES/DST/)**

Starting on julian day 97th and ending on julian day 99th an unmistakable magnetic storm took place. The Dst-Index shows values as low as -320 nT. These days correspond to April 6th and April 7th. They are listed as the most disturbed days of the month in Table 5. Data recorded on these days as well as on the other disturbed days listed in Table 5 and recognizable in Figure 30 were excluded from the interpreted magnetic data.

6.10 The Magnetic Anomaly Maps

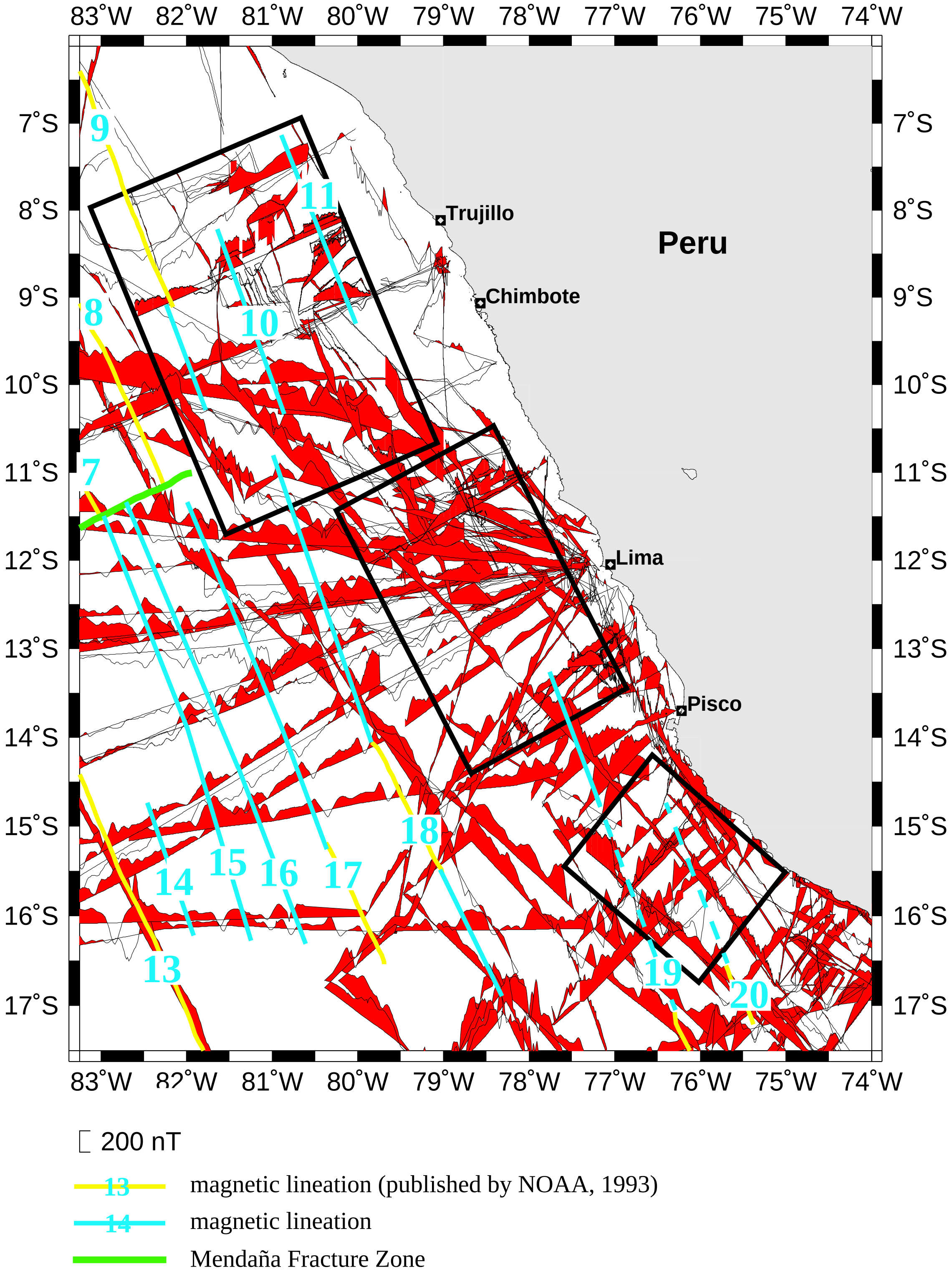

Figure 31: The Magnetic Anomalies Along the Peruvian Margin

Figure 31 shows the magnetic anomalies plotted along the ships' tracks. The magnetic data along the track lines are aligned northwards. The positive anomalies are filled red, the negative anomalies are filled white. Some magnetic profiles from the GEODAS data base were excluded, as they do not contribute to a clear image. Although only selected tracks are plotted some lines still do not have an optimal orientation and complicate the identification of magnetic anomalies. The locations of the magnetic sea floor spreading anomalies are plotted, labelled in blue. The darker blue lines are lineations formerly identified by NOAA (1993). The blue lines depict the lineations recognizable in the displayed magnetic data. The location of the Mendaña Fracture Zone, as published by NOAA (1993), is indicated by the northeast-southwest trending green line south of the lineations 7 and 8.

The northnorthwest-southsoutheastwards oriented magnetic lineations describe the direction of plate convergence. Anomaly 17 can be traced a long way north of the already identified part. Lineation 18 can be prolonged north- and southwards. This anomaly reaches into the southern part of the Yaquina Area. Lineation 9 in the northern part of the Yaquina Area is traceable further southwards. The formerly identified magnetic anomalies 19 and 20 may be traced throughout the Nazca Ridge Area. The lineations 14, 15 and 16 can be identified between the already recognized lineations 13 and 17. Not all the visible magnetic anomalies have to be caused by the lineations of the oceanic crust. Some of the profuse magnetic anomalies may be attributed to especially magnetic bodies like seamounts or lava flows on the subducting oceanic plate. The numerous tiny wiggles are either non-eliminated diurnal variations or subchrons between the major field reversals.

The closely spaced data distribution in the areas of three-dimensional modelling allows a detailed assignment of particular anomalies to specific magnetic bodies or to the lateral and vertical development of the especially magnetic basalt layers of the subducting oceanic crust.

The imaged data are residual magnetic anomalies calculated by substracting the International Geomagnetic Reference Field (IGRF). In the case of the newly acquired data from the GEOPECO expedition the IGRF 2000 was applied; the magnetic data from the GEODAS data base are already reduced with the appropriate IGRFs.

A histogram of the magnetic field differences at crossing points of all the processed profiles is displayed in Figure 32. 194 crossing points were determined. At a crossing point two profiles are at a distance of maximal 0.0001°, i.e. 11.1 m. Unfortunately the differences do not show an optimal Gaussian curve and errors of 20 nT are common. As magnetic investigations are highly sensible to the measurement positions, these errors maybe explained by the minor distances at the cross-over points. The partially large differences are certainly also due to not successfully eliminated magnetic variations. According to Gee & Kent (1998) discrepancies of typically <50 nT are caused by diurnal geomagnetic variations.

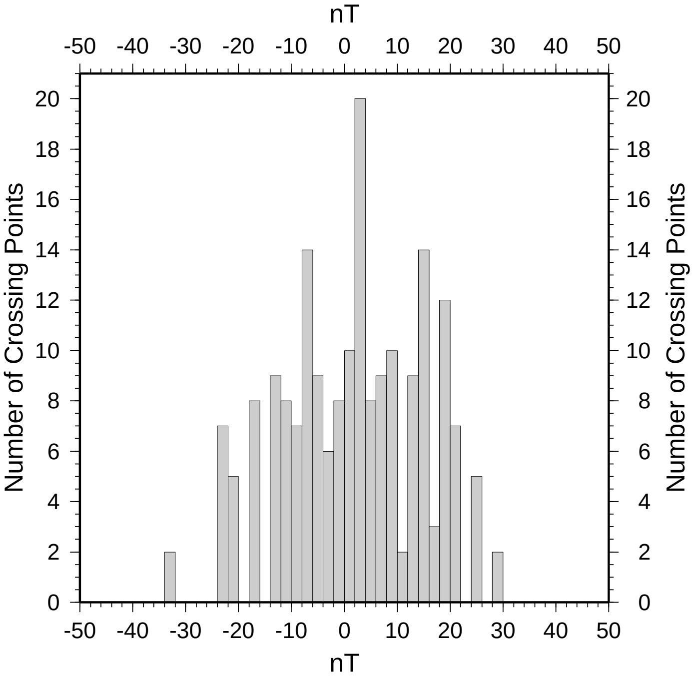

Figure 32: Histogram of the magnetic differences at crossing points of the GEOPECO profiles and of the GEODAS data

The data were combined to yield a data grid which is imaged in Figure 33. The magnetic profiles used for three-dimensional modelling were extracted from this grid. Before creating this data grid the residual magnetic field was low-pass filtered. The data were smoothed with an average weighted filter. A spectral analysis was performed to filter the magnetic data.

Most of the anomalies range between -300 and +400 nT. The map imaging the anomalies in a grid format partly lacks accuracy due to the locally great distances between the profiles. The data coverage in these areas is inadequate to examine the structures in detail.

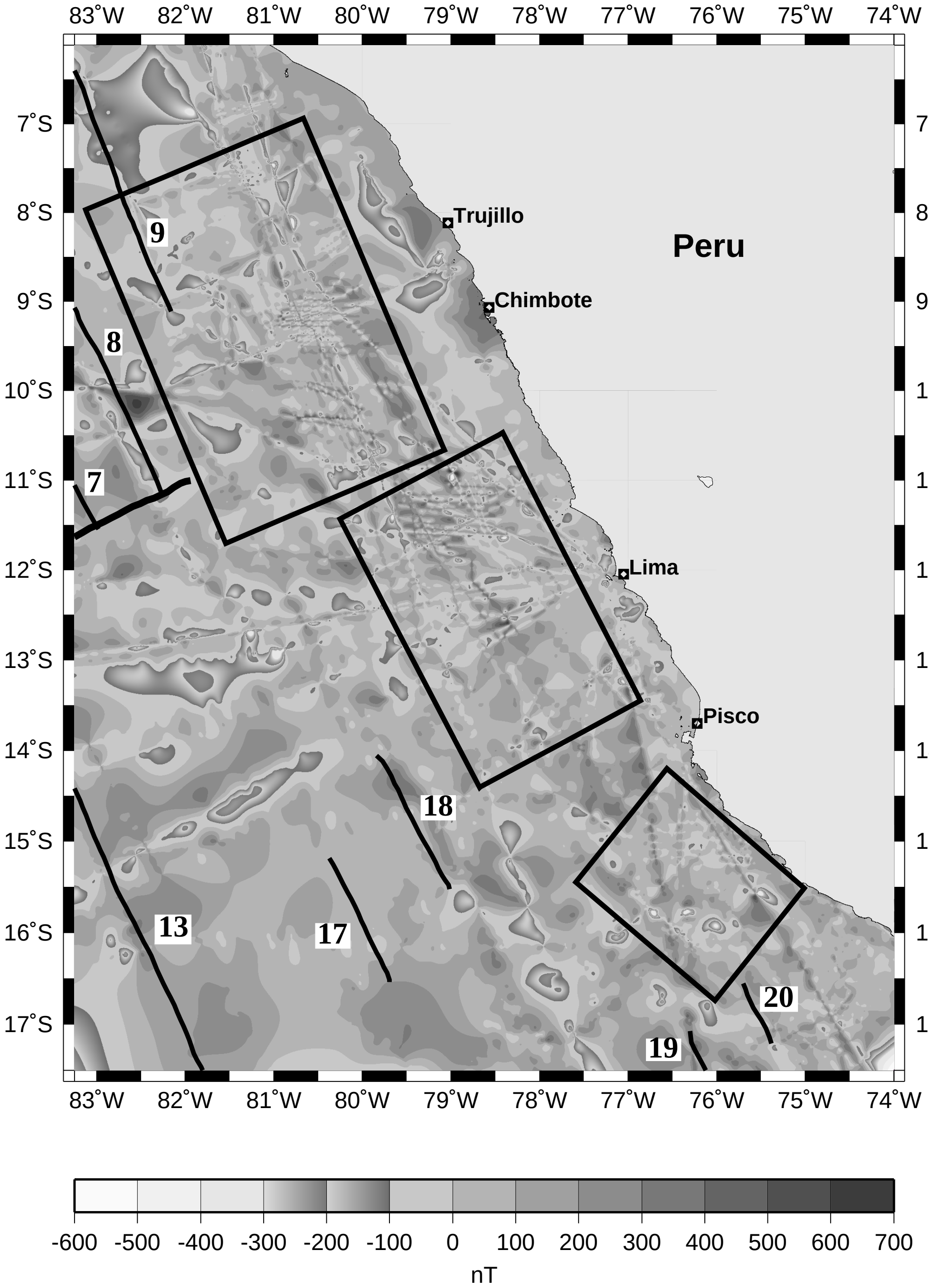

Figure 33: The Magnetic Anomalies

In the following the reduced magnetic data are displayed in detail along the ships' track lines and as projected profiles for each of the three areas of three-dimensional modelling. To render a clear image of the magnetic lineations the magnetic anomalies gravitate towards a selected direction in the following figures. In the individual views further magnetic anomalies are traceable.

6.10.1 Magnetic Anomalies in the Yaquina Area

Figure 34 shows a detailed map of the magnetic profiles in the Yaquina Area. The normally magnetised blocks are displayed in grey, the reversely magnetised anomalies are filled white. The area of three-dimensional modelling, is enclosed by the grey box.

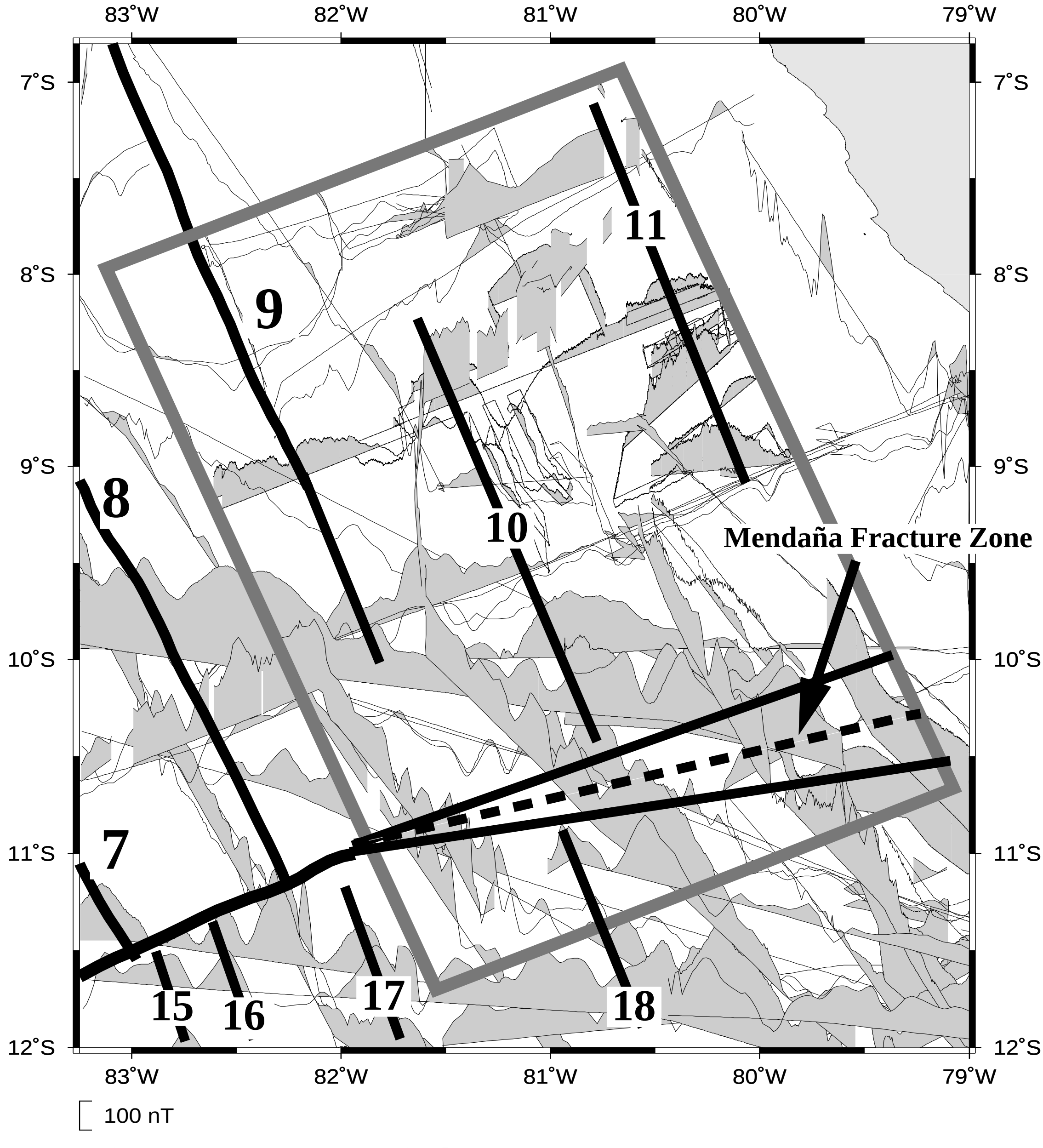

Figure 34: Magnetic Data in the Yaquina Area

The magnetic lineations 7 and 8 and 9 are predefined by NOAA (1993). The lineations 15, 16, 17 and 18, located in the southern part of the Yaquina Area, can be recognized in the illustration of the magnetic profiles acquired during the GEOPECO expedition and of the profiles included in the GEODAS data base (Figure 31). The magnetic lineations 10 and 11 are tentatively identifiable in Figure 34.

The Mendaña Fracture Zone crosses the southern part of the Yaquina Area and consequently the magnetic lineation pattern is disrupted. The dashed line is supposed to describe the central rift zone. The Mendaña Fracture Zone is not a clear line as can be seen in the bathymetric map (Figures 3 and 7). This situation is mirrored in the magnetic anomalies.

In the northwestern part of the Yaquina Area a region with mostly negative anomalies is observed. The magnetic lineation 10 cannot be traced all the way to the outer lines. The lineation may have been overprinted after its creation at the mid-oceanic ridge.

In Figure 35 the magnetic profiles of the Yaquina Area model which were extracted from the magnetic data grid are displayed.

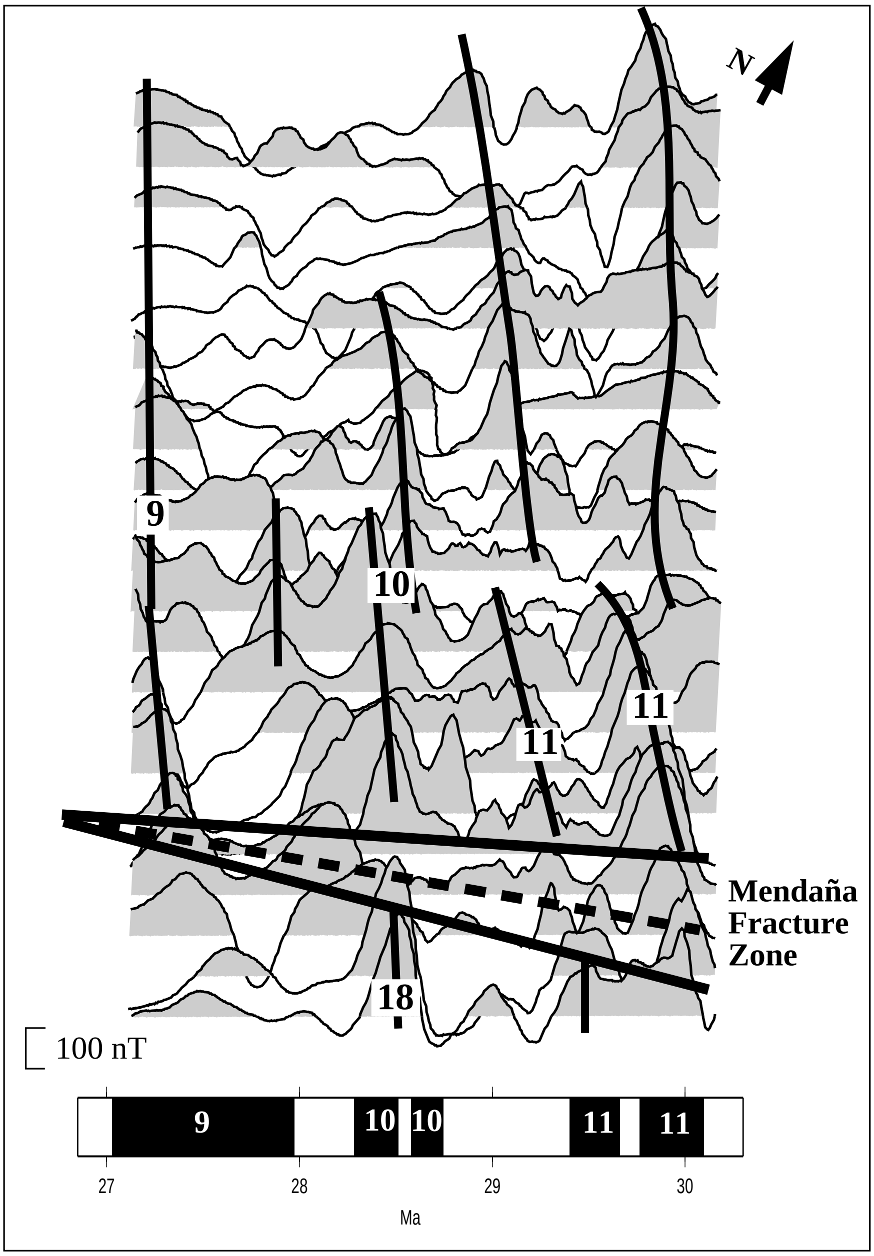

Figure 35: Magnetic Profiles of the Three-Dimensional Yaquina Area Model

North of the Mendaña Fracture Zone several anomalies can be traced. On the left and on the right side of the area clear anomalies can be followed. In the upper part magnetic anomalies can be traced as well. In the middle part, north of the Mendaña Fracture Zone, the picture is diffuse.

The Mendaña Fracture Zone cannot be clearly located on the basis of these magnetic profiles. In the wedge-shaped region of the fracture zone the magnetic anomalies show a different orientation. The new oceanic crust created along the Mendaña rift zone possesses magnetic lineations which are oriented perpendicular to the main trend. Consequently they are difficult to identify in the vertical planes of the three-dimensional model.

The assumable lineations 9, 10 and 11 are located north of the Mendaña Fracture Zone. The magnetic lineation 9 is 27.027 to 27.972 Ma old. Lineation 10 is separated into two parts, the first one being 28.283 to 28.512 Ma old and the second one being 28.578 to 28.745 Ma old. The magnetic lineation 11 consists of two parts as well. Part one is 29.401 to 29.662 Ma old, part two is 29.765 to 30.098 Ma old (Cande & Kent, 1995).

6.10.2 Magnetic Anomalies in the Lima Area

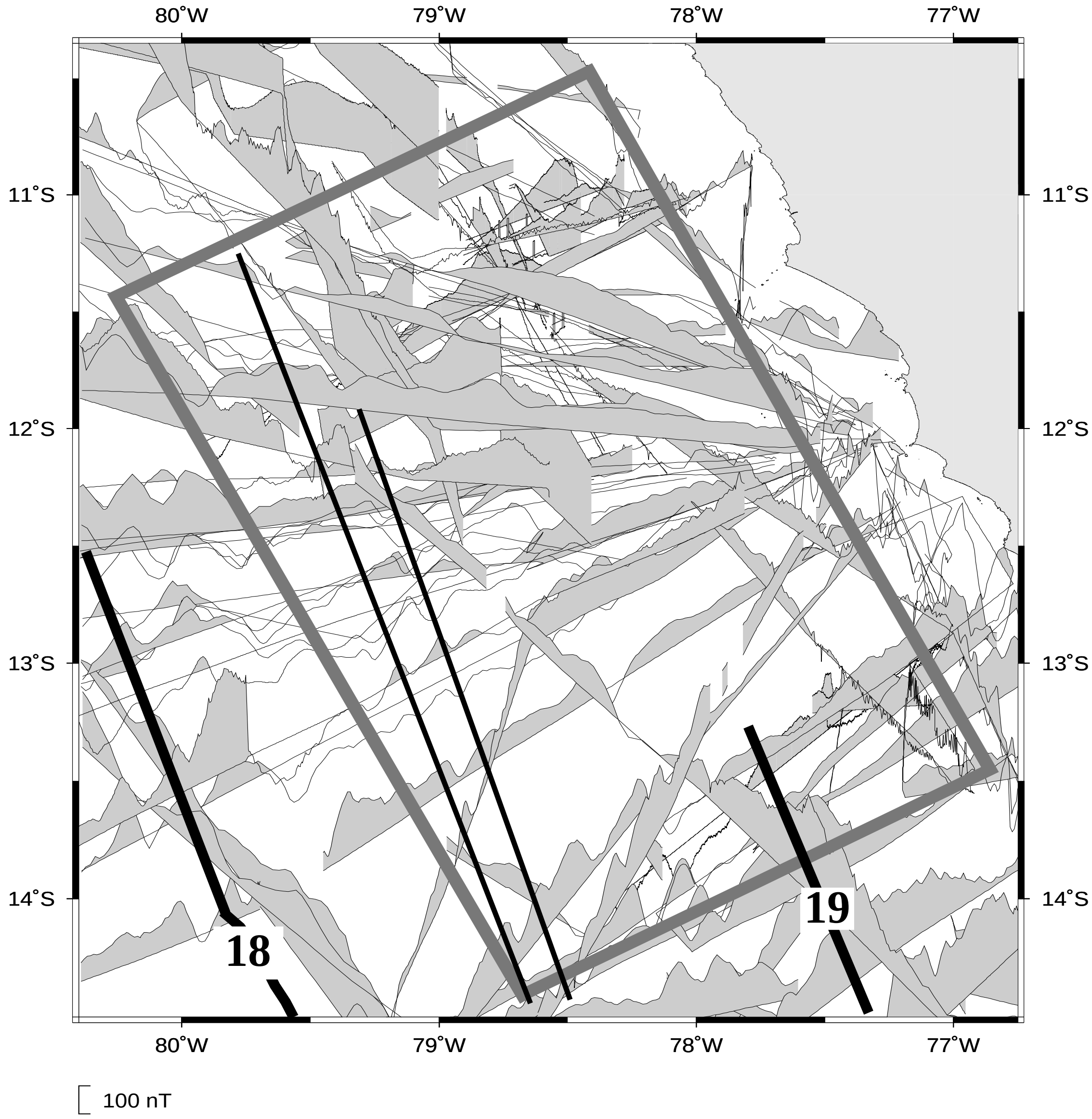

Figure 36: Magnetic Data in the Lima Area

West of the Lima Area, bounded by the grey box, the magnetic lineation 18 is identified by NOAA (1993). By interpolating the lineation pattern of the Nazca Plate it is possible to presume that the magnetic lineation 19 crosses the Lima Area. This assumption is based on Figure 31. Lineation 18 is 38.426 to 40.130 Ma old, lineation 19 is 41.257 to 41.521 Ma old and lineation 20 represents 42.536 to 43.789 Ma old oceanic crust (Cande & Kent, 1995).

In the western part of the Lima Area some magnetic anomalies can clearly be traced. Two of these anomalies are connected by a thin black line. As they are traceable throughout several track lines and as they lie between the lineations 18 and 19, these anomalies are probably subchrons. In the eastern part most of the track lines do not exhibit any clear anomalies.

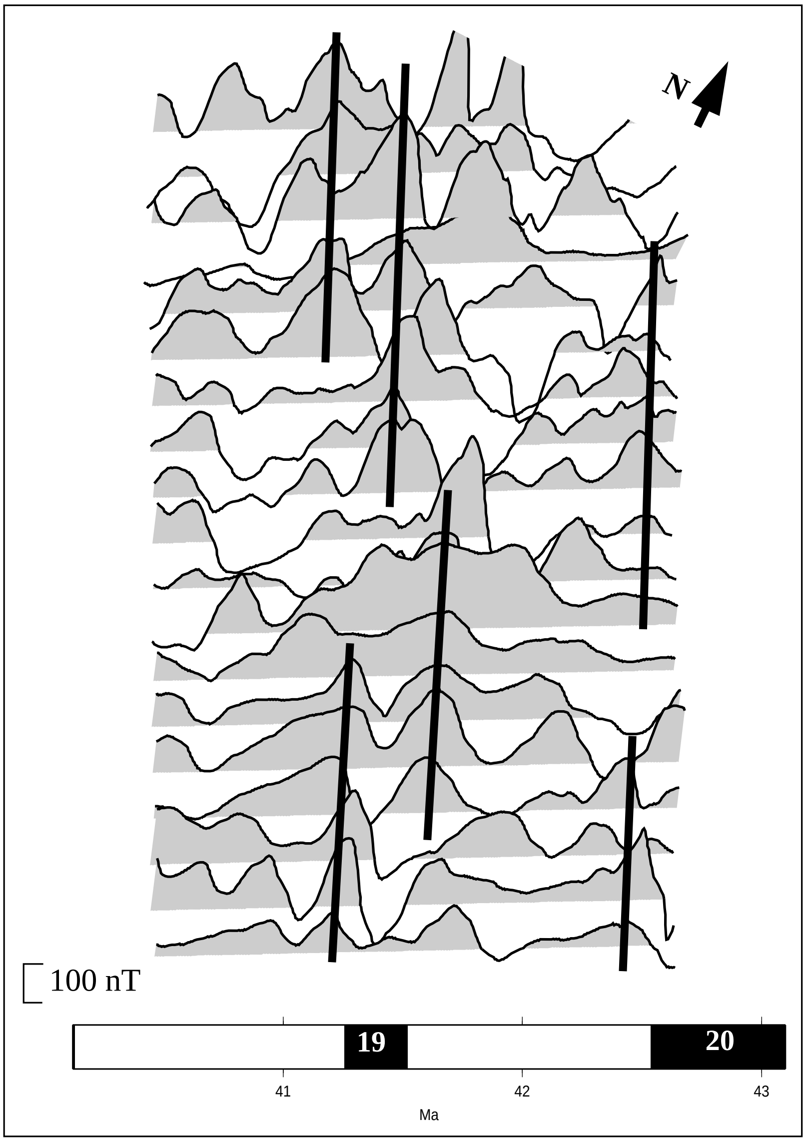

Figure 37: Magnetic Profiles of the Three-Dimensional Lima Area Model

In the Lima Area it is most difficult to identify any magnetic lineations. No clear anomaly pattern can be observed in the illustration of the magnetic profiles used for three-dimensional modelling. It appears to be difficult to identify the postulated anomaly 19 without doubt. The observable anomaly on the right side of the illustrated area is caused by the continental margin. It is very doubtful that the magnetic lineation 20, subducting underneath the continental margin, is still be observable.

In most areas of the region magnetic anomalies are not decipherable. Still, some anomalies can be tentatively followed throughout a few lines. One anomaly can be traced along most of the lines on the left side. In the middle right part an anomaly can also be followed. This diffuse pattern supports the presentiment that magnetic modelling is going to be very difficult.

6.10.3 Magnetic Anomalies in the Nazca Ridge Area

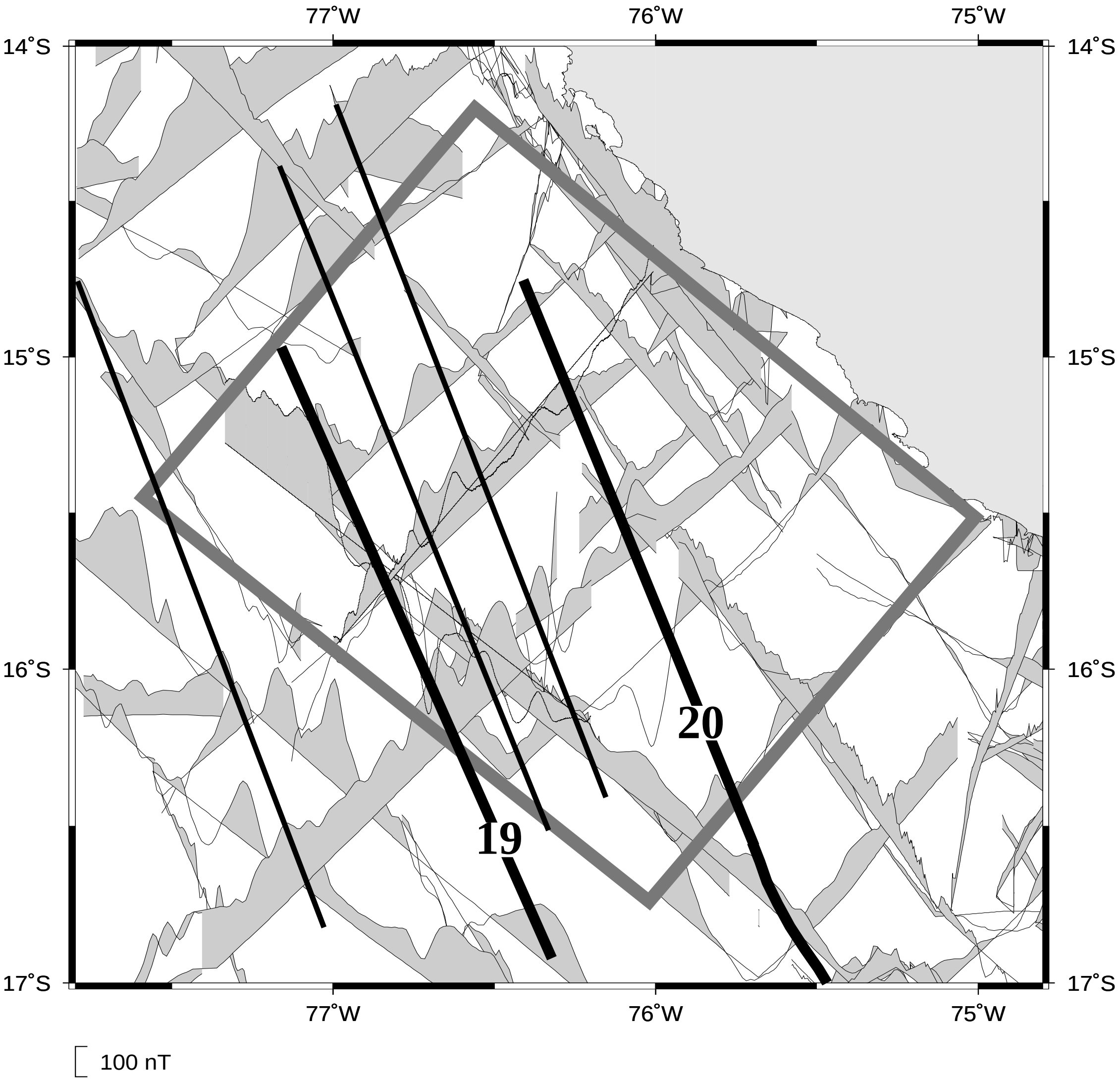

Figure 38: Magnetic Data in the Nazca Ridge Area

The strike of the magnetic anomalies describes the convergence direction of the Nazca Ridge. The long-wavelength anomalies are not well defined on all profiles as they are distorted by short-wavelength components. In the southeastern part of the area the distribution of the magnetic data is not altogether satisfying.

The interpreted magnetic lineation 19 represents 41.257 to 41.521 Ma old oceanic crust. The magnetic lineation 20 is 42.536 to 43.789 20 Ma old (Cande & Kent, 1995). In addition to these lineations several other magnetic anomalies can be traced throughout the contemplated area. These anomalies are indicated by thin black lines.

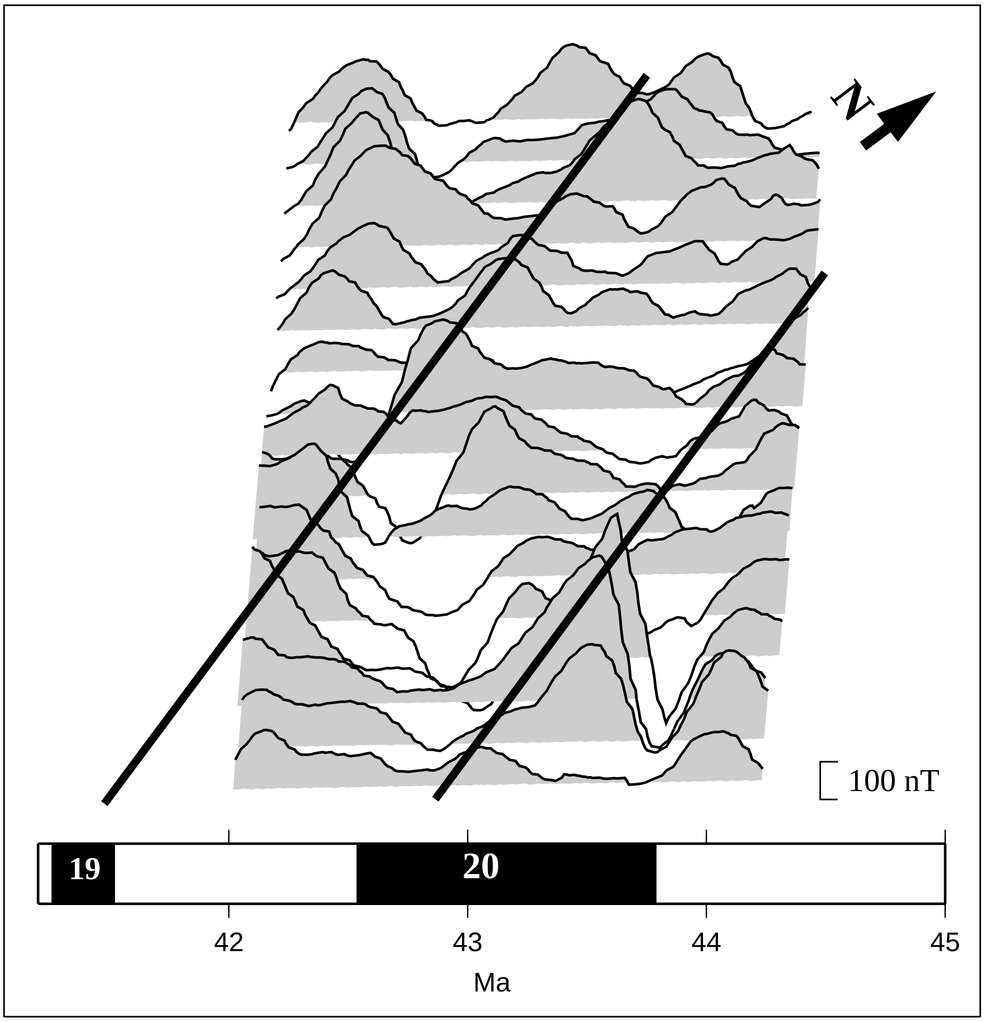

Figure 39: Magnetic Profiles of the Three-Dimensional Nazca Ridge Model

In Figure 39 the magnetic profiles of the Nazca Ridge model which were extracted from the magnetic data grid are displayed. The short-wavelength anomalies are almost completely attenuated. The magnetic lineation 20 can be identified tentatively. Lineation 19 is traced with more confidence. If the anomalies are observed without prior knowledge of the magnetic lineations a different anomaly pattern is apparent. Three anomalies propagating from lower part to the upper part of the region seem to be traceable. The right and left anomalies run rather straight, the middle one is bending in the middle part.

7 Three-Dimensional Modelling

The three-dimensional models were created using the software IGMAS (Götze et al., 2000). In the following the calculation of the gravitational and magnetic effects of a three-dimensional body as used in the program IGMAS (Götze, 1984; Götze & Lahmeyer, 1988) is described. The three-dimensional models consist of different bodies which are created as homogeneous polyhedrons. The geometric layout of a polyhedron is displayed in Figure 40. The polyhedrons are constructed of numerous vertices which are triangulated to form a triangle net. An impression of the applied equations is provided in the following.

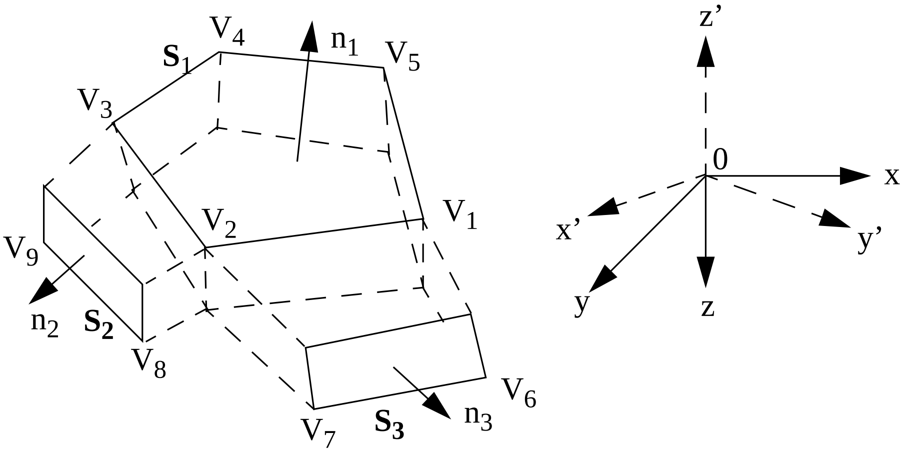

Figure 40: Geometric layout of a polyhedron (after Götze, 1984)

7.1 Gravity Equations

The volume integral describing the gravity potential U in point P is transformed into a sum of line integrals. Gauss's und Green's theorem on potential theory are applied. The gravity potential is given by:

$$U(P) = f\iiint \frac{dm}{R} \tag{1}$$

with: $U(P)$ = potential at P, R = distance between P and dm, f = gravitation constant, $dm = \rho \cdot dx \cdot dy \cdot dz = \rho \cdot dv$.
The derivation of the potential U gives the gravity g:

$$g(P) = \frac{\partial U}{\partial z}(P) = f\rho\iiint \frac{\partial}{\partial z}\left(\frac{1}{R}\right)dv \tag{2}$$

By using the Gauss formula this is transformed into:

$$g(P) = f\rho\iint \cos(n, z)\left(\frac{1}{R}\right)dS \tag{3}$$

with n = outer surface normal vector.

This surface integral is calculated for the whole polyhedron surface. The term cos(n,z) describes the direction of the surface element dS in the Cartesian coordinate system. The attraction of the whole polyhedron may be expressed as a superposition of the attractions emanated by its single plane surfaces S_j.

$$g(P) = f\rho \sum_{j=1}^{m} \left[\cos(n_j, z) \iint \left(\frac{1}{R}\right) dS_j \right] \tag{4}$$

m is the number of plane surfaces.

Equation (4) is transformed into a linear integral using the polygon P_j which comprises the surface S_j. The polyhedron is built of the vertices V_j. The parameters $h_{j,i}$, $r_{j,i}$, $a_{j,i}$ and $b_{j,i}$ describe the distances of the different vertices in a surface oriented coordinate system. The gravity g in point P, caused by a polyhedron, is described by:

$$\begin{aligned} g(P) = f\rho \Bigg(\sum_{j=1}^{m} \cos(n_j, z) \Bigg\{ \sum_{i=1}^{k_j} h_{j,i} \Bigg(\ln \frac{b_{j,i} + \overline{PV_{j,i-1}}}{a_{j,i} + \overline{PV_{j,i}}} \\ + \frac{\overline{|PP''_j|}}{h_{j,i}} \cdot \left(\operatorname{atan} \frac{(r_{j,i-1})^2 + b_{j,i}\overline{PV_{j,i-1}}}{\overline{|PP''_j|}|h_{j,i}|} - \operatorname{atan} \frac{(r_{j,i})^2 + a_{j,i}\overline{PV_{j,i}}}{\overline{|PP_j''|}|h_{j,i}|} \right) + 2\pi \overline{|PP_j''|} \delta\varepsilon \Bigg\} \Bigg] \Bigg) \end{aligned} \tag{5}$$

with:

$$\delta = \begin{cases} 0 & if \quad P'' \notin S_j \\ 1 & if \quad P'' \in S_j \end{cases}$$

$$\varepsilon = factor$$

7.2 Magnetic Equations

The magnetic field H in point P is obtained by solving similar integrals as for the calculation of gravity. The final equation is:

$$\left|\vec{H}(P)\right| = \sum_{j=1}^{m} (I_n)_j \cdot \left\{ \begin{bmatrix} (\gamma_1)_j \\ (\gamma_2)_j \\ (\gamma_3)_j \end{bmatrix} D_j + \sum_{i=1}^{k_j} \begin{bmatrix} (\alpha_1)_j & (\beta_1)_j & (\gamma_1)_j \\ (\alpha_2)_j & (\beta_2)_j & (\gamma_2)_j \\ (\alpha_3)_j & (\beta_3)_j & (\gamma_3)_j \end{bmatrix} \cdot \begin{bmatrix} A_i \\ -B_i \\ C_i \end{bmatrix} \right\} \qquad (6)$$

with: I = magnetization.

$$A_i = \beta_i'' \ln\left(\frac{b_{j,i} + \overline{PV}_{j,i-1}}{a_{j,i} + \overline{PV}_{j,i}} \right), \qquad B_i = \alpha_i'' \ln\left(\frac{b_{j,i} + \overline{PV}_{j,i-1}}{a_{j,i} + \overline{PV}_{j,i}} \right)$$

$$C_i = \frac{h_i \overline{PP}_j''}{|h_i| \left|\overline{PP}_j''\right|} \cdot \left(\operatorname{atan} \frac{a_{j,i} \left|\overline{PP_j''}\right|}{|h_i| \overline{\overline{PV}}_{j,i}''} - \operatorname{atan} \frac{b_{j,i} \left|\overline{PP_j''}\right|}{|h_i| \overline{\overline{PV}}_{j,i-1}} \right), \qquad D_j = 2\pi\delta\varepsilon \frac{\overline{PP_j''}}{\left|PP_j''\right|}$$

In equation (6) the terms A_i, B_i and C_i are multiplied by directional cosines.

A network or grid of values is modelled as a geological surface. This surface divides bodies with different density and/or susceptibility contrasts.

7.3 The Three-Dimensional Models

The areas of three-dimensional gravity and magnetic modelling are displayed in Figure 41. The closely spaced data distribution in these areas allows a detailed assignment of particular gravity or magnetic anomalies to specific bodies like the Nazca Ridge or to the lateral and vertical development of the especially magnetic basalt layers of the subducting oceanic crust. The profiles strike perpendicular to the main geological structure, i.e. the subduction zone.

For gravity modelling the free-air gravity data were used. The Bouguer gravity anomalies contain additional errors. For the calculation of the Bouguer gravity field the water depth is substantial. As the bathymetry is not satisfactorily known in the whole research areas, the Bouguer gravity field contains inaccuracies.

Both the short-wavelength and the long-wavelength components of the gravity field are investigated and consequently the complete free-air anomaly data and not the residual data were employed. The long-wavelength gravity components are related to crustal density variations or undulations of the crust/mantle interface. The short-wavelength components are caused by upper crustal structures, e.g. the accretionary complex.

In Figure 41 the vertical planes which are used to extend the models north- and southwards are marked blue. The green lines represent the wide-angle seismic profiles of the GEOPECO expedition. The vertical planes actually engaged for gravity and magnetic modelling are displayed in red. The lateral extension of the models along the single vertical planes exceeds the area of gravity and magnetic calculation by 50 km to avoid edge-effects. This amount of lateral extension depends on the thickness of the modelled blocks, the difference between the mean density of the modelled blocks and the surrounding density, and on the desired high modelling precision. The reference density is determined in such a way, that the edge-effect is as small as possible. This signifies that the average difference between the model densities and the reference density is close to zero. If there are no edge-effects an arbitrary constant value may be added to all density values. As a shift value is added the densities are relative values.

The seismic velocity models for the high-quality wide-angle seismic profiles P1 to P6 of the GEOPECO expedition are used to constrain layer geometry and thickness of the three-dimensional gravity and magnetic models and to provide initial estimates of the layer densities. The seismic velocity models were generated by Hampel et al. (2002a) and Broser et al. (2002). The velocities were determined by ray tracing; all available stations were taken into consideration. If identifiable in refection seismics, the information on layer geometries, especially on the position of the basement, was included in the wide-angle seismic models. The single layers were adjusted successively with increasing depth. The modelled data agree well with the real wide-angle data and the traveltime deviations are in the range of the picking accuracy. Mean traveltime deviations are 20 ms at near offset and 70 ms at far offset. The picking accuracy is ~50ms at near offset und ~100ms at far offset where a superimposition of multiple reflections is observed (Broser, 2002, pers. commun.). The total error for the upper layers ranges between 50 and 100 m, for the lower layers it ranges between 500 and 1000 m (Hampel, 2002, pers. commun.)

Firstly, 2.5-dimensional models were constructed. The profiles which are constrained by seismic velocity models were duplicated several times and laterally extrapolated in both directions. Now those sensible velocity-density conversions, providing the best fit between calculated and observed gravity anomalies, were determined. After this first accomplishment the appropriate gravity, magnetic and bathymetric data were appointed to the different vertical planes. Modelling in three dimensions is necessary as the magnetic lineations subduct obliquely and consequently the observable magnetic anomalies are caused by three-dimensional structures. These complexities are not negligible. Likewise the gravity anomalies are caused by three-dimensional formations. The gravity and the magnetic models possess the same layer geometries.

For three-dimensional modelling the different velocity-density relations were taken into consideration. The seismic velocities were converted to densities using the appropriate relations. Repeatedly the gravity and magnetic models were updated to the improved seismic velocity models generated by Broser (pers. commun.) and Hampel (pers. commun.). The layer geometries of the profiles which are constrained by wide-angle seismics were kept fixed and the layer densities were iteratively adjusted until a satisfactory fit between the observed and the calculated anomalies was achieved.

Different problems occur when attempting to integrate the seismic information into the gravity models. The seismic models are often very detailed and the different seismic layers may produce similar gravity effects. Such a detailed model which consists of numerous bodies causing almost the same gravity anomalies, is not sensible for gravity modelling.

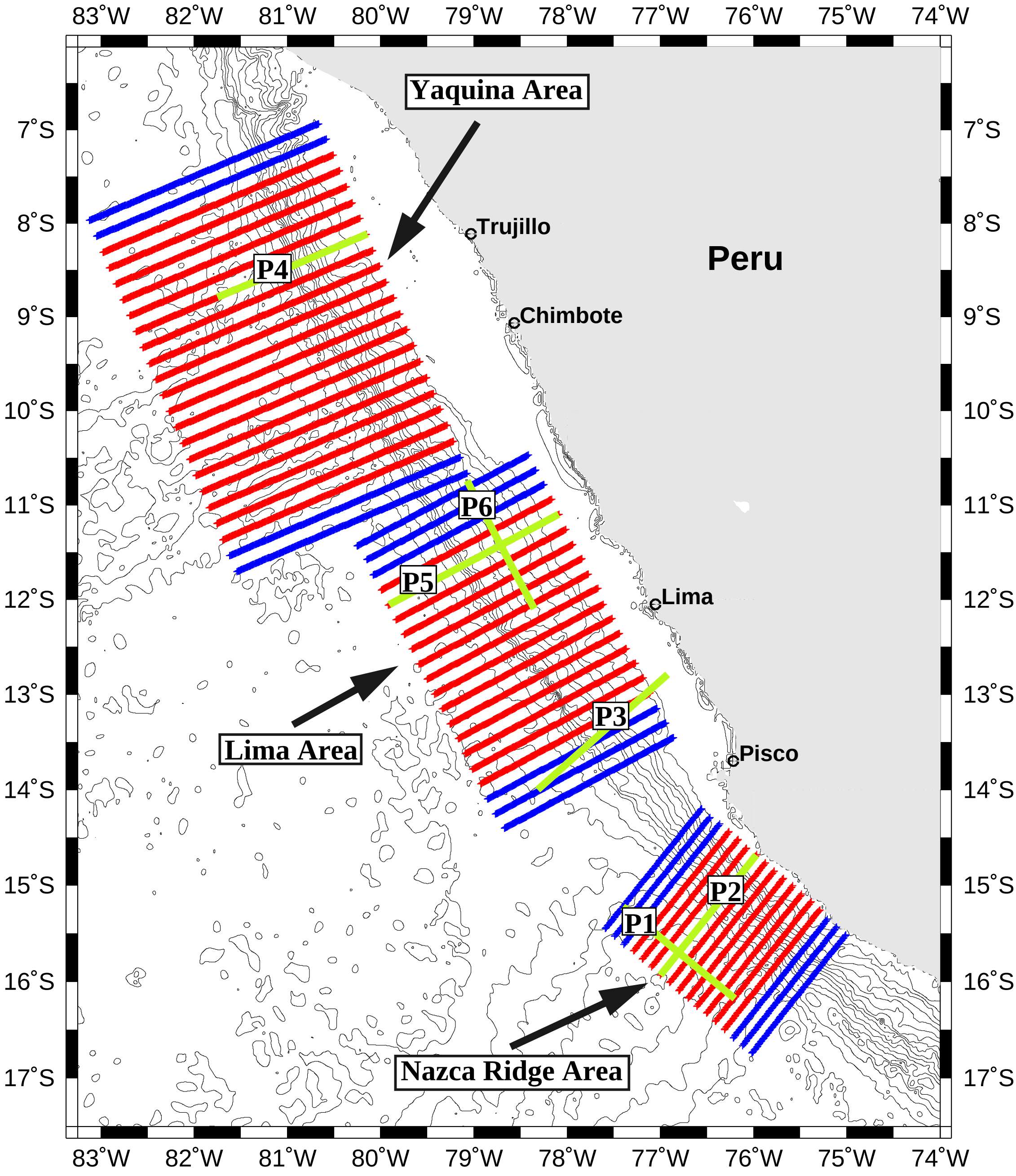

Figure 41: The Areas of Three-Dimensional Modelling
The red lines depict the planes of gravity and magnetic modelling. The blue lines describe the extensions of the different models which are necessary to avoid edge-effects. The green lines mark the wide-angle seismic profiles of the GEOPECO cruise.

The density models are created by introducing density anomalies deduced from the simplified velocity model. The average densities gained from the presented velocity-density relations are used as initial density estimates for the gravity modelling process. If the results are not acceptable on the planes which are not defined by seismics, a compatibility between the observed and calculated gravity and plausible densities can be achieved by changing the model geometry.

The three-dimensional models are developed iteratively. Forward modelling and inversion techniques are used simultaneously. The possibility to use inversion as a modelling tool is provided by the program IGMAS (Götze et al., 2000). In order to optimize the calculated model the densities and susceptibilities are calculated using inversion. Especially in magnetic modelling this technique is difficult to execute because the different parameters are influencing each other in a complex way. The geometry of the different layer boundaries is improved manually and iteratively. By applying inverse modelling the three-dimensional density-, susceptibility- and geometric model is computed to satisfy a given observed gravity or magnetic field. The output of a forward model is based on the calculated gravity or magnetic effect of the specified model geometries.

The mapped magnetic anomalies are simulated in three-dimensional modelling by a variation of magnetisation, the magnetic susceptibilities, the inclination and declination values, the Königsberg ratio and, of course, the model geometry. As starting values for the susceptibilities the average values for each rock type were used. In a first step, the general trends and the different blocks are determined with two-dimensional magnetic modelling. Besides the displayed magnetisations the different bodies of the model are assigned different values of susceptibility, inclination and declination as well as a varying rate of Königsberg ratio. The modelled oceanic crust consists of different blocks which possess a varying magnetisation. This partitioning is meant to describe the magnetic lineations, i.e. the geomagnetic field reversals. The relation between the remanent and the induced magnetisation is modelled using the Königsberg ratio. The inclination, the declination and the total magnetic field values for the areas are calculated using a program provided from the World Data Center-A and maintained by NOAA. Different models are considered. Three-dimensional magnetic models with and without remanent magnetisation are produced.

In the continental margin no extra magnetic bodies are included. Here, the number of bodies with different properties is the same as in gravity modelling. This restriction is an explanation why some magnetic anomalies cannot be reproduced completely. The main attention of magnetic modelling is focused on the subducting oceanic plate.

To determine geologically reasonable models the geophysical and geological constraints are very important for the non-unique potential field methods. The modelled profiles do not constitute unique solutions. As the various model parameters cannot vary arbitrarily along the Peruvian continental margin. The three models are regarded in dependence on each other. For the initial parameters of the model realistic values are applied.

7.3.1 The Resolution of the Three-Dimensional Models

The gravity and magnetic models possess a different resolution in the y- and in the x-direction. In the y-direction the distances between the vertical planes forming the model determines the resolution (see Figure 41). In every model the defined distance between the planes is suitable to resolve the observed geological structures. In the x-direction, i.e. along the planes, the data density is, at about one kilometre, by far higher. The gravity and magnetic values are extracted from the data grids presented in Chapters 5.5 and 6.10. Along the vertical planes the single bodies which are causing the gravity and magnetic anomalies are modelled in high detail.

The bathymetric data incorporated in the models are part of the 30 seconds etopo-grid by Sandwell et al. (2000, pers. commun.). Figure 42a shows a comparison of the bathymetric data measured during the GEOPECO expedition and the satellite data. The largest difference in depth between the two data sets amounts to 280 m and is located along the continental slope (see Figure 42b). The satellite data are incorporated in the three-dimensional models because the areas of three-dimensional modelling exceed the areas of bathymetric survey by far. In choosing the satellite bathymetric data for all the planes of the three-dimensional models, except for those planes which coincide with the wide-angle seismic profiles P2, P4 and P5, the bathymetric accuracy of the different models is comparable.

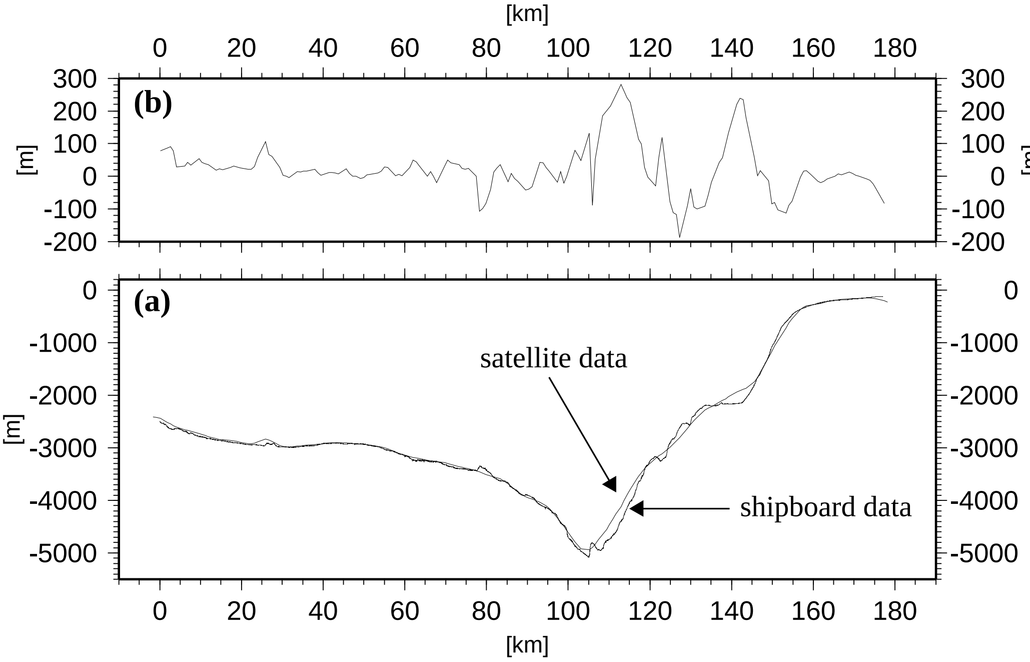

Figure 42: (a): A Comparison of the bathymetric data measured during the GEOPECO expedition with the bathymetric data provided by satellite altimetry. (b): The difference between satellite and shipboard data. This line represents profile P2. (The satellite data were obtained from Sandwell et al., 2000, pers. commun.)

7.4 The Yaquina Area Model

In the Yaquina Area it is possible to study the complex processes of tectonic deformation and the internal structure of the subduction zone by analysing the gravity and magnetic anomalies. The research area comprises the continental slope of the Peruvian margin, the trench and parts of the Nazca Plate as far as 240 km seawards of the collision zone. The area of three-dimensional modelling is 448.6 km by 295 km in size. The model consists of 23 vertical, parallel planes located at a distance of 21.5 km from each other. This distance is small enough to resolve the existing structures and it is adequately large, considering the immense size of the modelled area. The wide-angle seismic profile P4 of the GEOPECO expedition is integrated in the gravity and magnetic model. The location of this seismic profile is displayed in Figure 41.

A perspective view of the gravity and magnetic model is given in Figure 43. In this research area the Nazca Plate shows the structure of typical oceanic crust. The oceanic crust consists of the layers pillow basalts, sheeted dykes and gabbros, covered by sediments 1. The continental margin is modelled with the layers sediments 1, sediments 2, continental crust 1, continental crust 2 and continental crust 3. The layer continental crust 2 forms the seaward side of the continental block. The average thickness of the oceanic crust is 6.5 km.

In the southern part of the model lies the Mendaña Fracture Zone which divides the approximately 20 Ma old oceanic crust in the north from the approximately 33 Ma old crust in the south (see Figure 43). The older lithosphere in the south is cooler and denser and the impact of these attributes on the subduction process can be envisioned by gravity modelling. The magnetic investigation allows an interpretation of the lineation pattern north and south of the fracture zone.

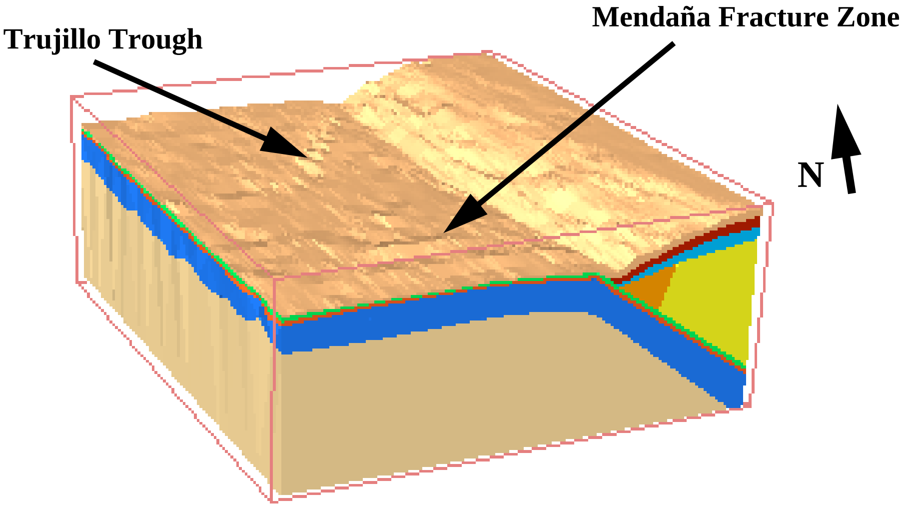

Figure 43: The Yaquina Area Model

7.5.1 Gravity Modelling in the Yaquina Area

In the following, all the planes of the gravity model are presented. Planes 1 and 2, as well as planes 22 and 23, are the north- and southward extension of the model. These planes prevent the occurrence of edge-effects. The actual potential field modelling starts on plane 3. The Yaquina Area model reaches into a depth of 30 km.

In Figure 44 a comparison of the calculated and the observed gravity field is presented. The calculated anomalies resemble the observed anomalies even in detail. The black lines represent the different vertical planes which build up the three-dimensional model. The anomalies are oriented roughly parallel to the Peru Trench. The gravity minimum along the Peru Trench lies between -150 and -170 mGal and shows an absolute minimum of -190 mGal on plane 7. Along the continental margin a prominent positive anomaly can be followed through planes 6 to 21. Observed more closely, the gravity values seaward of the Peru Trench form a complicated pattern. In the middle part of the region anomalies of about -20 mGal are crossed by areas of 0 to -10 mGal. In the northern and southern parts of the Yaquina Area the oceanic crust shows higher gravity values of 0 to 20 mGal with a local maximum of 40 mGal on plane 6. The seaward region, showing relatively low gravity values, faces the landward part which features the absolute maximum in free-air gravity values.

The differences between the modelled and the observed anomalies are displayed in Figure 45. The standard deviation of the gravity model is 3.07, the correlation coefficient is 1.00.

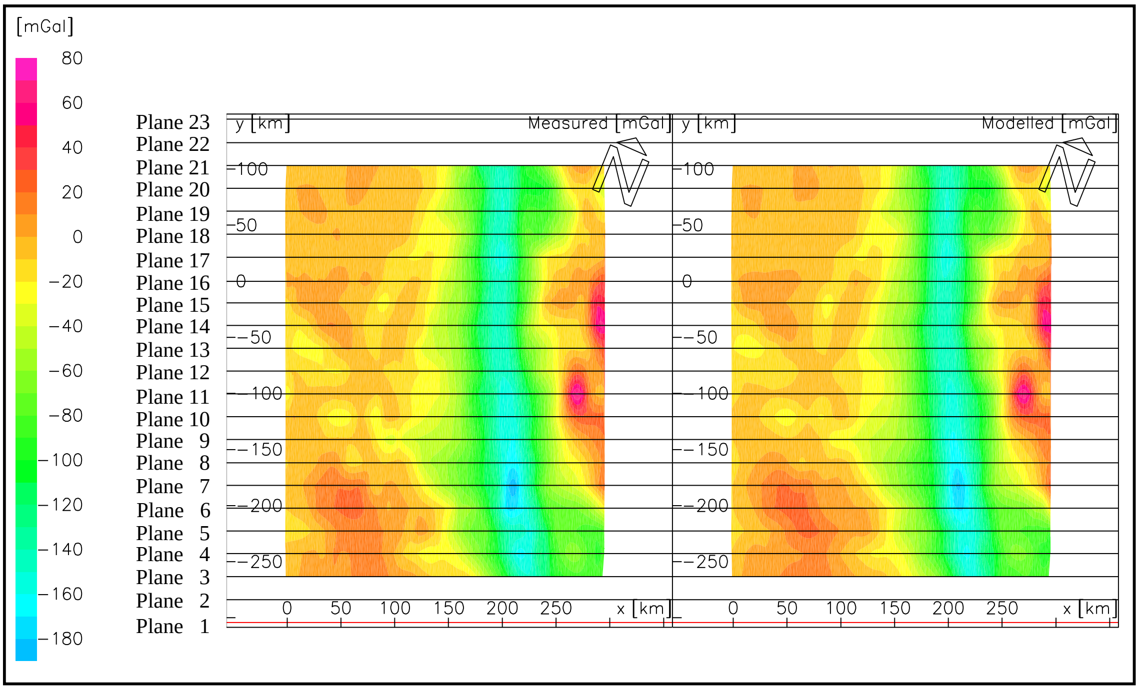

Figure 44: Observed and Calculated Gravity Fields in the Yaquina Area

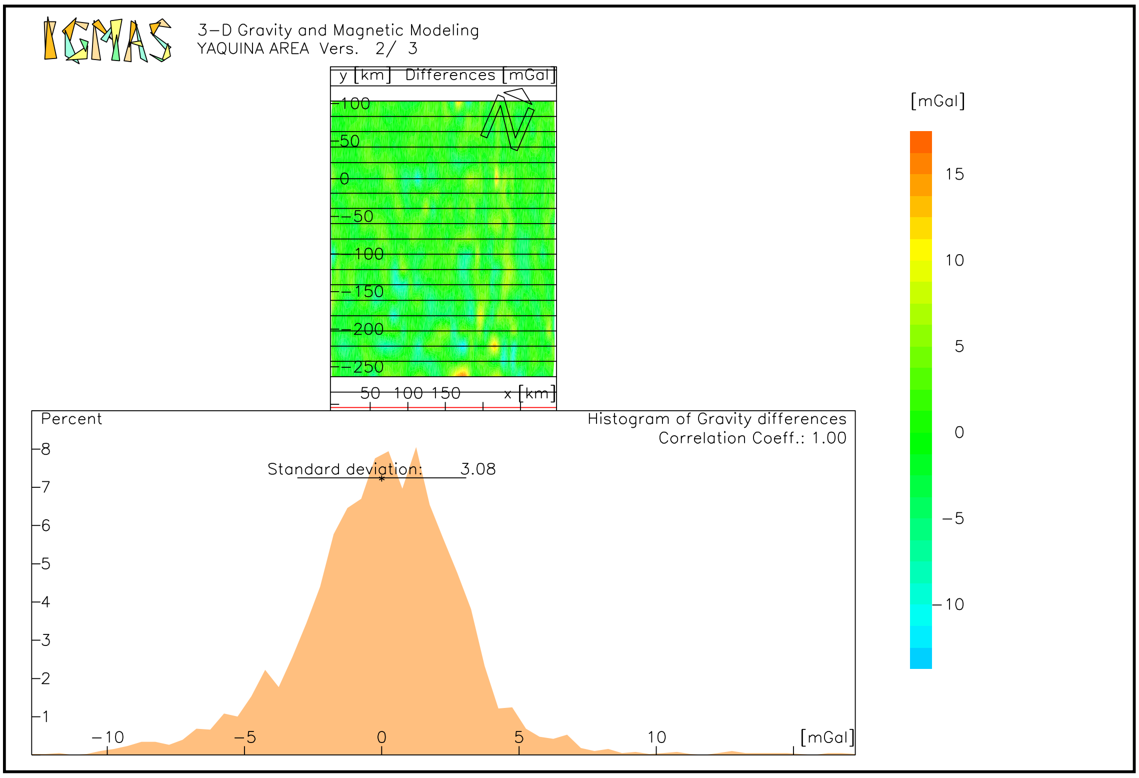

Figure 45: Yaquina Area - Gravity Modelling - Differences

Figure 46 shows plane 3, the southernmost plane of the model. As mentioned before, a shift value is added to the calculated anomalies and therefore the densities are relative values.

The densities of the oceanic crust increase to a small extent when subduction starts. Undulations of the oceanic crust are very remarkable in almost all the planes. The layer continental crust 2, a block with a slightly lower density than the main continental block, namely continental crust 3, forms the seaward tip of the continental margin.

On plane 3, seaward of the Peru Trench between kilometres 120 and 160, the oceanic crust is thickened by almost 2 km. The oceanic crust is rather thin on the seaward side of plane 3 and where it starts subducting underneath the continental crust. Further landwards, where the oceanic crust has already subducted underneath the continental margin and is located at a depth of 25 km, the oceanic crust shows its normal thickness for the Yaquina Area.

On the seaward side of plane 4 (Figure 47) the free-air gravity curve shows values around 0 mGal. This region is almost isostatically compensated. The continental slope is characterized by disturbances in its layer geometry. The relative gravity maximum at kilometre 270 reaches -70 mGal. A bathymetric high, causing a local maximum in gravity, is located around kilometre 230. Beneath the upper sediments the layer sediments 2 is raised upwards as well.

The planes 3 and 4 cross the Mendaña Fracture Zone. The undulations of the oceanic crust certainly are expressions of this fracture zone.

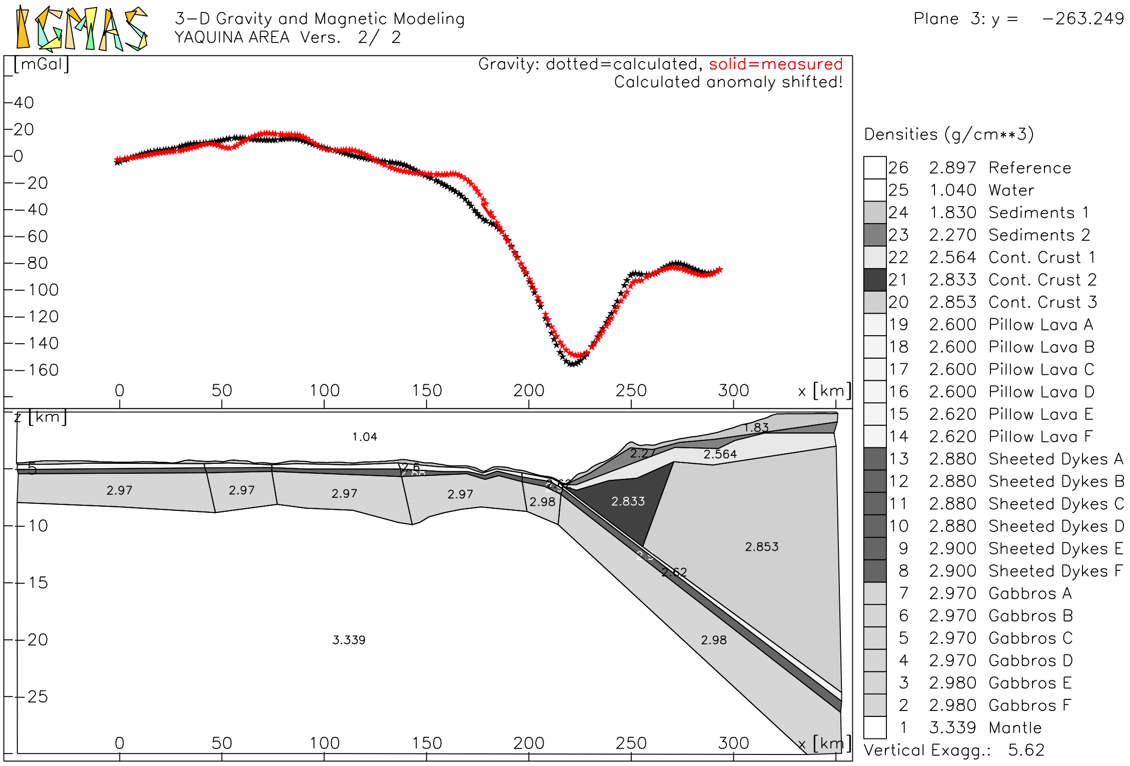

Figure 46: Yaquina Area - Gravity Modelling - Plane 3

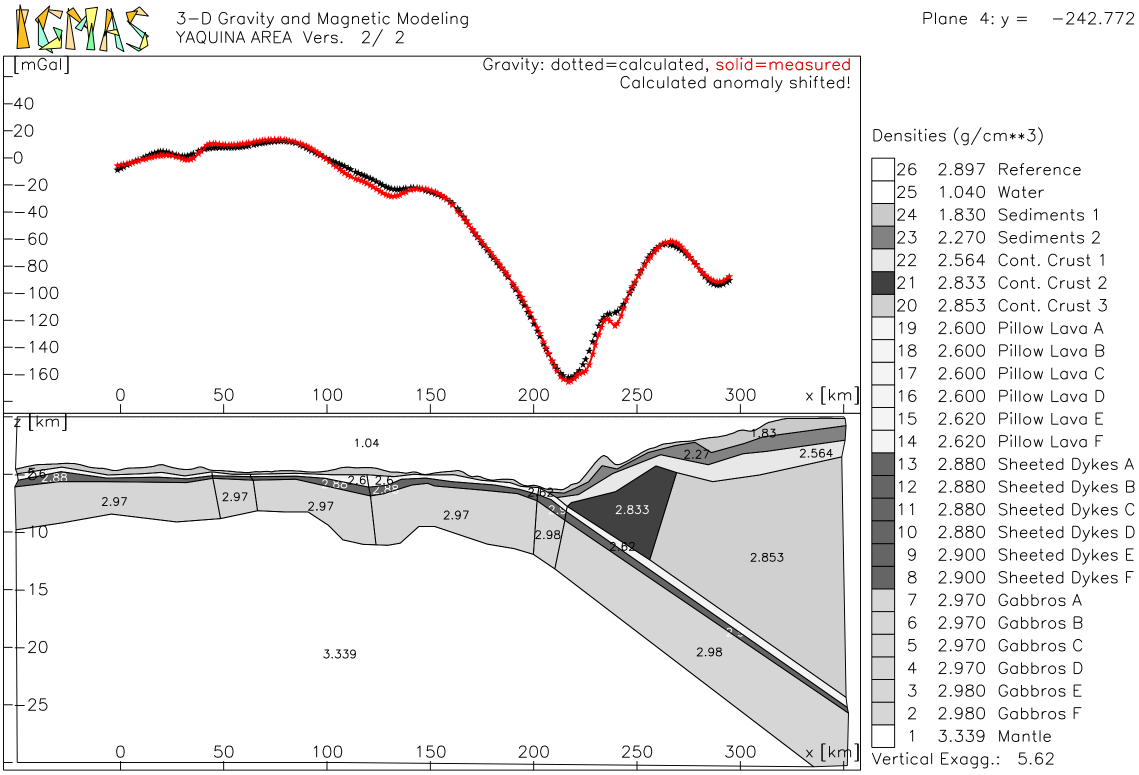

Figure 47: Yaquina Area - Gravity Modelling - Plane 4

On plane 4 the oceanic crust is remarkably thickened between kilometres 90 and 145. The continental slope features a striking elevation of the sediment layers at kilometre 230.

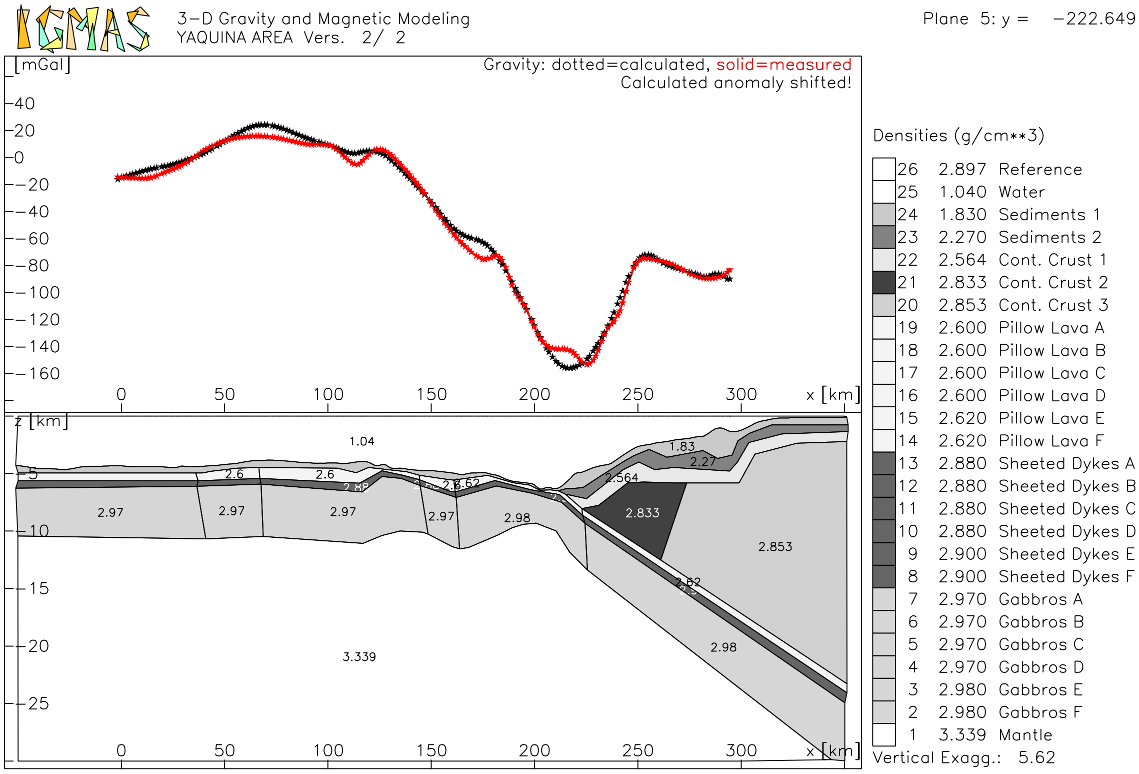

Figure 48: Yaquina Area - Gravity Modelling - Plane 5

On plane 5 strong undulations of the oceanic crust are modelled between kilometres 110 and 220. Underneath the Peru Trench, at kilometre 210, the oceanic crust is remarkably thin. An upwelling of the denser mantle is modelled. On the seaward side of the plane a minimum in gravity is observed. Along the lower continental slope the layer sediments 1 is rather thick. The observed free-air gravity is, with -145 mGal, especially high above the Peru Trench. Even with an extreme upwelling of the mantle underneath the trench these relatively high gravity values cannot be reproduced.

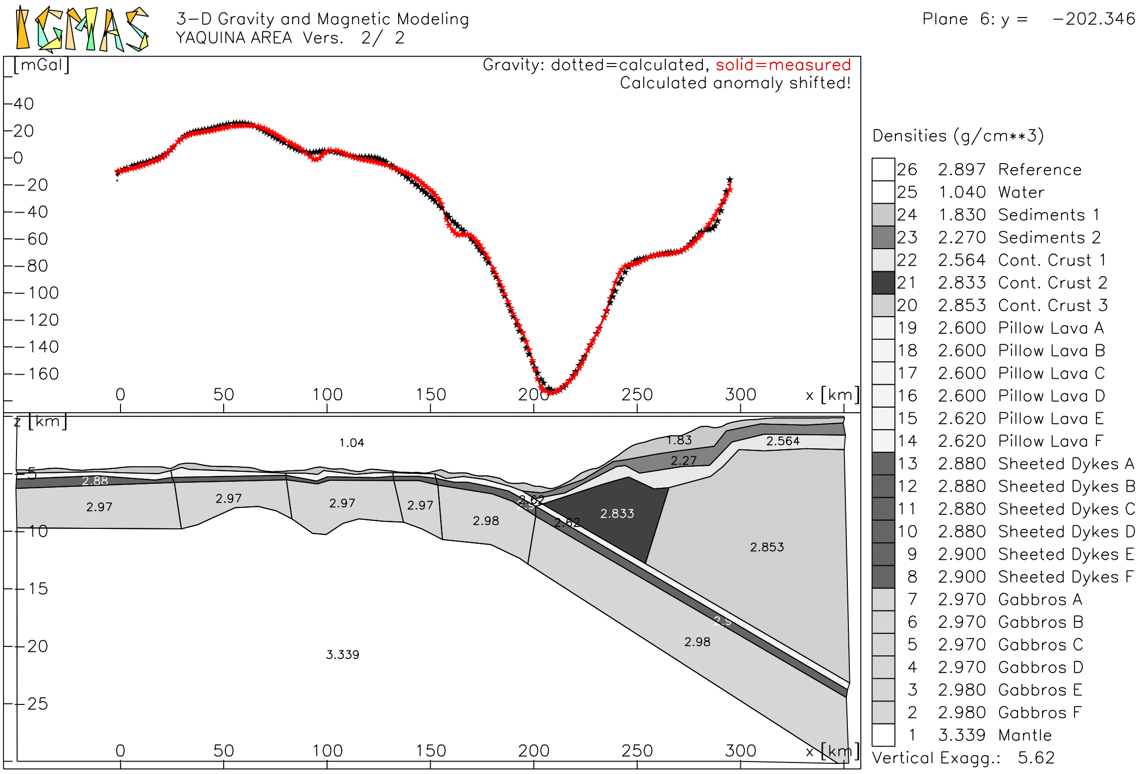

Figure 49: Yaquina Area - Gravity Modelling - Plane 6

On plane 6 (Figure 49) the undulations are located further seawards, between kilometres 30 and 150. The sea floor topography shows a rough relief.

On plane 7 (Figure 50) the upwelling of dense mantle material is very distinct between kilometres 30 and 75. Along the continental slope the denser layers are located close to the sea floor. Here, the minimum is particularly narrow and very distinct with gravity values as low as -180 mGal.

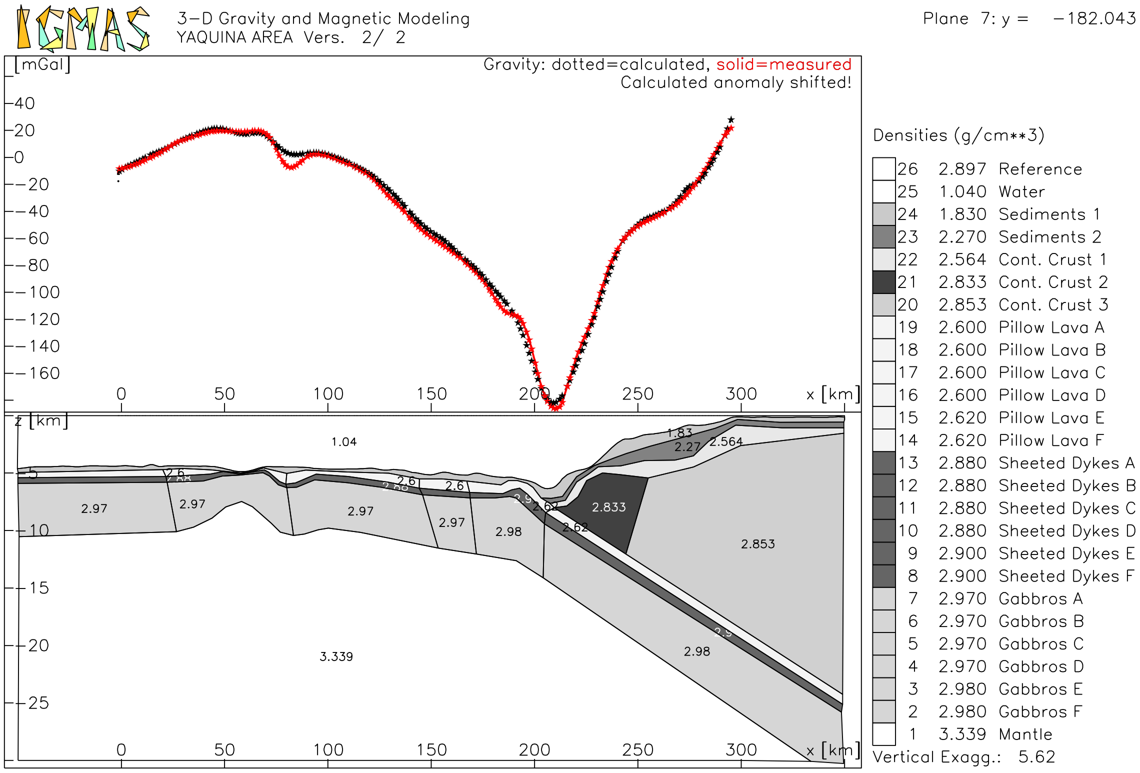

Figure 50: Yaquina Area - Gravity Modelling - Plane 7

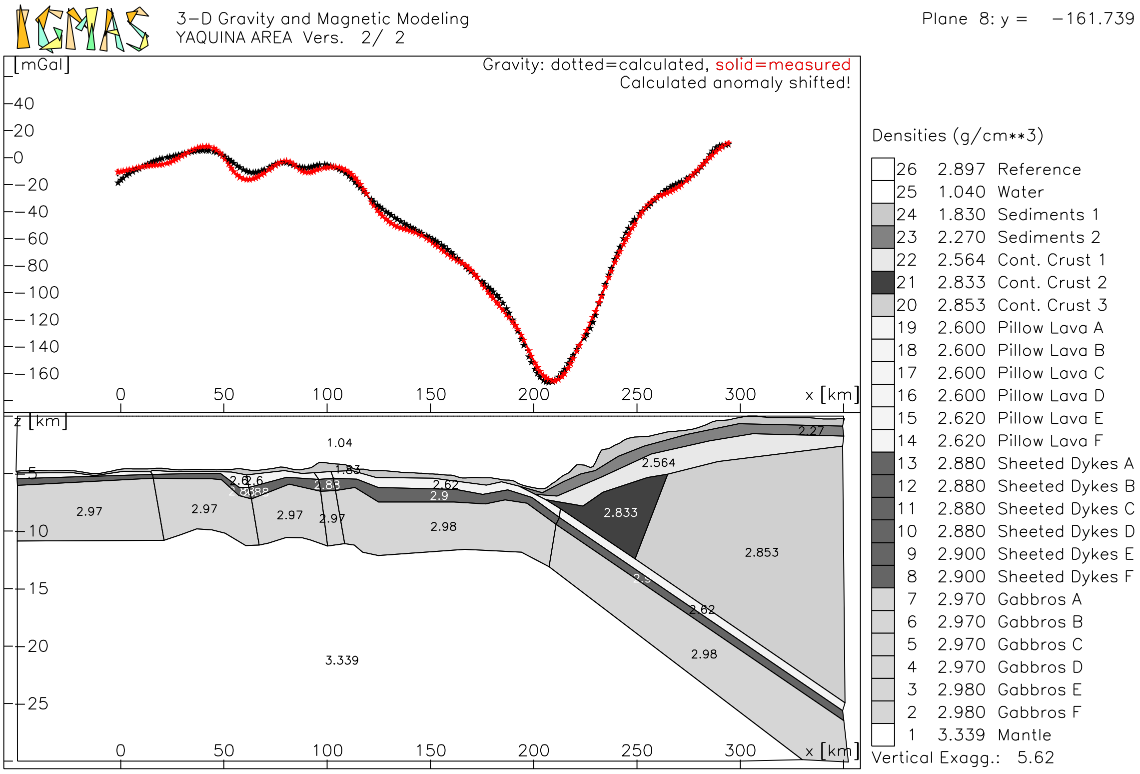

Figure 51: Yaquina Area - Gravity Modelling - Plane 8

Plane 8 features several undulations of the oceanic crust between kilometres 10 and 120. The layers of the continental margin are almost parallel (see Figure 51).

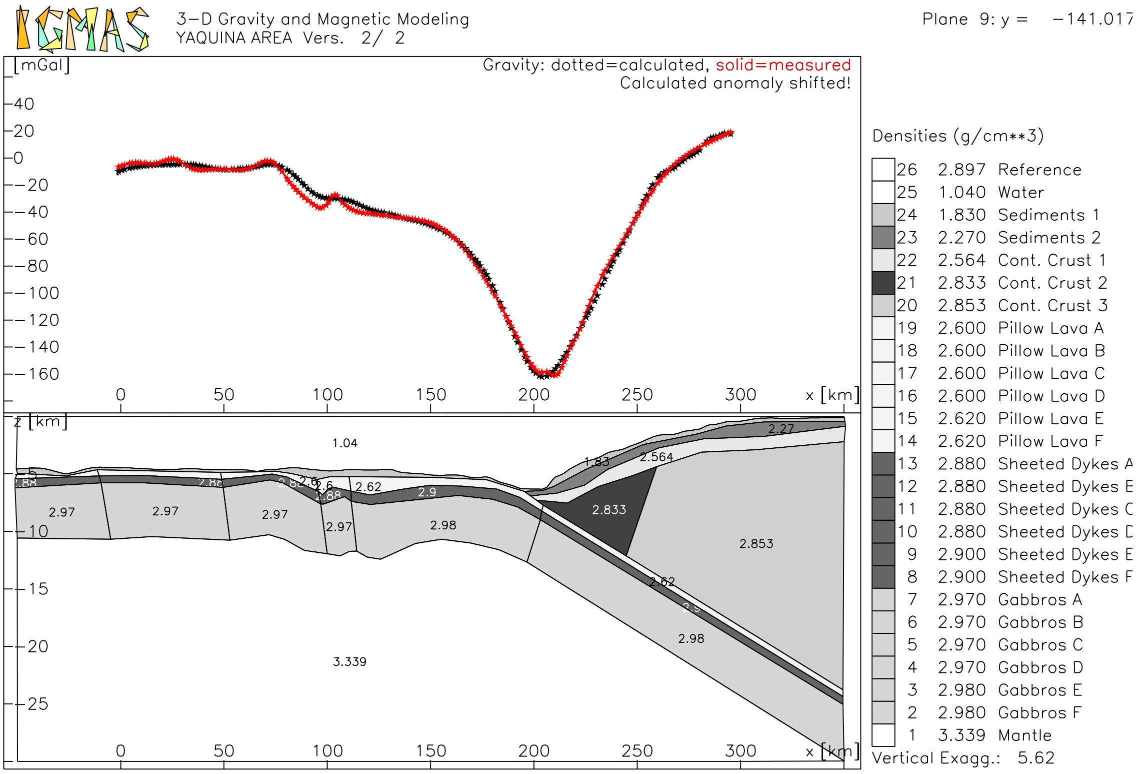

Figure 52: Yaquina Area - Gravity Modelling - Plane 9

On plane 9 a prominent thickening of the oceanic crust is modelled between kilometres 70 and 140. The variations in thickness of the oceanic crust are located further landward.

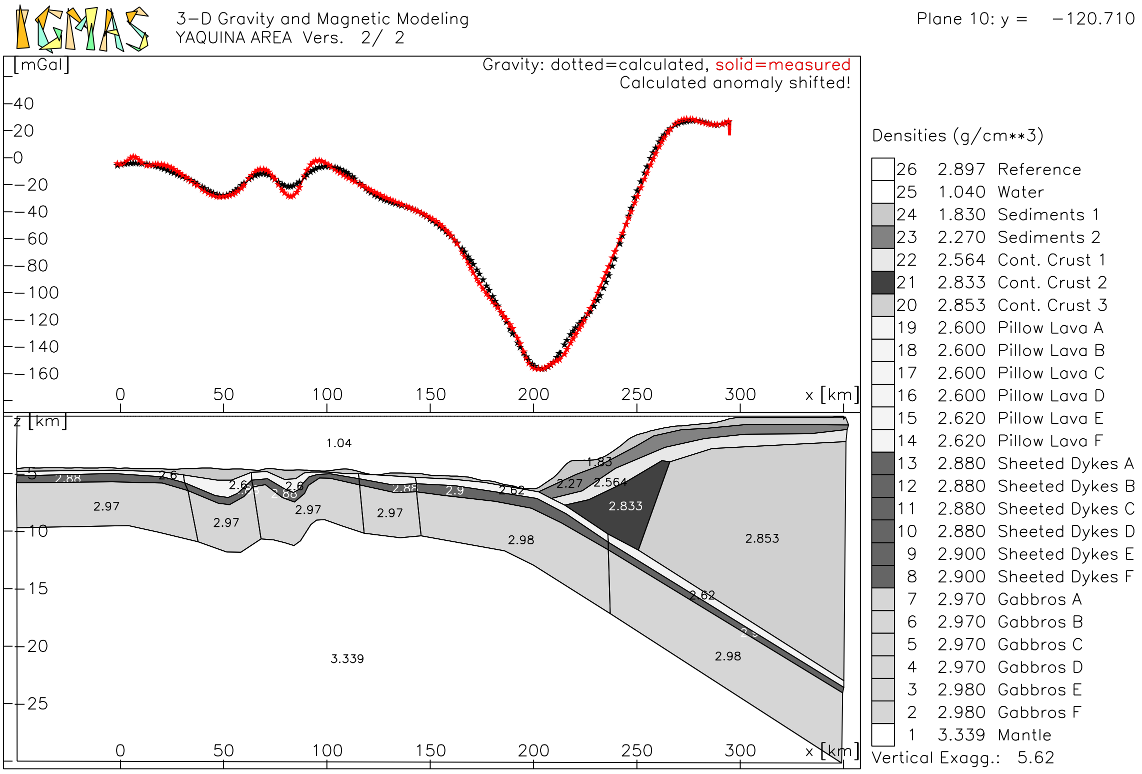

Figure 53: Yaquina Area - Gravity Modelling - Plane 10

Very strong undulations of the oceanic crust are located between kilometres 0 and 120 on plane 10 (see Figure 53). The high-frequency undulations possess a wavelength of only 25 km.

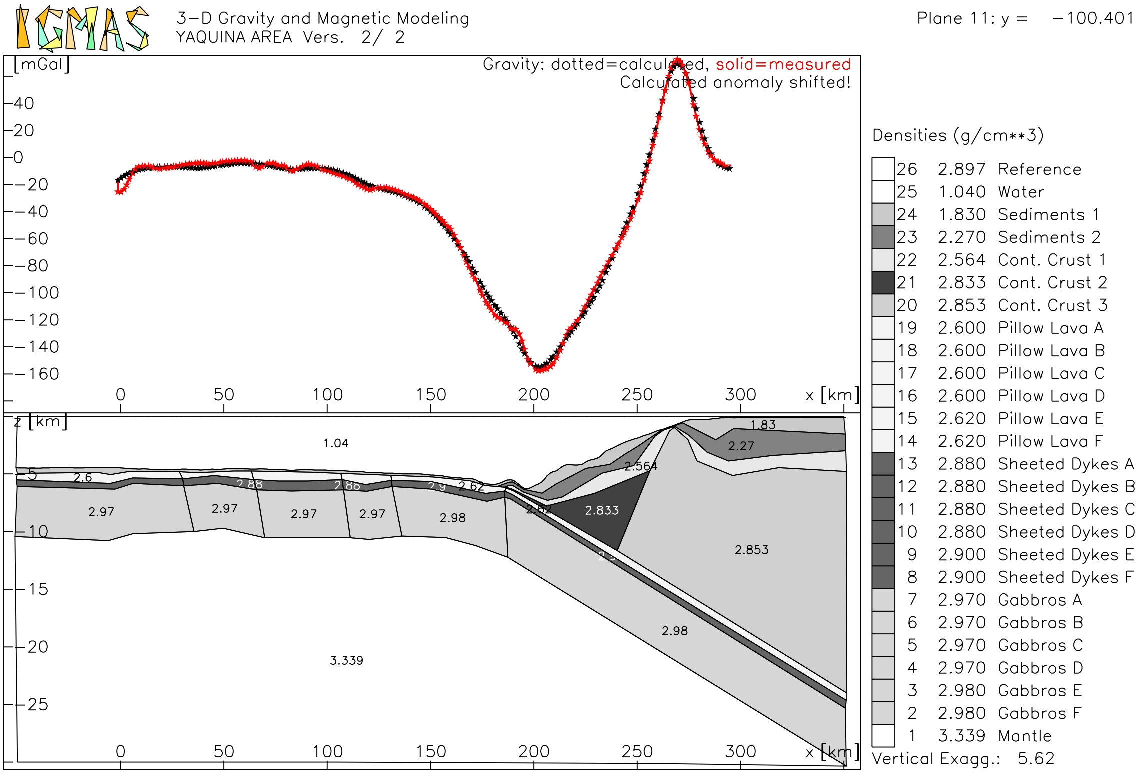

Figure 54: Yaquina Area - Gravity Modelling - Plane 11

On plane 11 the undulations are almost completely attenuated (see Figure 54). A prominent maximum of 65 mGal is located at kilometre 270 on the continental margin. The high-density continental crust 3 reaches up to the sea floor. The maximum exhibits very sharp edges. This is one of the areas where it is highly probable to sample metamorphic rocks on the ocean floor.

A prominent upwelling of the mantle is observed around kilometre 70 on plane 12. The free-air gravity exhibits the corresponding, relatively low-frequency maximum. Along the continental margin the maximum is subdued in comparison with plane 11. The free-air gravity values rise to 25 mGal. This maximum is followed by a local, relative minimum of around 0 mGal further landward.

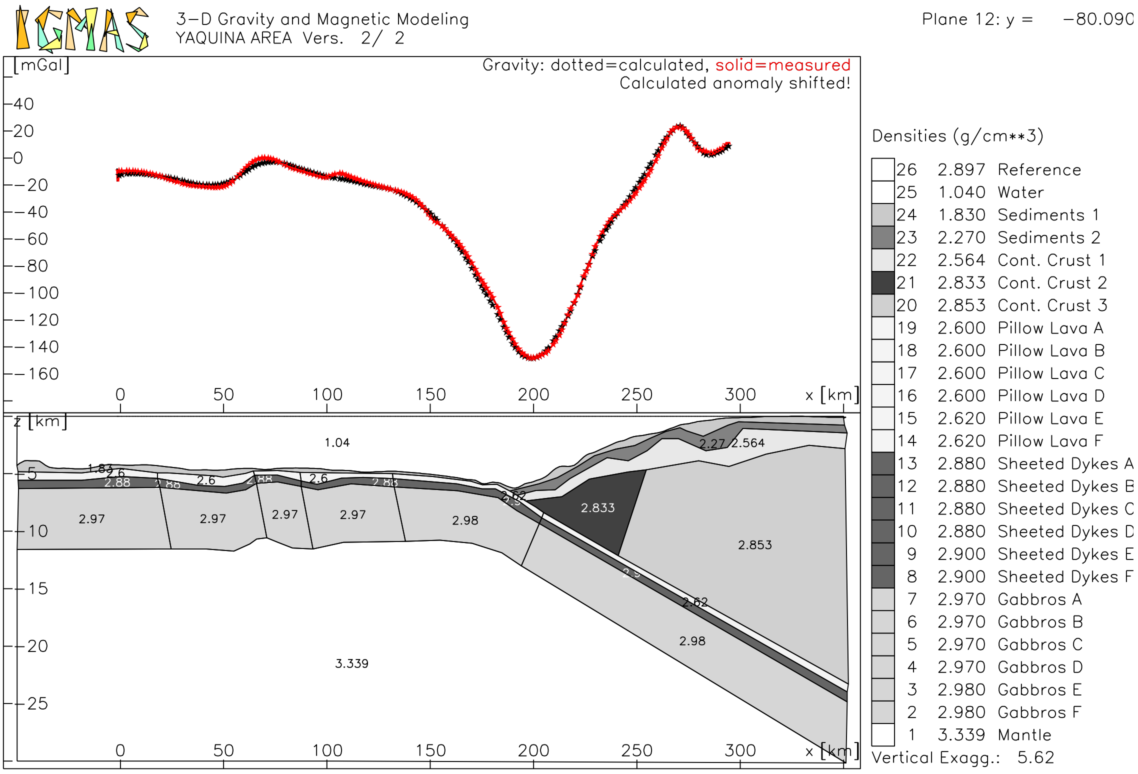

Figure 55: Yaquina Area - Gravity Modelling - Plane 12

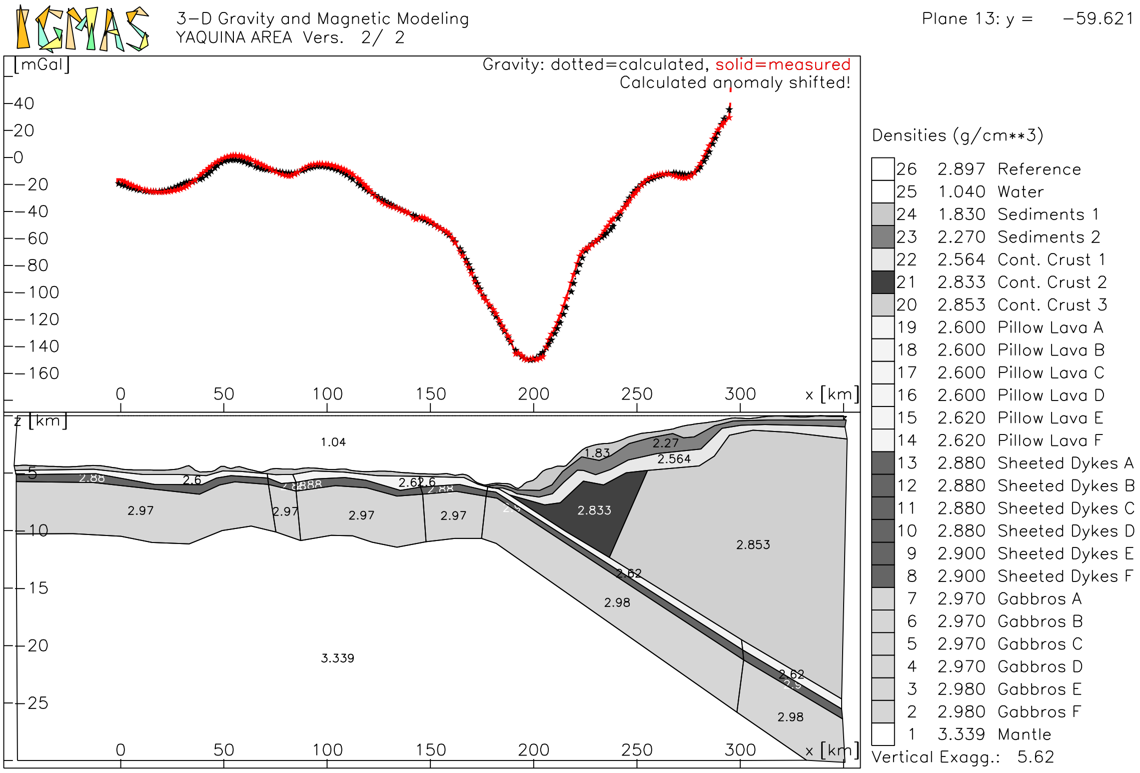

Figure 56: Yaquina Area - Gravity Modelling - Plane 13

On plane 13 the gravity curve shows negative values of less than -20 mGal on the seaward side of the model. Where the oceanic crust is locally thinned between kilometres 50 and

110 the free-air gravity anomalies show values of 0 mGal. This indicates that this area is isostatically compensated. On the landward side of the plane, between kilometres 255 and 280, a small plateau featuring 0 mGal is located. Further landward the gravity values are rising steeply.

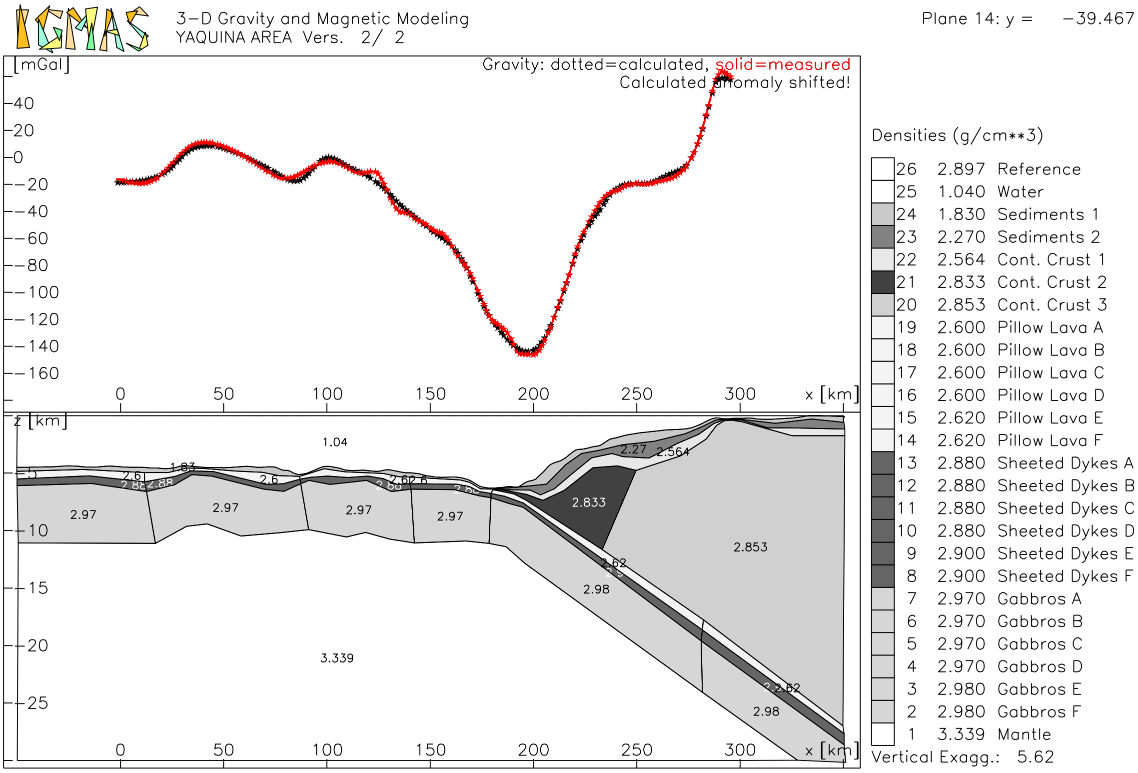

Figure 57: Yaquina Area - Gravity Modelling - Plane 14

On the seaward side of plane 14 the oceanic crust is rather thick. An upwelling of the mantle causes a maximum in gravity between kilometres 25 and 75. Subparallel to the trench axis, near kilometre 100, a ridge is observable on the Nazca Plate. The influence of this topographic high on the tectonic environment can be studied in the model from completed to not yet started subduction.

The depression seaward of the ridge causes a strong anomaly of -20 mGal in free-air gravity on plane 15. Above the continental margin a step in the steeply rising gravity values is located between kilometres 240 and 270. Further landward the denser layers of the continental block ascent abruptly in the direction of the sea floor (see Figure 58).

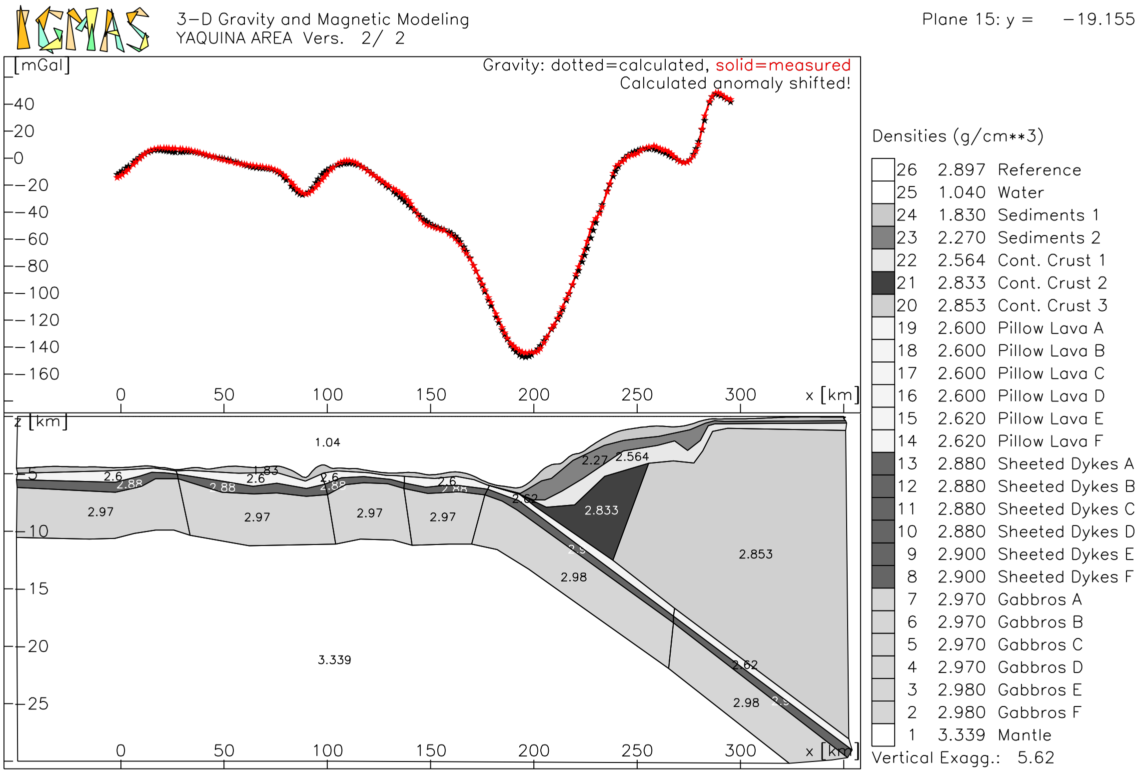

Figure 58: Yaquina Area - Gravity Modelling - Plane 15

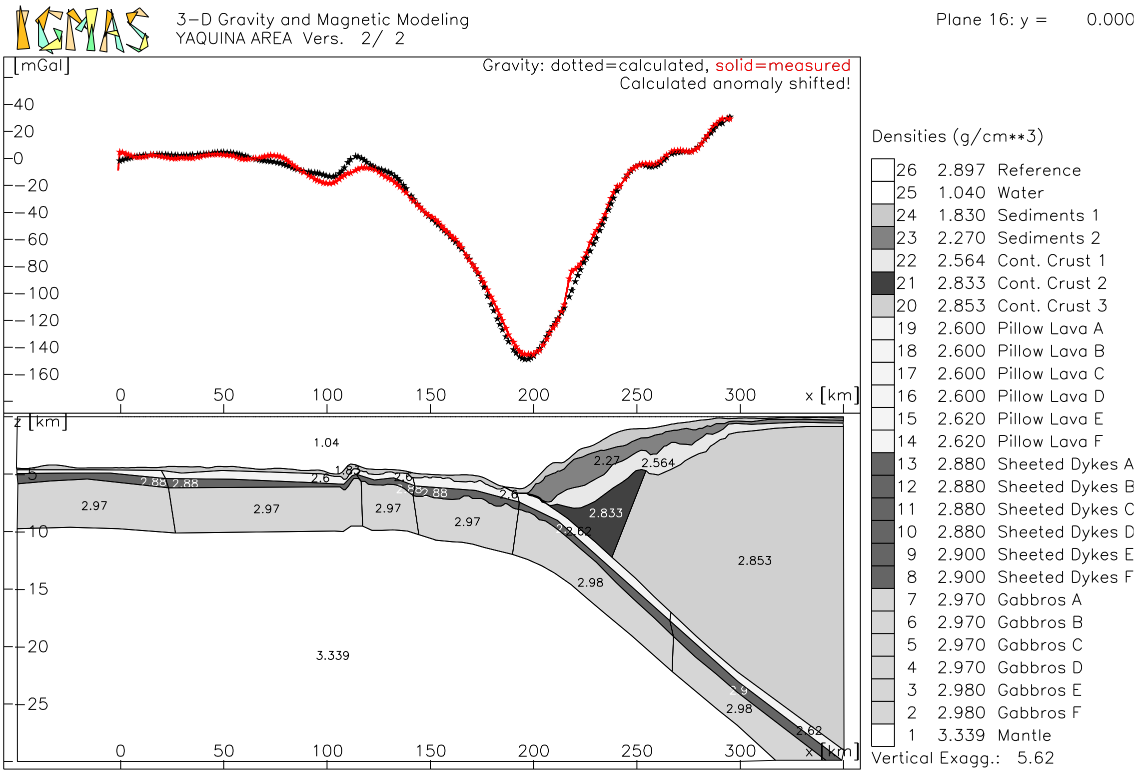

Figure 59: Yaquina Area - Gravity Modelling - Plane 16

Plane 16 is entirely based on seismic information between kilometres 100 and 300. This plane coincides with the seismic profile P4.

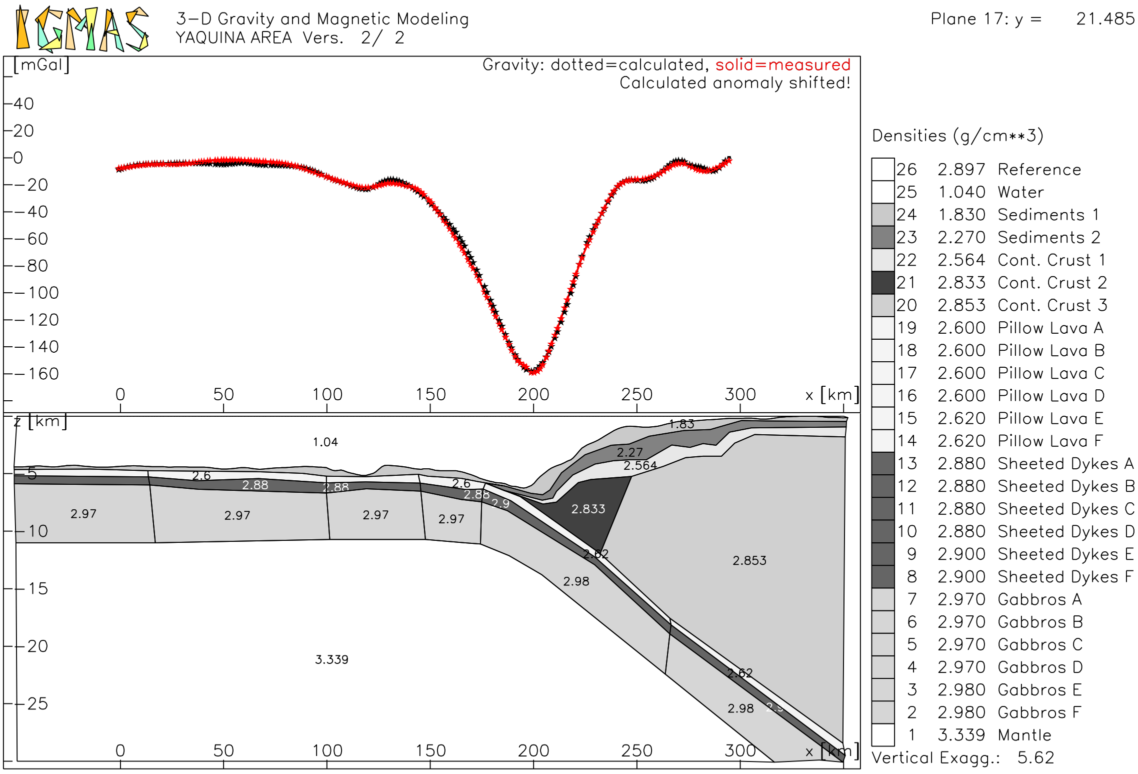

Figure 60: Yaquina Area - Gravity Modelling - Plane 17

Plane 17 shows a very smooth gravity curve. Seaward of the Peru Trench free-air values around 0 mGal are a sign of isostatic compensation. The bathymetric depression on the seaward side of the ridge causes a local minimum at kilometre 120. The large minimum connected with the Peru Trench shows an absolute minimum of -160 mGal. The gradients on the landward and on the seaward side of this minimum are approximately identical. Above the continental margin the gravity curve shows only small variations around 0 mGal. Accordingly the layers of the continental margin do not show any strong perturbations.

A step in the rising gravity values is seen above the continental margin on plane 18. The step is continued in the subsequent planes. Layer sediments 1 is rather thick in this area. Between kilometres 120 and 140 the Trujillo Trough is visible. This feature causes a minimum of -20 mGal.

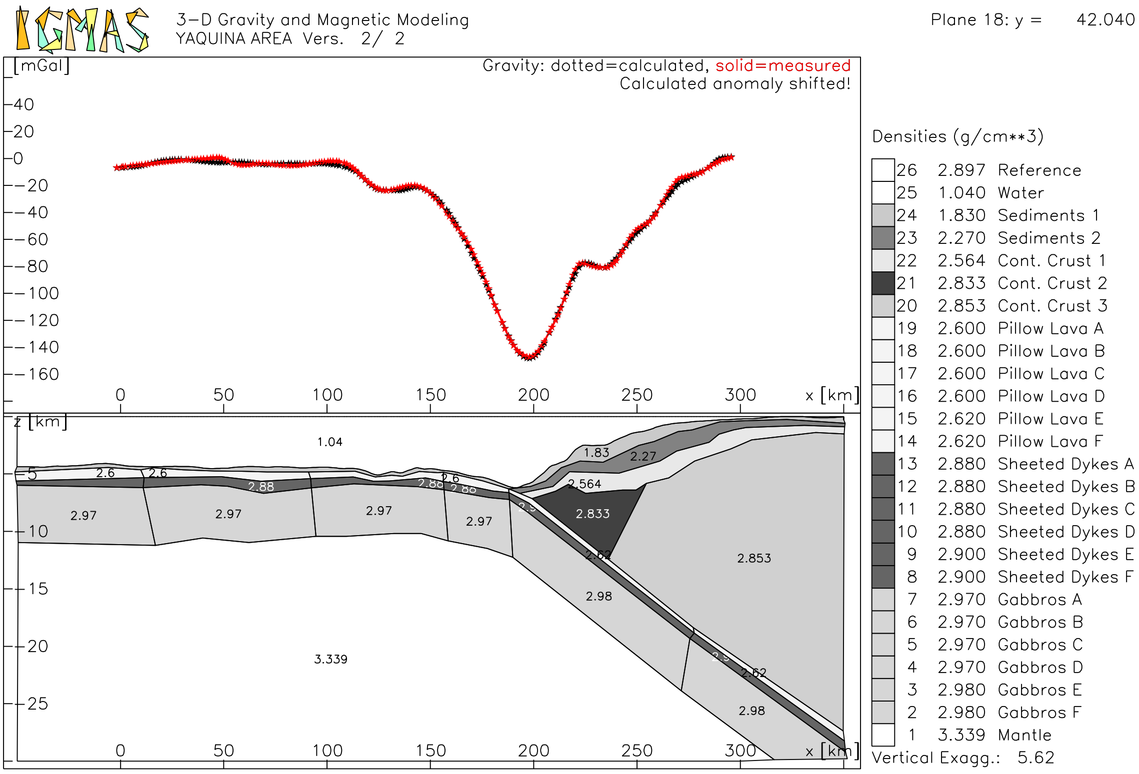

Figure 61: Yaquina Area - Gravity Modelling - Plane 18

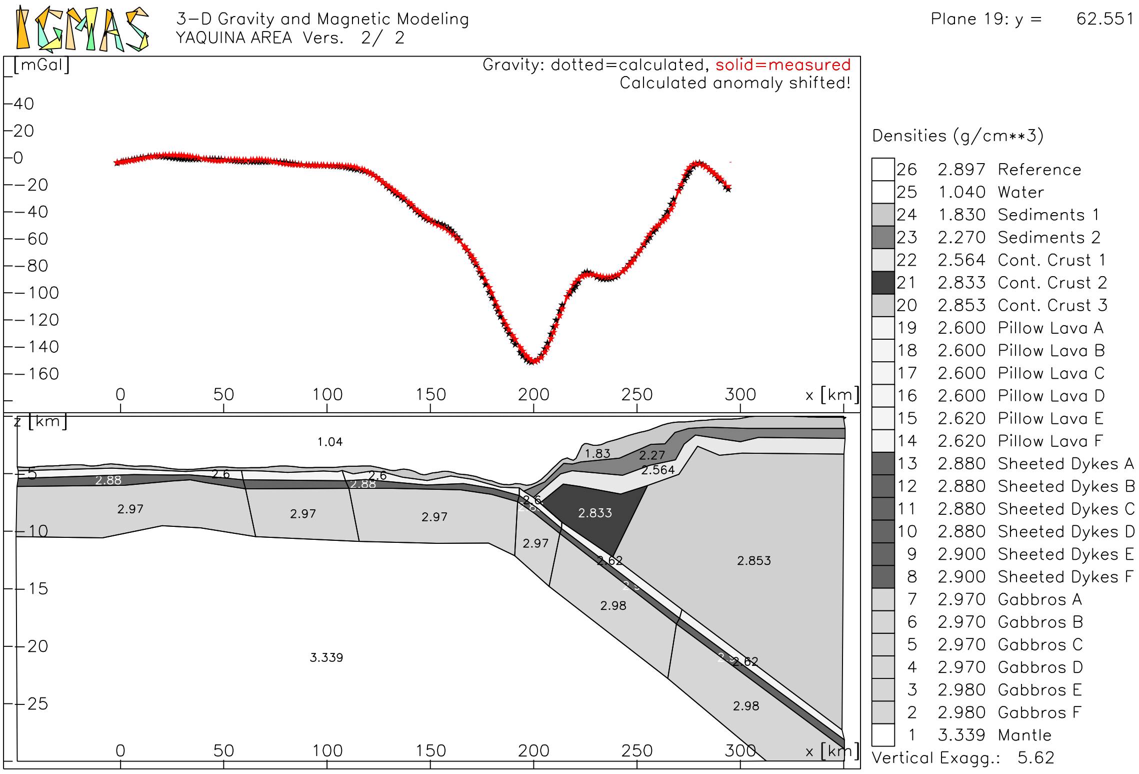

Figure 62: Yaquina Area - Gravity Modelling - Plane 19

Plane 19 shows the same plateau in the gravity curve as plane 18. The landwards succeeding increase in free-air gravity is rather sharper. Near kilometre 275 the layers of the continental crust well up and cause a local maximum.

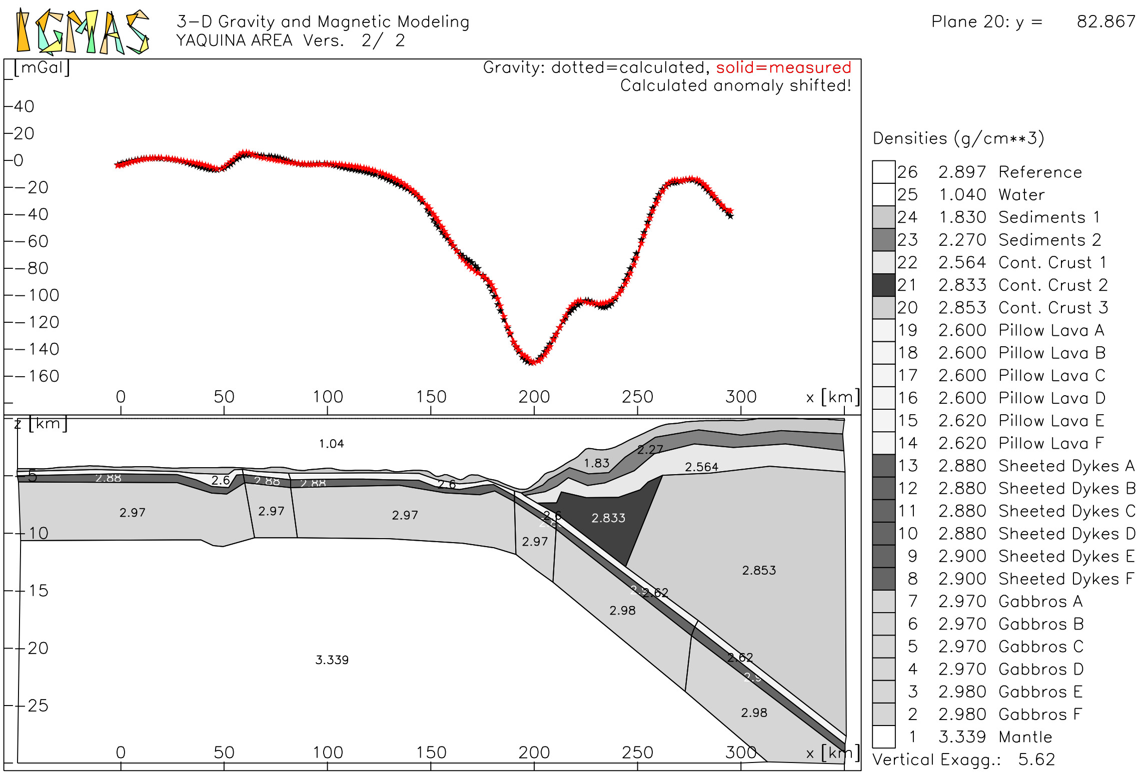

Figure 63: Yaquina Area - Gravity Modelling - Plane 20

Plane 20 shows that two about 1 km deep troughs are located between kilometres 150 and 170 on the Nazca Plate. The maximum connected with the continental shelf is broader than on plane 19. A prominent upwelling of the oceanic layers is occurring just before the Nazca Plate starts to subduct.

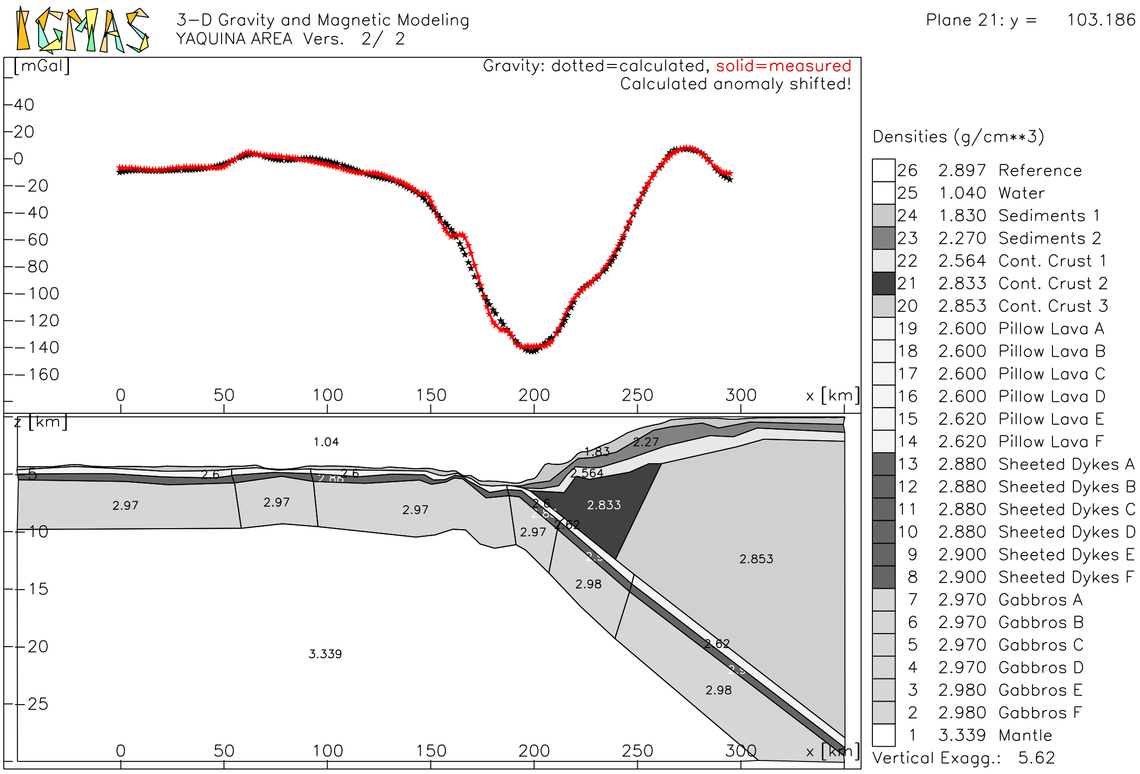

Figure 64: Yaquina Area - Gravity Modelling - Plane 21

On plane 21 two smaller upwellings of the mantle are located immediately seaward and directly beneath the Peru Trench.

7.5.2 Magnetic Modelling in the Yaquina Area

A different standard has to be accepted for magnetic modelling. The errors are by far greater than in gravity modelling. To approximate the magnetic stripe pattern, the oceanic crust consists of six different blocks, i.e. blocks A to F, with different magnetic properties. The magnetic north direction is determined as 67.130°. As a reference for the total magnetic field the value 27,637 nT is employed. The inclination angle is 6.367° and the declination angle is 2.900°. The magnetic model is characterized by polarity reversals. The remanent magnetisation values of the different blocks describe the magnetic lineations, i.e. the geomagnetic field reversals.

Magnetic anomalies of the subducting and of the overriding plate can be observed. The major subjective of magnetic modelling is the oceanic crust. Most of the main trends can be approximated with the three-dimensional model.

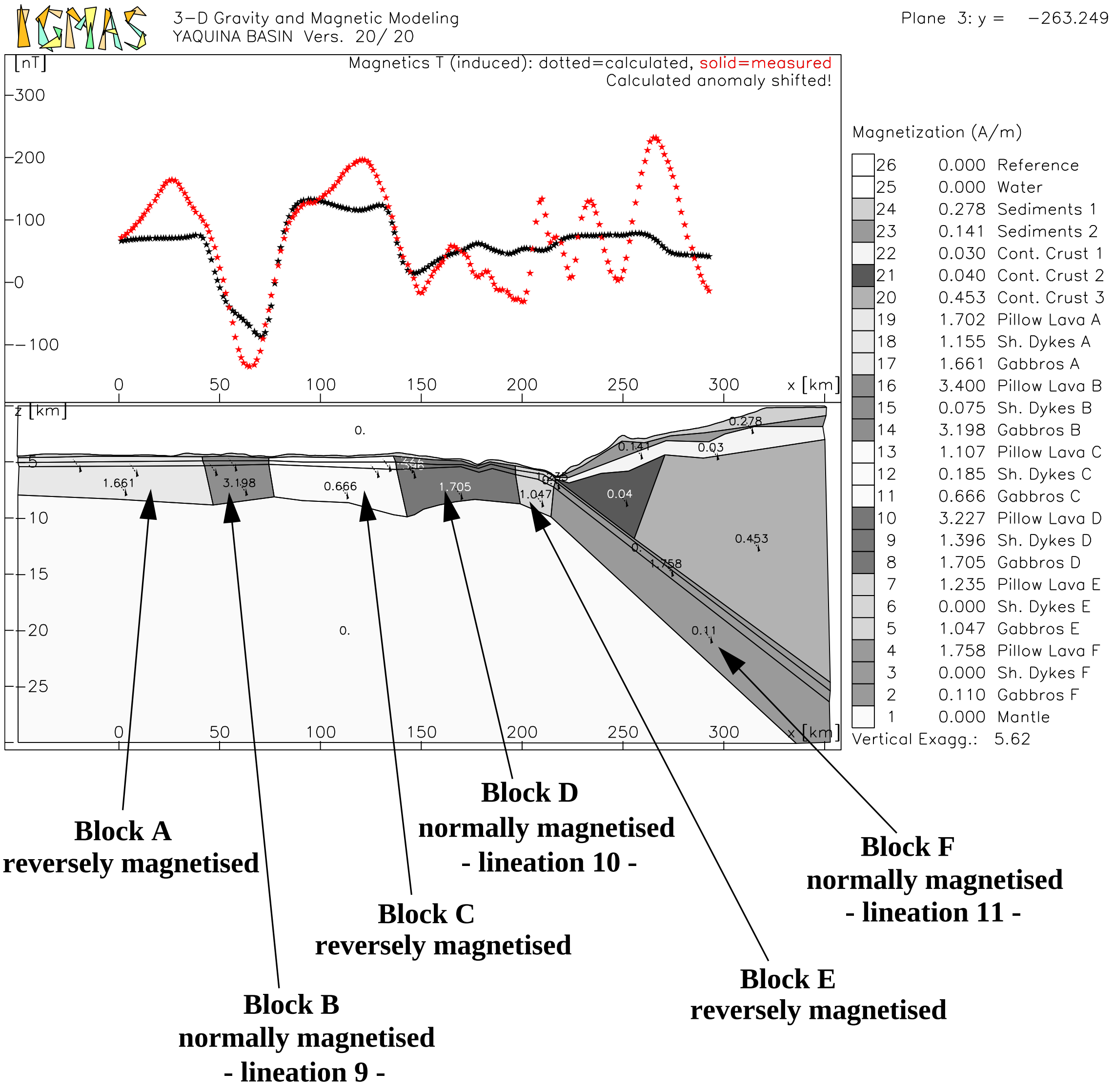

Figure 65: Yaquina Area - Magnetic Modelling - Plane 3

The magnetic model possesses the same geometry as the gravity model, just the colours are chosen differently to distinguish the differently magnetised blocks. The lineation pattern of the oceanic crust is integrated into the model. Blocks A, C and E are reversely magnetised, whereas blocks B, D and F are normally magnetised and represent the magnetic lineations 9, 10 and 11 respectively.

Block B is most strongly magnetised. Blocks C and F show an especially weak magnetisation. The mantle is treated as non-magnetic. The layers of the continental margin exhibit a weak magnetisation.

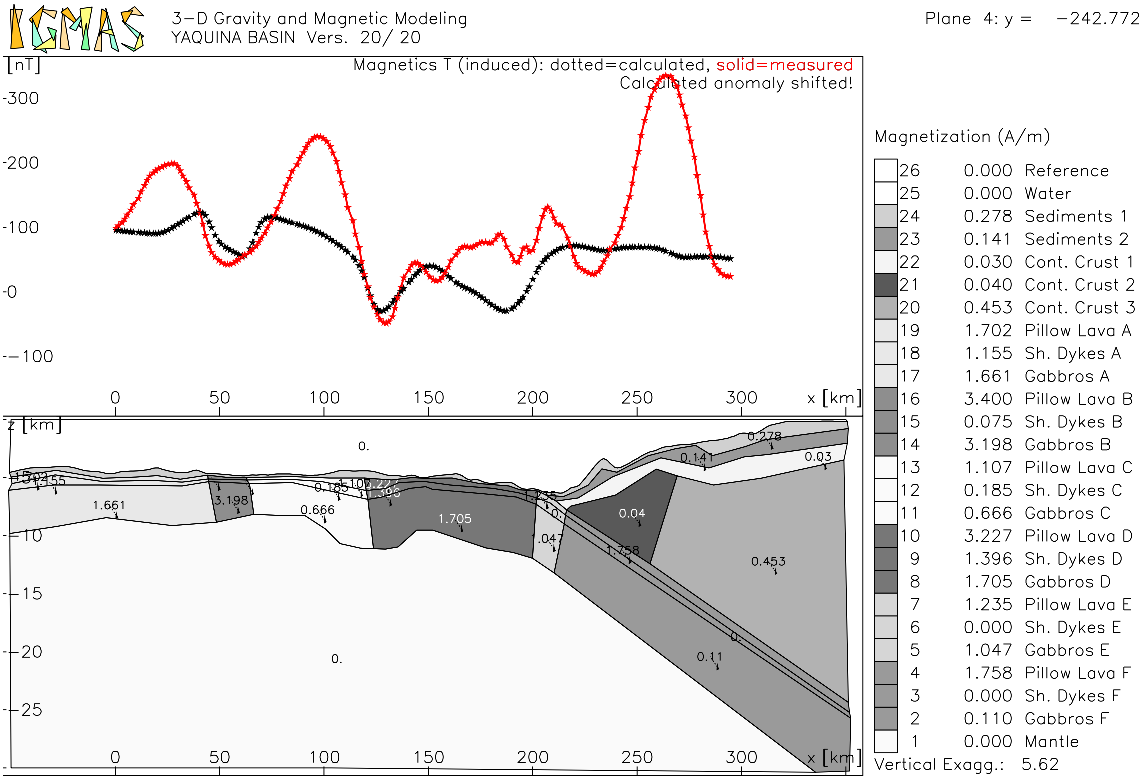

Figure 66: Yaquina Area - Magnetic Modelling - Plane 4

On the southern planes 3 and 4 (Figures 65 and 66) the main trends of the anomaly pattern over the oceanic crust are implied by the calculated magnetic values. The measured anomalies show a too high frequency to be reproduced by the block model. The high amplitudes of the observed data are difficult to reach either.

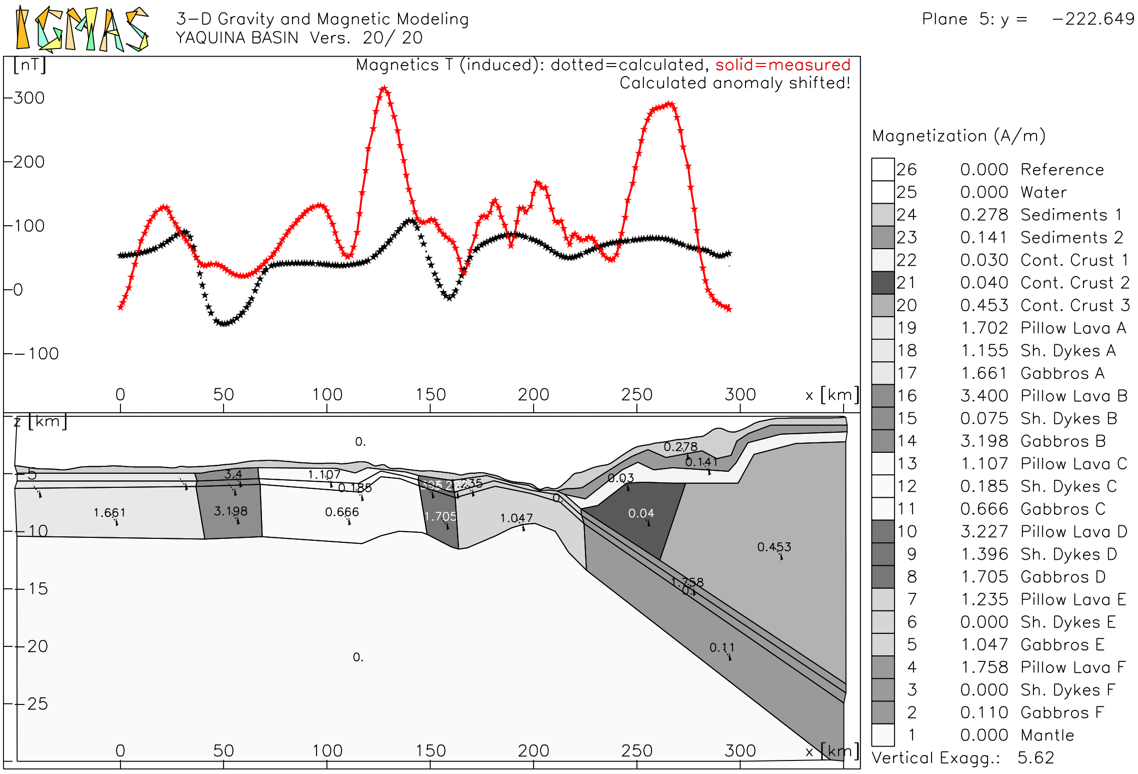

Figure 67: Yaquina Area - Magnetic Modelling - Plane 5

On plane 5 the modelled anomalies hint at the measured magnetic data.

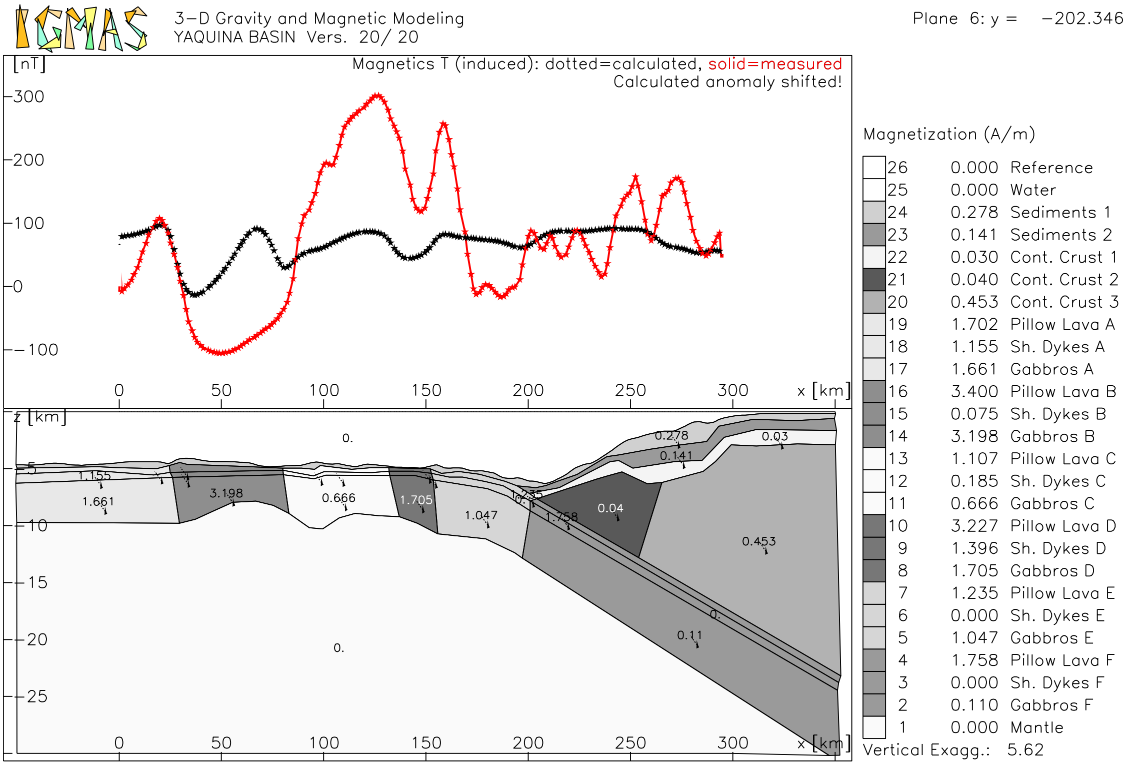

Figure 68: Yaquina Area - Magnetic Modelling - Plane 6

Plane 6 shows the worst relation between observed and calculated magnetic anomalies. This plane lies in the region of the Mendaña Fracture Zone. The positive anomaly centred at kilometre 50 is caused the thinning of the oceanic crust.

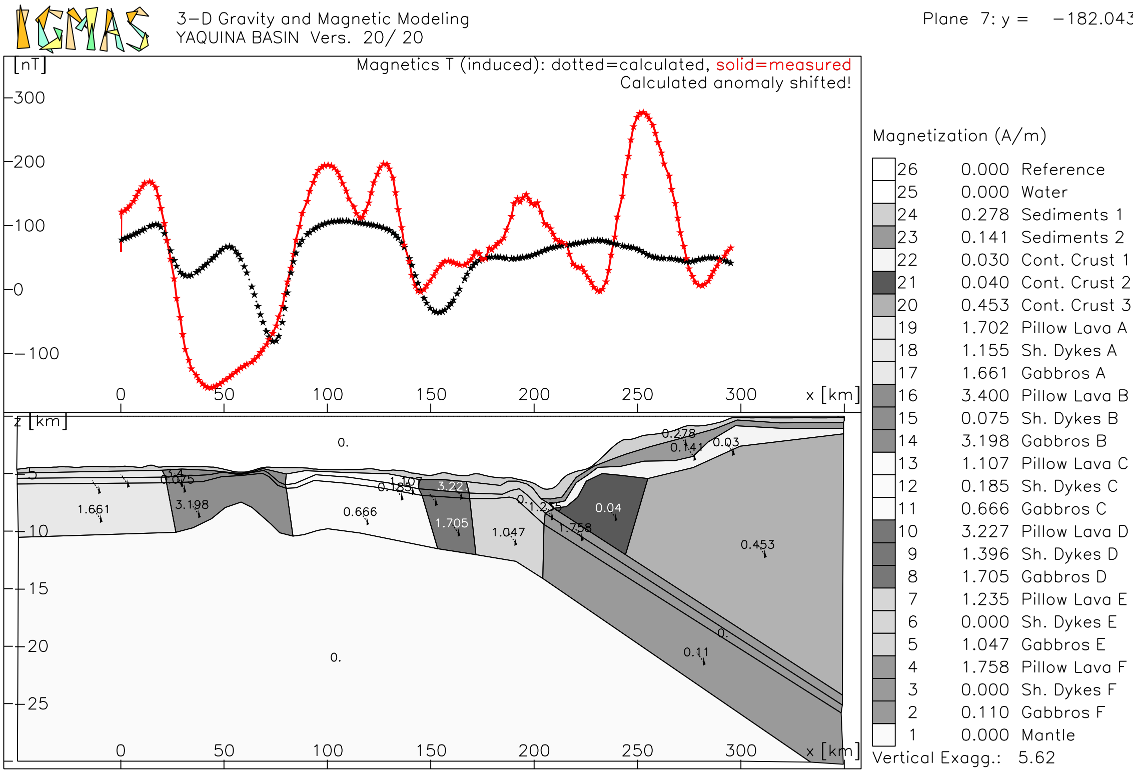

Figure 69: Yaquina Area - Magnetic Modelling - Plane 7

The maximum between kilometres 75 and 150 can be modelled but the appearing maximum at kilometre 50 is by far too high. A very small local maximum can be seen in the observed data but it really is negligible.

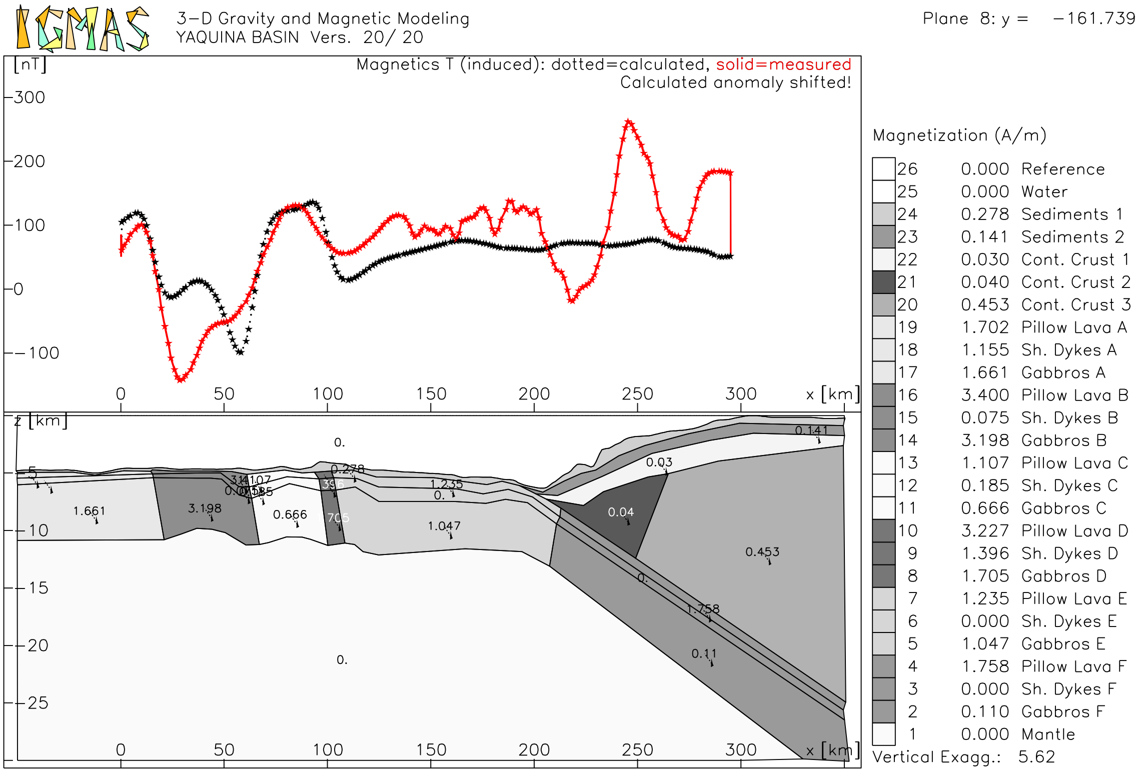

Figure 70: Yaquina Area - Magnetic Modelling - Plane 8

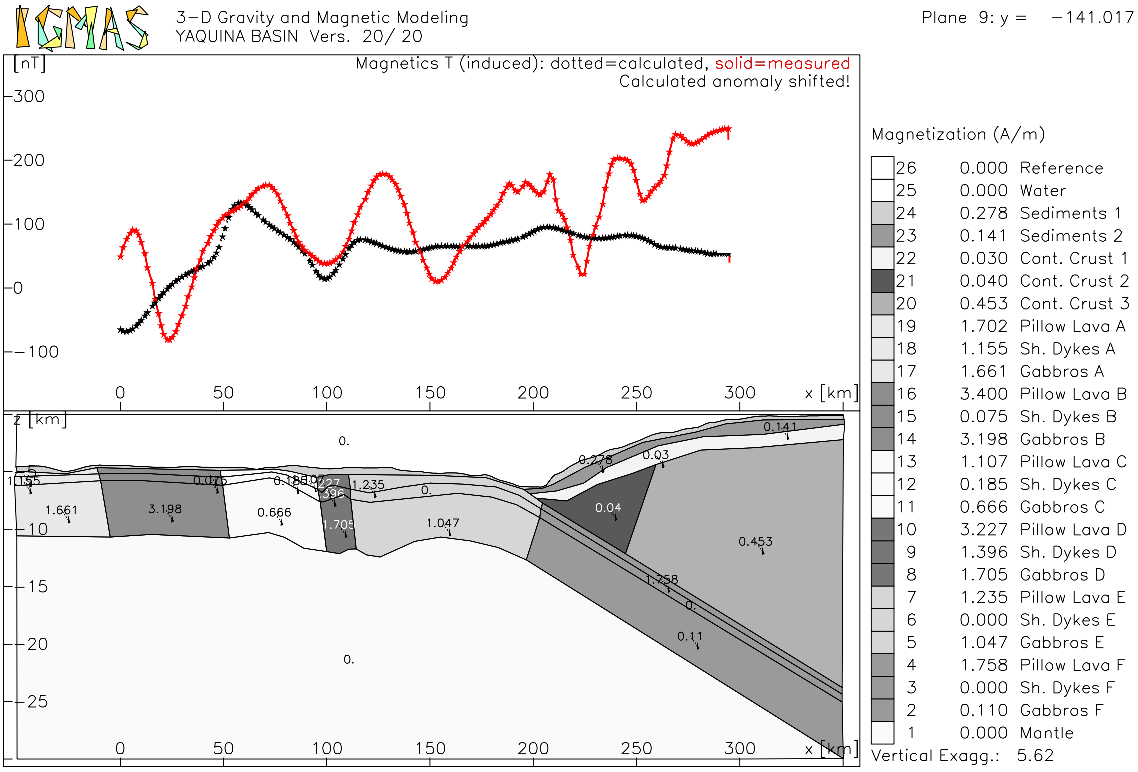

Figure 71: Yaquina Area - Magnetic Modelling - Plane 9

All trials to reach a maximum as high as the measured anomaly on plane 10 (Figure 72) are futile, however the positive trend can be imitated.

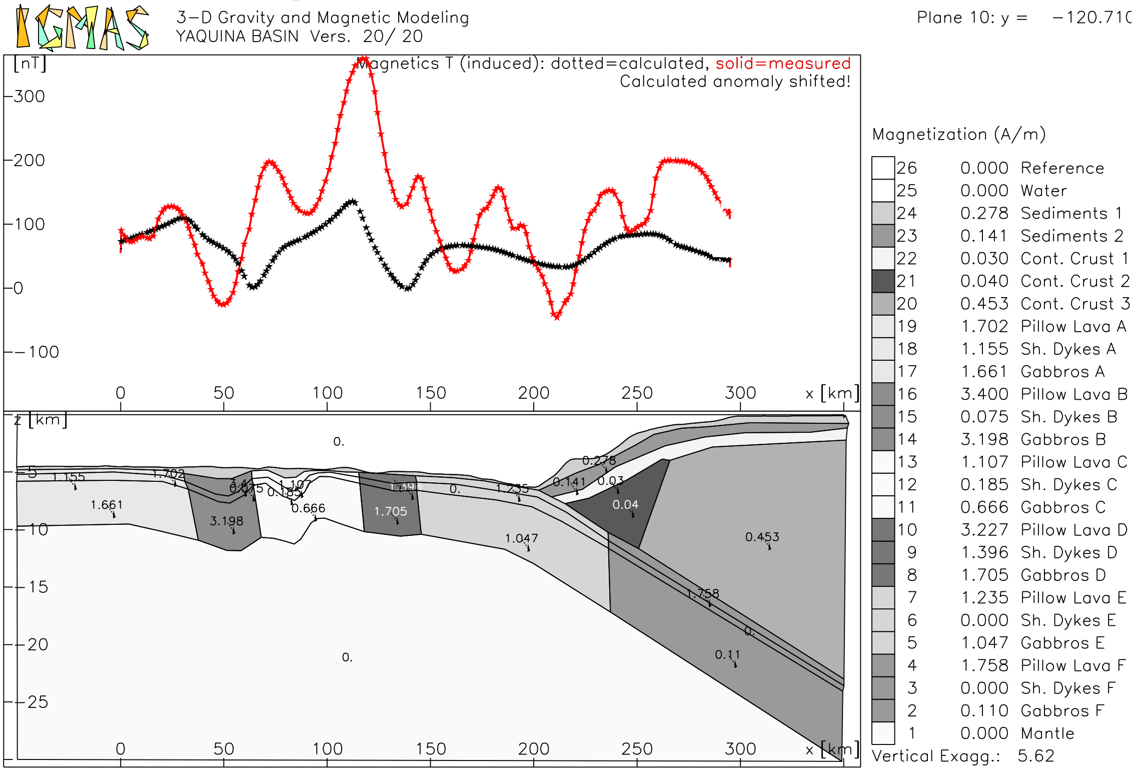

Figure 72: Yaquina Area - Magnetic Modelling - Plane 10

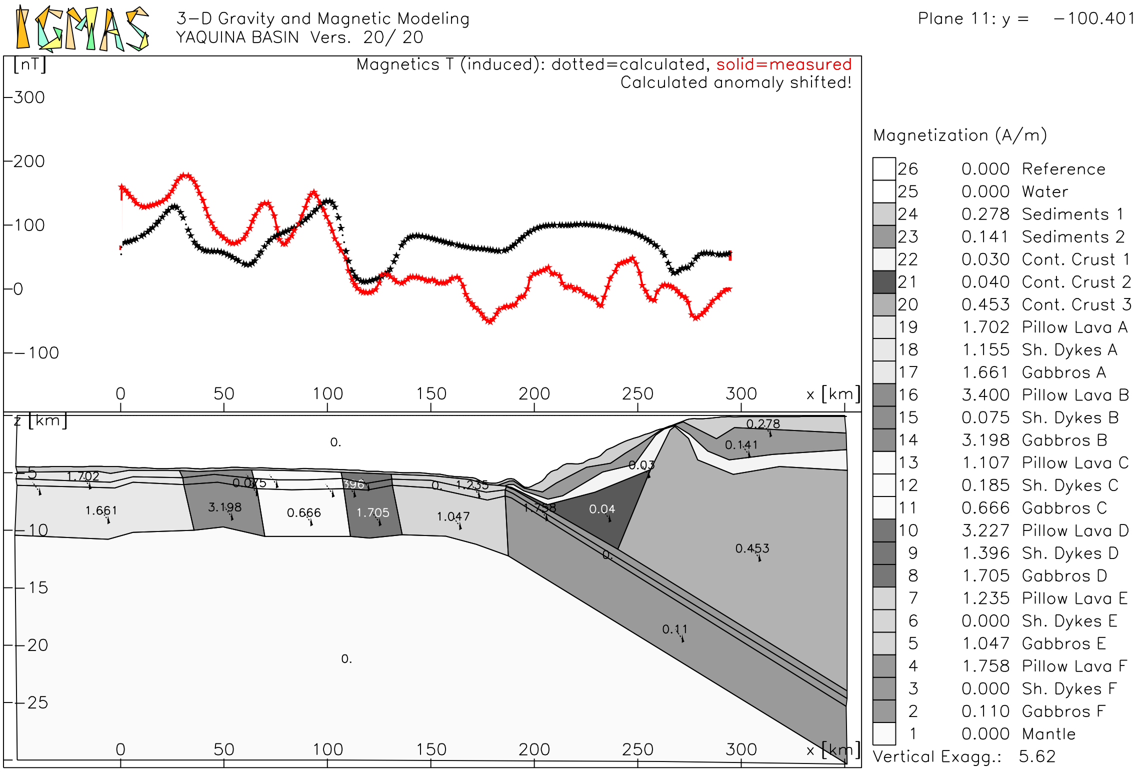

Figure 73: Yaquina Area - Magnetic Modelling - Plane 11

The high-frequency variation cannot be modelled. The short-wavelength anomalies along the continental margin are indicative of a series of small magnetic bodies close to the sea floor.

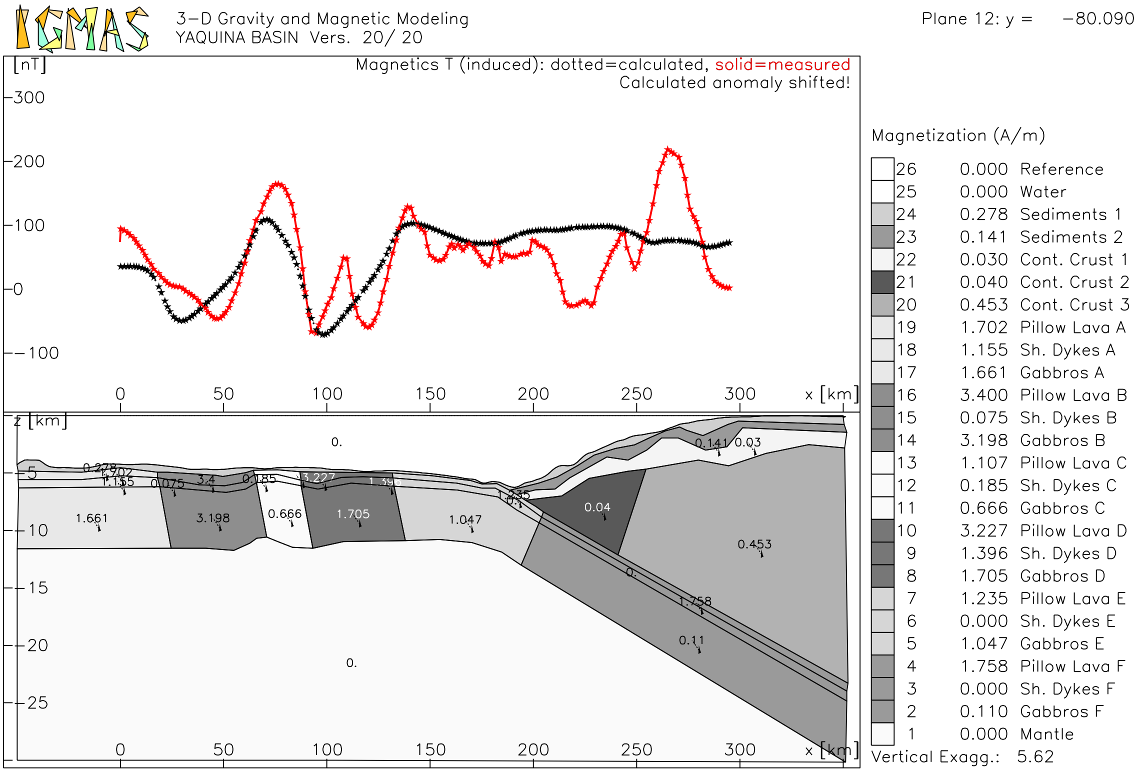

Figure 74: Yaquina Area - Magnetic Modelling - Plane 12

On plane 12 (Figure 74) the larger-wavelength observed anomalies are matched quite well.

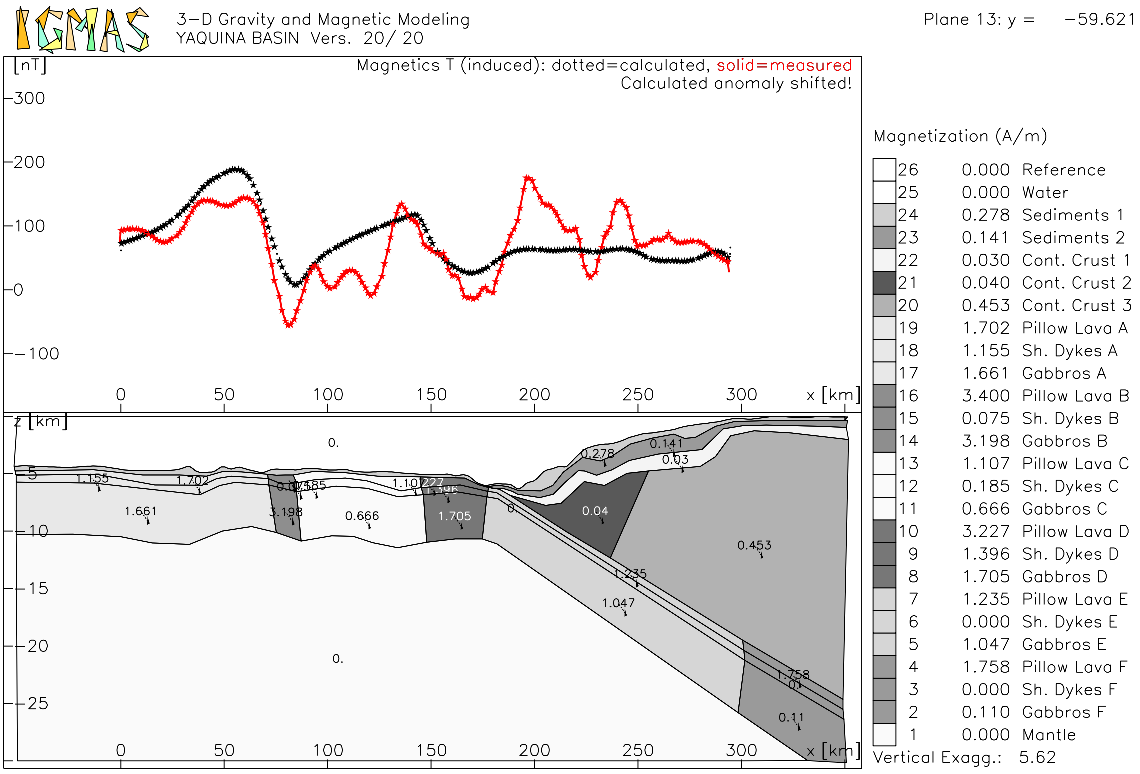

Figure 75: Yaquina Area - Magnetic Modelling - Plane 13

The measured anomalies possess too short wavelengths to be reproduced by the block model. They form an envelope over the high-frequency anomalies of the oceanic crust.

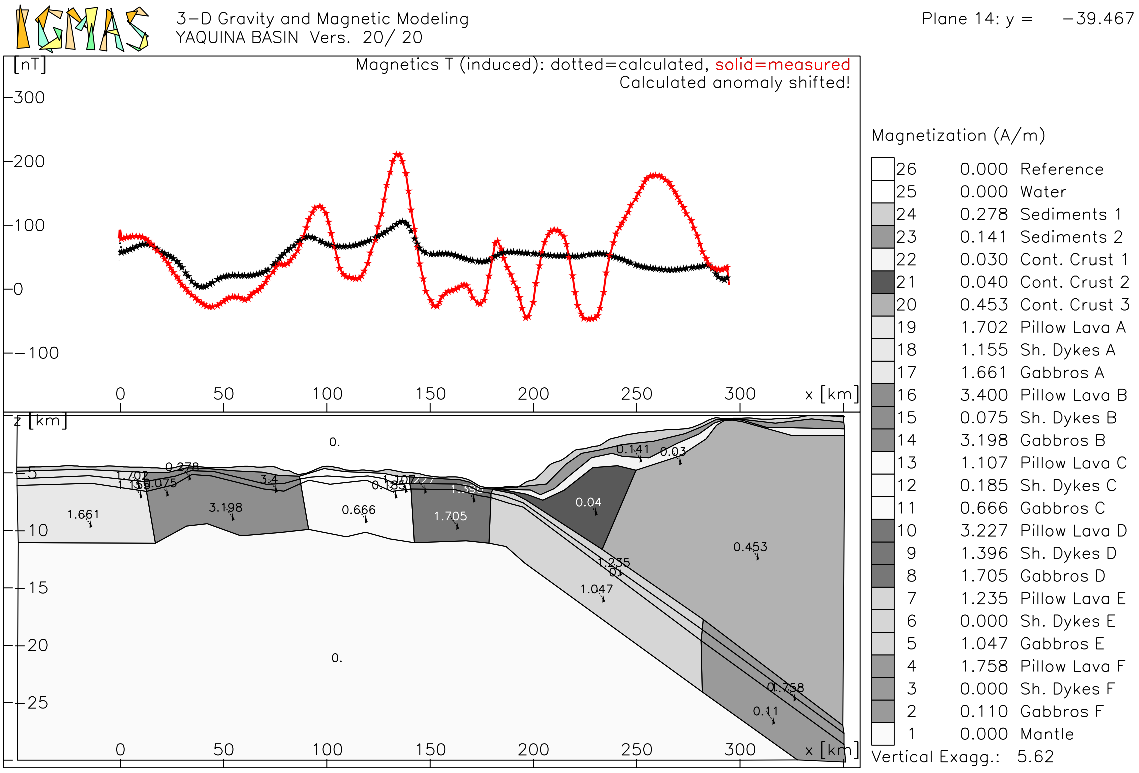

Figure 76: Yaquina Area - Magnetic Modelling - Plane 14

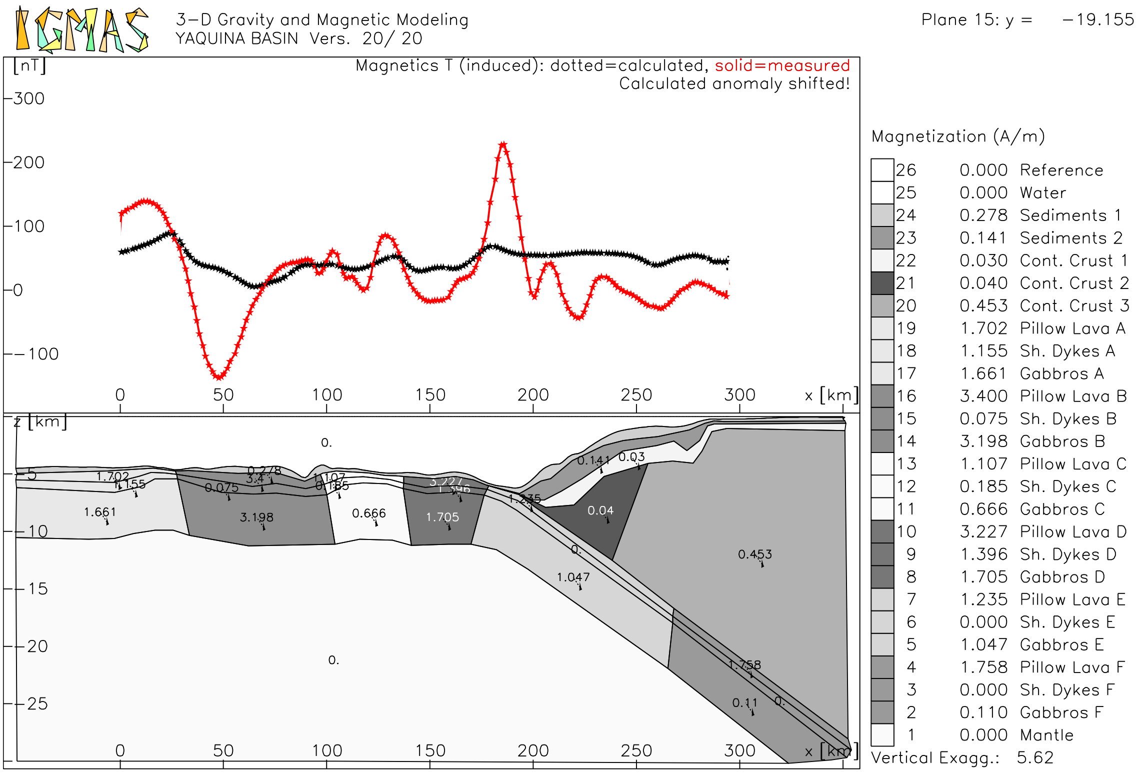

Figure 77: Yaquina Area - Magnetic Modelling - Plane 15

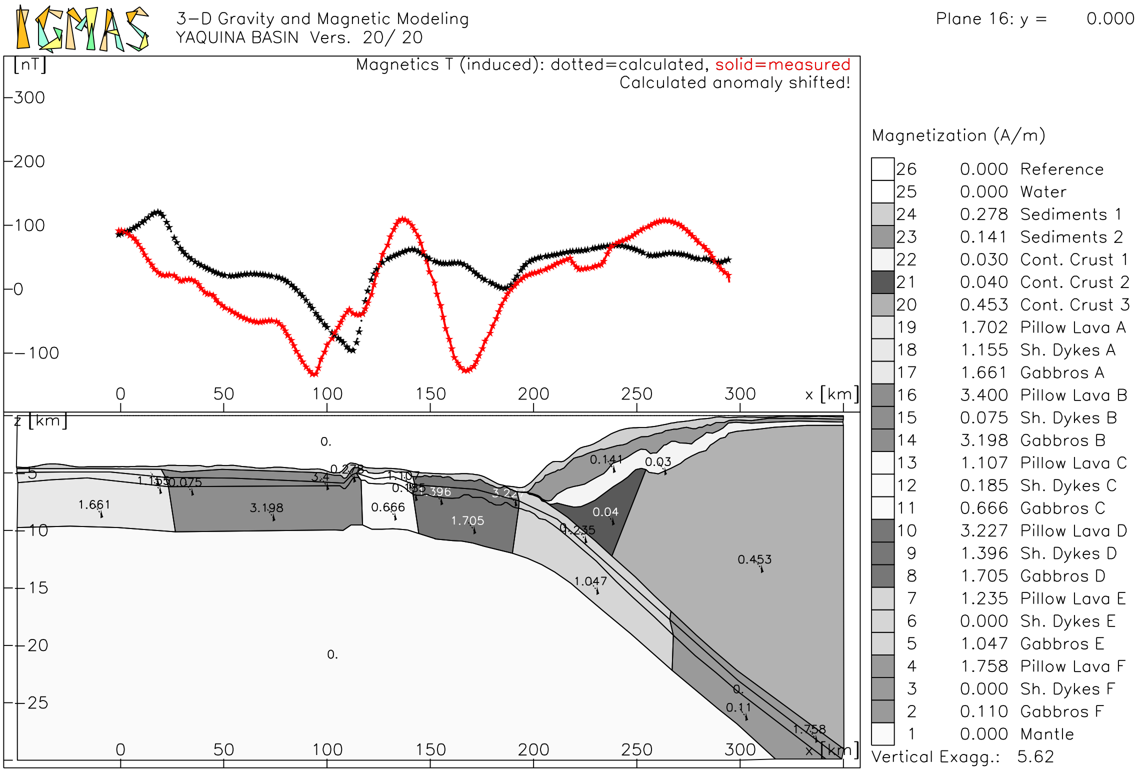

Figure 78: Yaquina Area - Magnetic Modelling - Plane 16

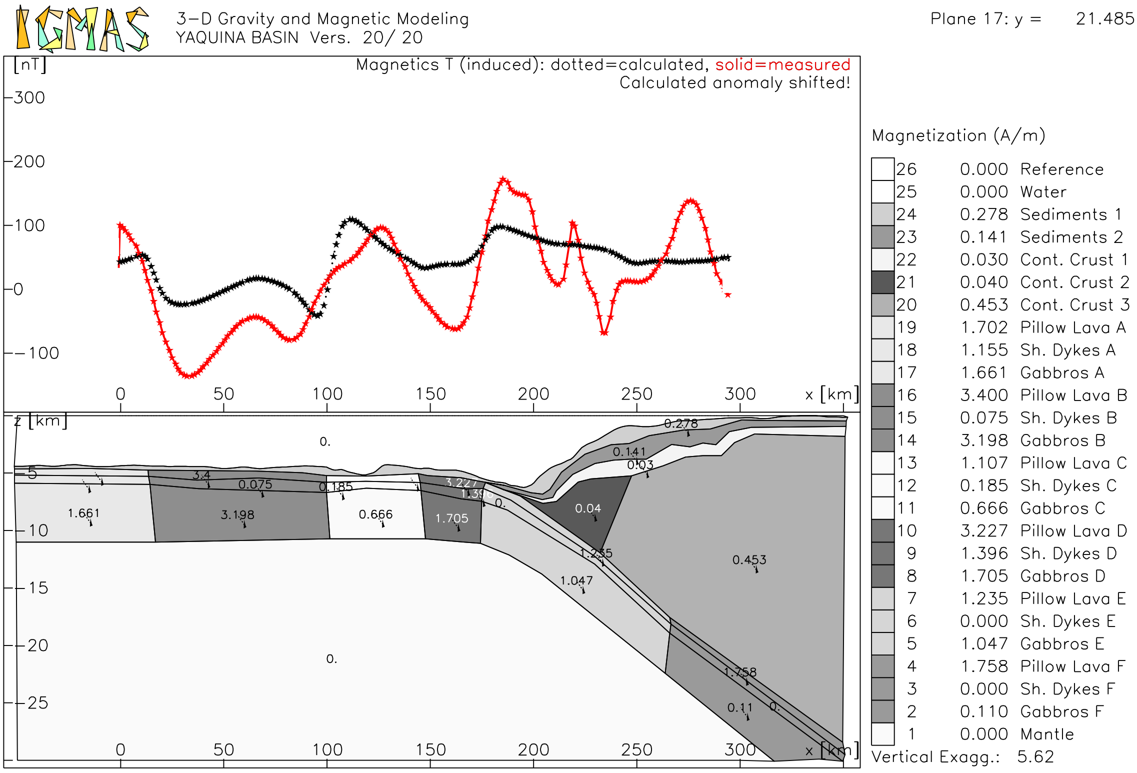

Figure 79: Yaquina Area - Magnetic Modelling - Plane 17

On plane 17 the positive gradient towards the south American continent can be modelled. This gradient is even more apparent on plane 18.

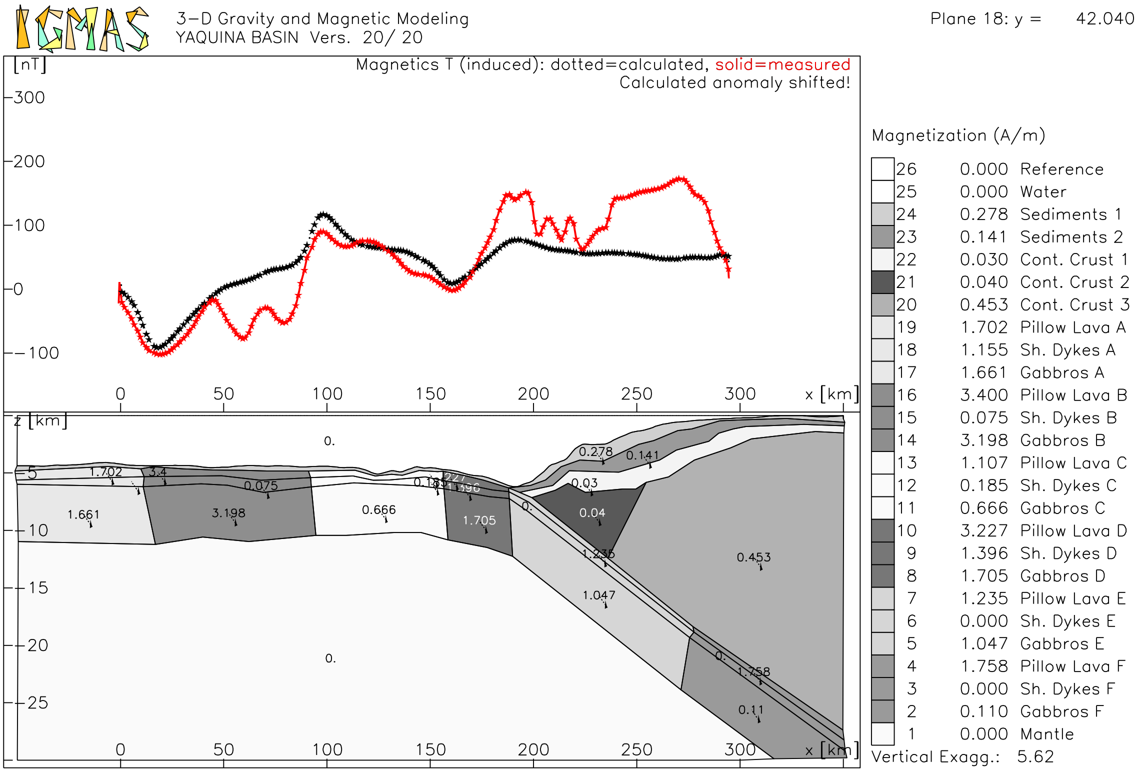

Figure 80: Yaquina Area - Magnetic Modelling - Plane 18

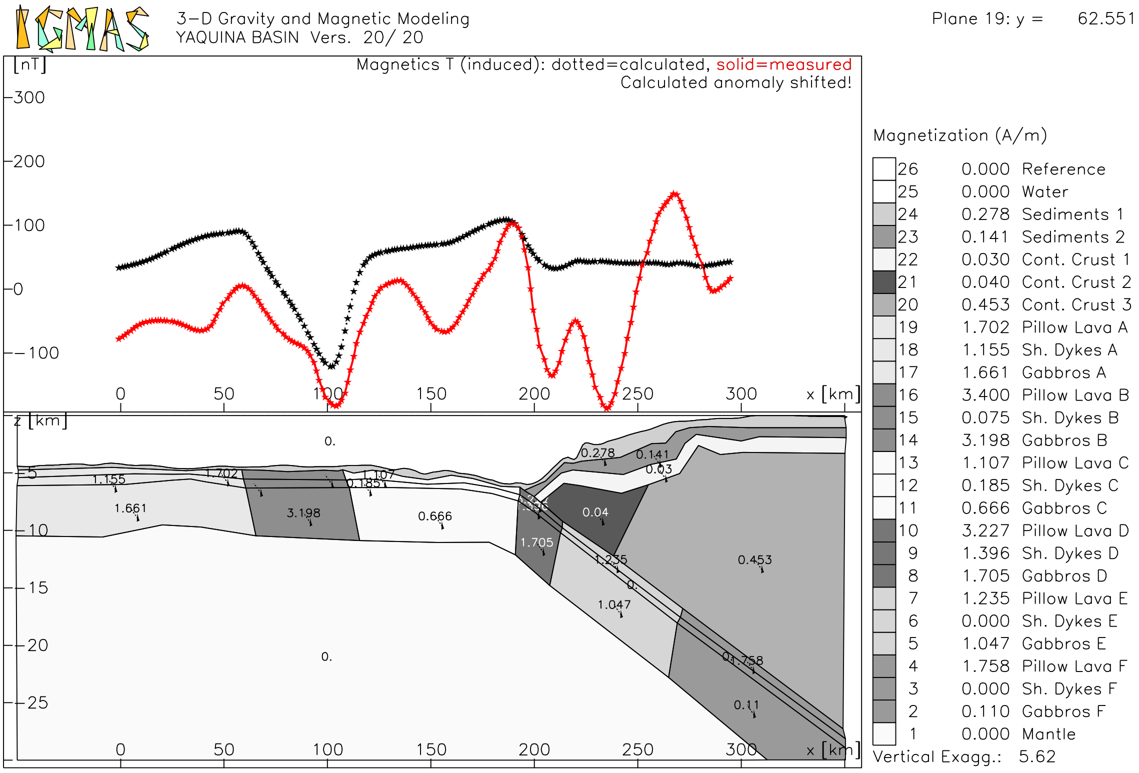

Figure 81: Yaquina Area - Magnetic Modelling - Plane 19

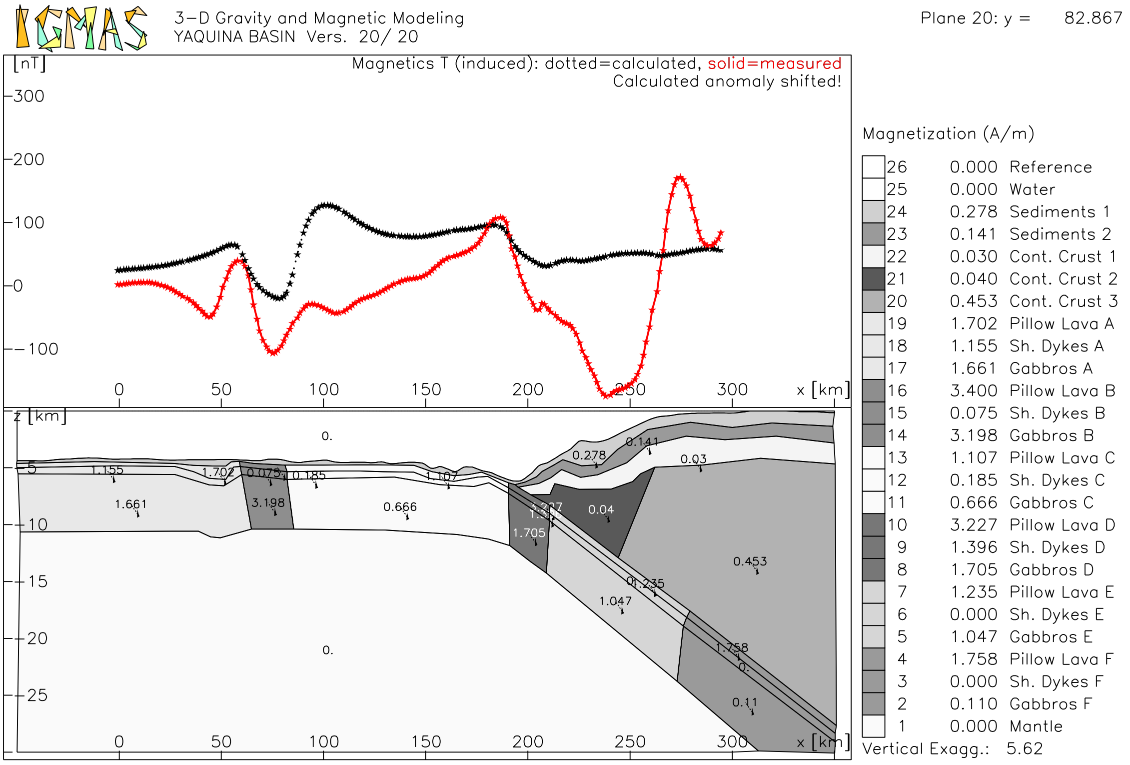

Figure 82: Yaquina Area - Magnetic Modelling - Plane 20

On plane 20 the observed maxima are, if not reached, suggested in the modelled anomalies. Although the absolute magnetic anomalies are quite different the critical points are approximated by the model.

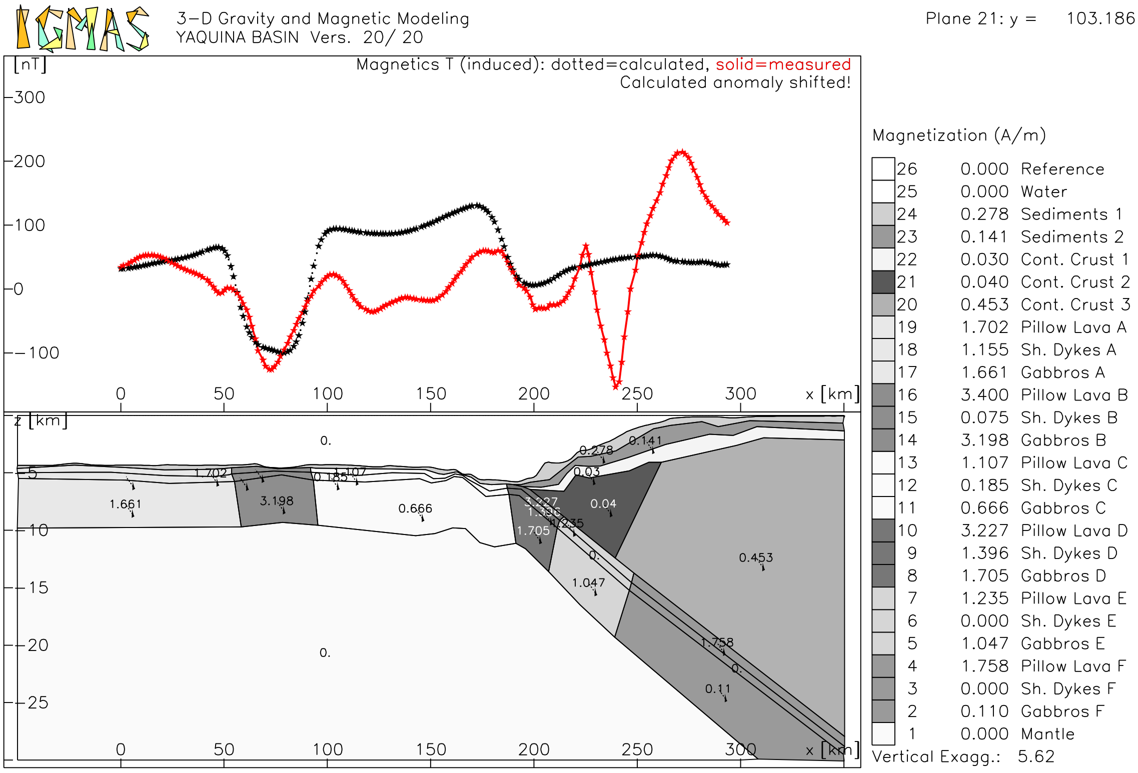

Figure 83: Yaquina Area - Magnetic Modelling - Plane 21

On plane 21 the prominent minimum on the oceanic crust is located above block B, possessing a higher magnetisation than the surrounding blocks.

Figure 84 shows the relation of remanent to induced magnetisation of the oceanic layers.

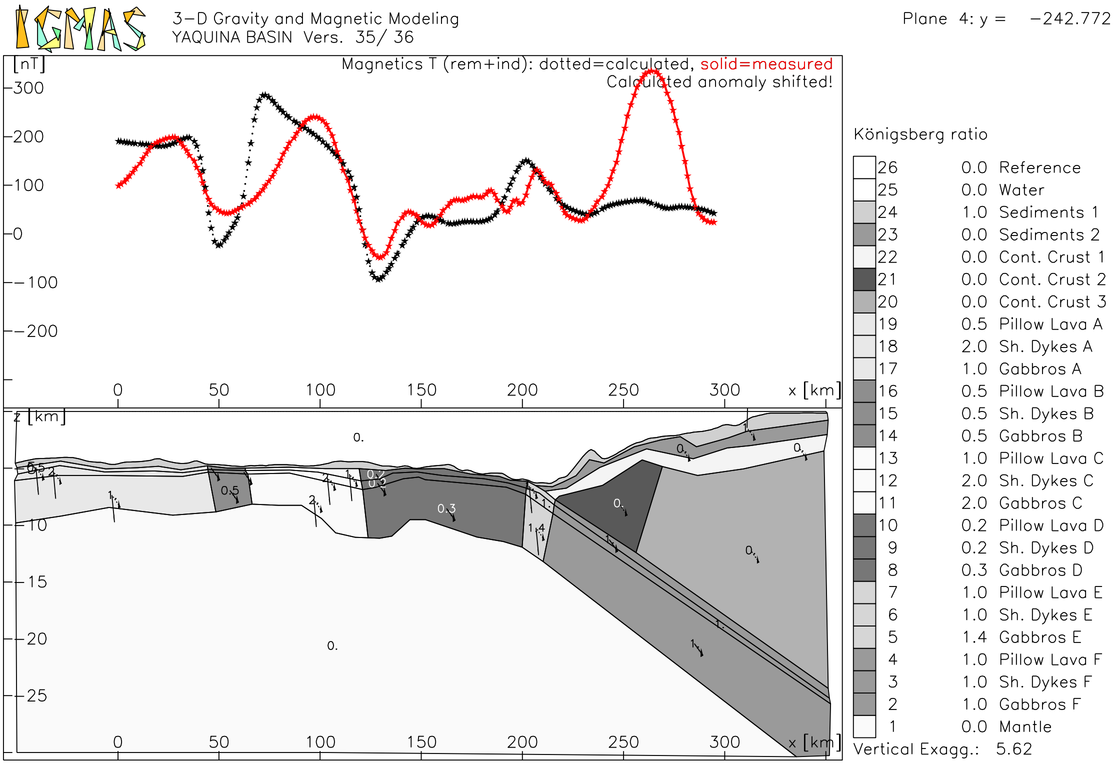

Figure 84: The modelled Königsberg ratios in the Yaquina Area

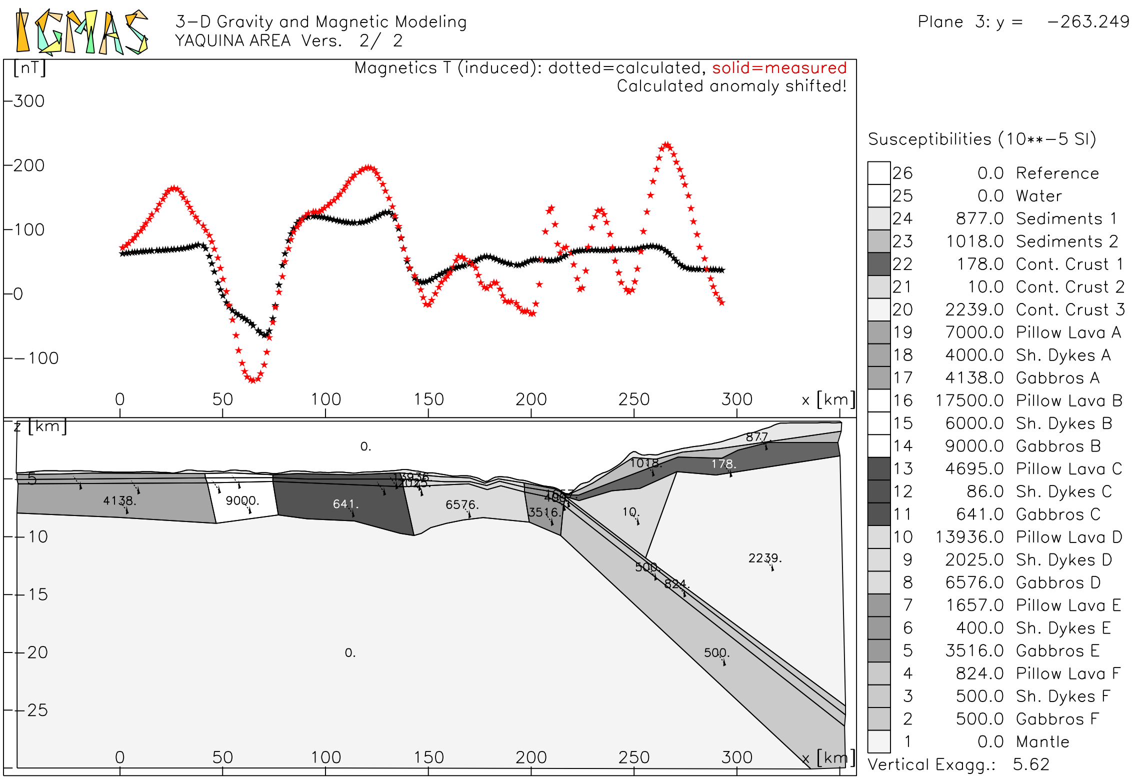

Figure 85: The modelled susceptibilities in the Yaquina Area

In Figure 85 the different bodies of the Yaquina Area model are displayed with respect to their susceptibilities.

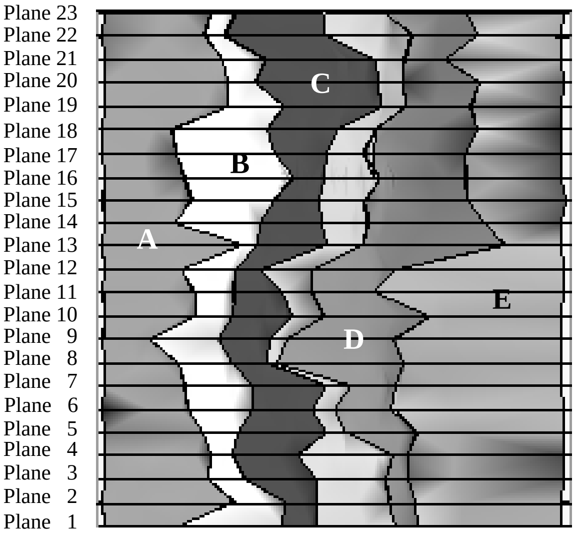

Figure 86: The differently magnetised blocks of the Yaquina Area model

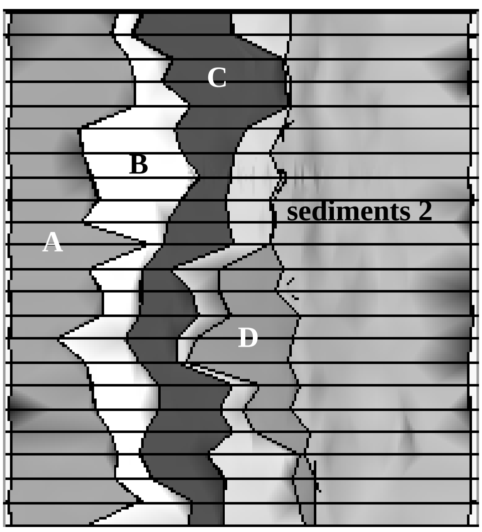

Figure 87: The differently magnetised blocks of the Yaquina Area model, partly covered by sediments 2

Figures 86 and 87 are top views of the three-dimensional Yaquina Area model. The oceanic crust and, in Figure 87, the layer sediments 2 are displayed. These illustrations demonstrate location and propagation of the blocks with different magnetisations.

7.6 The Lima Area Model

The Lima Area is located between 10.50°S and 14.40°S and is 370.7 km by 315.6 km in size. The three-dimensional model consists of 20 parallel vertical planes. These planes are located at a distance of 19.5 km from each other. This distance between the different plane, which is smaller than that of the Yaquina Area model and larger than that of the Nazca Ridge Area, is resolves the structures of the covered area satisfactorily. As in the other three-dimensional models each of the vertical planes comprises part of the oceanic plate, the Peru trench and the continental shelf. The three-dimensional model of the Lima Area is based on the seismic velocity models of profiles P3, P5 and P6. The location of all the planes of the Lima Area model and of the seismic profiles is displayed in Figure 41. Planes 1, 2 and 3 form the southward extension of the model to avoid edge-effects. Planes 18, 19 and 20 are the northward extension of the model. Accordingly the description of the gravity and magnetic model starts with plane 4.

As in the Yaquina Area model the oceanic crust of the Lima Area model consists of the layers sediments 1, pillow lava, sheeted dykes and gabbros. The continental margin is modelled with the layers sediments 1, sediments 2, sediments 3 and continental crust 1, continental crust 2, continental crust 3. Layer continental crust 2 again forms the seaward tip of continental crust 3. In this region the oceanic crust is about 8 km thick. The Lima Area model extends to a depth of 40 km.

7.6.1 Gravity Modelling in the Lima Area

In Figure 88 a comparison of the observed and the modelled free-air anomalies is plotted. Figure 89 images the errors between these gravity fields. A standard deviation of 2.22 and a correlation coefficient of 1.00 were achieved. The errors nearly form a Gaussian distribution.

The free-air gravity field shows a very distinct pattern. The negative anomalies connected with the Peru Trench are flanked by a well-defined gravity high on the landward side and a region with gravity values around 0 mGal on the seaward side. The positive anomalies over the continental margin reach as high as 20 to 25 mGal between the planes 10 and 14. The highest free-air gravity maximum is located on plane13. Here, maximal values of 30 mGal are observed.

The intensity of the negative anomalies over the trench is varying from north to south. The strongest negative anomaly of -150 mGal is located in the north between planes 10 and 11. Another strong minimum, possessing an amplitude as negative as -130 mGal, follows to the south. In the southernmost part of the Lima Area the Peru Trench features the highest gravity values of -110 mGal.

The errors between the observed and the calculated anomalies are more or less distributed arbitrarily over the three-dimensional model (see Figure 89). In summary the Lima Area model reproduces the observed gravity anomalies successfully. Plane 16, located at y=0, shows exceptionally strong deviations. This plane coincides with the wide-angle seismic profile P5 and the layer geometries of the seismic velocity model are directly integrated in the potential field model. The layer densities are adjusted within the bounds of the velocity-density relations. The rigid adoption of layer boundaries and the fact that the velocity model includes velocity gradients may explain the discrepancies between the observed and the modelled gravity field.

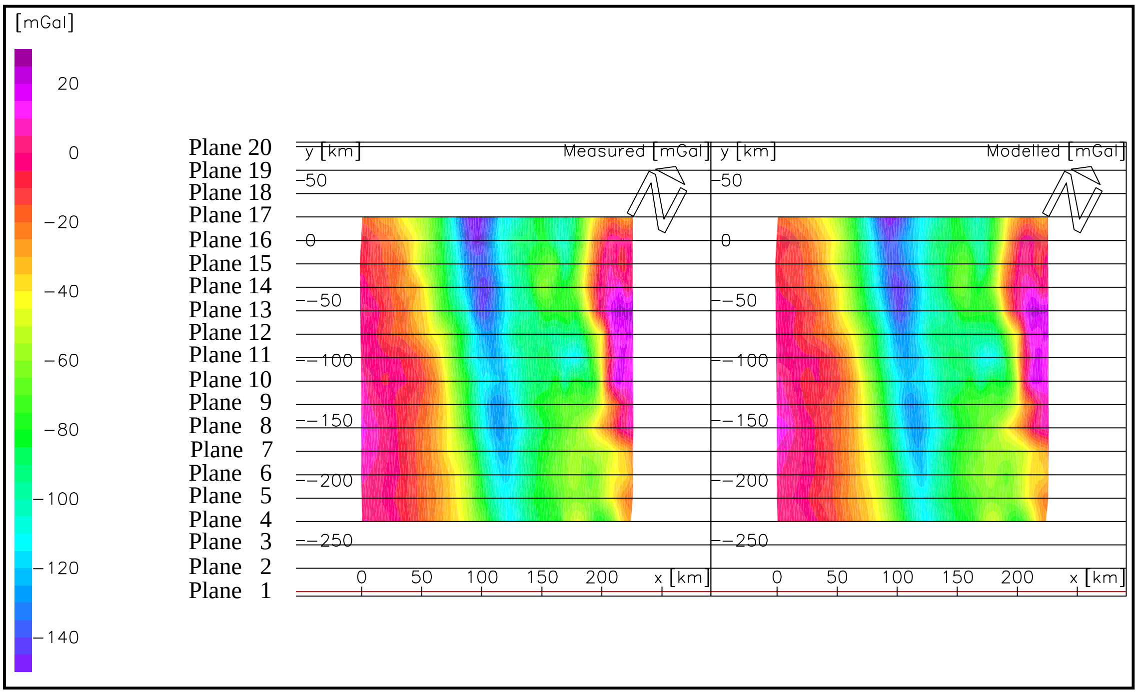

Figure 88: The Observed and the Modelled Free-Air Anomalies of the Lima Area Model

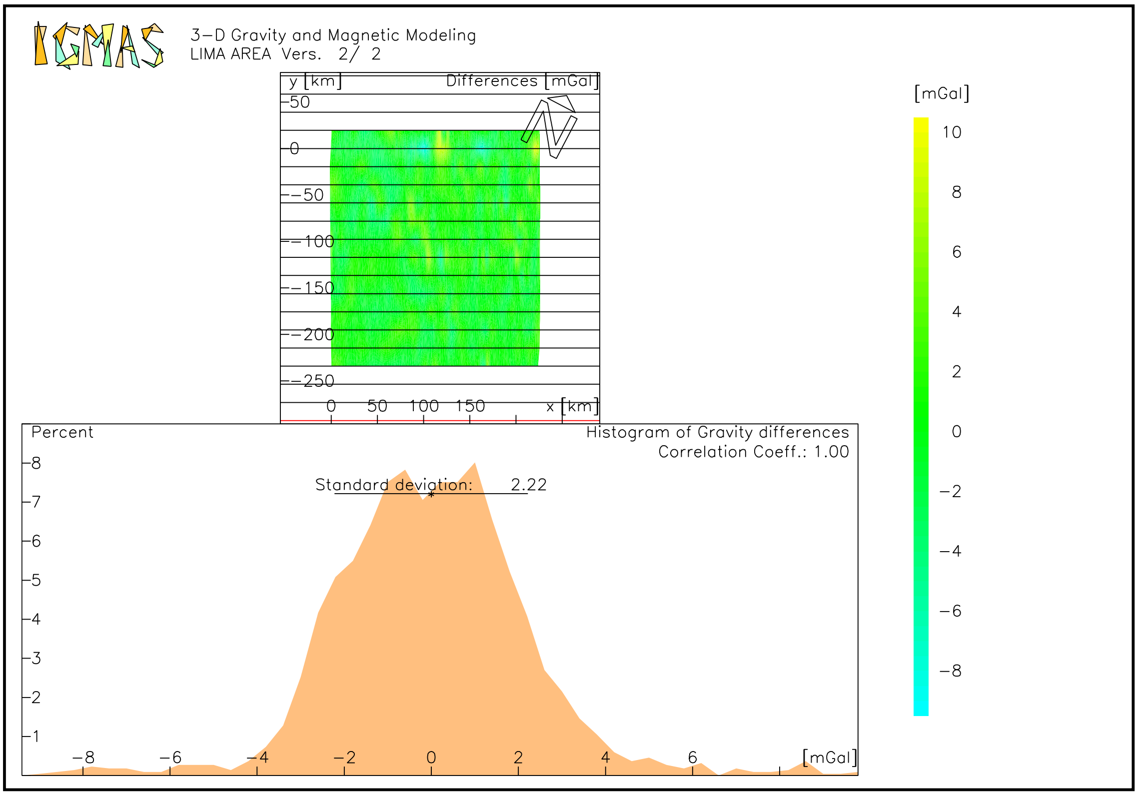

Figure 89: The Differences Between the Observed and the Modelled Gravity Anomalies in the Lima Area Model

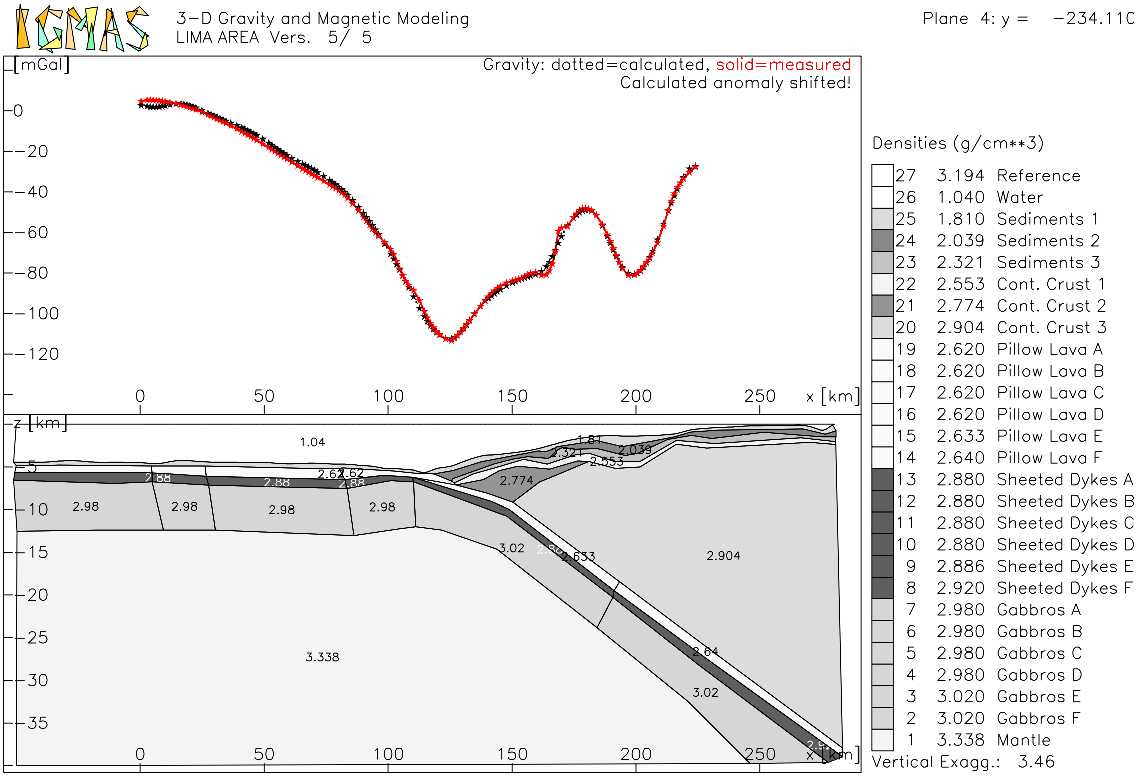

Figure 90: Lima Area - Gravity Modelling - Plane 4

In Figure 90 the southernmost plane of the gravity model is displayed. The gravity model shows a lateral density gradient in the layers of the oceanic crust. The densities increase remarkably when the lithospheric slab starts subducting beneath the South American Plate.

Above the relatively undisturbed oceanic crust at kilometre 0 the free-air gravity shows values of 0 mGal. A remarkable local maximum is located along the continental margin centred at kilometre 180. The immediately succeeding minimum landwards of the maximum is also an extraordinary feature.

On plane 5, in comparison, the local maximum and minimum along the continental crust are considerably reduced. Landward of the trench the layer sediments 1 is thickened (see Figure 91).

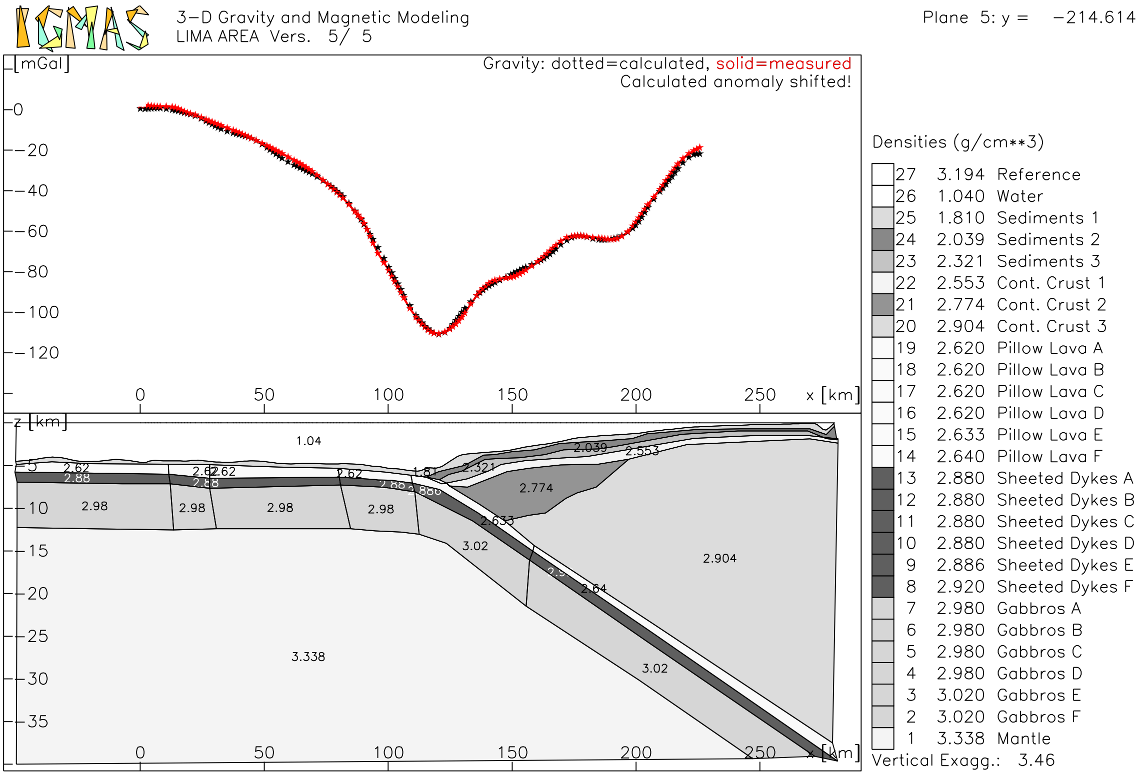

Figure 91: Lima Area - Gravity Modelling - Plane 5

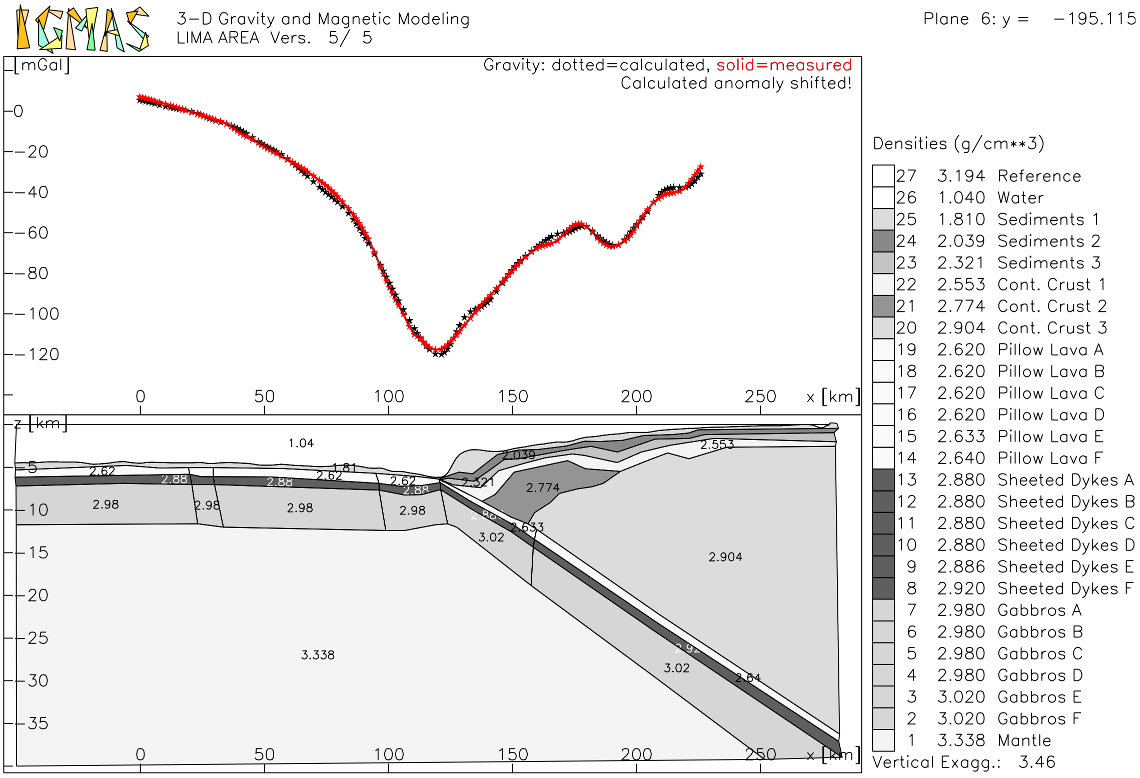

Figure 92: Lima Area - Gravity Modelling - Plane 6

On plane 6 the minimum has appeared again and is centred at kilometre 190. A prominent bulge of the upper sediments is observed at the front of the continental margin. This feature can be considered as an accretionary prism. Gravity modelling shows that the prominent elevation at the deformation front has to consist of low-density sediments.

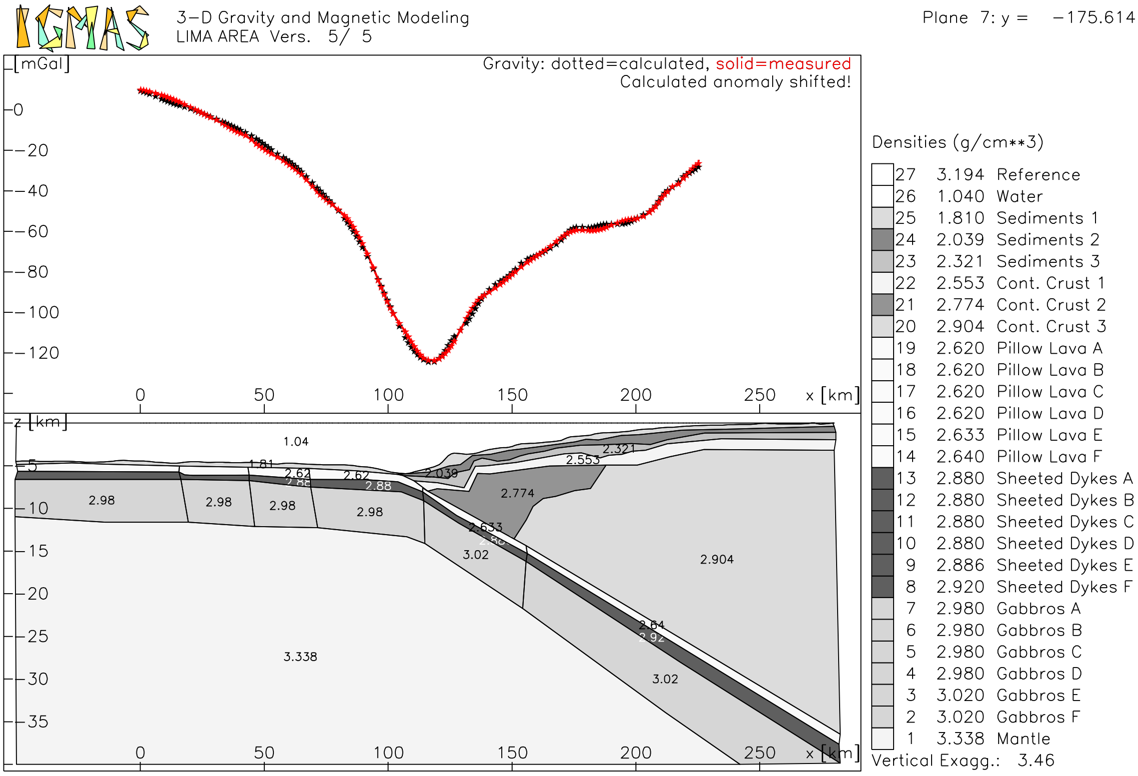

Figure 93: Lima Area - Gravity Modelling - Plane 7

Plane 7 features undulations along the lower continental slope. The landward rise in gravity values is very slow above the continental margin.

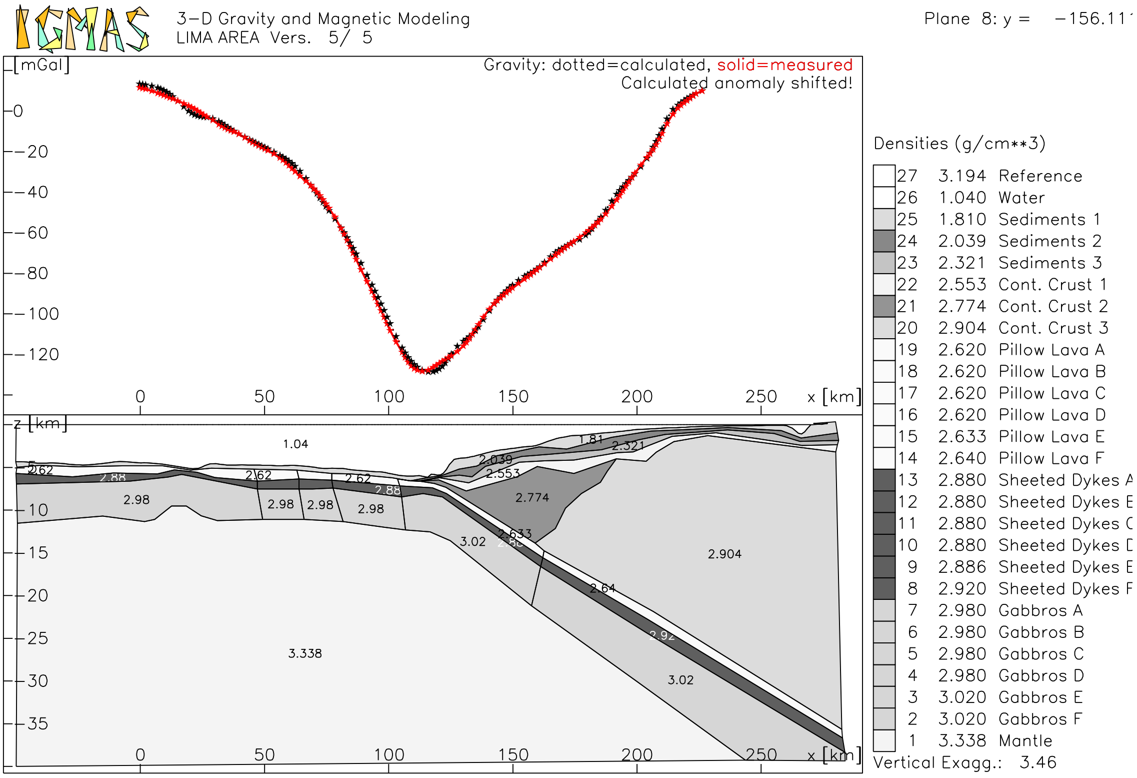

Figure 94: Lima Area - Gravity Modelling - Plane 8

On plane 8 an undulation of the oceanic crust is modelled at kilometre 20. The gradient of the gravity values is comparatively high above the continental crust.

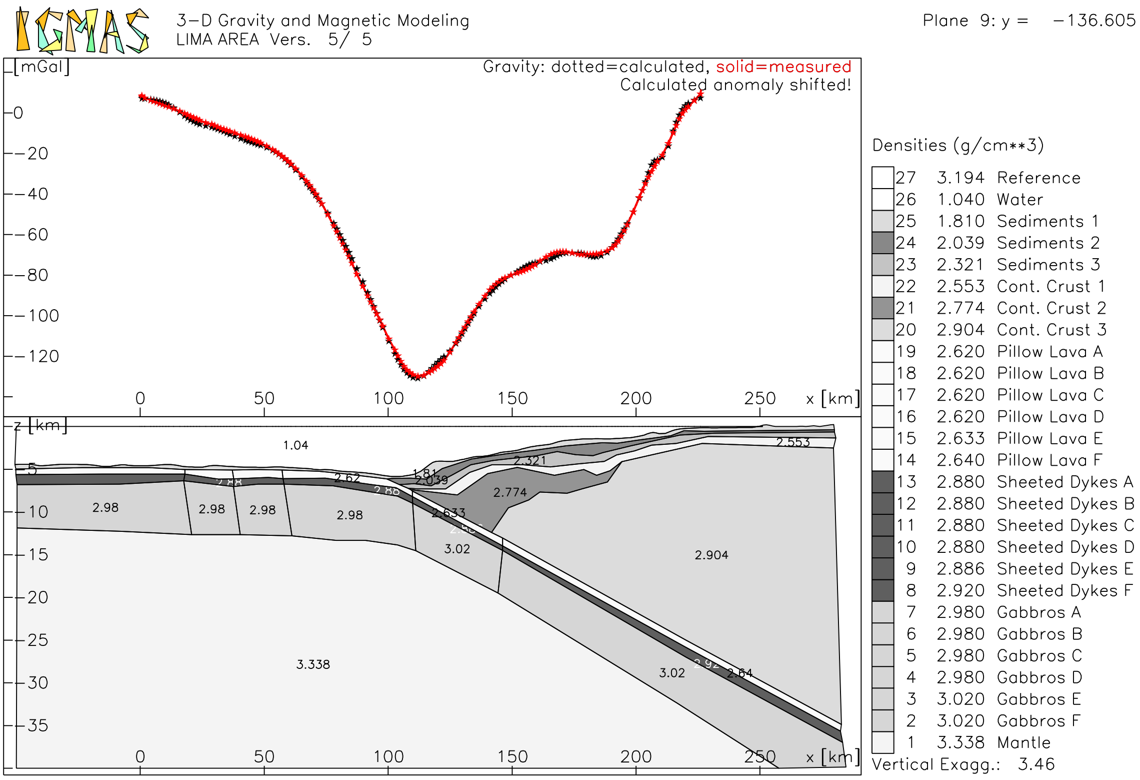

Figure 95: Lima Area - Gravity Modelling - Plane 9

Plane 9 shows a small plateau in free-air gravity between kilometres 170 and 190. Further landwards the gravity values rise to +10 mGal. The same gravity value is observed on the seaward side of the model.

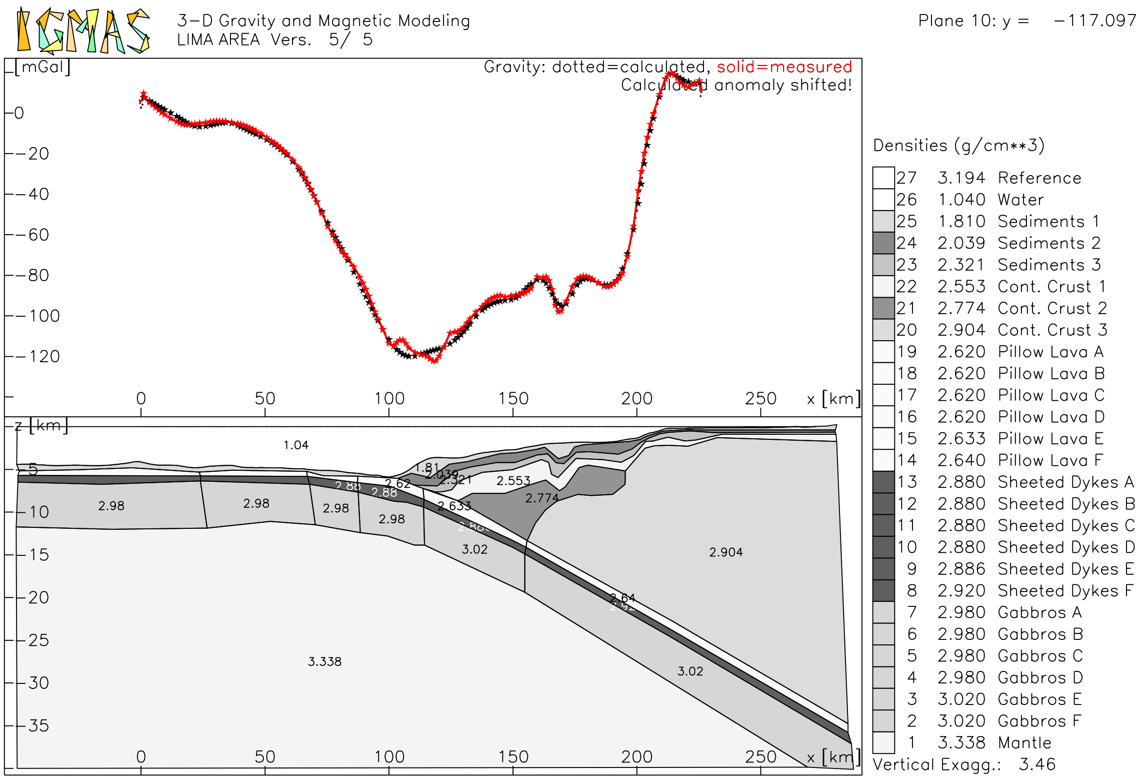

Figure 96: Lima Area - Gravity Modelling - Plane 10

On plane 10 an unusually broad gravity low can be seen between kilometres 110 and 200. The observed gravity anomaly on plane 10 shows short-wavelength anomalies from where the oceanic crust starts subducting to kilometre 200 where the gravity values rapidly increase and reach +20 mGal.

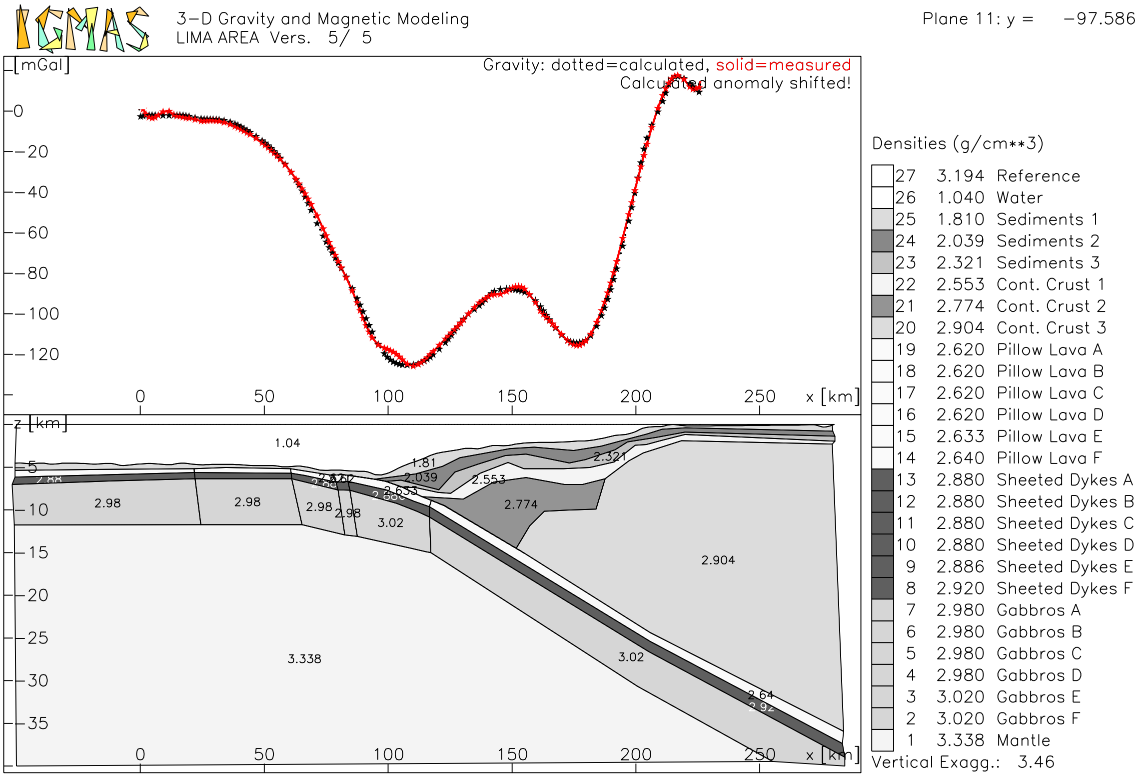

Figure 97: Lima Area - Gravity Modelling - Plane 11

On plane 11 the gradient of the free-air anomaly is even higher over the continental margin than over the oceanic crust. The minimum centred at kilometre 175 is almost as broad as the minimum connected with the Peru Trench.

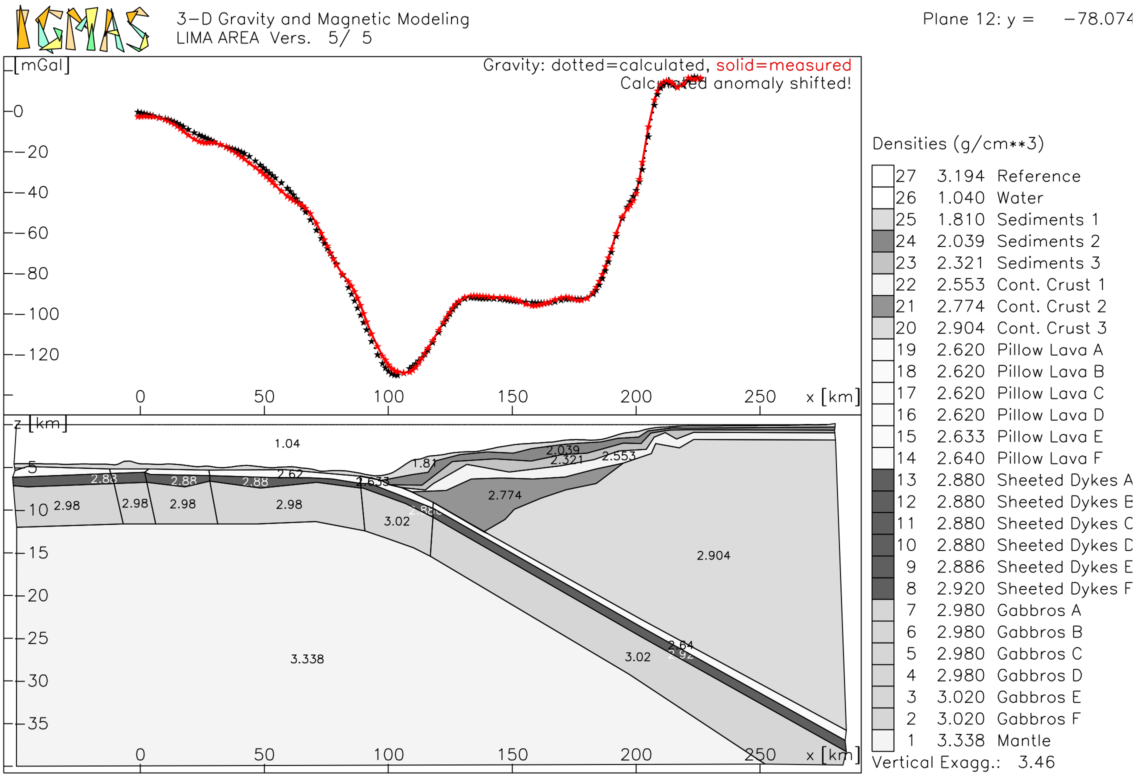

Figure 98: Lima Area - Gravity Modelling - Plane 12

Landward of the minimum related to the down-bending oceanic crust of plane 12 the free-air anomaly remains at a value of -90 mGal for about 70 km before rising steeply to almost +20 mGal. In the area of the plateau the layers of the continental margin are almost parallel.

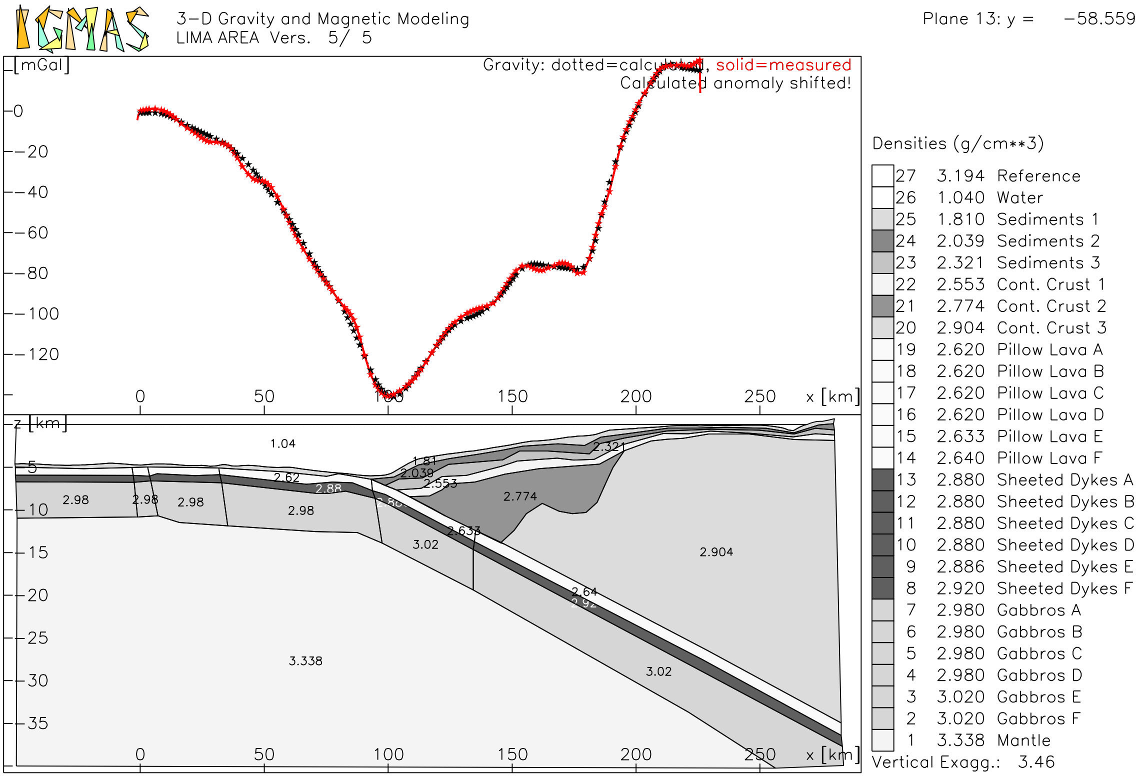

Figure 99: Lima Area - Gravity Modelling - Plane 13

On plane 13 the plateau in gravity is only 25 km long and shows values of -70 mGal. Underneath this plateau the layer continental crust 3 exhibits a depression. Continental crust 2 is thicker than on plane 12.

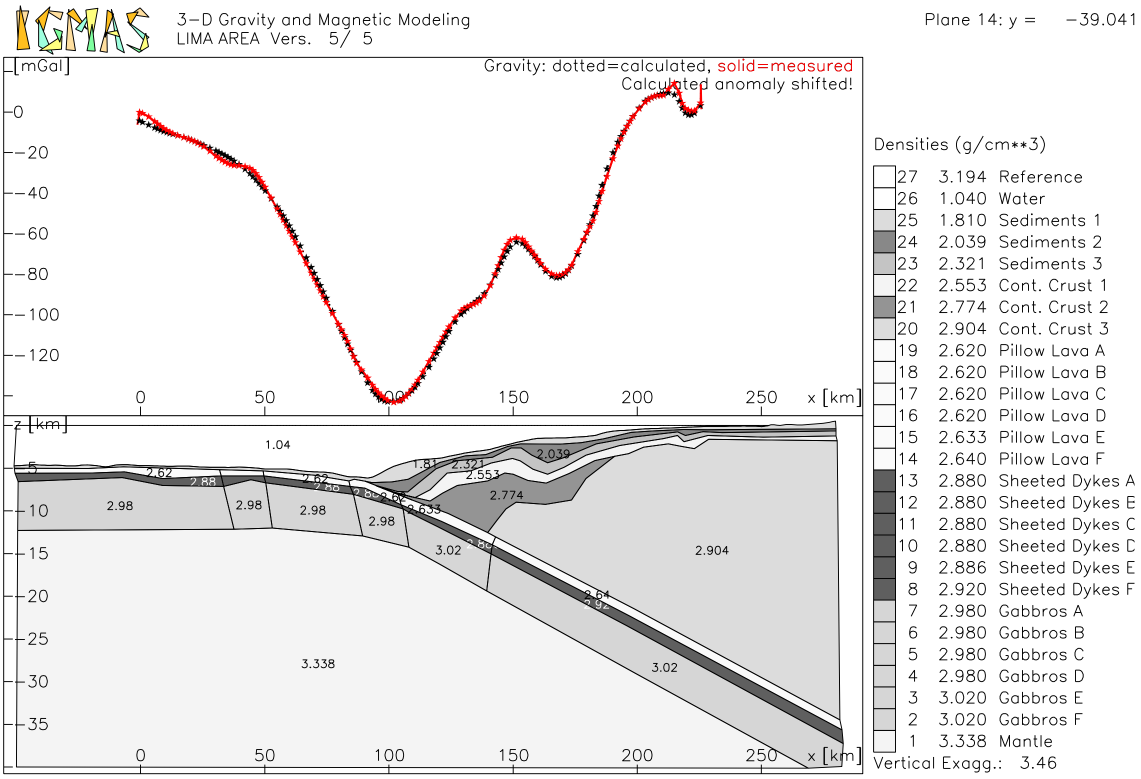

Figure 100: Lima Area - Gravity Modelling - Plane 14

On plane 14 a local maximum and minimum appear in the area of the former plateau. Undulations of the layers sediments 2 and 3 as well as continental crust 1 and 2 are causing these anomalies.

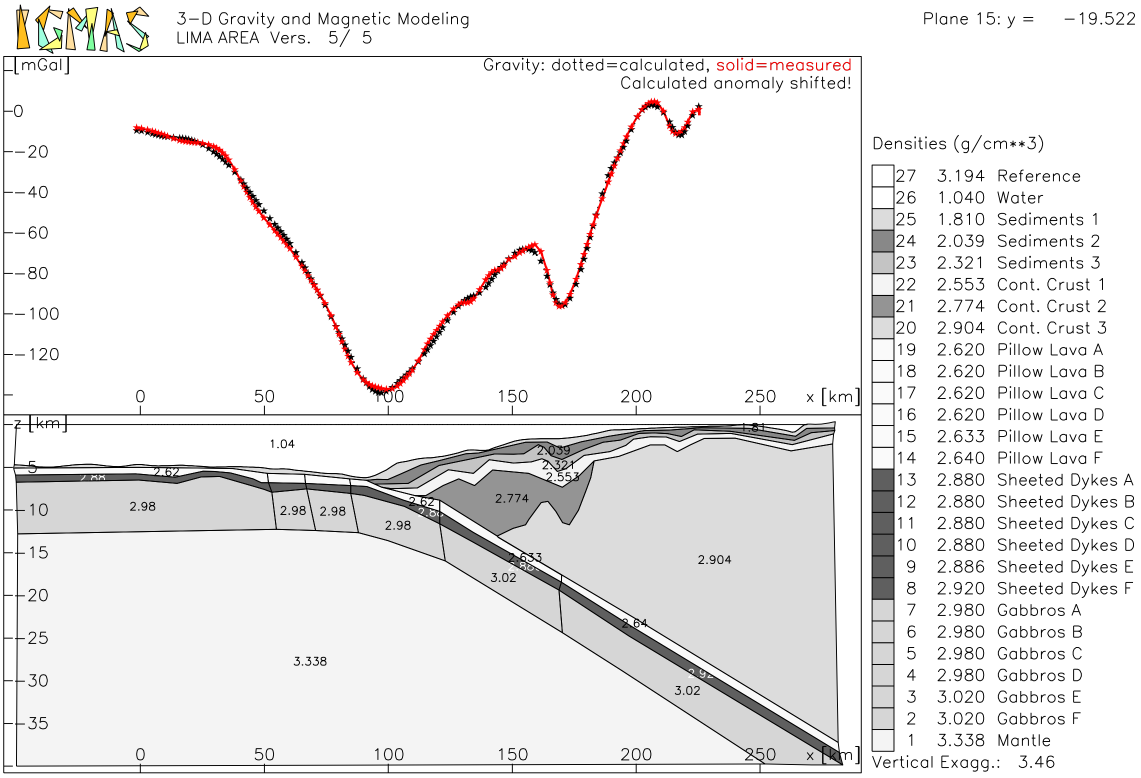

Figure 101: Lima Area - Gravity Modelling - Plane 15

On plane 15 (Figure 101) a prominent minimum is located at kilometre 170. This minimum is the expression of a depression in the layer continental crust 4.

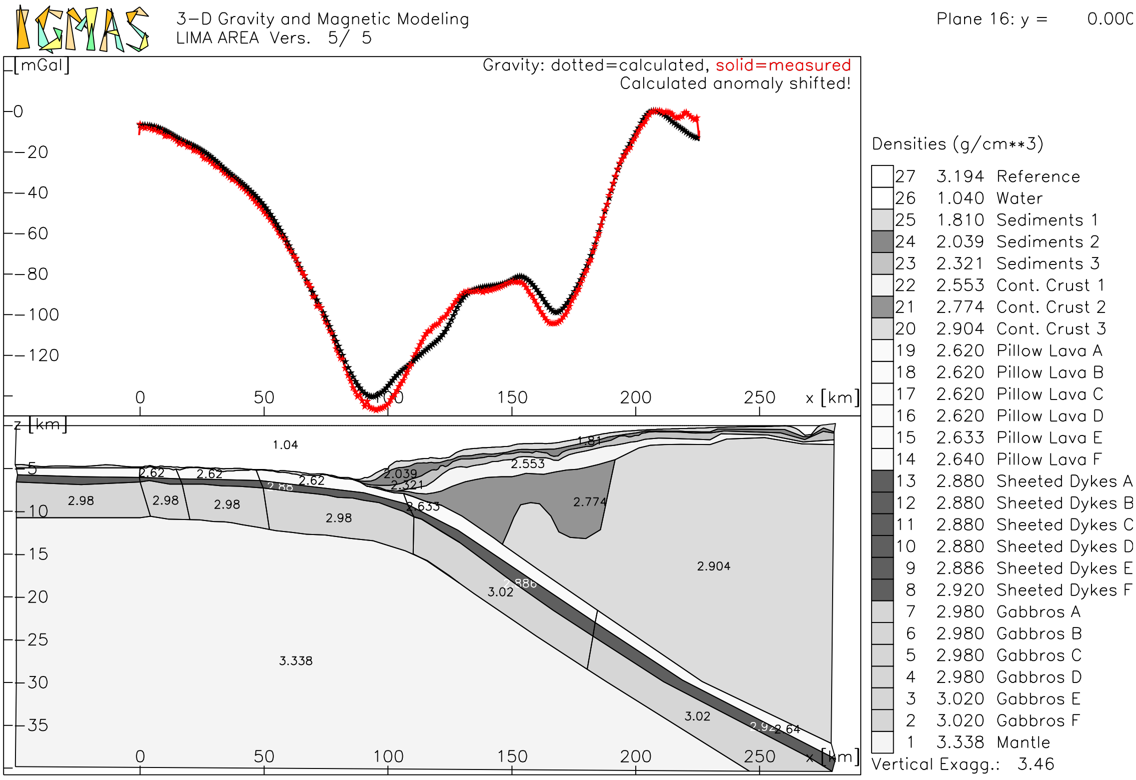

Figure 102: Lima Area - Gravity Modelling - Plane 16

Plane 16 corresponds to the seismic profile P5. The geometry is completely defined by the seismic velocity model (Broser et al., 2002). The densities were derived from the seismic velocities in the best possible way without violating the geological constraints. Between kilometres 160 and 190 the layer continental crust 1 shows a basin-like structure. In the gravity and magnetic model of the Lima Area this feature is extended laterally.

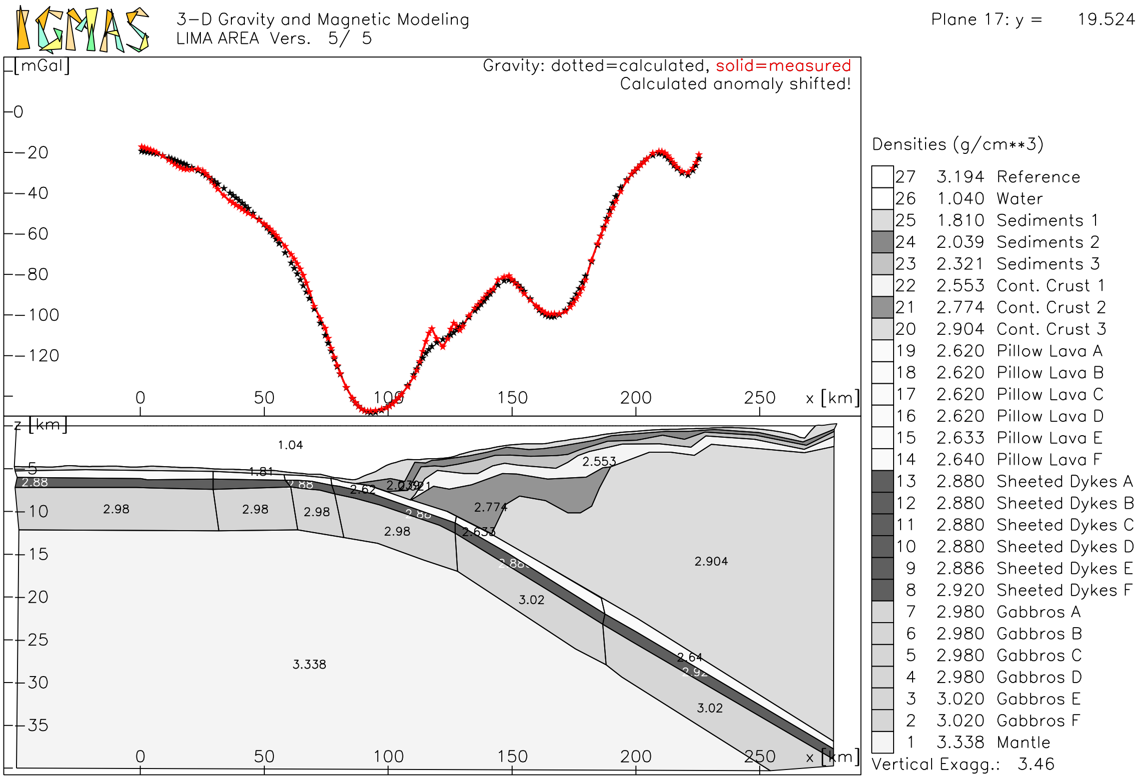

Figure 103: Lima Area - Gravity Modelling - Plane 17

At kilometre 0 of plane 17 the oceanic crust shows a negative value of -20 mGal. Contrary to most of the other planes here the oceanic crust is no longer in isostatic equilibrium. A short-wavelength local maximum is located at kilometre 120. Probably this feature is caused by outcropping high-density material.

7.6.2 Magnetic Modelling in the Lima Area

With magnetic modelling a standard deviation of 62.50 and a correlation coefficient of only 0.44 can be achieved.

In the Lima Area no clear magnetic lineation pattern can be observed in the magnetic profiles. Accordingly the assignment of model bodies to special magnetic anomalies is very difficult. Nevertheless it was attempted in three-dimensional modelling to reproduce the observed magnetic anomalies by six blocks with different magnetisations. In Figure 104 this subdivision of the oceanic crust is illustrated. The normally magnetised block C is tentatively identified as anomaly 19. Lineation 20 is simulated with the already subducted block F.

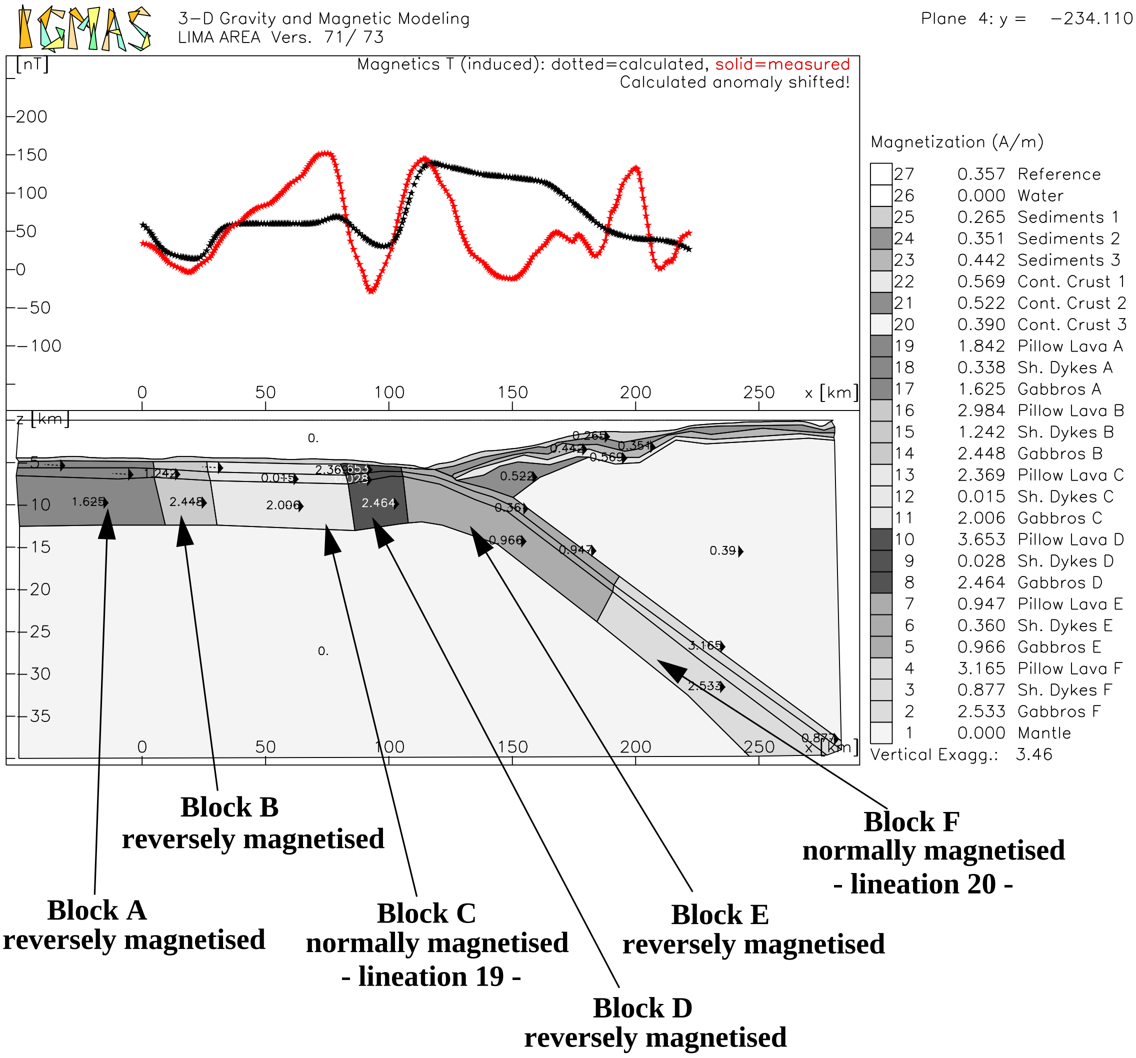

Figure 104: Lima Area - Magnetic Modelling - Plane 4: The magnetisations of the different magnetic bodies

In the Lima Area the magnetic north direction is 62.299° and the total magnetic intensity reference value is 26659 nT. The inclination angle is 0.5° and the declination angle is 2.65°.

The continental layers show only small magnetisations. The main continental block, continental crust 3 is appointed a magnetisation of 0.406 A/m. The Layer continental crust 2 shows a magnetisation of 0.46 A/m and continental crust 1 possesses a similar magnetisation of 0.649 A/m.

The blocks of the oceanic crust show a distinct pattern. The layer sheeted dykes is always considerably weaker magnetised than the other layers, ranging between 0.015 and 1.242 A/m. Blocks A and B show a high magnetisation of gabbros and an intermediate magnetisation of pillow lavas. Blocks C and D show a high magnetisation of pillow lavas and of gabbros. Block possesses a weaker magnetisation for pillow lavas and gabbros and block F again shows a high magnetisation for pillow lavas and gabbros.

In the following the planes of the magnetic model are presented displaying the relation between remanent and induced magnetisation. The magnetisation values are those presented in Figure 104.

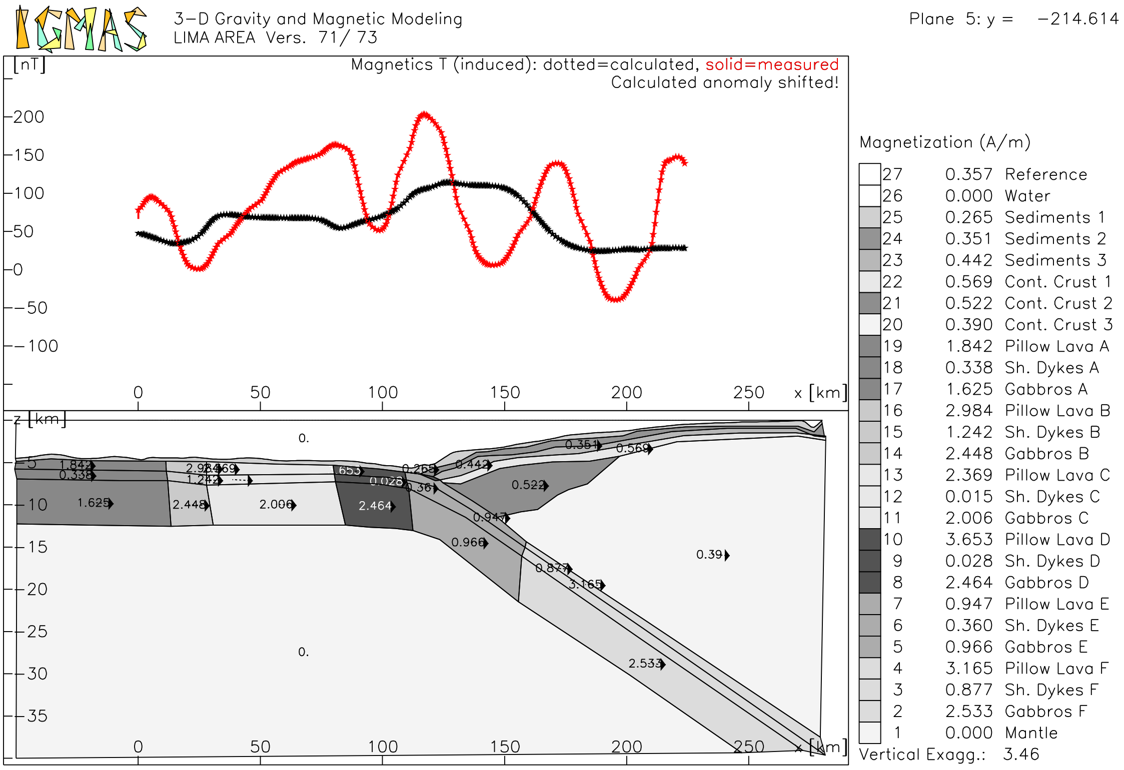

Figure 105: Lima Area - Magnetic Modelling - Plane 5

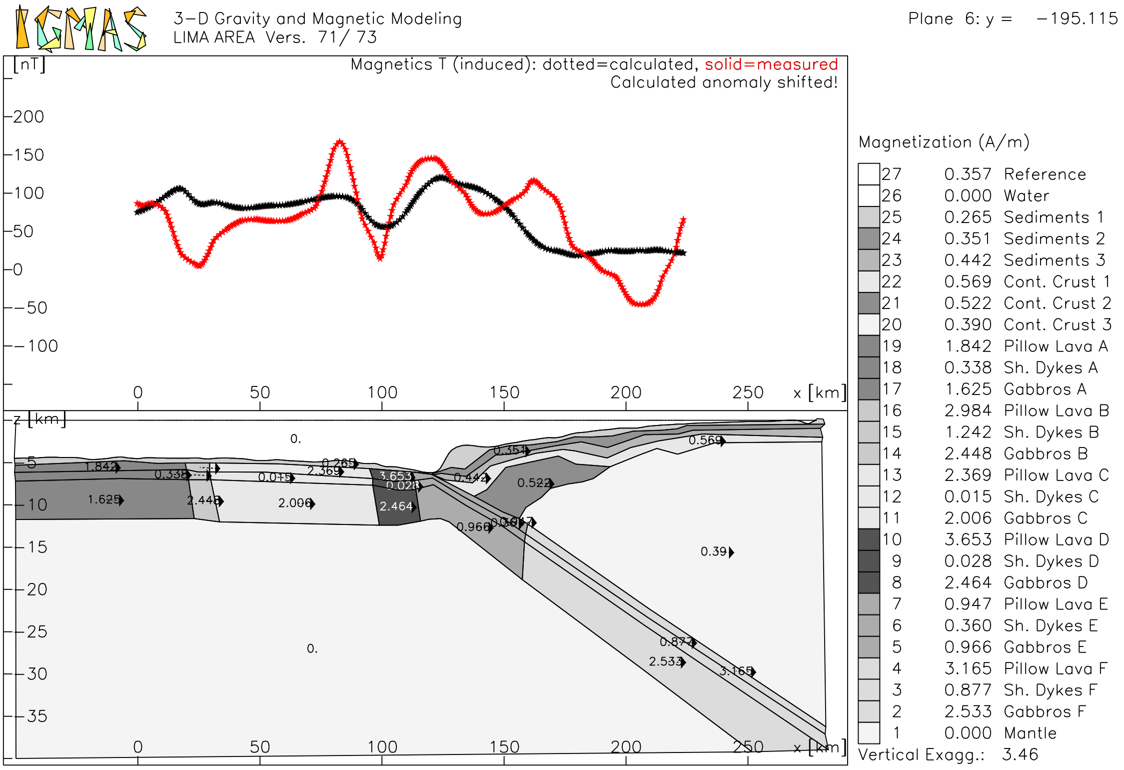

Figure 106: Lima Area - Magnetic Modelling - Plane 6

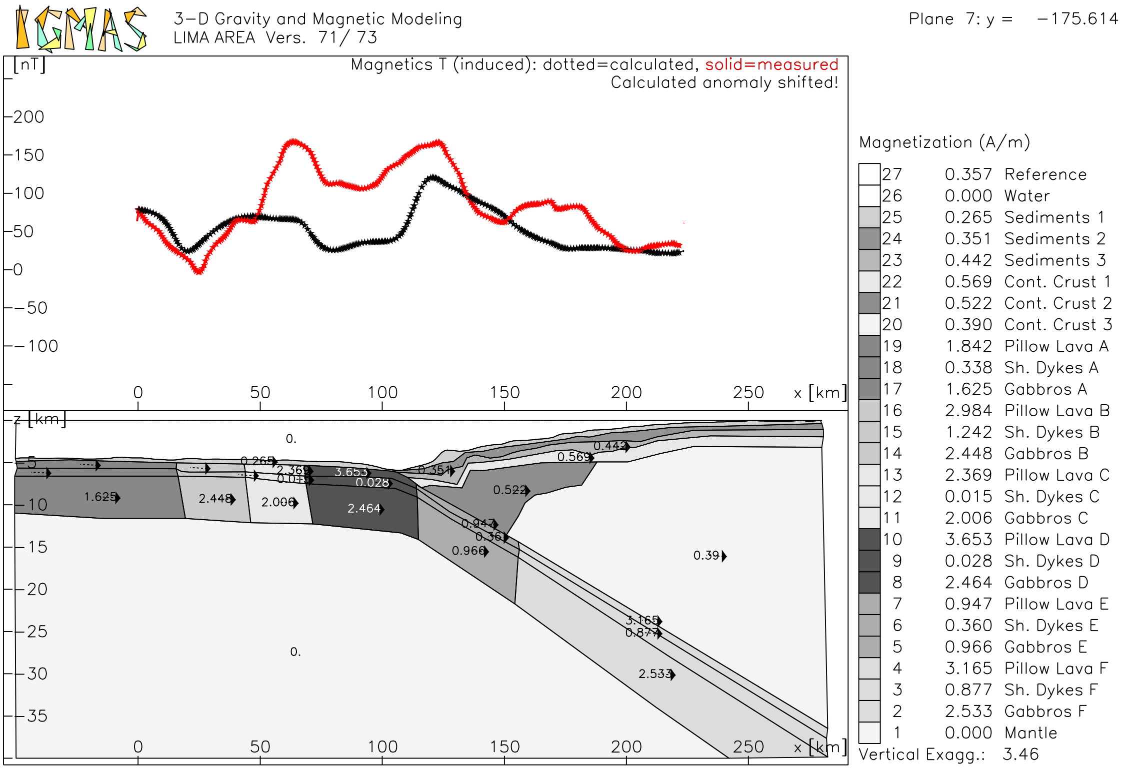

Figure 107: Lima Area - Magnetic Modelling - Plane 7

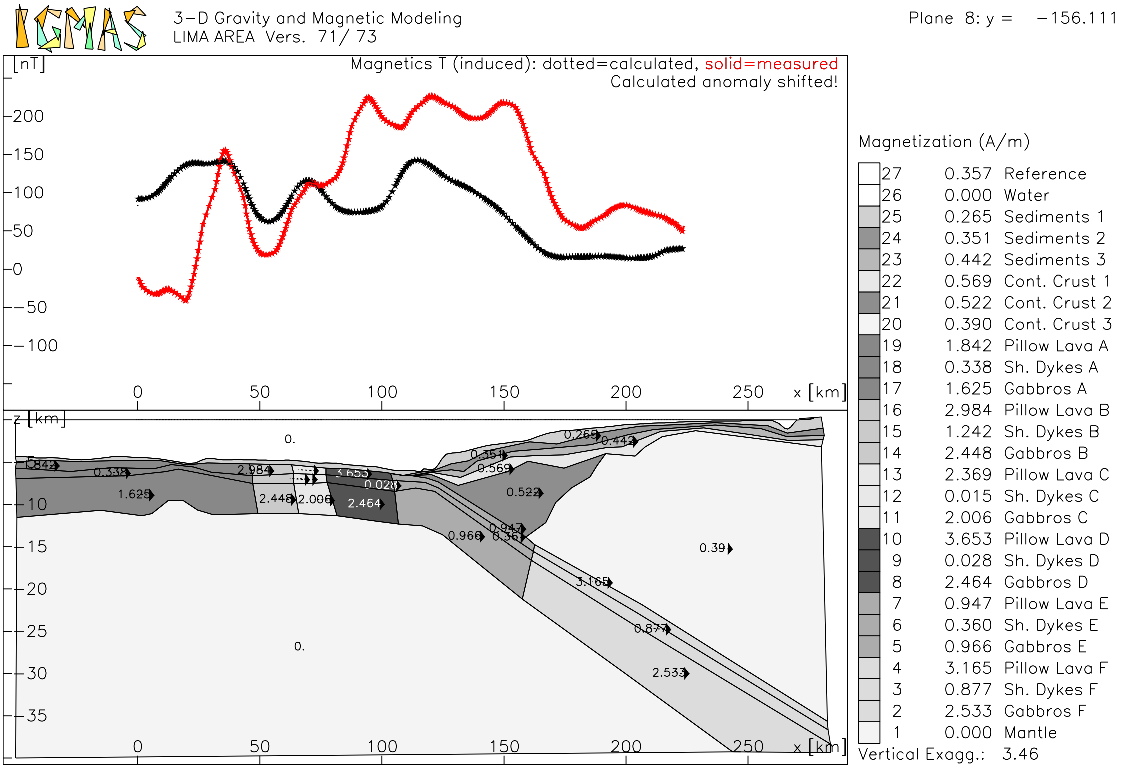

Figure 108: Lima Area - Magnetic Modelling - Plane 8

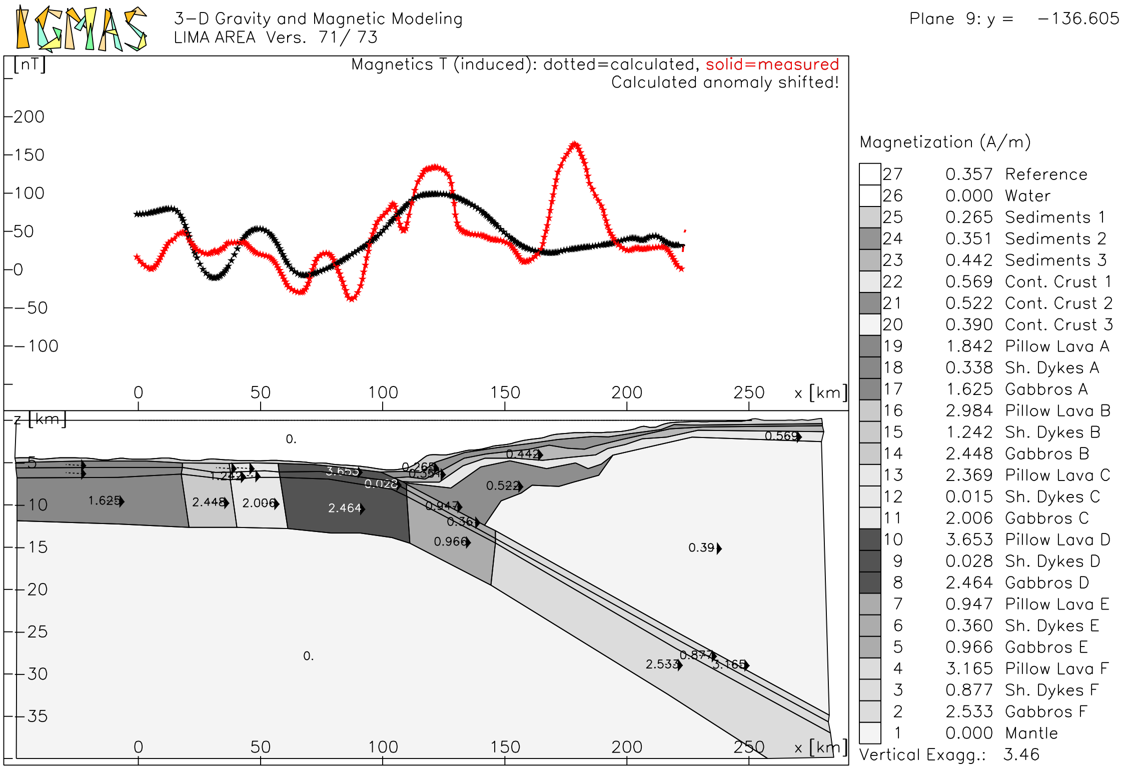

Figure 109: Lima Area - Magnetic Modelling - Plane 9

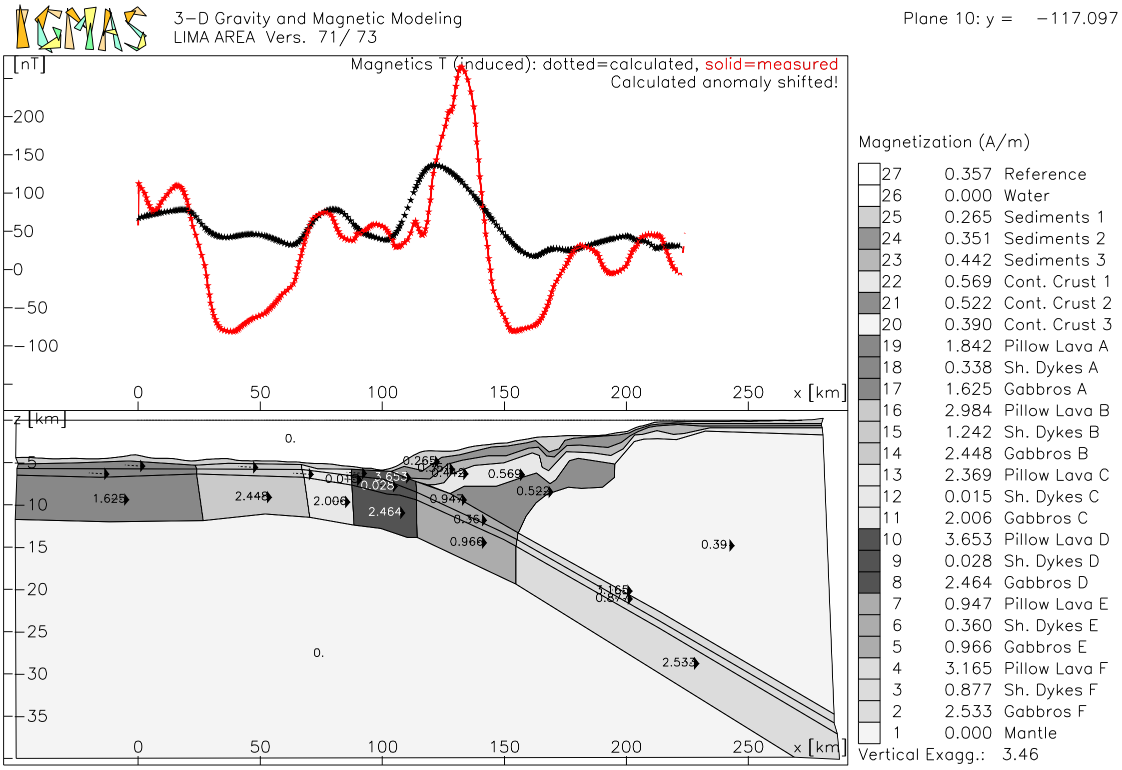

Figure 110: Lima Area - Magnetic Modelling - Plane 10

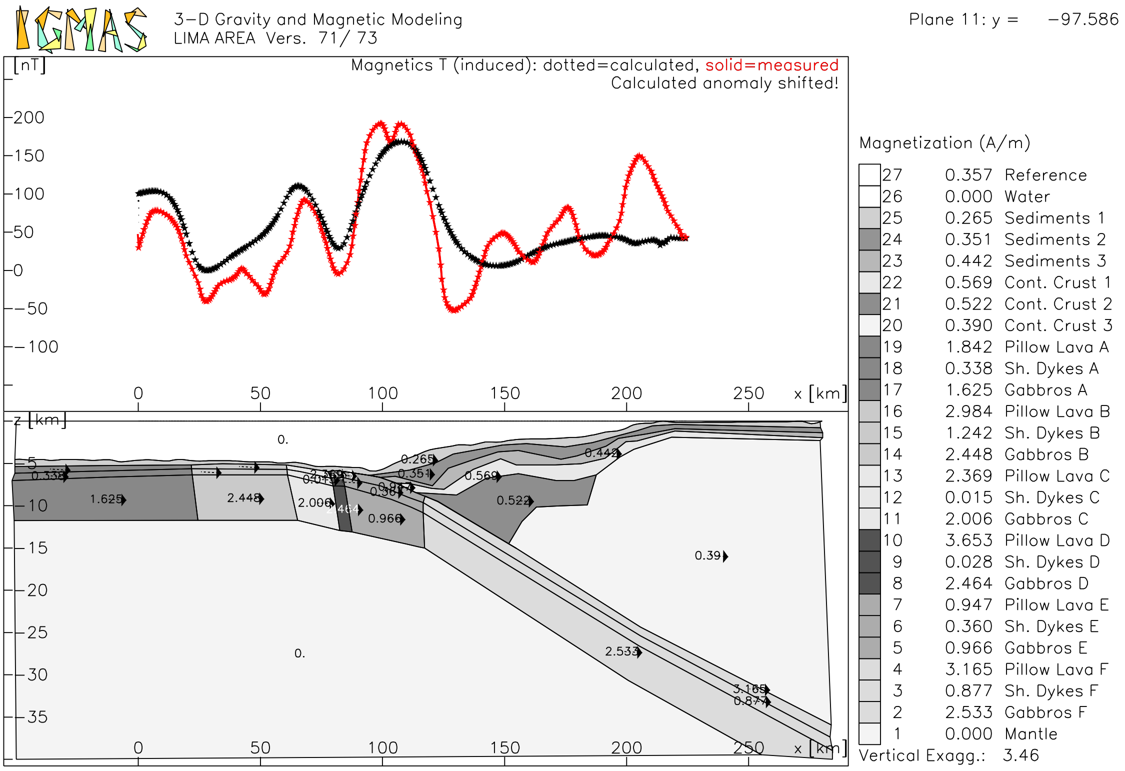

Figure 111: Lima Area - Magnetic Modelling - Plane 11

Actually the model along plane 11 fits exceptionally well. All the three prominent maxima can be reproduced.

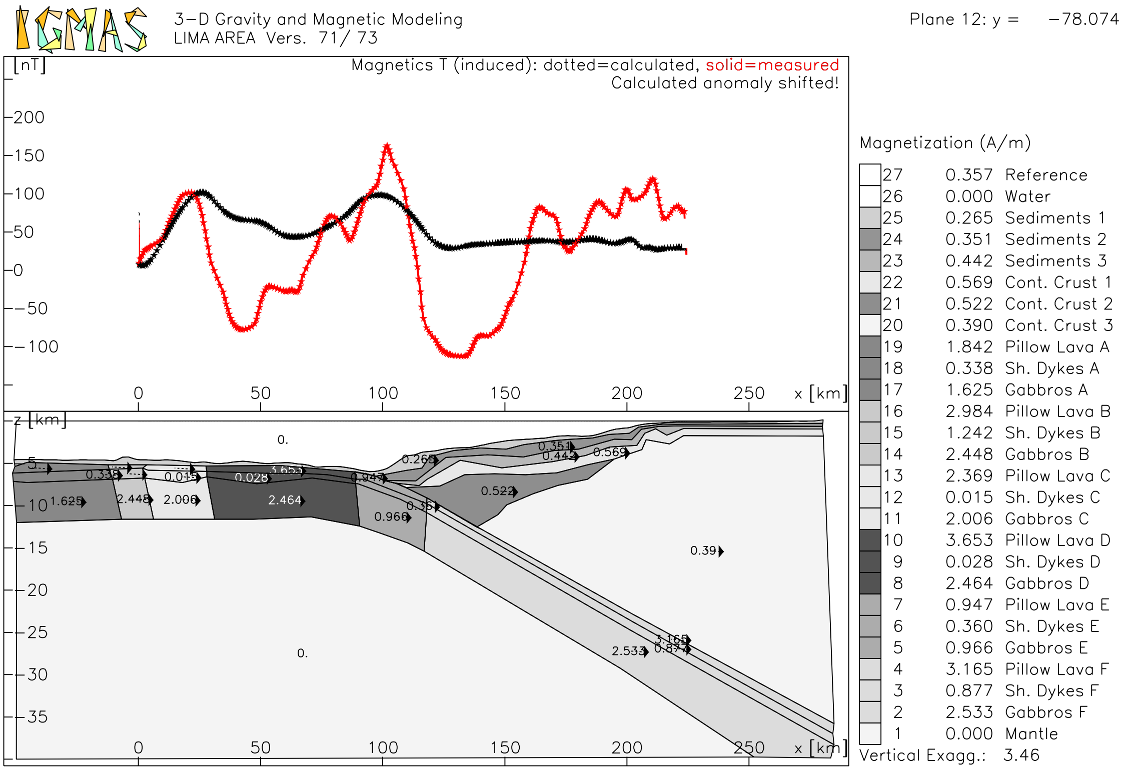

Figure 112: Lima Area - Magnetic Modelling - Plane 12

On plane 12 the two maxima on the oceanic plate can, to some extent, be seen in the calculated anomalies. The distinct minimum, located where the Nazca Plate has just started subduction, cannot be modelled satisfactorily.

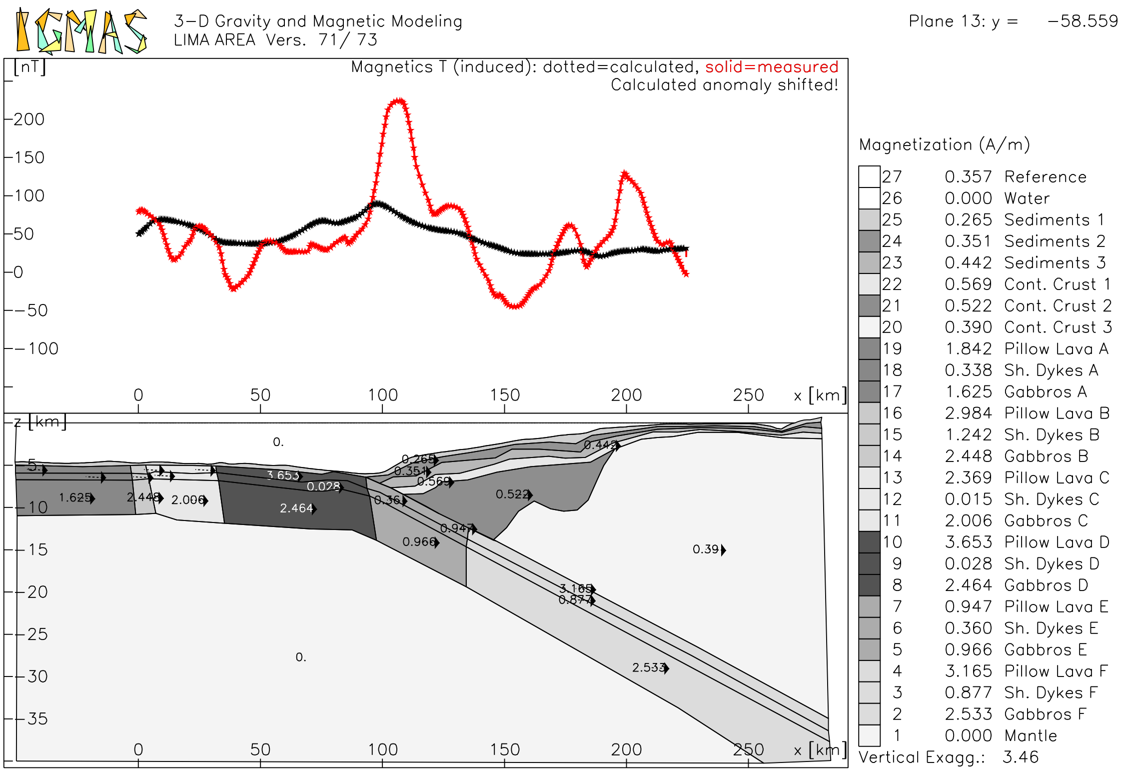

Figure 113: Lima Area - Magnetic Modelling - Plane 13

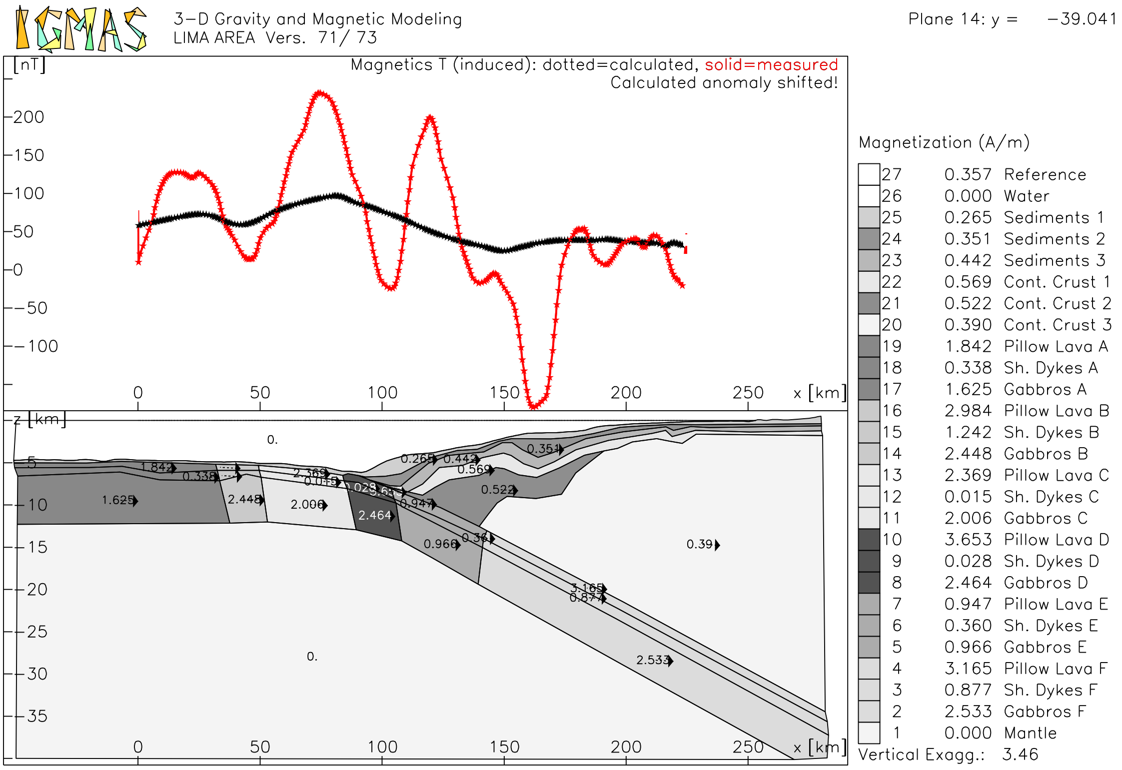

Figure 114: Lima Area - Magnetic Modelling - Plane 14

All modelling efforts to approximate the large amplitude anomalies were futile.

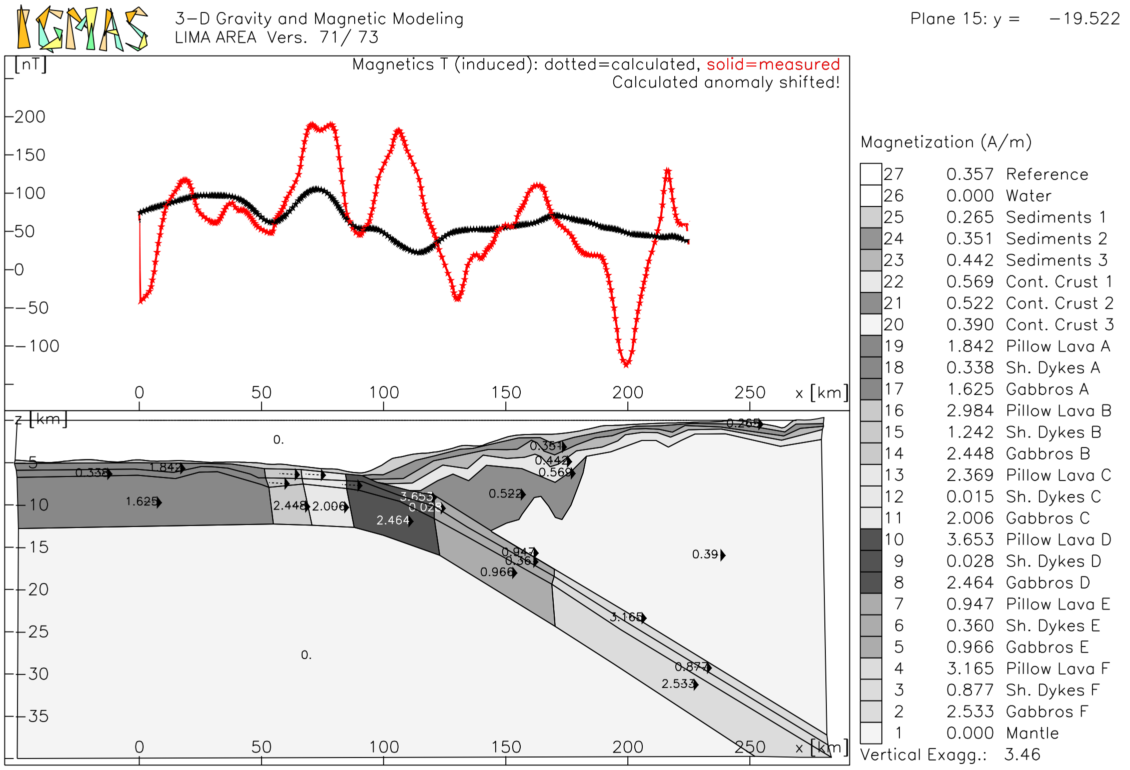

Figure 115: Lima Area - Magnetic Modelling - Plane 15

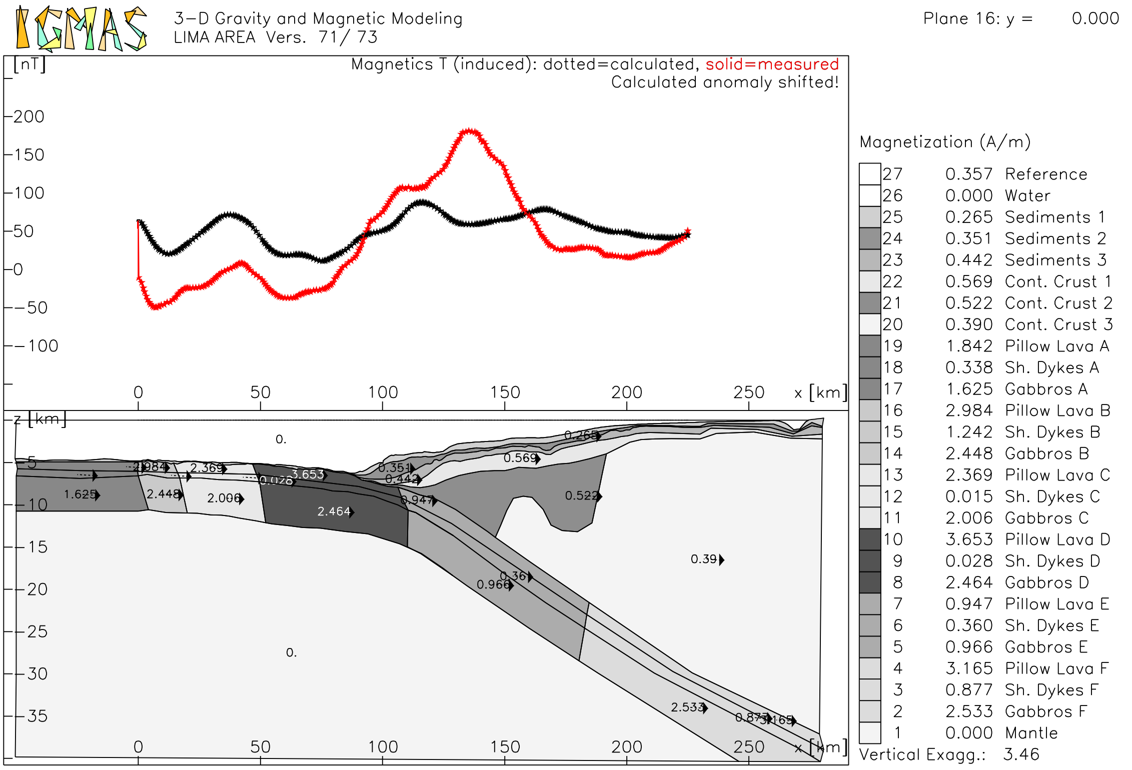

Figure 116: Lima Area - Magnetic Modelling - Plane 16

On plane 16 the two maxima can only be modelled with an offset. The increase in magnetisation values toward the continent is reproduced.

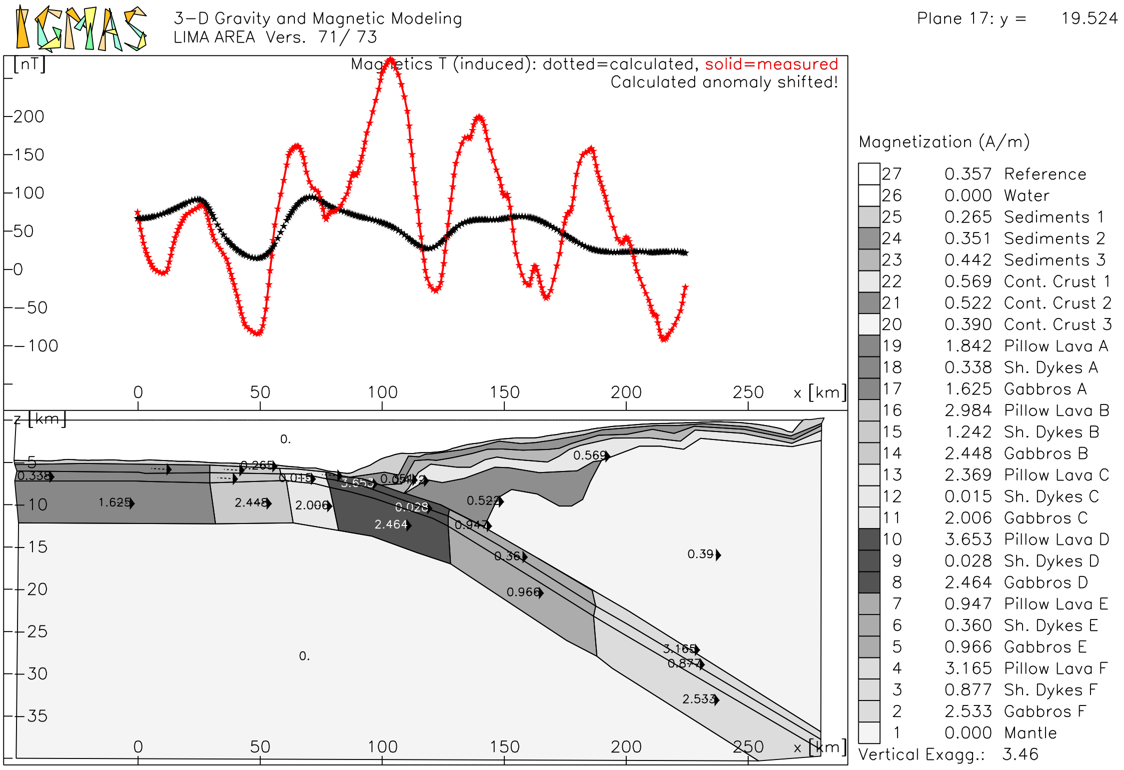

Figure 117: Lima Area - Magnetic Modelling - Plane 17

The observed magnetic data possess a very high frequency along plane 17. Here, the discrepancies between modelled and observed anomalies become very distinct.

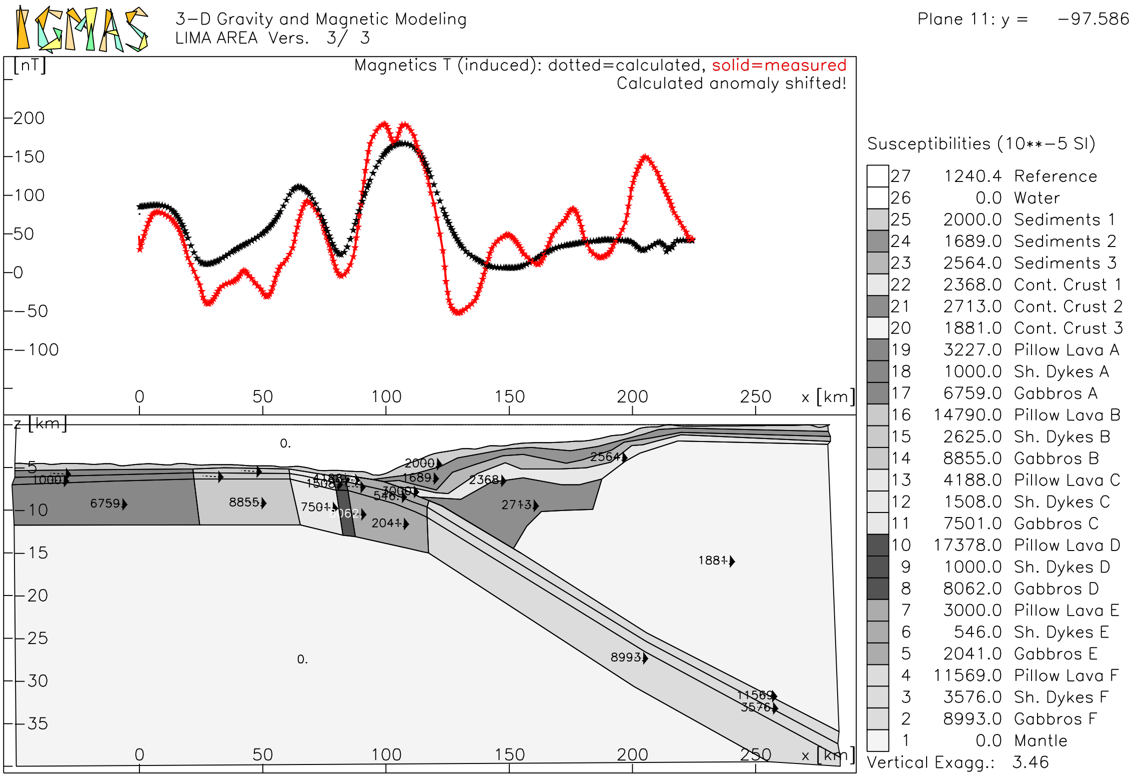

Figure 118: The modelled susceptibilities in the Lima Area

Figure 118 shows a different presentation of the Lima Area model. The differently magnetised layers are displayed regarding their susceptibilities.

A top view of the oceanic crust is displayed in Figures 119 and 120. The differently magnetised blocks show local variations in their expansion but, examined over the whole research area, they run more or less parallel to the model boundaries. The layer sediments 2 roughly describes the seaward extent of the continental slope.

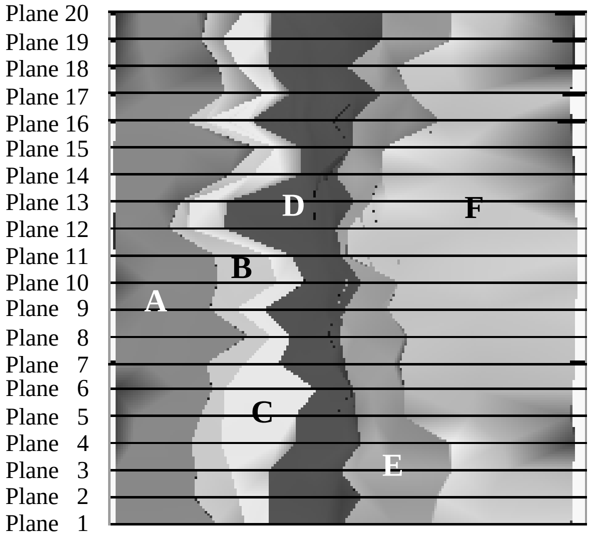

Figure 119: The differently magnetised blocks of the Lima Area model

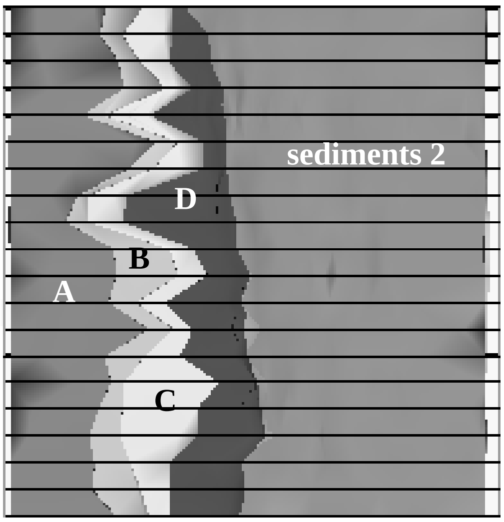

Figure 120: The differently magnetised blocks of the Lima Area model, partly covered by sediments 2

7.7 The Nazca Ridge Model

The area of the three-dimensional gravity and magnetic Nazca Ridge model is located between 14.25°S and 16.75°S. and is 220.5 km by 178 km in size. The Nazca Ridge model is comprised of 17 parallel vertical planes at a distance of 13.8 km. This distance is considerably smaller than in the other three-dimensional models; the crustal structure of the Nazca Ridge is imaged in detail. Each vertical plane includes part of the oceanic plate, the Peru Trench and the continental shelf of the South American Plate. The three-dimensional model images the aseismic Nazca Ridge during its subduction beneath the continental South American Plate.

The results from the two crossing refraction seismic profiles P1 and P2 (Hampel et al., 2002a) are directly included in the three-dimensional model. The location of these profiles is illustrated in Figure 41. Profile P2 is following the crest of the Nazca Ridge and is oriented perpendicular to profile P1 which is located parallel to the Peru Trench. The vertical plane of the three-dimensional gravity model corresponding to profile P2 is plane 11, displayed in Figure 129. There is a very good conformity between the observed and the calculated values. The second seismic profile, P1, is crossing the vertical planes at an approximately right angle at about kilometre 33. Here the layer geometry of the potential field models is constrained by the seismic velocities of profile P1.

In the Nazca Ridge model the layers of the oceanic crust are more detailed. The layer pillow basalts is subdivided into the layers 2A and 2B. The layer sheeted dykes corresponds to layer 2C. The layer gabbros is subdivided into layers 3A and 3B. Again the oceanic crust is split into blocks with different magnetisations. The oceanic crust, forming the Nazca Ridge, is significantly thicker than in the other three-dimensional models. Like the Lima Area model the Nazca Ridge model reaches into a depth of 40 km.

7.7.1 Gravity Modelling in the Nazca Ridge Area

For the gravity model a standard deviation of 4.14 and a correlation coefficient of 1.00 can be reached. In Figure 121 the observed gravity field is displayed in comparison with the calculated gravity anomalies. Figure 122 shows the minimal differences between these gravity anomalies.

In Figure 121 the buffer zone, surrounding the three-dimensional model, is apparent. This zone surrounds the area documented by potential field data to exclude edge-effects. The imaged planes represent the extent of the model, the gravity data are located only on planes 5 to 14.

The highest maximum, reaching +40 mGal, is located above the oceanic crust near the seaward boundary of the model. On average, the free-air gravity anomalies show values of 20 mGal on the seaward side of the different planes. The negative anomalies related to the Peru Trench are narrowing between planes 10 and 12 as well as north of plane 13. In the north the gravity anomaly increases to -140 mGal. In the narrow middle part a free-air gravity value of -160 is observed and in all other areas a negative anomaly of -180 mGal is measured. South of plane 7 both the positive anomalies seawards and landwards of the trench shift further towards the South American continent.

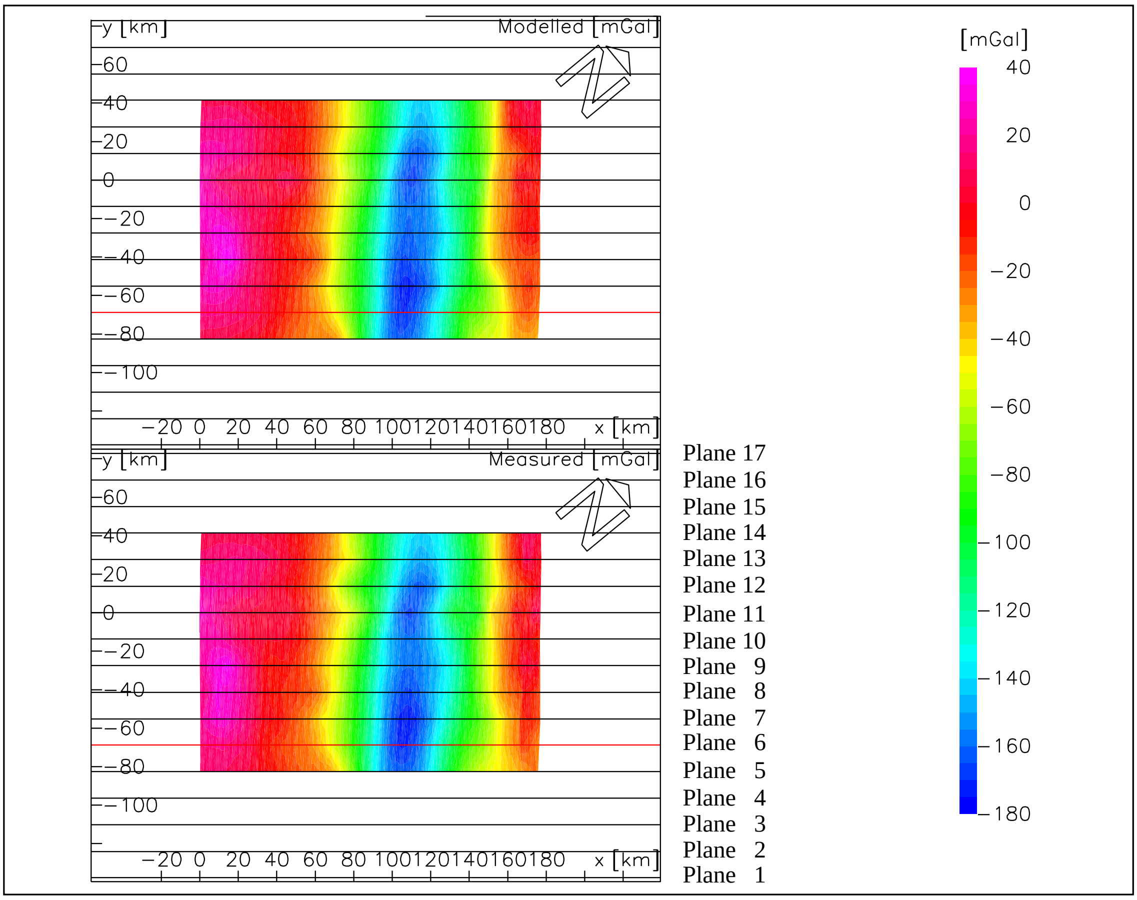

Figure 121: The Observed and the Modelled Free-Air Anomalies of the Nazca Ridge Model

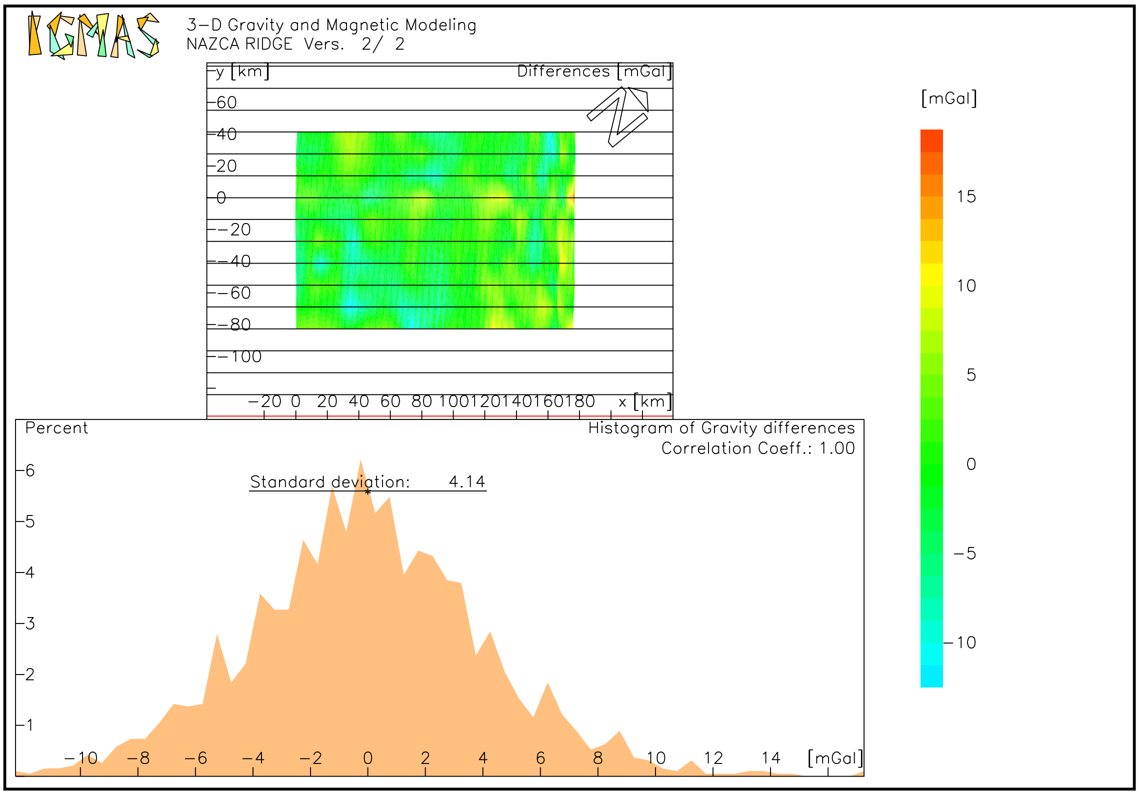

Figure 122: The Differences Between the Observed and the Modelled Gravity Anomalies in the Nazca Ridge Model

In the following all the planes of the Nazca Ridge model are presented.

For the mantle a density of 3.34 g/cm^3 is employed. The layers of the oceanic crust acquire a slightly higher density when starting subduction. The continental crust is modelled in a different way compared to the Yaquina Area and to the Lima Area. The main continental block, continental crust 3 reaches as far seaward as the Peru Trench. No wedge possessing a lower density is modelled at the tip of the continental margin.

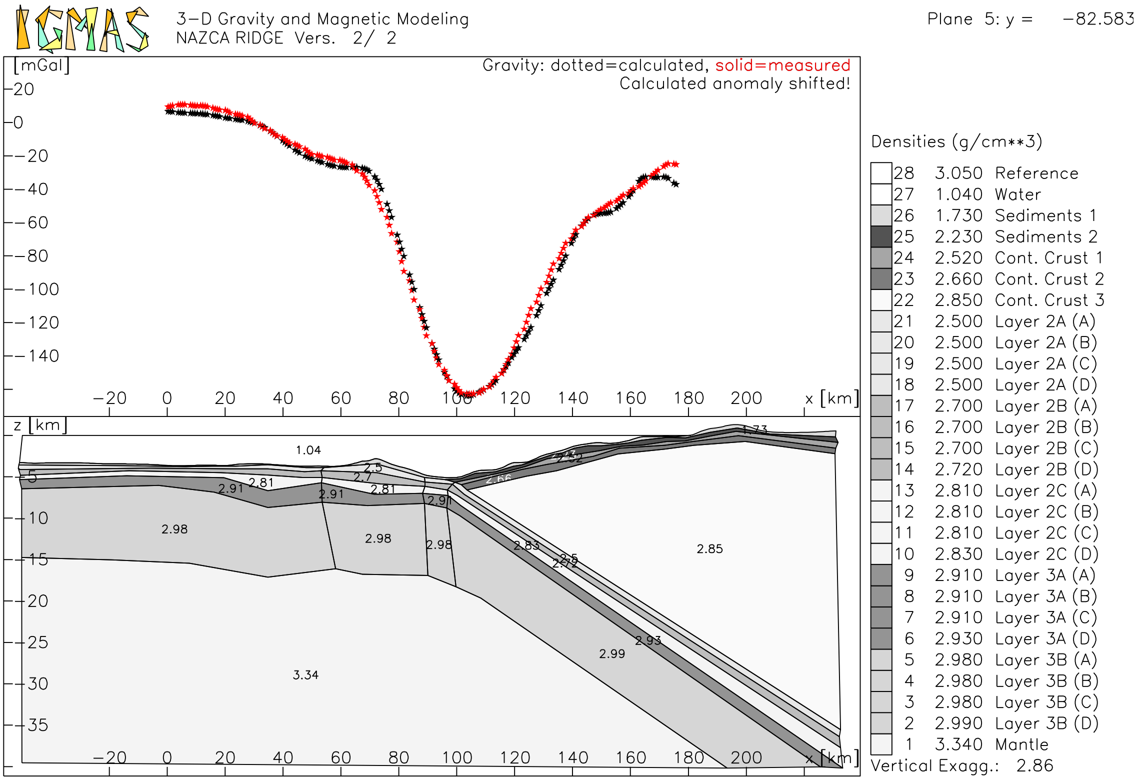

Figure 123: Nazca Ridge - Gravity Modelling - Plane 5

On this southernmost plane of the Nazca Ridge model the oceanic crust is 12 km thick. The boundary between the layers 3A and 3B lies at a depth of about 7 km.

A topographic high is situated at kilometre 70, bordering the trench. Most probably this feature will influence the subduction zone in the future. The oceanic crust is thickened seaward of this elevation. At kilometre 33 the crust is 16 km thick, 1 km thicker than land- and seawards. This thickening is constrained by the seismic velocity model of profile P1. The layers of the continental crust, possessing lower densities, lie close to the sea floor. The continental margin is dominated by the layer continental crust 3. On the landward side of the plane, where gravity data are no longer calculated, the continental layers already rise above sea level.

Plane 6 does not show any remarkable features. The distinguished elevation of the sea floor is no longer visible (see Figure 124). Around kilometre 33 the modelled oceanic crust, as defined by the seismic profile P1, is not thick enough to produce the observable free-air anomaly.

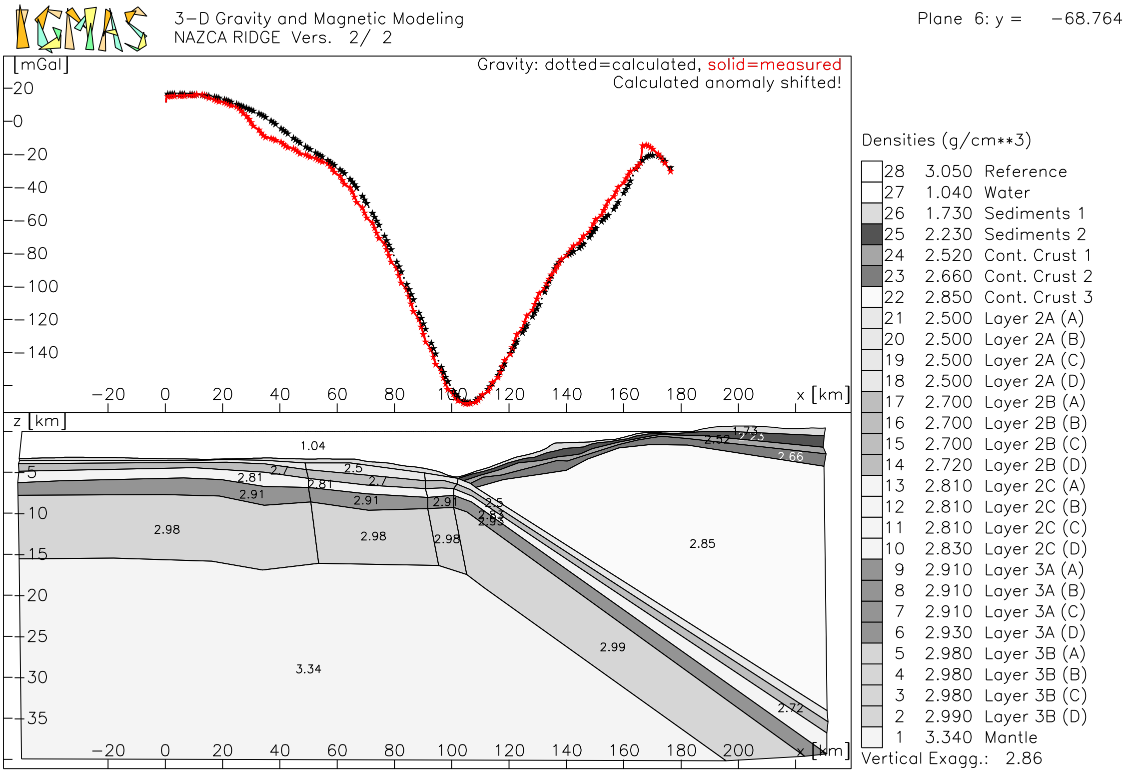

Figure 124: Nazca Ridge - Gravity Modelling - Plane 6

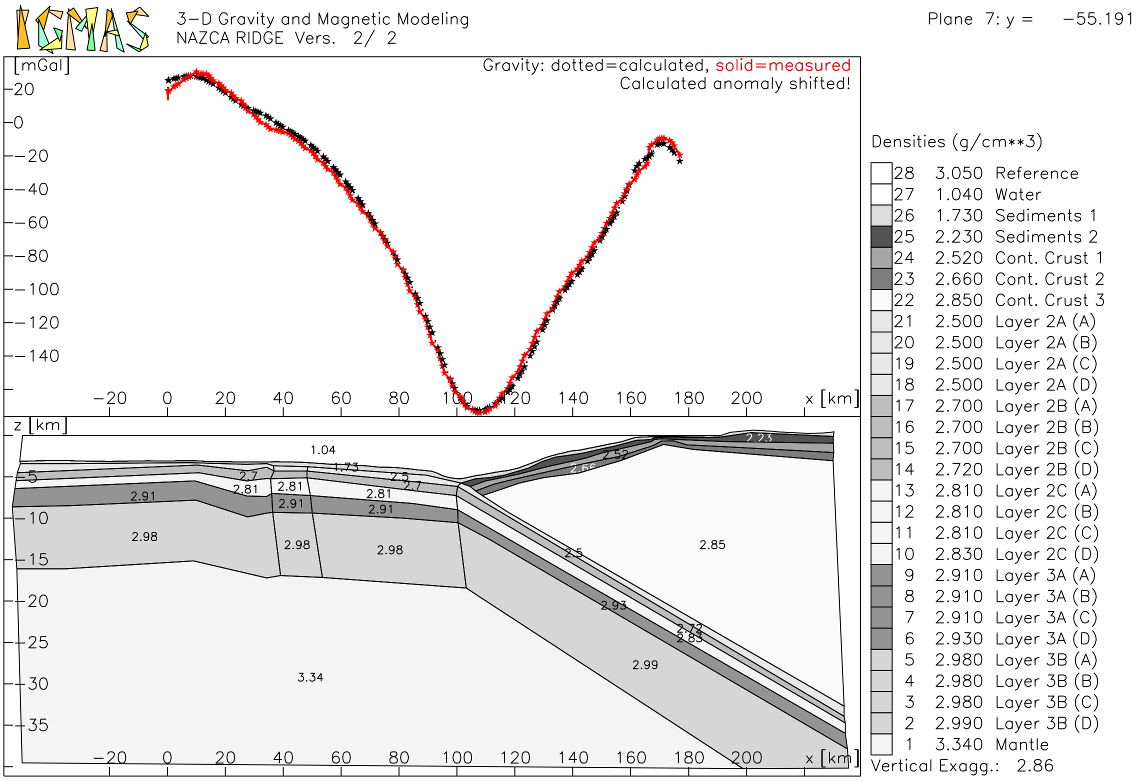

Figure 125: Nazca Ridge - Gravity Modelling - Plane 7

On the seaward side of plane 7 the free-air gravity is as positive as +30 mGal. Here, local isostatic compensation does no longer apply. Above the continental shelf a relative maximum of -10 mGal is reached.

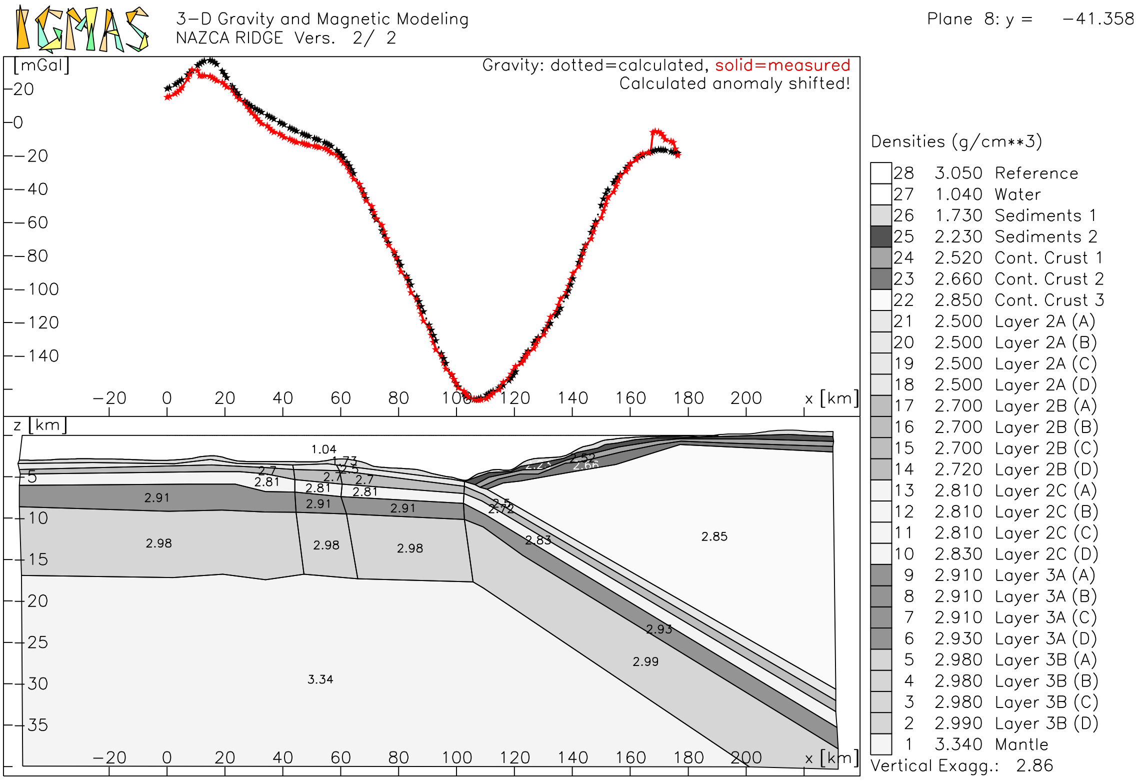

Figure 126: Nazca Ridge - Gravity Modelling - Plane 8

The seaward side of plane 8 is not at all isostatically compensated. The measured free-air gravity values reach 30 mGal. On planes 8 and 9 (Figures 126 and 127) the observed free-air anomalies are especially high above the eastern part of the profiles. Although the high-

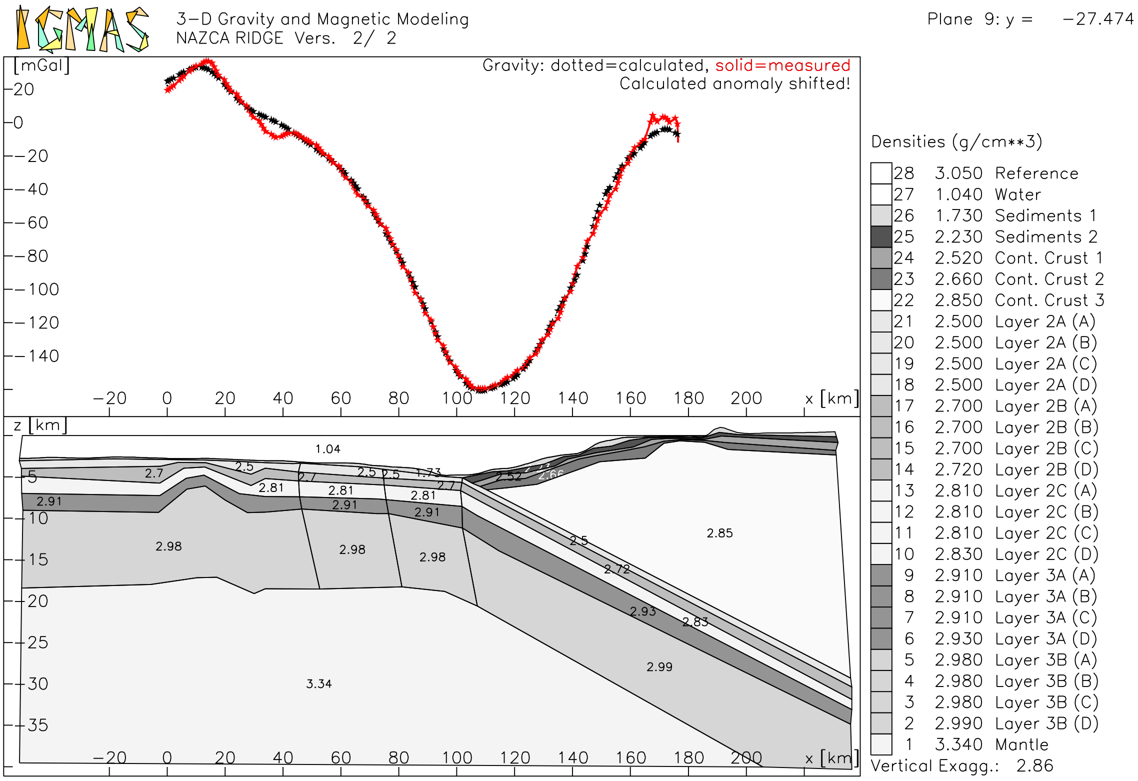

Figure 127: Nazca Ridge - Gravity Modelling - Plane 9

density layers of the continental margin bulge upwards these high gravity values cannot be modelled. On plane 9 a prominent upwelling of the oceanic crust is modelled between kilometres -10 and 30. This feature is expressed in a local maximum of the free-air gravity values. Landward of the maximum the crustal layers bend downwards producing a minimum in gravity. At kilometre 180 the dense layer continental crust 3 surges upwards and displaces the other layers.

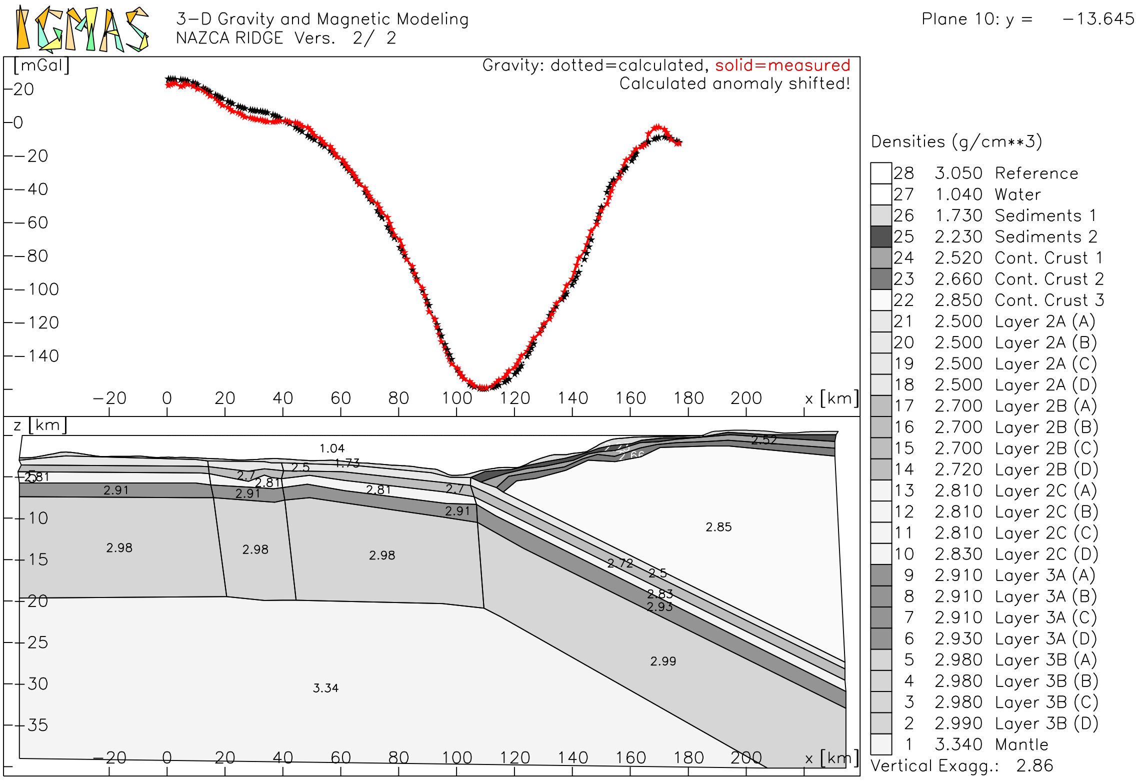

Figure 128: Nazca Ridge - Gravity Modelling - Plane 10

On plane 10 the oceanic crust is 17 km thick. On this plane and on plane 11 the Nazca Ridge exhibits its maximum thickness.

Plane 11 (Figure 129) corresponds to the seismic profile P2. The upwelling of the oceanic crust is located further towards the trench on plane 11. A retardation of the increasing gravity is observed between kilometres 130 and 140 above the continental margin. On the eastern side of profile P2 the observed free-air gravity anomalies show considerably higher values than those gravity anomalies calculated from the given model geometry.

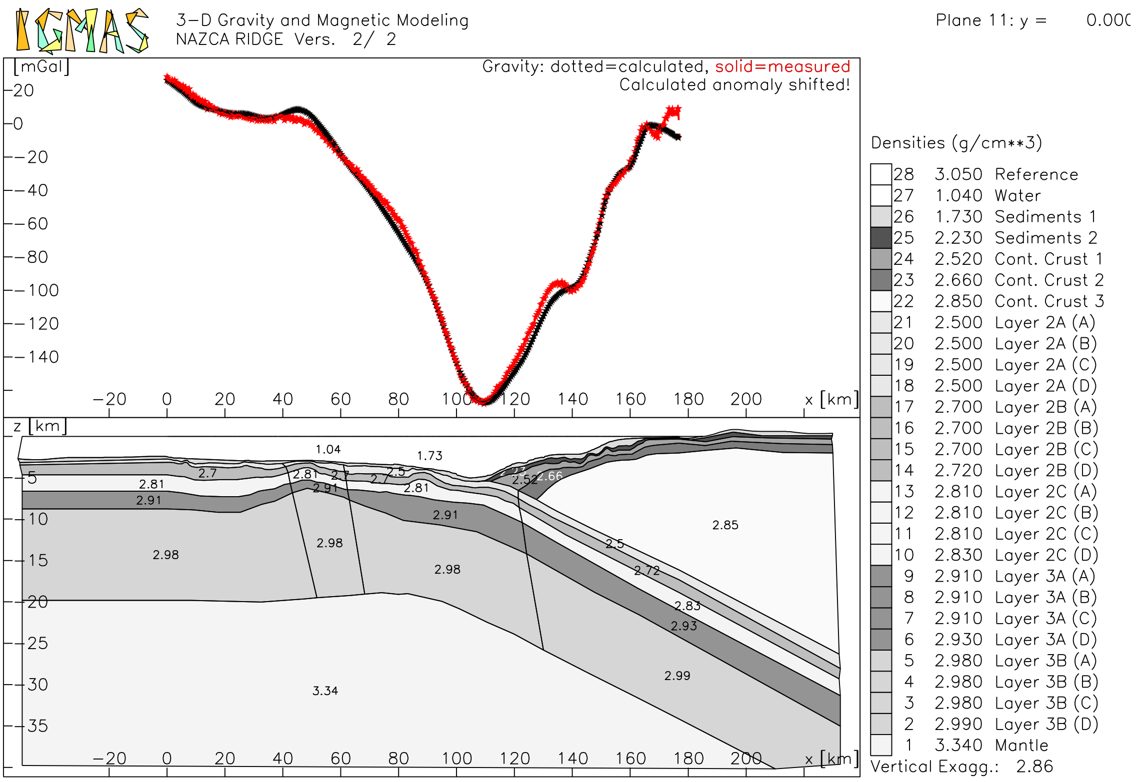

Figure 129: Nazca Ridge - Gravity Modelling - Plane 11

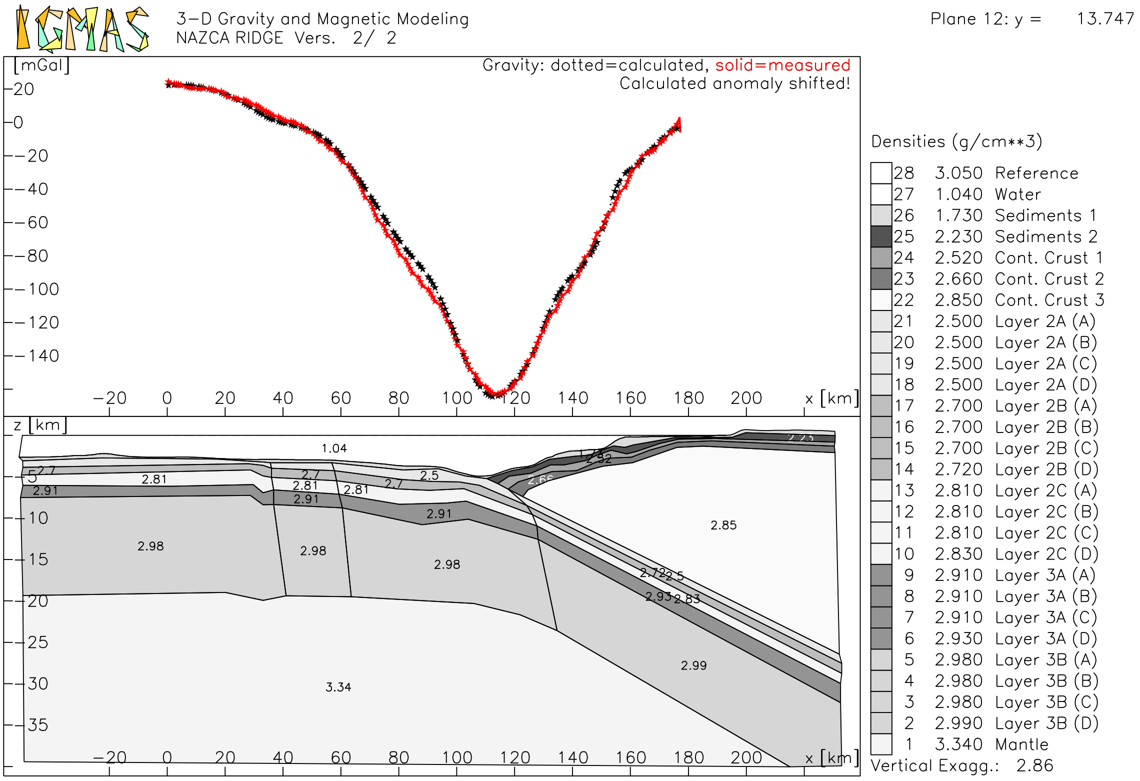

Figure 130: Nazca Ridge - Gravity Modelling - Plane 12

On plane 12 the oceanic crust is extremely thick with 16.5 km. The flanks of the minimum connected to the Peru Trench are very steep. The layers of the continental margin feature minor undulations.

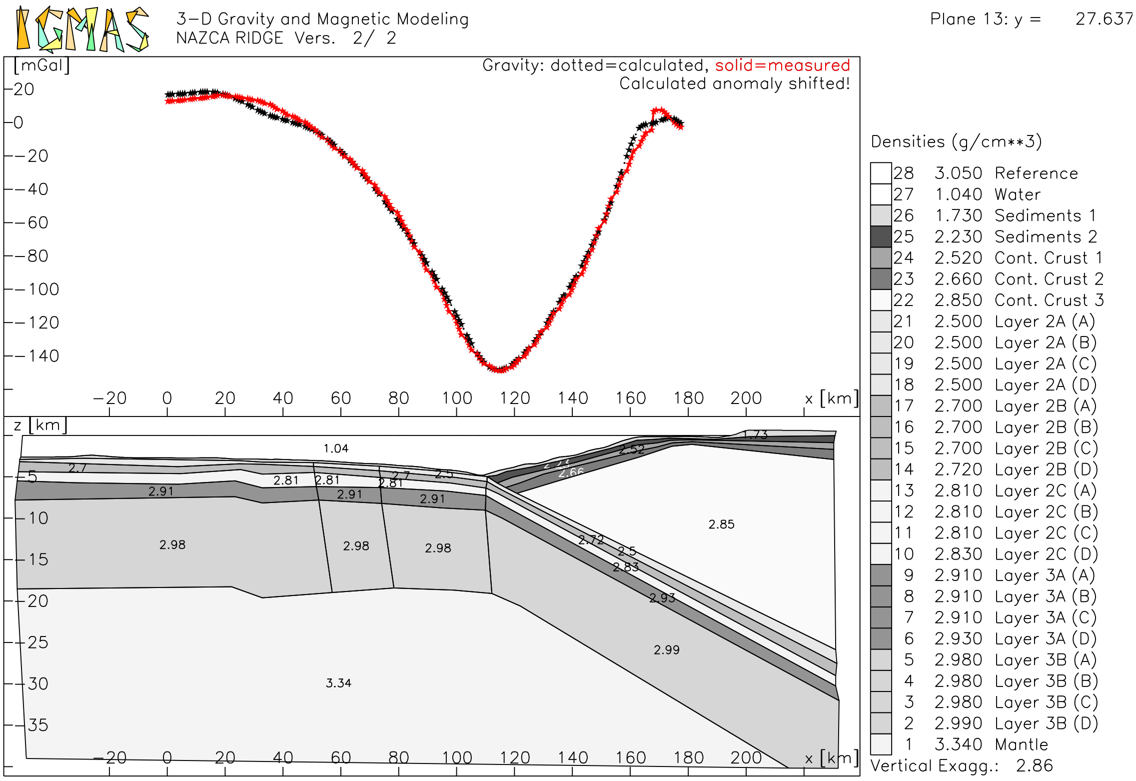

Figure 131: Nazca Ridge - Gravity Modelling - Plane 13

At kilometre 30 of plane 13 the oceanic layer thickness is constrained by the seismic velocity model of profile P1 (see Figure 131). The observed gravity values would rather require a thinner oceanic crust or, alternatively, higher density values. Otherwise this plane does not show any distinctive features. The free-air gravity curve, as well as the layers of the oceanic and continental crust are very undisturbed.

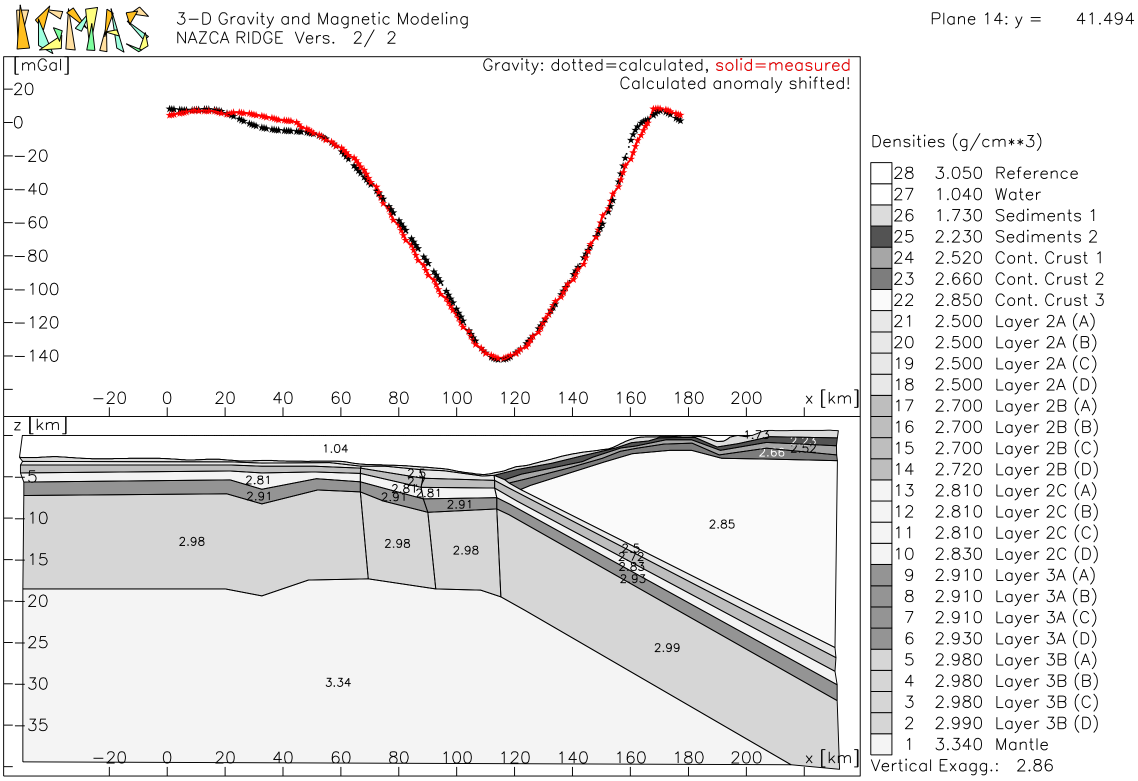

Figure 132: Nazca Ridge - Gravity Modelling - Plane 14

On the northernmost plane 14 the oceanic crust is 15 km thick (see Figure 132). The crustal thickness of 16 km at kilometre 30, defined by the crossing seismic profile P1, does not satisfy the observed free-air gravity.

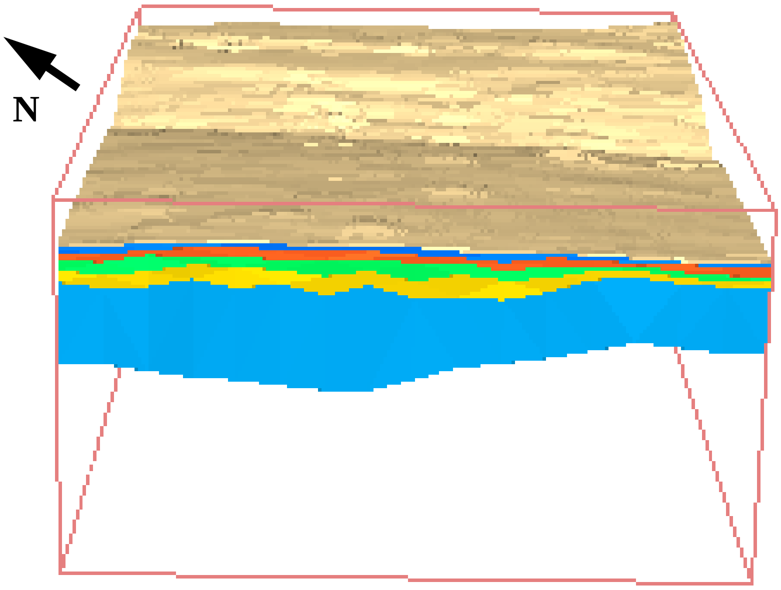

Figure 133: The thickened oceanic crust of the Nazca Ridge

In Figure 133 a three-dimensional view of the model is plotted. Displayed are the layers of the oceanic crust including layer sediments 1 which covers the continental margin as well. The submarine basement high is clearly envisioned in the model. The gravity anomalies support the conclusion from refraction seismics that the Nazca Ridge possesses an asymmetric crustal structure. On the northern side of the model the crust is 15.5 km thick, underneath the Nazca Ridge nearly 18 km and on the southern side 12.5 km. In the whole research area the crust is thicker than typical oceanic crust. In Figures 133 and 134 the thickened oceanic crust of the Nazca Ridge is clearly visible. The buoyant effect of the Nazca Ridge is indicated.

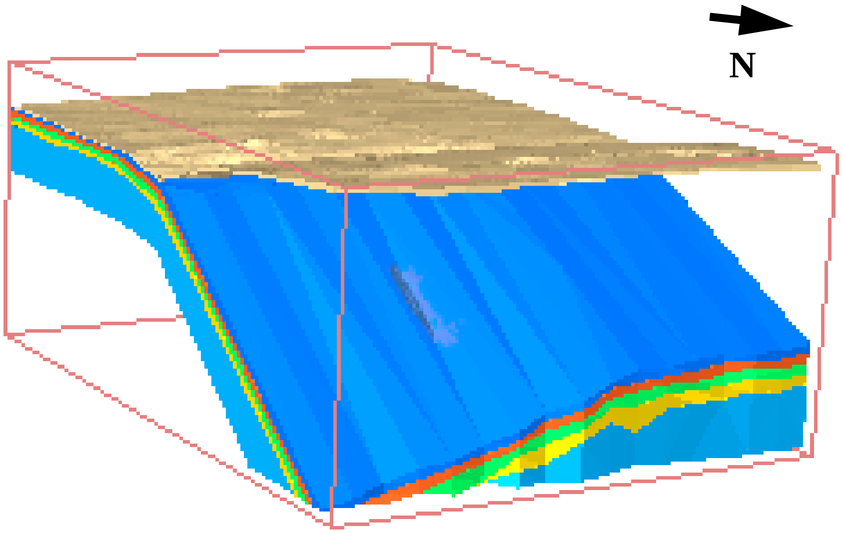

Figure 134: The subducting Nazca Ridge

7.7.2 Magnetic Modelling in the Nazca Ridge Area

The Nazca Ridge shows strong magnetic anomalies which enable a regional and temporal examination of the creation of the Nazca Ridge. Figures 135 to 146 show the vertical planes of the magnetic model with the respective observed and calculated magnetic data. Again the oceanic layers are subdivided into different sections to allow magnetic modelling. The four blocks with different magnetic properties are illustrated in Figure 135. As no influence of the magnetic oceanic crust can be determined after the crust has subducted for 30 km, the eastern block is extended to the eastern bound of the model.

Block A represents the magnetic lineation 19, block C represents anomaly 20. These blocks are magnetised in the direction of the present magnetic field. Blocks B and D define the reversely magnetised oceanic crust and possess higher susceptibilities.

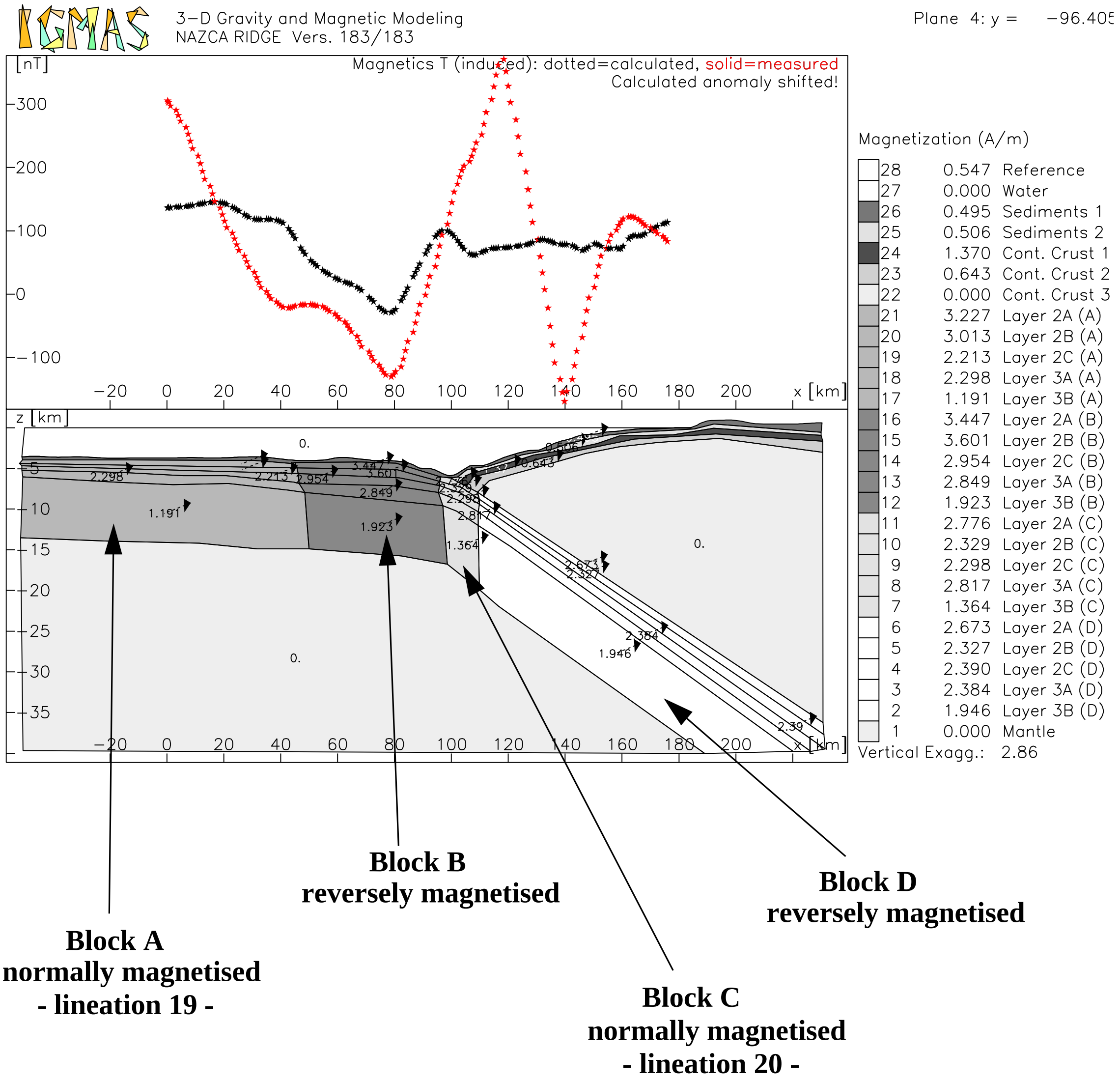

Figure 135: Nazca Ridge - Magnetic Modelling - Plane 4

For magnetic modelling the following parameters are applied. The magnetic north direction is defined as 39.415°. The total magnetic field is determined by the reference value 25614 nT. The inclination angle is -6.35°, the declination angle is 1.9167°. For the Nazca Ridge model the calculation of the remanent magnetisation is easier as the ridge originated from the fixed Easter Island hotspot. For the remanent magnetisation an inclination angle of -35.9167° and a declination angle of 15.467° are determined. For the model blocks with reverse magnetisation an inclination value of 54.033° and a declination value of 10.267° is used. The Königsberg ratio is determined to be less than 1 for all magnetic layers. For the magnetic model a standard deviation of 70.56 and a correlation coefficient of 0.50 is achieved.

The layer continental crust 1 shows a remarkable high magnetisation. The best fit between observed and calculated anomalies is achieved with the main continental block, i.e. continental crust 3, being non-magnetic.

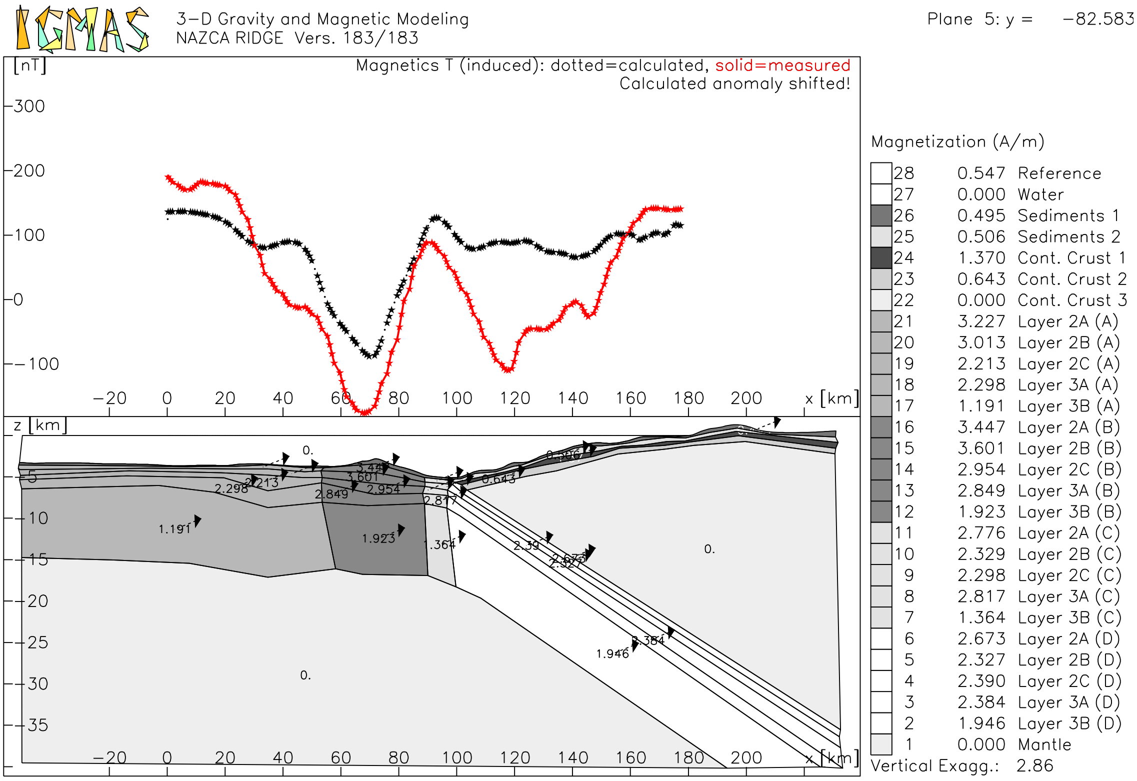

Figure 136: Nazca Ridge - Magnetic Modelling - Plane 5

On planes 5 and 6 the trend of the magnetic anomalies can be modelled satisfactorily. The prominent minimum and the landwards following maximum are approximated. On these southern planes block C is very narrow.

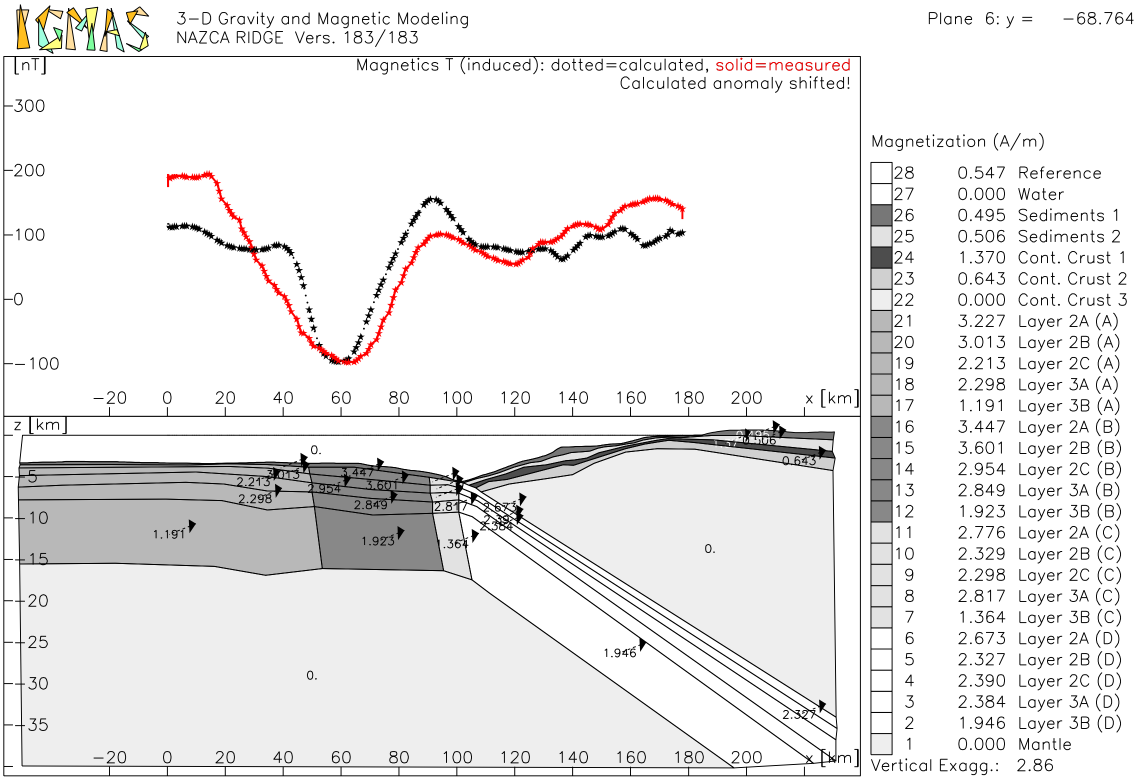

Figure 137: Nazca Ridge - Magnetic Modelling - Plane 6

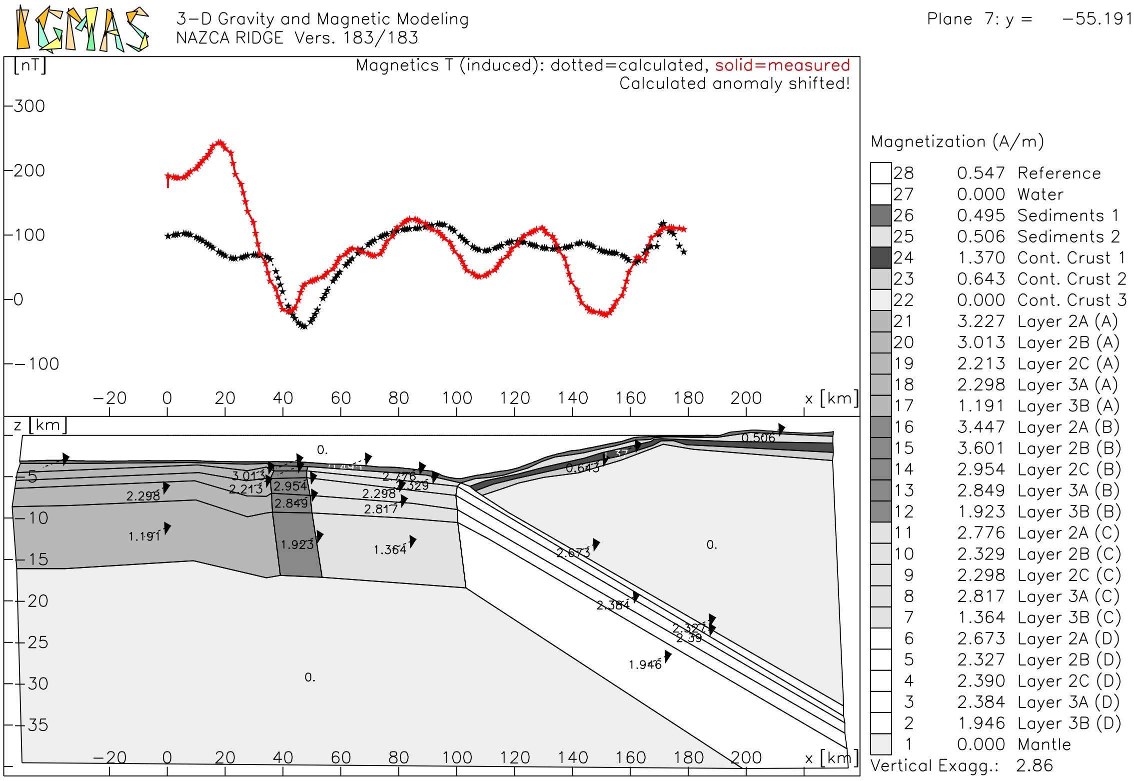

Figure 138: Nazca Ridge - Magnetic Modelling - Plane 7

The minimum above the oceanic crust, centred at kilometre 50, is observable in many planes in a row. The maximum located seaward of the minimum on plane 7 and situated landwards on plane 8 can be reproduced with a lower amplitude. The minimum connected with the continental slope at kilometre 130 cannot be reproduced.

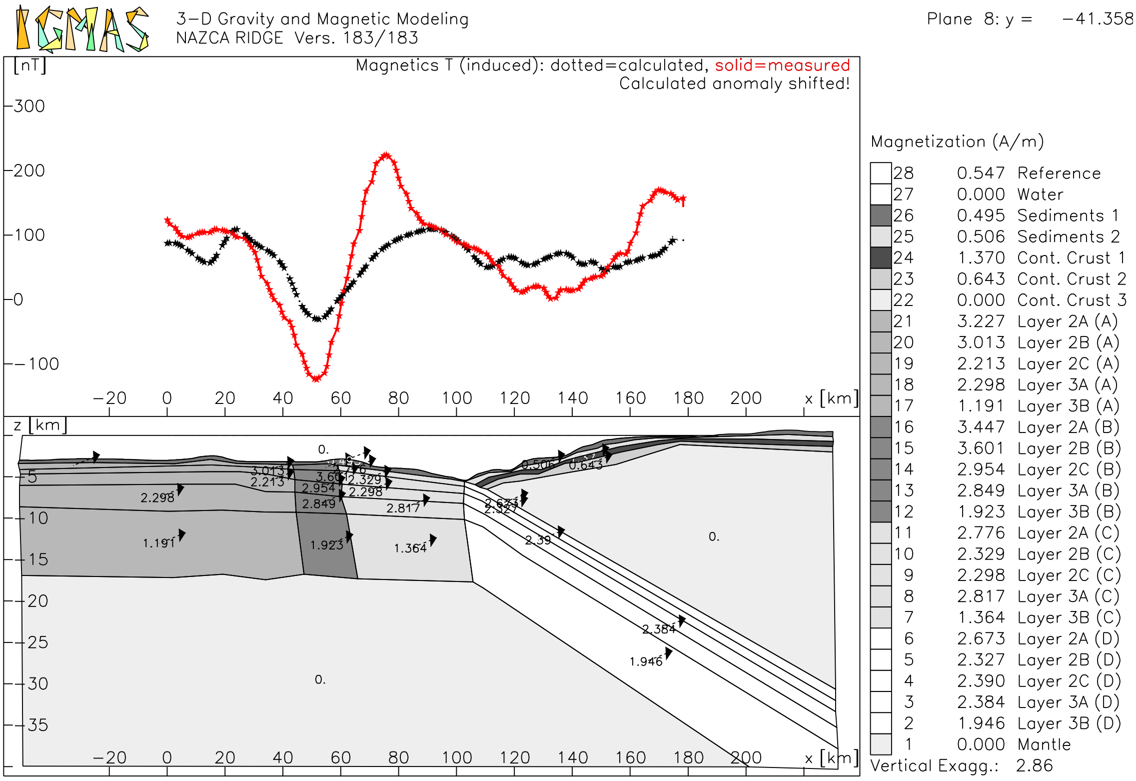

Figure 139: Nazca Ridge - Magnetic Modelling - Plane 8

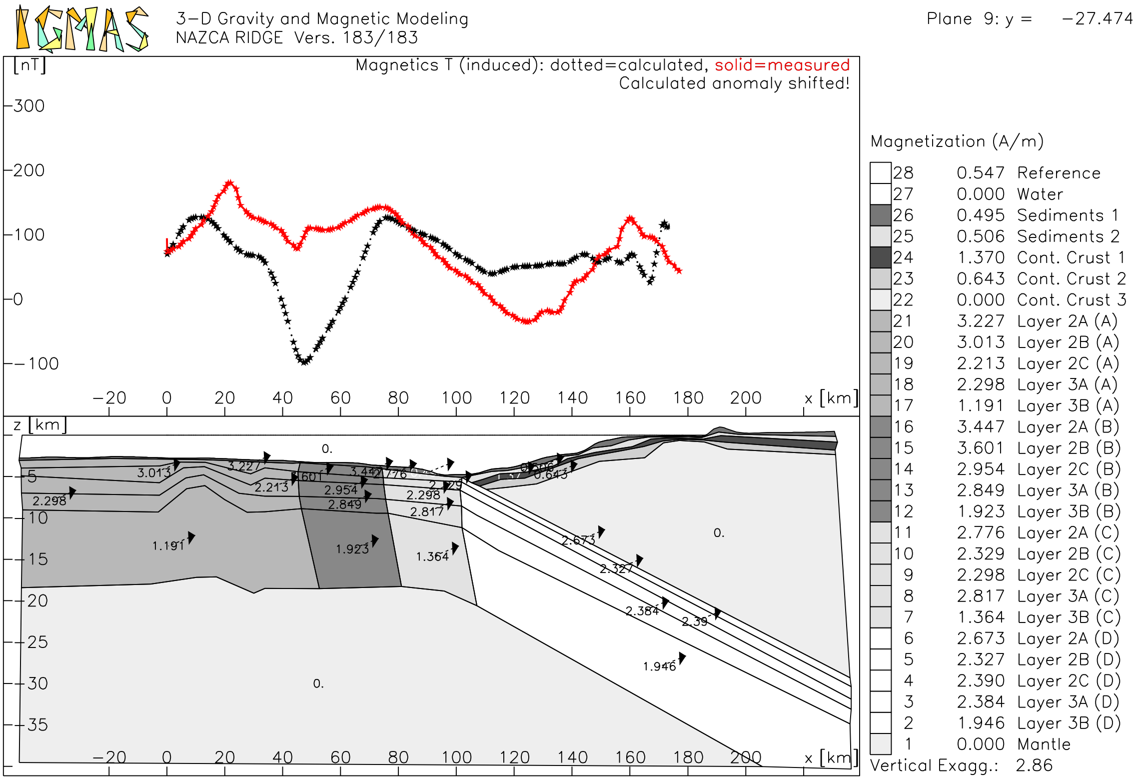

Figure 140: Nazca Ridge - Magnetic Modelling - Plane 9

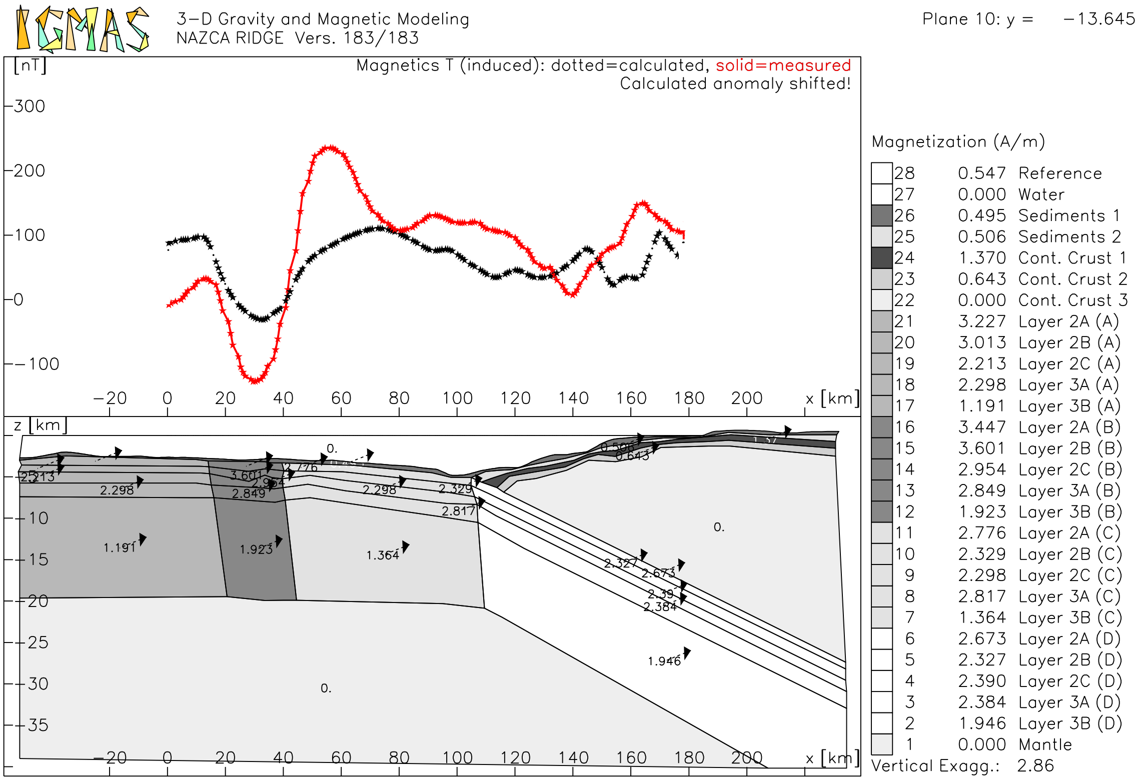

Figure 141: Nazca Ridge - Magnetic Modelling - Plane 10

On plane 10 the magnetic minimum centred at kilometre 30 is reproduced by the model.

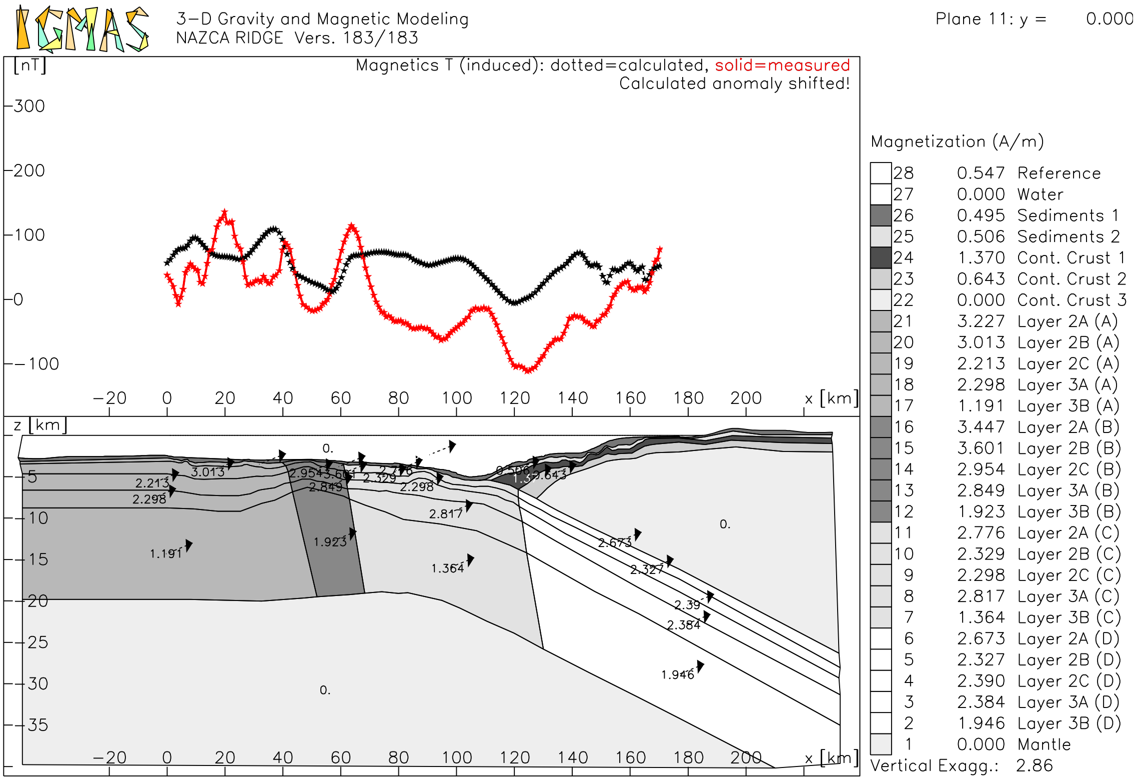

Figure 142: Nazca Ridge - Magnetic Modelling - Plane 11

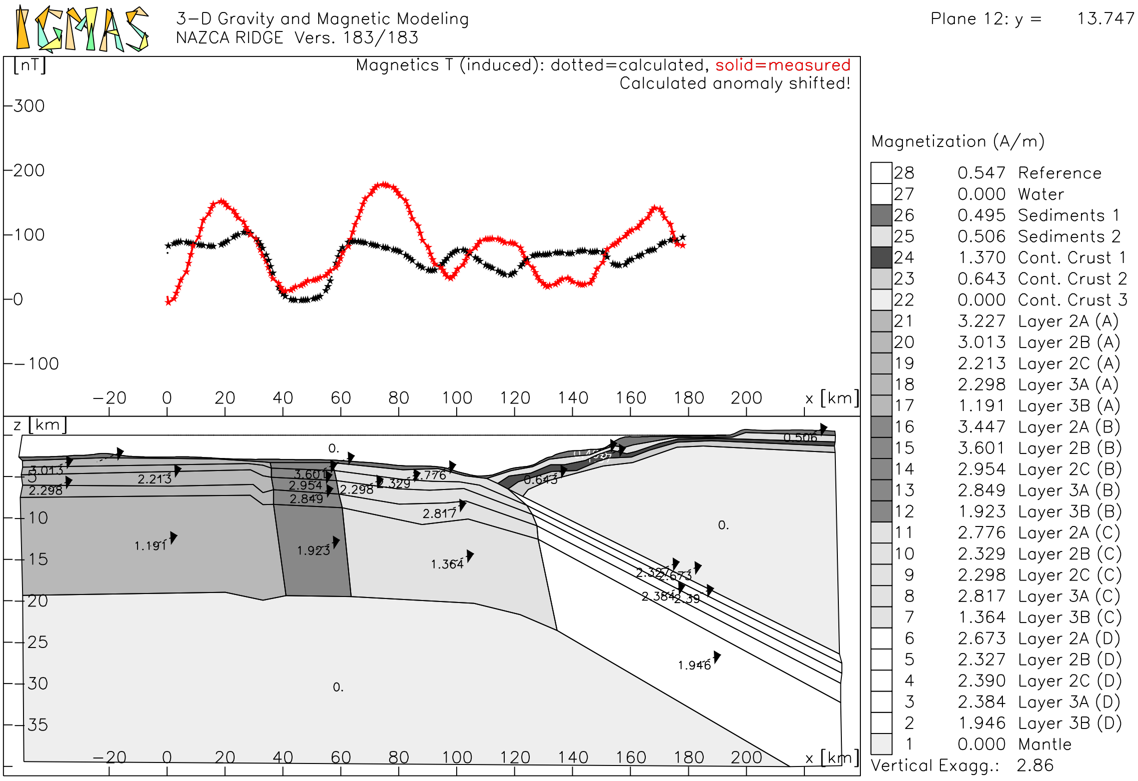

Figure 143: Nazca Ridge - Magnetic Modelling - Plane 12

The general trend is reproduced on plane 12. Only near kilometre 100 the observed and the modelled anomalies are phase-shifted.

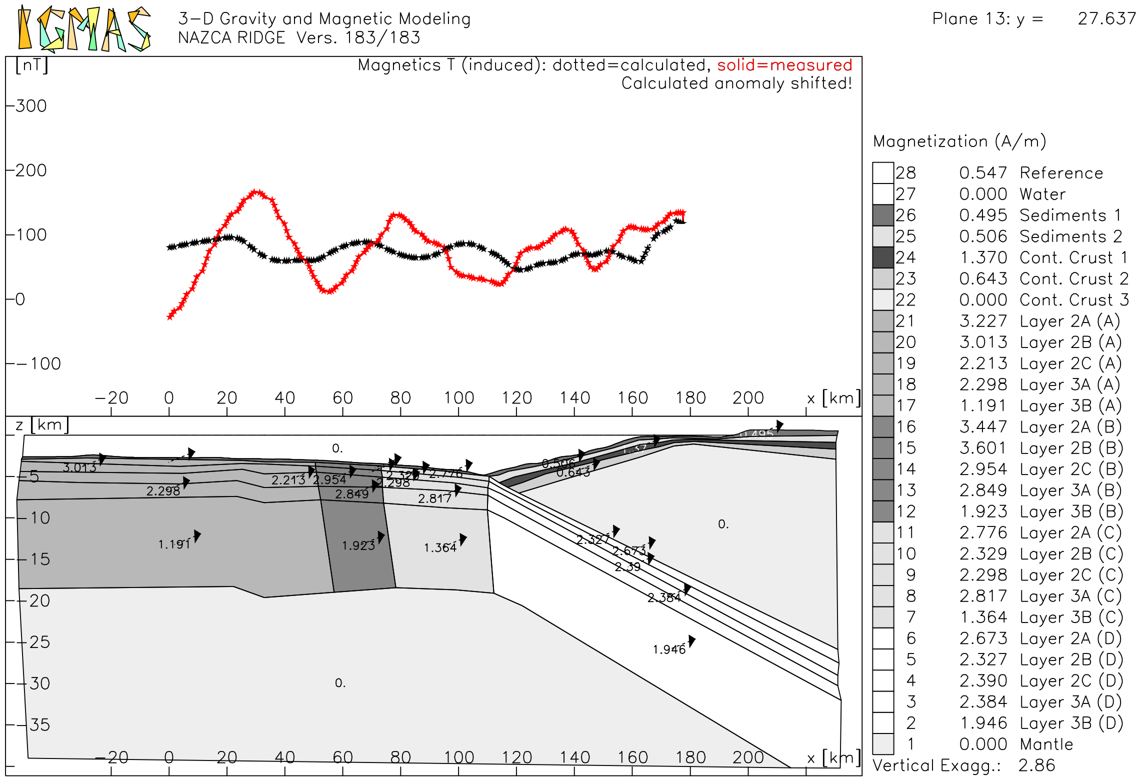

Figure 144: Nazca Ridge - Magnetic Modelling - Plane 13

Plane 13 features the worst alignment of the magnetic Nazca Ridge model. The oceanic crust is thickened at kilometre 30 in plane 13. This thickening is constrained by the seismic velocity model of the perpendicular profile P1.

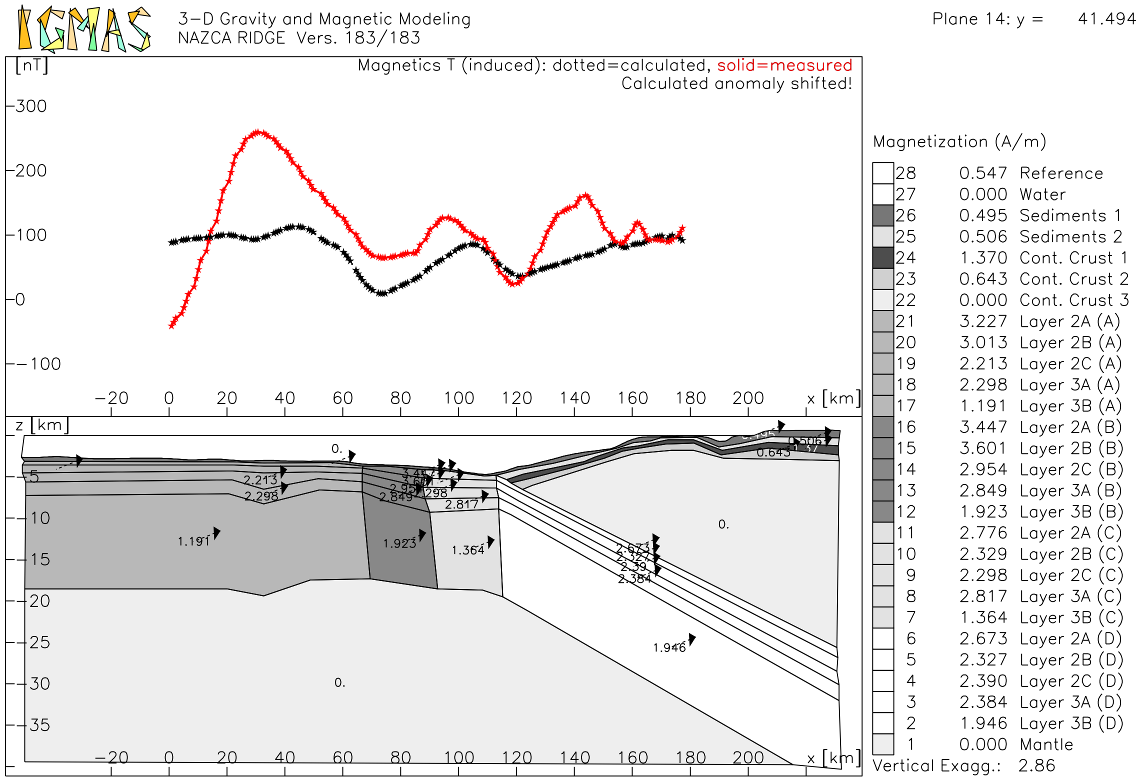

Figure 145: Nazca Ridge - Magnetic Modelling - Plane 14

Plane 14 shows a remarkably good concordance between observed and calculated magnetic anomalies.

Figure 146 shows the Königsberg ratios applied in the Nazca Ridge model. The relation between induced and remanent magnetisation is very small. Blocks B and C show a Königsberg ratio of 0.1 in all layers. In block A the layers 2C, 3A and 3B possess a Königsberg ratio of 0.1 and in block D layer 3B exhibits the highest ratio of 0.3.

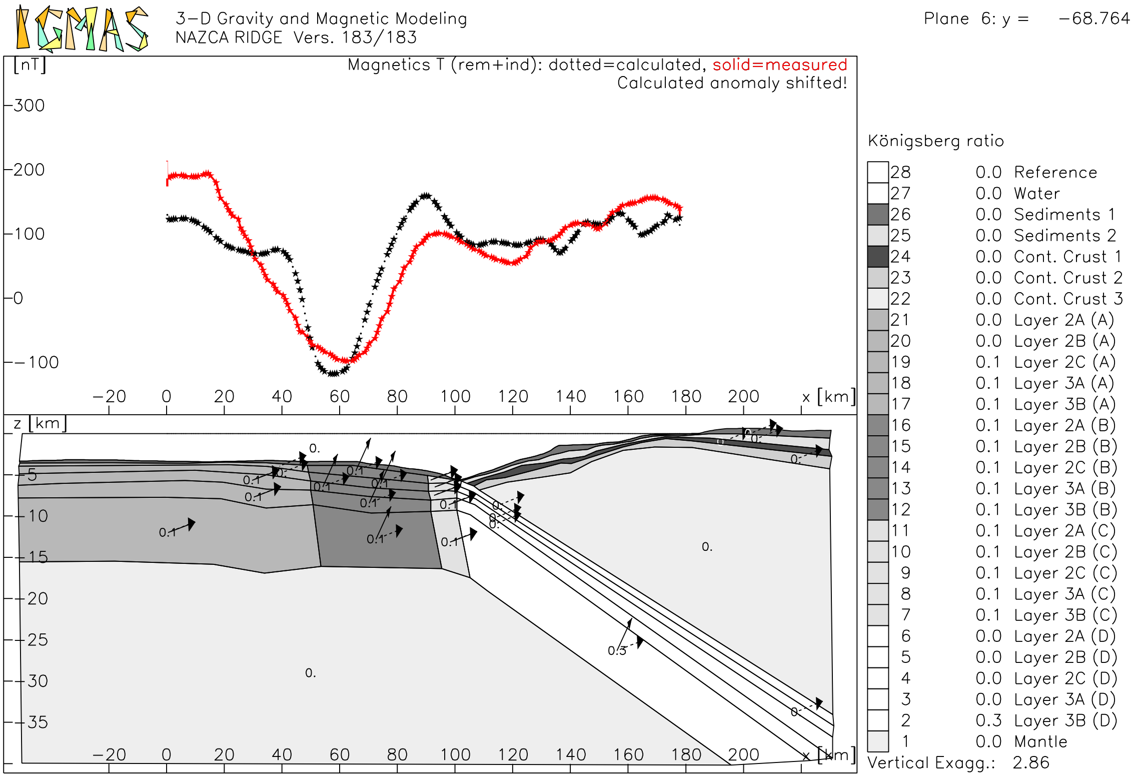

Figure 146: The relation between induced and remanent magnetisation values

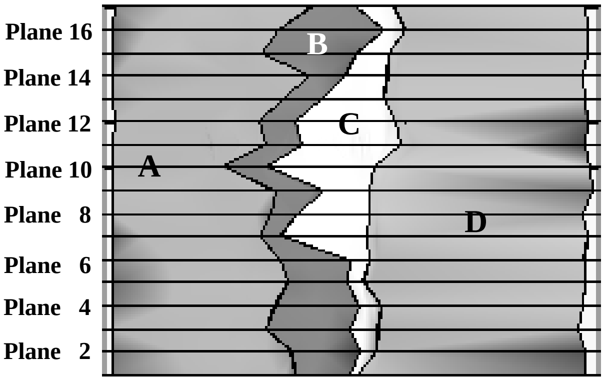

Figure 147: The differently magnetised blocks of the oceanic crust

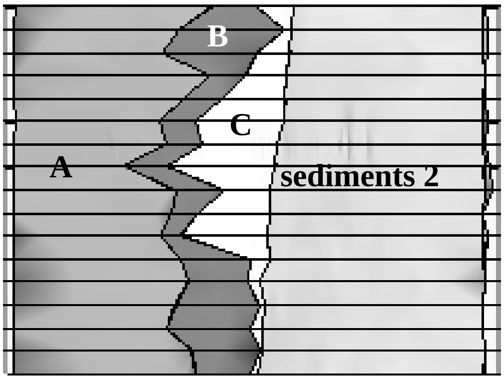

Figure 148: The differently magnetised blocks of the oceanic crust, partially covered by the layer sediments 2

In Figures 147 and 148 a top view of the magnetic model is shown. Block C gets wider in the middle part of the model. Block D has already started subduction in all the vertical planes. In Figure 148 this block is completely covered by the layer sediments 2. The magnetic lineations 19 and 20 cannot be reproduced in magnetic modelling. The identification of these anomalies has already been difficult in the illustration of the magnetic anomalies along the ships' tracks (Figure 38) and along the different planes of the three-dimensional model (Figure 39). The results of three-dimensional modelling underline the impression that three lines of anomalies, which do not coincide with the magnetic lineations, run throughout the Nazca Ridge Area.

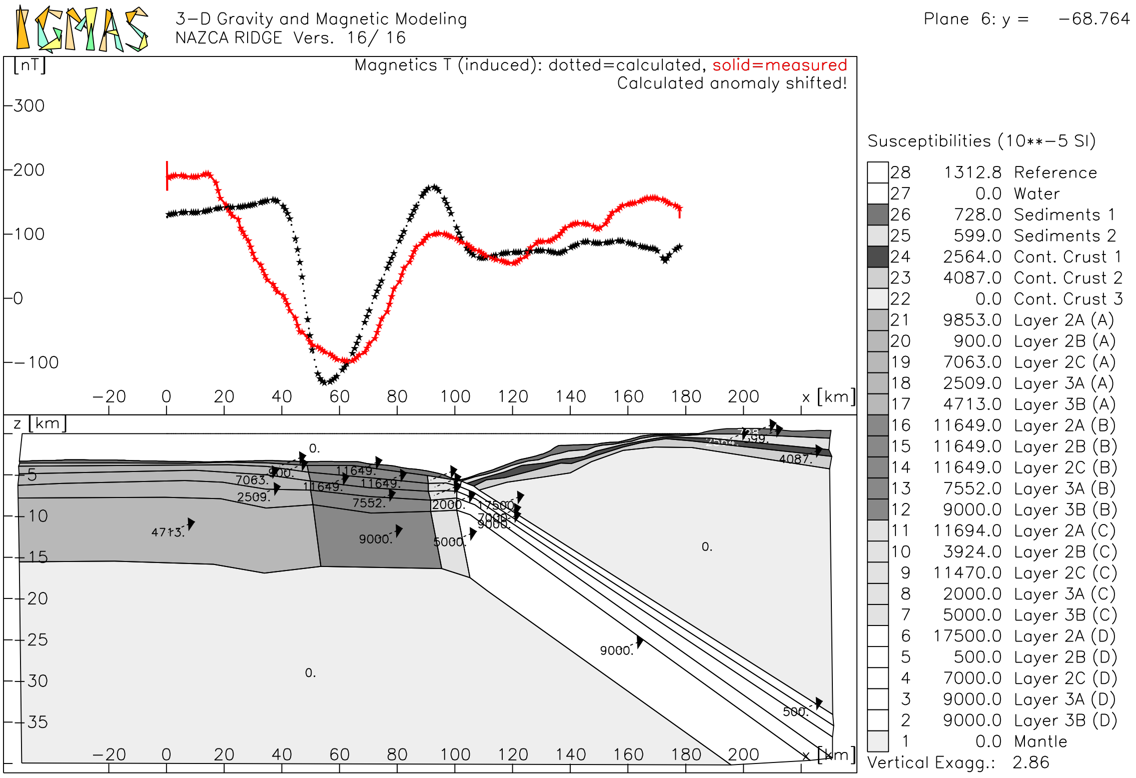

Figure 149: The modelled susceptibilities in the Nazca Ridge Area

Figure 149 shows the magnetic susceptibilities appointed to the different magnetic bodies. The modelled susceptibilities lie in the range of the typical values (see Table 3, p. 68). A remarkable similarity in shape and amplitude of the anomalies can be observed.

8 Results and Discussion

The aim of the model calculations is to get a principal understanding of the crustal structures and the subduction processes. An objective is to recognize the geological structures which are causing the gravity and magnetic anomalies. Significant contrasts in densities and susceptibilities determine the characteristics of the observable anomalies. The age of the oceanic plate, its temperature, dip angle and rock composition vary along the Peruvian margin and cause different tectonic features.

Since potential field modelling is non-unique, the applied densities, magnetisations, magnetic susceptibilities, Königsberg ratios and model geometries can be viewed only as a guide to the general crustal structure of the region. Caution has always been taken that the models are consistent with the available data sets from the different geophysical and geological investigations. Furthermore, attention has been paid that the three different gravity and magnetic models do not contradict each other.

The discrepancies between the measured and the modelled anomalies may be explained by the non-uniqueness of the techniques and, partially, by a lack of sufficient constraints. In the case of magnetic modelling the remanent magnetisation is difficult to determine. The magnetic models are by far less definite than the gravity models.

Modelling of the gravity and magnetic fields is an iterative process. Three-dimensional forward modelling of the potential fields is combined with inversion techniques. The three-dimensional gravity and magnetic models are based on wide-angle seismic velocity models. The seismic velocities are converted to densities by applying the appropriate velocity-density relations. The relation of Carlson & Raskin (1984) is adopted for the crystalline layers of the oceanic crust; the relation of Nafe & Drake (1957) is employed for both layers of the oceanic and the continental margin (see tables in the Appendix). The relation of Birch (1960, 1961) proved to render unduly low densities for the, most probably, metamorphic rocks of the continental margin.

8.1 Gravity Interpretation

The resolution of the gravity fields is dependent on the proximity of the ships' tracks. The data density is especially high in the areas of three-dimensional modelling. A comparative analysis of topography, free-air and Bouguer anomalies, as well as residual free-air and Bouguer anomalies proves that the subduction zone exerts a strong influence on the gravity fields. In three-dimensional modelling the gravity anomalies with wavelengths of about 10 km are interpreted on each plane. The resolution of the models in the y-direction is determined by the distances of the vertical planes, i.e. 21.5 km for the Yaquina Area model, 19.5 km for the Lima Area model and 13.8 km for the Nazca Ridge model.

The isostatic compensation in the region of the continent to ocean transition is not yet understood. The isostatic status of the crust is modelled depending on erosion and the calculated isostatic anomalies. Along most planes of the three-dimensional models the free-air gravity field is strongly positive. These positive anomalies are an expression of a mass surplus in the compressional region of the continental margin.

The rheological characteristics and the flexural rigidity of the upper and the lower plate influence the shape and dynamics of the Peruvian margin. By studying the gravity anomalies it is possible to gain information on the rheology of the continental and oceanic lithosphere.

The modelling of gravity anomalies is a powerful means of studying an accretionary complex. Furthermore the extent of uplift along the continental margin, caused by compressional stress, is modelled. The interaction of subduction and erosional processes is described. The gravity models provide a good estimate of how much sediment is located on the continental margin. The low-density sediments and the high-density crystalline rocks of the continental block produce a strong density contrast.

Discrepancies between the observed and the calculated anomalies may be explained by an erroneous topography. Especially free-air gravity modelling is very sensitive to topography and the 0.5’ by 0.5’ bathymetric grid may include errors. A comparison of the shipboard measured data with the satellite data shows that in the region of the continental slope errors of up to 280 m may occur. In a water depth of 4000 m this discrepancy causes a gravity deviation of about 2 mGal in three-dimensional free-air gravity modelling. Accordingly the model accuracy is higher along the planes which coincide with the wide-angle seismic profiles P2, P4 and P5, because here the shipboard measured bathymetric data is employed. On the other planes the use of the satellite data is preferable to the usage of the bathymetric grid produced with the arbitrarily spaced shipboard data. As the data coverage is not sufficient in the entire study areas the resulting errors in the calculated gravity and magnetic fields would vary remarkably. A regional interpretation would no longer be sensible.

A comparison of the shipboard gravity measurements with the satellite data secures, although the satellite gravity data possess a considerably lower resolution than the shipboard data, that the data compiled from different surveys are compatible.

The three-dimensional forward and backward modelling is carried out with the help of the program IGMAS (Götze et al., 2000). Unfortunately it is not possible to integrate vertical or lateral gradients with this modelling program. In gravity modelling especially vertical gradients should be considered in the layered oceanic crust. The seismic model shows that clear boundaries can only be an approximation. All the seismic velocity models include vertical velocity gradients. The model for profile P6, located in the Lima Area, even consists entirely of velocity gradients. No separating layer boundaries are specified. Lateral gradients are also to be expected in a subduction zone where the compressional stresses increase with decreasing distance to the collision front and where conditions within the oceanic plate change during subduction. In the three research areas this gradient is approximated by a subdivision into blocks possessing increasing densities. This subdivision is only a very rough approximation.

8.1.1 Gravity Interpretation in the Yaquina Area

In the Yaquina Area gravity modelling is very successful. The observed anomalies can be reproduced with realistic densities and layer geometries. A special characteristic of the free-air gravity field is that the continental margin exhibits strong negative anomalies on planes 3 to 6 (Figures 46 to 49). The continental crust features positive free-air anomalies on planes 7 to 16 (Figures 50 to 59). A striking maximum of almost +70 mGal is observed above the continental margin of plane 11 (Figure 54). On planes 17 and 18 (Figures 60 and 61) the imaged anomalies reach gravity values of 0 mGal and on the northernmost planes 19 to 21 (Figures 62 to 64) a gravity minimum follows the relative maximum of 0 mGal further landwards. Planes 18 to 21 (Figures 61 to 64) exhibit a step in the rising gravity values above the continental margin.

In the Yaquina Area model the oceanic crust features various undulations. The strongest undulations of the oceanic crust are modelled on planes 4 to 10 (Figures 47 to 53). Somewhat smaller undulations are seen on planes 12 to 16 (Figures 55 to 59). The remaining planes show a relatively undisturbed oceanic crust. In unperturbed areas the oceanic crust is between 6 and 7 km thick. On the southernmost plane 3 (Figure 46) the oceanic crust is, on average, only 5 km thick.

The density of the gabbro layer increases slightly from 2.97 to 2.98 g/cm^3 when starting subduction. The sheeted dykes increase in density from 2.88 to 2.90 g/cm^3. The pillow lavas change in density from 2.60 to 2.62 g/cm^3. The increasing densities may be explained by compaction of the pore spaces due to the strong compressional forces. In greater depth the higher densities in the subducting slab may be explained by metamorphism (Kirchner, 1997).

The seaward block of the continental crust is thought to be fractured by the subduction process. Consequently its density is lower. The size of the seaward block of the continental margin is comparable in the whole Yaquina Area model.

On almost all the planes of the Yaquina Area model an accretionary prism is imaged. On the southern planes 3 and 4 (Figures 46 and 47) the accretionary prism is located quite far up the continental slope. Not only the low-density upper layer sediments 1 is welled upwards but also the denser layer sediments 2. If this feature consisted only of sediments 1 it would probably slump into the trench quite soon. The accretionary prism is located at such an exposed location on the continental slope that it has to be subject to massive erosion. On the following planes to the north the accretionary prism is located further towards the trench. Here, the layer sediments 1 forms the major part of the prism. On plane 19 (Figure 62) the slope is very steep and a noticeable thickening of the uppermost layer is observed only at a considerable height. On plane 21 (Figure 64) the accretionary prism is located immediately landwards of the trench again.

The gravity model points at certain areas along the continental margin, e.g. on plane 11 (Figure 54), where high-density rocks reach up to the sea floor. These results are indicative for the selection of sampling sites.

When considering the changes of the continental slope, surficial and basal erosion of the upper plate as well as underplating along the plate boundary have to be considered.

A further improvement in fit is achieved for plane 16 (Figure 59), corresponding to the seismic profile P4 in the Yaquina Area model. Very slight changes in the layer boundaries have a considerable effect. The modifications always have to be seismically acceptable. As the seismic velocity models include vertical velocity gradients minor changes in layer boundaries can locally be justifiable.

8.1.2 Gravity Interpretation in the Lima Area

The Lima Area shows a remarkable gravity signature above the continental margin. The gravity values rise very slowly and show distinguished local extrema.

On almost all the planes a second, smaller minimum is located directly above the continental margin. Three-dimensional modelling has shown that this minimum is caused by a depression in the layer continental crust 3. Layer continental crust 2, located seaward of layer continental crust 3 thickens away from the trench, then thins, and thickens again further landward. The gravity values rise until the thinnest part of continental crust 2 is reached and decrease to a local minimum further landward where continental crust 2 becomes thicker again. In the transition zone between the easternmost part of layer continental crust 2 and layer continental crust 3 the free-air gravity values rise steeply. This behaviour is observed on planes 14 to 17 (Figures 100 to 103). Where continental crust 2 does not show a second thickening, but thins slowly and continuously, the free-air gravity values feature an extended plateau. This feature is seen on plane 12 (Figure 98). The southernmost plane 4 (Figure 90) shows an exceptional relative maximum above the continental margin. Here the layer continental crust 2 has slowly graded into continental crust 3. The minimum located landwards of the local maximum is caused by a depression of the layers sediments 2, sediments 3 and continental crust 1.

In the Lima Area the oceanic crust shows a very uniform appearance. No outstanding variations of the crustal layers are necessary to satisfy the observed gravity field. On average the oceanic crust is 8 km thick. On planes 4 and 5 (Figures 90 and 91) the free-air gravity shows values of 0 mGal on the seaward side of the model. Planes 6 to 10 (Figures 92 to 96) feature positive gravity values of +10 mGal on the seaward side. Planes 11 to 14 (Figures 97 to 100) again show values of 0 mGal promoting an isostatic equilibrium. The northern planes 15 to 17 (Figures 101 to 103) show negative values of about -10 mGal. Except for plane 10 (Figure 96), all the planes feature an evenly decreasing gravity curve towards the Peru trench. On plane 10 the descent is halted by a small plateau in gravity, caused by a bathymetric high.

The layers of the oceanic crust increase in density when starting subduction. The density of the pillow lavas increases from 2.62 to 2.63 g/cm^3 and, still further downdip, to 2.64 g/cm^3. The sheeted dykes increase in density from 2.88 to 2.92 g/cm^3 and the density of the gabbros changes from 2.98 to 3.02 g/cm^3.

The layer of pillow basalts does not show a significant increase in density when starting subduction because subducted, low-density sediments have to be taken into account. Further downwards the density increases again when the large pore spaces in the subducted sediments are closed by the strong compressional forces. Underthrust sediments seem to be a characteristic of the South American margin as they have also been observed near the Mejillones Peninsula off Antofagasta in northern Chile (von Huene et al., 1999). The density changes in the subducting slab may result from mineral phase- transitions.

On almost all the planes of the Lima Area model an accretionary prism is visible. In order to satisfy the observed gravity values the uppermost layer sediments 1 is needed to bulge upwards. As the continental layers, possessing high densities, do not lie close to the seafloor just landwards of the Peru Trench, the gravity values rise rather slowly. The accretionary complex is about 20 km wide and consists mostly of the layer sediments 1. The denser sediments 2 form the lower part of the accretionary prism.

8.1.3 Gravity Interpretation in the Nazca Ridge Area

In the Nazca Ridge Area highly thickened oceanic crust is modelled. On the southern plane 5 (Figure 123) the oceanic crust is 12.5 km thick. The oceanic crust continuously thickens until it reaches its maximum thickness of almost 18 km on plane 11 (Figure 129). This plane describes the crestal part of the Nazca Ridge and coincides with the wide-angle seismic profile P2. Further northwards the oceanic crust thins again and on the northernmost plane 14 (Figure 132) it is 15.5 km thick. This is still considerably thicker than in the other research areas to the north. Plane 8 (Figure 126) is located at the same distance of 41.5 km away from plane 11 as plane 14. On plane 8 the oceanic crust is only 14.5 km thick and therefore the Nazca Ridge features a slight asymmetrical shape.

The Nazca Ridge produces positive free-air anomalies and consequently it is not isostatically compensated.

In the Nazca Ridge Area the minimum produced by the Peru Trench is especially narrow. This is certainly due to the uplift of the continental margin caused by the subducting, buoyant Nazca Ridge. The free-air anomalies around 0 mGal along the continental margin suggest an isostatic compensation of this region.

The free-air gravity over the continental slope rises very steeply and relatively uniformly in the whole research area. The continental margin can be modelled without a seaward wedge forming the tip of the main continental block. On most planes the layer continental crust 3 rises upwards until a certain point where the free-air gravity features a maximum and recedes slightly further landwards. On plane 9 (Figure 127) the continental crust 3 remains close to the surface for about 15 kilometres. On plane 11 (Figure 129) a small step in free-air gravity is modelled by secondary undulations of the continental layers, namely sediments 2, continental crust 1 and continental crust 2. A local minimum above the oceanic crust is modelled by an upwelling of the crustal layers.

On the landward side of planes 8 to 11 (Figures 126 to 129) the observed, especially high, free-air anomalies cannot be modelled by a mere upwelling of the continental layers. Here, the continental block probably contains an additional high-density body.

In the Nazca Ridge Area layer 2B increases in density from 2.7 to 2.72 g/cm^3 when starting subduction. The density of layer 2C increases from 2.81 to 2.83 g/cm^3. The density of layer 3A changes from 2.91 to 2.93 g/cm^3 and the density of layer 3B changes from 2.98 to 2.99 g/cm^3. The fact that layer 2A does not show an increased density may be explained by subducted sediments. The Nazca Ridge is eroding the continental margin and some of the eroded debris will slump into small local depressions on the Nazca Plate. These sediments will subduct together with the oceanic crust.

The subducted sediments may have important implications. They possess weak mechanical properties and can lubricate the fault. The presence of sediments involved in the subduction process may cause a slow rupture during an earthquake. Such a slow rupture is thought to be responsible for tsunami earthquakes (Satake & Tanioka, 1999).

One of the results from wide-angle seismic modelling is that no accretionary wedge has been produced in the area of the Nazca Ridge (Hampel at al., 2002a). Gravity modelling asserts this conclusion and produces an expanded image of the lower continental slope in the collision zone. In none of the planes a bulge of the upper sediment layers is modelled. The different layers of the continental margin rise very uniformly landwards. The uppermost sediment layer is very thin, indicating erosional processes. The relatively steep continental slope with high-density layers rather close to the sea floor explains the narrow minimum connected with the Peru Trench. The sediment cover on the oceanic crust is thin in the whole modelled area.

The gravity effects computed for the given seismic models show a general good agreement. Only small local deviations occur. A significant improvement in fit can be achieved by minor changes in the layer boundaries.

The density values and the source depths of the anomalies are constrained by sensible geological considerations. Density alone does not identify the petrology of the rocks but the modelled densities correspond to rocks drilled in typical oceanic crust as well as to sediments and metamorphic rocks recovered from the continental margin.

Table 6 gives an overview of the applied densities in relation to the seismic velocities in the different three-dimensional models. The same mantle densities are employed in all three models. This is in accordance with the measured seismic velocities. The uppermost layer sediments 1 is increasing in density from the southern Nazca Ridge Area to the northern Yaquina Area. The range of seismic velocities appointed to this layer is the same in the Lima Area and in the Yaquina Area. Accordingly the densities differ only marginally. As the seismic velocity is noticeably lower in the Nazca Ridge Area, the density is clearly lower as well.

In the Lima Area the density contrast between the main continental block, i.e. continental crust 3, and the seaward wedge, namely continental crust 2, is higher than in the Yaquina Area. This density contrast probably enables the complex intermingling of continental crust 2 and continental crust 3 in the Lima Area. As the densities of these two bodies are similar in the Yaquina Area they merge less strikingly.

	Yaquina Area		**Lima Area**		**Nazca Ridge Area**	
Layers	**p-wave velocity [km/s]**	**density [g/cm^3]**	**p-wave velocity [km/s]**	**density [g/cm^3]**	**p-wave velocity [km/s]**	**density [g/cm^3]**
Sediments 1	1.7-2.0	1.83	1.7-2.0	1.81	1.6-1.8	1.73
Sediments 2	2.0-2.3 2.8-3.7	2.27	2.0-2.7	2.04	2.0-2.5 2.5-3.0	2.23
Sediments 3	-	-	4.2-5.0 3.1-3.7	2.32	-	-
Continental Crust 1	4.5-5.0 3.3-4.0	2.56	5.0-5.7	2.55	5.15-4.88	2.52
Continental Crust 2	5.2-5.6	2.83	5.3-5.4	2.77	5.25-5.7	2.66
Continental Crust 3	5.5-6.2	2.85	5.5-6.0	2.90	6.0-6.6	2.85
Pillow Lava	4.7-6.0	2.60	4.7-6.0	2.62		
	6.1-6.5	2.62	6.3-6.5	2.64		
Layer 2A					3.5-5.0	2.50
Layer 2B					5.5-6.0	2.70-2.72
Sheeted Dykes	4.7-6.0	2.88	4.7-6.0	2.88		
	6.1-6.5	2.90	6.3-6.5	2.92		
Layer 2C					5.2-6.1	2.81-2.83
Gabbros	6.4-7.2	2.97	6.5-7.3	2.98		
	6.3-7.1	2.98	6.2-7.2	3.02		
Layer 3A					6.2-6.7	2.91-2.93
Layer 3B					6.5-7.8	2.98-2.99
Mantle	7.9-8.1	3.34	7.9-8.1	3.34	7.9-8.1	3.34

Table 6: Comparison of the different velocities and associated densities applied in the three models. The seismic velocities were determined by Broser (2002, pers. commun.) and Hampel (2002, pers. commun.)

According to Hampel (2002) the Nazca Ridge was not subducted north of 11°S and consequently the most of the Yaquina Area was not effected by the subducting Nazca Ridge. The influence of the subducting, southward moving Nazca Ridge on the continental margin is extremely strong and leaves the seaward part of the continental crust fractured. This explains why the seaward wedge is less dense, i.e. more fractured in the Lima Area. It was fractured by the impact of the subducting Nazca Ridge. Although most parts of the Yaquina Area were not influenced by the subducting Nazca Ridge a low-density seaward wedge of the continental margin is modelled. Here, the erosional forces related to the subduction process must have been remarkably strong. As the layer continental crust 2 of the Nazca Ridge Area runs more or less subparallel to continental crust 1 it is not comparable to continental crust 2 of the other research areas. The main continental block possesses the same densities in all three models.

The layers pillow lava, sheeted dykes and gabbros are very similar in the Yaquina Area and in the Lima Area. In the Nazca Ridge Area the layers sheeted dykes and gabbros of the thickened oceanic crust are notably lower. This adds to the buoyancy of the Nazca Ridge.

A more detailed comparison of the seismic velocities and densities of the different three-dimensional models is provided in the appendix.

The three-dimensional models are constructed using all available seismic data. The differences between observed and modelled gravity anomalies never exceed 17 mGal. On plane 11 of the Nazca Ridge Area (Figure 129), where this difference occurs, the layer geometry is constrained by the seismic velocity model of profile P2 (Hampel et al., 2002a). Here, a better fit of the calculated gravity anomalies to the observed anomalies could be achieved if the denser layers of the continental crust were located closer to the sea floor. A discrepancy of more than 5 mGal is reached only in very few and very limited areas.

8.2 Magnetic Interpretation

Magnetic modelling proved to be very time consuming. The achieved conformity between calculated and observed values is not altogether satisfying. However, it demonstrates the complexity of three-dimensional magnetic modelling. The results gained from the magnetic investigation certainly allow only qualitative and regional statements.

Up to now three-dimensional magnetic modelling has been attempted only very rarely. It is well known that three-dimensional magnetic modelling is remarkably more difficult than three-dimensional gravity modelling. In a complex environment, e.g. a subduction zone, the observable magnetic anomalies are produced by three-dimensional structures and consequently magnetic modelling, like gravity modelling, is only reasonable in three dimensions. As magnetic modelling is similarly difficult in all three research areas this difficulty cannot be attributed to a local situation.

The magnetisations and the magnetic field structures are changing along the Peruvian margin and within each three-dimensional model. During forward modelling the results from other magnetic investigations, from borehole measurements and from the investigation of ophiolites, are taken into account.

The magnetic structures of both the overlying continental and the underlying oceanic plate are investigated in three-dimensional modelling, but the main objective is to model the anomalies of the oceanic crust. The magnetic anomalies of the oceanic crust are, by great parts, identical with magnetic lineations, i.e. they are due to the process of seafloor spreading.

The observed magnetic anomalies are determined by the geometry and the varying magnetisations of the source layers. The discrepancies between the observed and the modelled anomalies may be attributed to a whole range of possible error sources. It is most probable that not all the diurnal variations of the geomagnetic field have been eliminated. The very short-wavelength anomalies may be caused by diurnal variations during the acquisition campaign and by intensity changes of the paleo-magnetic field. The errors at crossing points do not show an ideal Gaussian distribution. After filtering with an average weighted filter the magnetic anomalies appear to be generally very smooth.

High-frequency variations of the magnetic anomalies are observed along the continental margin. This is certainly due to the complexities of the upper crustal layers. The reason for these variations are changes in layer thickness, geochemistry and/or degree of alteration of the magnetic rocks.

According to Gee & Kent (1998) the variations in the magnetisation of comparable age basalts are, by great parts, caused by differences in geochemistry. These rocks can be interpreted as altered geochemically.

The shallow formations of pillow lava cause high-frequency anomalies. The pillow lavas are determined as the magnetic source layer of specific smaller anomalies. In magnetic modelling it is obvious that the sediment layer can be only very thin because the high-frequency anomalies are very sensitive to the position of the pillow basalts located beneath the sediments. Along the single vertical planes magnetic anomalies with a minimum wavelength of 20 km can be reproduced by the models. Along the y-direction the resolution of the calculated magnetic fields is constrained by the distance between the vertical planes.

An aim is to realize whether seafloor-spreading anomalies can be identified and used to determine the age of the oceanic lithosphere. Several magnetic anomalies can be identified with confidence (see Figure 31). The lineations 10, 11, 14, 15 and 16, which have not yet been interpreted in the studied region, are imaged. The magnetic lineations 9, 18, 19 and 20, which have been partly known before can be prolonged considerably (Figure 31). The location and orientation of these anomalies defines the convergence rate and the convergence direction of the Nazca Plate.

The lineations 13 to 18 in the southwestern part of the studied Peruvian margin are correlatable. They can be traced for a long way and run almost parallel to the Peruvian margin. The corresponding age of these magnetic anomalies is about 33 Ma for the southern seaward part of the studied Peruvian margin according to the geomagnetic polarity time scale by Cande & Kent (1995). Close to the South American continent, in the southern part of the studied region, the magnetic lineation 20 defines oceanic crust of about 43 Ma.

North of the Mendaña Fracture Zone the oceanic crust is about 25 Ma old on the seaward side of the considered region. Further landwards the magnetic lineation 11 denotes approximately 30 Ma old oceanic crust.

In several areas the magnetic anomalies lack obvious correlations. In addition to the seafloor-spreading anomalies remarkable magnetic anomalies can be observed on the Nazca Plate. The emplacement of lava flows may have obliterated or, at least, obscured the magnetic anomaly signature of the original oceanic crust. Intraplate volcanism occurred after the oceanic lithosphere was formed at the spreading ridge. In these areas the original magnetisation was overprinted. A too wide spacing of the profiles is also responsible for the fact that the magnetic lineations cannot be clearly seen everywhere.

The resolution of the magnetic field is considered and the magnetic field data are being evaluated. The resolution is determined by the available amount of detailed data. A problem with interpreting magnetic lineations is that many magnetic profiles are not perpendicular to the spreading fabric. These profiles do not resolve the magnetic lineation pattern.

Three-dimensional modelling has shown as well that not all the magnetic anomalies on the oceanic Nazca Plate may be explained by the magnetic lineation pattern. Especially the model of the Nazca Ridge Area stresses this fact. Here, a magnetic anomaly pattern can be observed and modelled, which does not coincide with the predicted magnetic lineations. Distinct local anomalies are observed in the Nazca Ridge Area.

An objective of three-dimensional modelling is to find out which layers of the oceanic crust make a significant contribution to the marine magnetic anomalies. In all models the magnetisation of the layer sheeted dykes is considerably lower than the magnetisation of the upper pillow lavas and the lower gabbros. The mantle is assumed to be non-magnetic.

The skewness of the magnetic anomalies is imitated in three-dimensional modelling. The reversal boundaries, i.e. the edges of the magnetised blocks, are tilted. At the mid-oceanic ridges the creation of new oceanic lithosphere results in a complicated system of dykes and intrusions. The cooling history of the Nazca Plate is described by the magnetic lineations.

Modelling has proved that some of the magnetic anomalies observed over the slope cannot be caused by the subducting oceanic crust. The magnetic layers of the subducting oceanic crust exert nearly no influence on the anomalies observable at the sea surface when they have subducted to a depth of 25 km and more. The anomalies over the continental slope have to be caused by a strongly magnetised rock units of the continental margin. These magnetic variations can be associated with the presence of metamorphic rocks.

A rock unit on the Nazca Plate off Antofagasta in northern Chile shows local variations of magnetisation. Schreckenberger (1998) postulates that the magnetic source layers are disintegrated mechanically just landward of the trench. Some magnetic anomalies may be explained by magnetic seamounts like Barckhausen et al. (1998) modelled off Costa Rica. Several magnetic anomalies may not be due to differences in magnetisation of the source rocks but to differences in topography.

An aim is to find out what happens to the subducting magnetic lineations during subduction and which influence they exert on the observable anomalies. An unexplained question is until what depth the oceanic plate is still magnetic. The magnetisation anomalies are indicators of special temperature situations. They are indicators of the Curie temperature and depth of the subducted oceanic plate. As the magnetic models cannot reproduce the observed anomalies satisfactorily it is difficult to estimate the Curie temperature depth and the corresponding isotherm of approximately 600˚C. In three-dimensional modelling the crust-mantle boundary is assumed to represent this isotherm. The mantle is treated as non-magnetic. Alternative models, which include a magnetised mantle do not render better results. Accordingly, the crust-mantle boundary might represent the boundary between regions below and regions above the Curie temperature. According to the generally accepted isotherms expected in the subducting slab (e.g. Kearey & Vine, 1990) the Curie temperature is definitely not yet reached at a depth of 30 or 40 km, i.e. at the maximum depth of the three-dimensional models.

It is disappointing that the second sensor of the gradiometer did not work. Nevertheless, even if the magnetic data from the GEOPECO expedition could be corrected for diurnal variations in a more precise way, it would not change too much. The superposition of the other available magnetic data is not perfect either. The combination of different data sets produces further errors. It may be possible that not all the magnetic data of the GEODAS data base are thoroughly comparable. It is not completely assured that all corrections were applied. The respective IGRF was substracted from all the data but whether the other corrections were applied in the same way is not certain.

An explanation for the large differences between observed and modelled magnetic anomalies lies in the variability of the magnetic parameters. The magnetic anomalies possess wavelengths of only a few meters to more than 100 kilometres. A comparison between gravity, seismic and magnetic investigations shows that the applied densities vary between 1.73 and 3.34 g/cm^3, the seismic velocities lie between 1.6 and 8.1 km/s. These variations lie in the same order of magnitude. In contrast the average magnetic susceptibilities for the rocks integrated in the models range between 0.009 and 0.15 (see Table 3, p. 68), i.e. they vary about 2 orders of magnitude. Furthermore the magnetisation is a vector and is not always parallel to the current magnetic field of the earth. A magnetic body produces a significantly different magnetic anomaly if it is tilted. In all the models the magnetic anomalies are simulated by a variation of the parameters magnetisation, susceptibility, Königsberg ratio and model geometry. Due to the moderate success in magnetic modelling, the three-dimensional models represent a qualitative interpretation of the magnetic source bodies.

In magnetic modelling, similar to gravity modelling, it is unfortunate that gradients within the single magnetic bodies cannot be modelled with the program IGMAS. The lateral gradient in the y-direction, parallel to the Peru Trench, is especially important. In the x-direction the lateral gradient can be simulated by splitting the model into different blocks. In the y-direction the splitting into blocks makes the model too complex. Vertical gradients are probably geologically sensible but even without these gradients the model is complex enough. It was tried to model with changing blocks in the y-direction, but no satisfactory results could be achieved.

8.2.1 Magnetic Interpretation in the Yaquina Area

In the Yaquina Area the magnetic anomalies describe a complex situation. In the south, where the Mendaña Fracture Zone is located, the discrepancies between the modelled and the observed magnetic anomalies are notably higher. This is a sign that in the Mendaña Fracture Zone new oceanic crust, possessing a different lineation pattern, has been created. The newly formed magnetic lineations are oriented approximately perpendicular to the surrounding spreading fabric and cannot be reproduced by the model geometry.

The oceanic crust is subdivided into 6 different blocks. Block B is most strongly magnetised. The highly magnetic pillow lavas and gabbros enclose the weakly magnetised sheeted dykes. Block B is modelled as the normally magnetised magnetic lineation 9. Block D is representing the magnetic lineation 10 and possesses comparably strong magnetised pillow lavas.

The layer geometry is based on the seismic velocity models (Hampel et al., 2002a; Broser et al., 2002). Contrary to gravity modelling, where layers with different seismic velocities represent layers with contrasting densities, the velocity boundaries do not necessarily always coincide with the layer boundaries of bodies with different magnetic properties. On plane 7 (Figure 69) of the Yaquina Area model the observed positive anomaly at kilometre 50 is caused by the upwelling of mantle material. As the mantle is treated as non-magnetic this local maximum cannot be reproduced by the thinned oceanic crust. The upwelling may have developed by a thermal anomaly. This is an example that the boundaries are not always the same for magnetisation and density.

Most of the high-frequency magnetic anomalies which are observed above the continental margin cannot be reproduced by the presented models. The layer geometries of the continental block are determined by the rocks’ velocities and, consequently, the rocks’ densities. The bodies responsible for the observable magnetic anomalies partly seem not to be represented by these chosen layer boundaries.

The differently magnetised blocks of the oceanic crust show varying Königsberg ratios, i.e. separate relations between remanent and induced magnetisation. The Blocks B and D have a notably lower Königsberg ratio than blocks A, C and F. The former possess Königsberg ratios between 0.2 and 0.5, the latter show ratios of 1 to 2. Consequently the observed magnetic anomalies are partly caused by source layers dominated by their remanent magnetisation and partly by magnetic bodies controlled by the induced magnetisation.

8.2.2 Magnetic Interpretation in the Lima Area

In the Lima Area magnetic modelling is most difficult. The magnetic anomalies do not show a clear anomaly pattern. In three-dimensional modelling the normally magnetised lineation 19 is flanked by four blocks consisting of reversely magnetised crust. On the landward side of the model the magnetic lineation 20 is modelled. The subdivision into several blocks with reverse magnetisation is necessary because the anomaly pattern is extremely diverse.

Unfortunately the presence of two DSDP holes just west of the Lima Area is of no concrete help in determining the orientation of the remanent magnetisation. The study of the inclination and declination angles determined for the basalts of the DSDP holes is not conclusive. The values vary by far too much.

In the Lima Area the layers of the continental margin show a similarly weak magnetisation as in the Yaquina Area.

8.2.3 Magnetic Interpretation in the Nazca Ridge Area

In the Nazca Ridge Area the determination of the remanent magnetisation angles, i.e. the remanent inclination and the remanent declination, is easier as the Nazca Ridge originated from the fixed Easter Island hotspot. The magnetic model reproduces the general trends of the measured anomalies quite well. The magnetic lineations which are expected to cross this area are not imaged in the three-dimensional model. Rather, another magnetic anomaly pattern is apparent which crosses the usual lineation pattern on the surrounding Nazca Plate at an angle of about 30°.

These magnetic lineations were most probably created when the Nazca Ridge developed at the Easter Island hotspot. The newly formed ridge obliterated the magnetic anomaly pattern on the Nazca Plate. This result does not support the theory that the Nazca Ridge was created at the same time as the surrounding Nazca Plate. The observable anomaly pattern, and consequently the Nazca Ridge, has to be younger than the adjacent, undisturbed oceanic crust.

In the Nazca Ridge Area the Königsberg ratio is less than 1 for all magnetic bodies. This modelling result proves that for all magnetic bodies the induced magnetisation is higher than the remanent magnetisation. Either the paleo-magnetic field, which existed when the rocks were created was weak, or the rocks have experienced a history of warming and/or chemical alteration which has partly destroyed their remanent magnetisation.

In all three research areas the modelled susceptibilities are in the, admittedly wide, range of the typical values as specified by Telford et al. (1990).

The main trends of the observed, low-pass filtered, magnetic anomalies are reproduced by three-dimensional modelling but, unfortunately, deviations of 100 nT occur several times. Ultimately the maps imaging the magnetic anomalies along the planes of the three-dimensional models (Figures 35, 37 and 39) are more meaningful than the three-dimensional modelling itself.

9 Conclusions

This work is an investigation into a better understanding of the character and shape of the convergent Peruvian margin. A major aim is to find out how the continental margin is modified by the subduction of the oceanic Nazca Plate and especially by the subduction of the prominent Nazca Ridge. A further objective is to find out more about the internal structure of the oceanic Nazca Plate with respect to its different features like the Nazca Ridge, the Mendaña Fracture Zone and the Trujillo Trough.

Gravity modelling renders very satisfactory results. The misfit between the observed and the calculated free-air anomalies can be reduced to less than 5 mGal on average. The following main conclusions can be drawn from interpreting the gravity data:

- Maps of the free-air anomalies and Bouguer anomalies as well as maps of the residual free-air and Bouguer anomalies underline that the subduction zone imprints a strong signature on the gravity fields. The continental margin, close to the trench, is characterised by positive free-air anomalies of varying amplitudes. Accordingly, the influence of the long-term subduction zone on the appearance of the margin has not been uniform. Most probably the margin has been shaped by the subduction of bathymetric features, e.g. seamounts, in the past.

- In the Yaquina Area three-dimensional modelling proves that the tectonic features of the Trujillo Trough and the Mendaña Fracture Zone, which are not constrained by seismic profiles, are characterised by strong undulations in the layer geometry of the oceanic crust.

- The continental margin shows remarkable features in the Lima Area. The strong undulations of the layers continental crust 2 and continental crust 3 influence the upper sedimentary layers and most probably support the development of basins along the Peruvian margin.

- A seaward wedge of the continental crust possesses a lower density than the main continental block. In my opinion this block has been fractured by the subducting Nazca Ridge. In the Nazca Ridge Area, where the ridge is currently subducting, this wedge is not yet observed.

- The highly thickened and slightly asymmetrical crust of the Nazca Ridge is envisaged. This supports the results from the two crossing, two-dimensional seismic profiles P1 and P2 (Hampel et al., 2002a). Constrained by these seismic lines the three-dimensional gravity model covers a larger area and proves that the thickened and asymmetrical crustal structure also agrees with the extended, overall gravity anomaly caused by the subducting Nazca Ridge.

- As the Nazca Ridge produces positive free-air anomalies, it is not isostatically compensated. This is contrary to the conclusion of Hayes (1966).

- The theory stating that the Peruvian margin is uplifted by the subducting Nazca

Ridge (Cross & Pilger, 1982) is supported by gravity modelling. Consequently the buoyant Nazca Ridge is, at least partly, responsible for the extended region of flat subduction. The buoyancy of the thick crust forming the Nazca Ridge is responsible for the observed gravity anomalies.

- In the Nazca Ridge Area the subduction of eroded sediments is probable. Layer 2A probably comprises eroded sediments, trapped in local depressions, when starting subduction. Although subject to strong compressional forces, layer 2A does not increase in density when starting subduction. As no accretionary prism is observed and as the Nazca Ridge is thought to erode the continental margin the amount of subducted material has to be higher than the incoming sediments on the Nazca Plate.

- Erosion of the continental margin, as well as the presence or absence of an accretionary prism, is successfully simulated by a varying thickness of the upper sediment layer.

- The increasing densities, modelled for the layers of the oceanic crust, are indicative of an originally high degree of porosity.

- In the Nazca Ridge Area no accretionary prism is modelled. Consequently the theory that the Nazca Ridge is eroding the continental margin during subducting (von Huene et al., 1996; von Huene & Pecher, 1999) is confirmed by three-dimensional gravity modelling.

- Further north in the Lima Area a pretty uniform accretionary complex is observed supporting the theory that, after the subducting Nazca Ridge has moved further southwards, an accretionary prism developed and rapidly reached its stable size (von Huene et al., 1996).

- In the Yaquina Area an accretionary prism is modelled in the whole research area but local variation of its location and structure are observed. As most parts of the Yaquina Area have not been influenced by the subducting Nazca Ridge other features of the convergent margin must have been responsible for the varying size of the accretionary prism. Most probably seamounts on the Nazca Plate have subducted in the past where the accretionary prism is not as thick, where the margin must have been eroded because the high-density layers are exposed.

The magnetic investigation of the Peruvian margin leads to the following conclusions:

- The main objective of magnetic modelling is to find out more about the lineation pattern of the oceanic crust. The lineations 13 to 18 are identified with confidence and can be traced from the southern part of the studied region as far north as the Mendaña Fracture Zone. The orientation of these anomalies, together with the lineations 19 and 20 in the south, is nearly parallel to each other and, between Chimbote and Pisco, approximately parallel to the Peruvian coast. Consequently the Nazca Plate has not significantly changed its convergence direction between 12°S and 17.5°S in the past 33Ma. The distances between the observed lineations agree with the geomagnetic polarity time scale published by Cande & Kent (1995) and with the variable paleo convergence rates as specified by Somoza (1998).

- The most diverse magnetic condition is found in the Yaquina Area. North of the Mendaña Fracture Zone the lineations 9, 10 and 11 are observed. These anomalies run almost parallel to the Peruvian margin. South of the fracture zone the magnetic lineation 18 reaches into the Yaquina Area. In three-dimensional modelling the Mendaña Fracture Zone is recognizable as the area where the least fit between the modelled lineations and the observed magnetic anomalies is reached. The newly formed oceanic crust possesses an orientation which is almost perpendicular to the orientation of the modelled magnetic lineations. Consequently, it is impossible that the model geometry satisfies the magnetic characteristics of the Mendaña Fracture Zone. Accordingly, the misfit of observed and calculated anomalies is a support of the theory that the fracture zone is a divergent rift zone, where new oceanic crust is created.

- In the Lima Area the magnetic lineation 19 is tentatively recognized. In this region the magnetic anomaly pattern is especially irregular. Different explanations for this heterogeneity are possible. On the one hand the available magnetic data may not be sufficing or they may not be sufficiently compatible due to the influence of magnetic variations. On the other hand the Nazca Plate may have experienced extensive volcanism after its creation at the spreading centre.

- In the Nazca Ridge Area the predicted magnetic lineations 19 and 20 cannot be reproduced by three-dimensional modelling. A different anomaly pattern is observed. The surveyed magnetic anomalies strike at an angle of about 30° to the orientation of the expected lineations. In my opinion these anomalies developed when the Nazca Ridge was created at the Easter Island hotspot. The ridge was formed on the already existing Nazca Plate and obliterated the original magnetic anomalies. The Nazca Ridge is younger than the surrounding sea floor.

- In all three models the basaltic layer sheeted dykes is considerably weaker magnetised than the upper pillow lavas and the lower gabbros. The rocks of the continental margin generally possess a weak magnetisation. The magnetisation of the upper sediments, covering both the oceanic crust and the continental margin, is not negligible. This is a contrary result to the assumption of Roeser (2000) that sediments normally do not contribute noticeably to the observable anomalies.

- The ratio of the remanent to the induced magnetisation, i.e. the Königsberg ratio, is small for all layers of the oceanic crust. These modelling results signify that the induced magnetisation is higher than the remanent magnetisation. Either the initial magnetic field, which existed when the rocks were formed, was weak, or the rocks have experienced a history of warming and/or chemical alteration which has partly destroyed their remanent magnetisation.

- An aim is to find out until what depth the oceanic plate is still magnetic. In three-dimensional modelling almost no influence of the magnetised oceanic crust can be observed after it has subducted to a depth of 25 km. The effect of the overlying continental margin is dominating the observable magnetic anomalies. It is not possible to say whether the subducting oceanic crust is still highly magnetic or not.

- The magnetic models depend on many different, interdependent parameters and consequently the possible error sources are manifold. Accordingly the three-dimensional magnetic models render mostly qualitative results.

As the potential field data alone do not provide definite models of the geological structures, the seismic constraints are indispensable. Additionally the results of geological investigations and other geophysical experiments play a major role in the creation of the models. The combined and simultaneous modelling of the gravity and magnetic anomalies provides further constraints on the three-dimensional models.

In order to obtain better results in the magnetic investigation of the Peruvian margin additional magnetic profiles, preferably oriented perpendicular to the magnetic lineations, are required. Naturally, deep-reaching drill holes could verify the modelled magnetisation values. In situ magnetisation measurements of the crystalline oceanic crust would provide valuable constrains which could reduce the possible errors in three-dimensional models significantly. This would facilitate a concentration on the objective to identify magnetic lineations. In the Nazca Ridge Area samples of the crystalline oceanic crust would render a definite time for the creation of the ridge. Further seismics profiles are desirable to verify the results of gravity and magnetic modelling, e.g. the undulations in the layer geometry of the oceanic crust.

Acknowledgements

I would like to express my gratitude to my supervisor Dr. Gholam Ali Dehghani for his support, advice and patience throughout my Ph.D. education. Thank you for making this work possible and for guiding me throughout my research.

I wish to thank Prof. Dr. Dirk Gajewski for supporting my work and for approving of this research topic.

To Anne Krabbenhoeft, who I have cited by her maiden name Anne Broser, and to Andrea Hampel I am very grateful for providing and explaining the velocity models. Many inspiring discussions were encouraging and essential for the progress of this research.

I wish like to thank Dr. Christian Hübscher for helping me with seismics.

I would like to thank Prof. Dr. Sabine Schmidt for enabling me to work with the program IGMAS.

I wish to express my appreciation to the members of my dissertation committee: Dr. Gholam Ali Dehghani, Prof. Dr. Dirk Gajewski, Dr. Christian Hübscher, Prof. Dr. Claus-Dieter Reuther and Prof. Dr. How Kin Wong.

I especially wish to thank Ali Sabetian for his invaluable support in all situations. I am deeply grateful for reviewing the manuscript of this thesis and for all the critical comments and encouragements.

I would like to thank Franziska Kähler and Prof. Dr. Helmuth Kähler for their love and support.

I wish to thank the members of the Institute of Geophysics Hamburg. Tina Kaschwich, Gesa Netzeband and Marco Brönner deserve my warmest thanks for many helpful comments and discussions.

I would like to thank the Federal Ministry of Education and Research (BMBF) for financial support of the whole project (No. 03 G 0146 B) and I thankfully appreciate the graduate scholarship of the city of Hamburg.

List of Figures

List of Tables

References

Allmendinger, R. W., Ramos, V. A., Jordan, T. E., Palma, M., Isacks, B. L.; 1983: Paleogeography and Andean structural geometry, northwest Argentina, Tectonics 2, pp. 1-16

Angermann, D., Klotz J., Reigber, C.; 1999: Space-geodetic estimation of the Nazca-South America Euler vector, Earth and Planetary Science Letters 171, pp. 329-334

Babuska, V., Cara, M.; 1991: Seismic Anisotropy in the Earth, Kluwer Academic, Dordrecht

Ballesteros, M. W., Moore, G. F., Taylor, B., Ruppert, S.; 1988: Seismic stratigraphic framework of the Lima and Yaquina forearc basins, Peru, in: Suess, E., von Huene, R. (eds.): Proc. Ocean Drilling Program (ODP), Init. Reports 112, College Station, TX, pp. 77-90

Barazangi, M., Isacks, B. L.; 1979: Subduction of the Nazca plate beneath Peru: evidences from spatial distribution of earthquakes, Geophys. J. R. astron. Soc. 57, pp. 537-555

Barckhausen, U., Roeser, H. A., von Huene, R.; 1998: Magnetic signature of upper plate structures and subducting seamounts at the convergent margin off Costa Rica, J. Geophys. Res. 103, B4, pp. 7079-7093

Barckhausen, U., Ranero, C., von Huene, R., Cande, S. C., Roeser, H. A.; 2001: Revised tectonic boundaries in the Cocos Plate off Costa Rica implications for the segmentation of the convergent margin and for plate tectonic models, J. Geophys. Res. 106, B9, pp. 19207-19220

Bartels, J.; 1949: The standardized index, ks, and the planetary index, kp, in: IATME Bulletin 12b, IUGG Publications Office, Paris, p. 97

Barton, P. J.; 1986: The relationship between seismic velocity and density in the continental crust - a useful constraint?, Geophys. J. R. astr. Soc. 87, pp. 195-208

Beck, Jr., M. E.; 1998: On the mechanism of crustal block rotations in the central Andes, Tectonophysics 299, pp. 75-92

Bialas, J., Kukowski, N., GEOPECO Working Group; 2000: Subduction Along the Peruvian Margin - First Results of the SO146 GEOPECO Cruise, AGU Fall Meeting

Bialas, J., Broser, A., Hampel, A., Kukowski, N.; 2002: Structure of the Peruvian Margin as imaged by Wide Angle and Reflection Seismic Data, in: Bialas, J., Kukowski, N., GEOPECO-Arbeitsgruppe: GEOPECO, Zwischenbericht 2001

Birch, F.; 1960: The Velocity of Compressional Waves in Rocks to 10 Kilobars, Part 1, J. Geophys. Res. 65, B4, pp. 1083-1102

Birch, F.; 1961: The Velocity of Compressional Waves in Rocks to 10 Kilobars, Part 2, J. Geophys. Res. 66, B7, pp. 2199-2224

Bird, R. T., Naar, D. F., Larson, R. L., Searle, R. C., Scotese, C. R.; 1998: Plate tectonic reconstructions of the Juan Fernandez microplate: Transformation form internal shear to rigid rotation, J. Geophys. Res. 103, B4, pp. 7049-7067

Bodenseewerke Geosystems; 1981: Instruction Manual for the Marine/Air Gravity System KSS30

Bourgois, J., Pautot, G., Bandy, W., Boinet, T., Chotin, P., Huchon, P., Mercier de Lépinay, B., Monge, F., Monlau, J., Pelletier, B., Sosson, M., von Huene, R.; 1988: Seabeam and seismic reflection imaging of the tectonic regime of the Andean continental margin off Peru (4˚S to 10˚S), Earth and Planetary Science Letters 87, pp. 111-126

Breiner, S.; 1973: Applications Manual for Portable Magnetometers, Geometrics, Sunnyvale, California

Broser, A., Bialas, J., Hampel, A., Kukowski, N.; 2002: Subduction Processes Along the Peruvian Margin From Wide Angle Seismic Data, EGS, XXVII General Assembly, Nice, France

Cahill, T., Isacks, B. L.; 1992: Seismicity and Shape of the Subducted Nazca Plate, J. Geophys. Res. 97, B12, pp. 17503-17529

Cande, S. C.; 1985: Nazca-South American Plate interactions since 50 my b.P. to present, in: Hussong, D. M., Dang, S. P., Kulm, L. D., Couch, R. W., Hilde, T. W. C. (eds.): Atlas of the Ocean Margin Program, Peru Continental Margin, Region VI, Woods Hole, Marine Science International 14

Cande, S. C., Kent, D. V.; 1992: Ultrahigh resolution marine magnetic anomly profiles: a record of continuous paleointensity variations?, J. Geophys. Res. 97, B11, pp. 15075-15083

Cande, S. C., Kent D. V.; 1995: Revised calibration of the geomagnetic polarity time scale for the Late Cretaceous and Cenozoic, J. Geophys. Res. 100, B4, pp. 6093-6095

Carlson, R. L., Raskin, G. S.; 1984: Density of the ocean crust, Nature 311, pp. 555-558

Carlson, R. L., Herrick, C. N.; 1990: Densities and Porosities in the Oceanic Crust and Their Variations With Depth and Age, J. Geophys. Res. 95, B6, pp. 9153-9170

Christensen, N. I., Salisbury, M. H.; 1975: Structure and constitution of the lower oceanic crust, Rev. Geophys. Space Phys. 13, pp. 57-86

Cobbing, E. J.; 1985: The tectonic setting of the Peruvian Andes, in: Pitcher, W. S., Atherton, M. P., Cobbing, E. J., Beckinsale, R. D. (eds.): Magmatism at a Plate Edge: The Peruvian Andes, Glasgow, Blackie and Son, pp. 3-18

Cobbing, E. J., Pitcher, W. S.; 1972: The coastal batholith of central Peru, Geol. Soc.

London Journal 128, pp. 421-460

Cobbing, E. J., Pitcher, W. S.; 1983: Andean plutonism in Peru and its relationship to volcanism and metallogenesis at a segmented plate edge, Geol. Soc. Am. Mem. 159, pp. 277-291

Couch, R. W., Whitsett, R. M.; 1981: Structures of the Nazca Ridge and the Continental Shelf and Slope of Southern Peru, Geological Society of America Memoir 154, pp. 569-586

Couch, R. W., Whitsett, R. M., Huehn, B., Briceno-Guarupe, L.; 1981: Structures of the continental margin of Peru and Chile, Geological Society of America Memoir 154, pp. 703-726

Cross, T. A., Pilger, R. H.; 1982: Controls of subduction geometry, location of magmatic arcs, and tectonics of arc and back-arc regions: Geological Society of America Bulletin 93, pp. 545-562

Dahlen, F. A., Suppe, J, Davis, D.; 1984: Mechanics of fold-and-thrust belts and accretionary wedges: cohesive Coulomb theory, J. Geophys. Res. 89, B12, pp. 10087-10101

Dalziel, I. W. D.; 1986: Collision and Cordilleran orogenesis: an Andean perspective, In: Coward, M. P., Ries, A. C. (eds.): Collision tectonics, Geological Society Special Publication 19, pp. 389-404

Davis, D., A., Suppe, J., Dahlen, F. A.; 1983: Mechanics of fold and thrust belts and accretionary wedges, J. Geophys. Res. 88, B2 pp. 1153-1172

DeMets, C. D., Gordon, R. G., Argus, D. F., Steins, S.; 1990: Current plate motions, Geophys. J. Int. 101, pp. 425-478

Dewey, J. F., Lamb, S. H.; 1992: Active tectonics of the Andes, Tectonophysics 205, pp. 79-95

Dickinson, W. R., Seely, D. R.; 1979: Structure and stratigraphy of forearc regions, American Association of Petroleum Geologists Bulletin 63, pp. 2–31

Dominguez, S., Lallemand, S. E., Malavieille, J., von Huene, R.; 1998: Upper plate deformation associated with seamount subduction, Tectonophysics 293, pp. 207-224

Erlandson, D. L., Hussong, D. M., Campbell, J. F.; 1981: Sediment and Associated Structure of the Northern Nazca Plate, Mem. Geol. Soc. Am. 154, pp. 295-314

Fukao, Y., Hori, S., Ukawa, M.; 1983: A seismological constraint on the depth of basalt-eclogite transition in a subducting oceanic crust, Nature 303, pp. 413-415

Flueh, E. R., Vidal, N., Ranero, C. R., Hojka, A., von Huene, R., Bialas, J., Hinz, K., Cordoba, D., Dañobeitia, J. J., Zelt, C.; 1998: Seismic investigation of the continental margin off- and onshore Valparaiso, Chile, Tectonophysics 288, pp. 251-263

Gee, J., Kent, D. V.; 1998: Magnetic telechemistry and magnetic segmentation on the Southern East Pacific Rise, Earth and Planetary Science Letters 164, pp. 379-385

Gee, J., Kent, D. V.; 1999: Calibration of magnetic granulometric trends in ocean basalts, Earth and Planetary Science Letters 170, pp. 377-390

Gee, J., Schneider, D. A., Kent, D. V.; 1996: Marine magnetic anomalies as recorders of geomagnetic intensity variations, Earth and Planetary Science Letters 144, pp. 327-335

GEOMETRICS; 1975: Assembly & Maintenance Manual for Marine Towing Systems, Model G-801/G-801G/G-866 Marine Proton Magnetometers

Götze, H.-J.; 1984: Über den Einsatz interaktiver Computergraphik im Rahmen 3-dimensionaler Interpretationstechniken in Gravimetrie und Magnetik. Habilitations-Schrift, Technische Universität Clausthal

Götze, H.-J., Lahmeyer, B.; 1988: Application of three-dimensional interactive modeling in gravity and magnetics, Geophysics 53, No. 8, pp. 1096-1108

Götze, H.-J., Kirchner, A.; 1997: Interpretation of Gravity and Geoid in the Central Andes between 20˚ and 29˚S, Journal of South American Earth Sciences 10, pp. 179-188

Götze, H.-J., Schmidt, S., Goltz, G., Alvers, M., Klesper, Ch. Hoffmann, M.; 2000: IGMAS Interactive Gravity and Magnetic Application System, http://userpage.fu-berlin.de/~sschmidt/Sabine_IGMAS.html

Gutscher, M.-A., Malavieille, J., Lallemand, S., Collot, J.-Y.; 1999a: Tectonic segmentation of the North Andean margin: impact of the Carnegie Ridge collision, Earth and Planetary Science Letters 168, pp. 255-270

Gutscher, M. A., Olivet, J.-L., Aslanian, D., Eissen, J.-P., Maury, R.; 1999b: The “lost Inca Plateau”: cause of flat subduction beneath Peru?, Earth and Planetary Science Letters 171, pp. 335-341

Haederle, M., Atherton, M. P.; 2002: Shape and intrusion style of the Coastal Batholith, Peru, Tectonophysics 345, pp. 17-28

Hagen, R. A., Moberly, R.; 1994: Tectonic Effects of a Subducting Aseismic Ridge: The Subduction of the Nazca Ridge at the Peru Trench, Marine Geophysical Researches 16, pp. 145-161

Hampel, A., Kukowski, N., Bialas, J.; 2002a: Effects of the Oblique Subduction of the Nazca Ridge on the Peruvian Convergent Margin: Insights from Bathymetric and Wide-Angle Seismic Data, in: Bialas, J., Kukowski, N., GEOPECO-Arbeitsgruppe, GEOPECO, Zwischenbericht 2001

Hampel, A., Kukowski, N., Bialas, J., Barckhausen, U.; 2002b: Effects of the oblique subduction of the Nazca Ridge on the Peruvian margin: A re-evaluation of its migration and the present collision zone, EGS, XXVII General Assembly, Nice, France

Hampel, A.; 2002: The migration history of the Nazca Ridge along the Peruvian active margin: a re-evaluation, Earth and Planetary Science Letters 203, pp. 665-679

Hamza, V. M., Muñoz, M.; 1996: Heat flow map of South America, Geothermics 25, pp. 599-646

Handschumacher, D. W.; 1976: Post-Eocene plate tectonics of the Eastern Pacific, in: Sutton, G. H., Manghnani, M. H., Moberly, R. (eds.): The Geophysics of the Pacific Ocean and its margins, American Geophys. Union, pp. 177-202

Harmon, R. S., Barreiro, B. A., Moorbath, S., Hoefs, J., Francis, P. W., Thorpe, R. S., Deruelle, B., McHugh, J., Viglino, J. A.; 1984: Regional O-, Sr- and Pb-isotope relationships in late Cenozoic calc-alkaline lavas of the Andean Cordillera., J. Geol. Soc. Lond. 141, p. 805

Hasegawa, A., Sacks, I. S.; 1981: Subduction of the Nazca Plate beneath Peru as determined from seismic observations, J. Geophys. Res. 86, B6, pp. 4971-4980

Hayes, D. E.; 1966: A geophysical investigation of the Peru-Chile Trench, Marine Geology 4, pp. 309-351

Helffrich, G. R., Stein, S.; 1993: Study of the structure of the slab-mantle interface using reflected and converted seismic waves, Geophys. J. Int. 115, pp. 14-40

Henry, S. G., Pollack, H. N.; 1988: Terrestrial heat flow above the Andean subduction zone, Bolivia and Peru, J. Geophys. Res. 93, B12, pp. 15153-15162

Hey, R.; 1977: Tectonic evolution of the Cocos-Nazca spreading center, Geol. Soc. Am. Bull. 88, pp. 1404-1420

Hilde, T. W. C., Warsi, W. E. K.; 1982: Subduction induced Rifting of the Nazca Plate along the Mendaña Fracture Zone, Eos Trans. AGU 63, No. 18, p. 444

Hilde, T. W. C., Warsi, W. E. K.; 1984: Magnetic Anomaly Profiles along Ship Tracks and Lineations, Peru-Chile Trench Offshore Peru, Atlas 9, sheet 4, in: Hussong, D. M., et al. (eds.): Ocean Margin Drilling Program Reg. Atlas Ser., Marine Science International, Woods Hole

Housen, B. A., Musgrave, R. J.; 1996: Rock-magnetic signature of gas hydrates in accretionary prism sediments, Earth and Planetary Science Letters 139, pp. 509-519

Huchon, P., Bourgois, J.; 1990: Fragmentation of the Nazca plate: Mendaña fracture zone and Trujillo trough revisited, J. Geophys. Res. 95, B6, pp. 8419-8436

Hübscher, Ch.; 2000: Parasound, Cruise report SO146-1&2, GEOMAR Report 96, p. 134

Hübscher, Ch., Kück, N., Krüger, M., Wenz, Ch.; 2000: Reflection Seismic, Cruise report SO146-1&2, GEOMAR Report 96, p. 129

Hübscher, Ch., Gajewski, D., Greinert, J., Kukowski, N., Pecher, I., Bialas, J.; 2001: BSR and Bright Spot distribution in the Yaquina Forearc Basin off Peru, EGS, XXVI General Assembly, Nice, France

von Huene, R., Kulm, L. D., Miller, J.; 1985: Structure of the frontal part of the Andean convergent margin, J. Geophys. Res. 90, B7, pp. 5429-5442

von Huene, R., Suess, E., Leg 112 Shipboard Scientists; 1988: Ocean Drilling Program Leg 112 Peru continental margin, part 1, Tectonic history, Geology 16, pp. 934-938

von Huene, R., Miller, J.; 1988: Migrated multichannel seismic-reflection records across the Peru continental margin, Proc. Ocean Drilling Program (ODP), Init. Reports 112, College Station, TX, pp. 109-124

von Huene, R., Lallemand, S.; 1990: Tectonic erosion along convergent margins, Geol. Soc. Am. Bull. 102, pp. 704-720

von Huene, R., Scholl, D. W.; 1991: Observations at convergent margins concerning sediment subduction, subduction erosion, and the growth of continental crust, Reviews of Geophysics 29, pp. 279-316

von Huene, R., Pecher, I. A., Gutscher, M.-A.; 1996: Development of the accretionary prism along Peru and material flux after subduction of Nazca Ridge, Tectonics 15, pp. 19-33

von Huene, R., Pecher, I. A.; 1999: Vertical tectonics and the origins of BSRs along the Peru margin, Earth and Planetary Science Letters 166, pp. 47-55

von Huene, R., Weinreebe, W., Heeren, F.; 1999: Subduction erosion along the North Chile margin, Geodynamics 27, pp. 345-358

Hussong, D. M., Wipperman, L. K.; 1981: Vertical movement and tectonic erosion of the continental wall of the Peru-Chile Trench near 11˚ 30'S latitude, in: Kulm, L. D., Dymond, J., Dasch, E. J, Donald, M. (eds.): Crustal formation and Andean convergence, Geological Society of America Memoir 154, pp. 509-524

Hussong, D. M., Dang, S. P., Kulm, L. D., Couch, R. W., Hilde, T. W. C. (eds.); 1985: Atlas of the Ocean Margin Program, Peru Continental Margin, Region VI: Woods Hole, Marine Science International

Hussong, D. M., Reed, T. B., Bartlett W. A.; 1988: SeaMARC II Sonar Imagery and Bathymetry of the Nazca Plate and Peru Forearc, Ocean Drilling Program (ODP) Leg 112, in: Suess, E., von Huene, R., et al.: Proc. Ocean Drilling Program (ODP), Init. Reports 112, College Station, TX, pp. 125-130

Hsu, J. T.; 1992: Quaternary uplift of the peruvian coast related to the subduction of the Nazca Ridge: 13.5 to 15.6 degrees south latitude, Quaternary International 15/16, pp. 87-97

Isacks, B. L.; 1988: Uplift of the central Andean plateau and bending of the Bolivian orocline, J. Geophys. Res. 93, B4, pp. 3211-3236

Jacobs, J. A.; 1970: Geomagnetic micropulsations, Springer Verlag, New York

Jarrard, R. D.; 1986: Relations among subduction parameters, Rev. Geophys. 24, pp. 217-284

Jischke, M.; 1975: On the dynamics of descending lithospheric plates and slip zones, J. Geophys. Res. 80, B2, pp. 4809-4813

Johnson, S. H., Ness, G. E.; 1981: Shallow Structures of the Peru Margin 12°S-18°S, Mem. Geol. Soc. Am. 154, pp. 525-544

Jordan, T. E., Isacks, B. L., Allmendinger, R. W., Brewer, J. A., Ramos, V. A., Ando, C. J.; 1983: Andean tectonics related to geometry of subducted Nazca plate, Bulletin of the Geological Society of America 94, pp. 341-61

Kearey, P., Vine, F. J.; 1990: Global Tectonics, Blackwell Scientific Publications, Oxford, UK

Kirchner, A.; 1997: 3D-Dichtemodellierung zur Anpassung des Schwere- und des Schwerepotentialfeldes der zentralen Anden, Berliner Geowissenschaftliche Abhandlungen, Reihe B, Band 25, Berlin

Kudrass, H.-R., Delisle, G., Goergens, R., Heeren, F., von Huene, R. et al.; 1995: Crustal investigations off- and onshore Nazca/central andes, CINCA, Sonne-Cruise 104, Leg 3, Bundesanstalt für Geowissenschaften und Rohstoffe Hannover, Archiv-Nr. BGR 114 281

Kukowski, N., Pecher, I.; 1999: Thermo-hydraulics of the Peruvian accretionary complex at 12˚S, Geodynamics 27, pp. 373-402

Kukowski, N., Bialas, J.; 2000: Deformation and the role of fluids along the Peruvian margin - first results of cruise SO146 GEOPECO, AGU Fall Meeting

Kukowski, N., Hampel, A., Bialas, J., Hübscher, Ch., Barckhausen, U., Bourgois, J.; 2002: Tectonic Erosion at the Peruvian Margin: Evidence from Swath Bathymetry Data and Process Identification from 3D Sandbox Analogue Modelling, in: Bialas, J., Kukowski, N. und die GEOPECO-Arbeitsgruppe, GEOPECO, Zwischenbericht 2001

Kulm, L. D., Prince, R. A., French, W., Johnson, S., Masias, A.; 1981: Crustal structure and tectonics of the central Peru continental margin and trench, Geol. Soc. Am. Mem. 154, pp. 445-468

Kulm, L. D., Thornburg, T. M, Dang, S.; 1985: Drill hole stratigraphy, dredge lithologies, and sample locations, in: Hussong, D. M., et al. (eds.): Atlas of the Ocean Margin Drilling Program, Peru Continental Margin, Region VI: Woods Hole, Marine Science International, Sheet 18

Kulm, L. D., Thornburg, T. M., Suess, E., Resig, J., Fryer, P.; 1988: Clastic, diagenetic, and metamorphic lithologies of a subsiding continental block: central Peru forearc, in: E.

Suess, R. von Huene (eds.): Proc. Ocean Drilling Program (ODP), Init. Reports 112, College Station, TX, pp. 91-107

Lallemand, S. E., Schnürle, P., Malavieille, J.; 1994: Coulomb theory applied to accretionary and nonaccretionary wedges: Possible causes for tectonic erosion and/or frontal accretion, J. Geophys. Res. 99, B6, pp. 12033-12055

Leeman, W. P.; 1983: The influence of crustal structure on subduction-related magmas, J. Volcanol. Geotherm. Res. 87, pp. 561-588

Ludwig, W. J., Nafe, J. E., Drake, C. L.; 1970: Seismic refraction, in: The Sea, 4, A.E. Maxwell (ed.), pp. 53-84, Wiley-Interscience, New York

Macedo-Sanchez, O., Surmont, J., Kissel, C., Laj, C.; 1992: New temporal constraints on the rotation of the Peruvian central Andes obtained from paleomagnetism, Geophys. Res. Lett. 19, pp. 1875-1878

Mandea, M.; 2001: Business Meeting Minute 2001 for IAGA V5 Working Group 8, http://www.ngdc.noaa.gov/IAGA/wg8/min2001.html

Masson, D. G.; 1991: Fault Patterns at Outer Trench Walls, Marine Geophys. Res. 13, pp. 209-225

McFadden, P. L., McElhinny, M. W.; 1982: Variations in the geomagnetic dipole 2: statistical analysis of VDMs for the past 5 million years, J. Geomag. Geoelectr. 34, pp. 163-189

McFadden, B., Anaya, F., Perez, H., Naeser, C., Zeitler, P., Campbell, K.; 1990: Late Cenozoic paleomagnetism and chronology of the Andean basins of Bolivia: evidence for possible oroclinal bending, J. Geol. 98, pp. 541-555

McNutt, M. K.; 1998: Superswells, Rev. Geophys. 36, pp. 211-244

Meschede, M., Barckhausen, U.; 2001: The relationship of the Cocos and Carnegie ridges: age constraints from paleogeographic reconstructions, Int. J. Earth Sciences (Geol. Rundschau) 90, pp. 386-392

Miller, J. J., Lee, M. W., von Huene, R.; 1991: An Analysis of a Seismic Reflection from the Base of a Gas Hydrate Zone, Offshore Peru, The American Association of Petroleum Geologists Bulletin 75, No. 5, pp. 910-924

Moore, G. F., Taylor, B.; 1988: Structure of the Peru Forearc from Multichannel Seismic Reflection Data, in: Suess, E., von Huene, R., et al.: Proc. Ocean Drilling Program (ODP), Init. Reports 112, College Station, TX, pp. 71-76

Nafe, J. E., Drake, C. L.; 1957: Variation with depth in shallow and deep water marine sediments of porosity, density and the velocities of compressional and shear waves, Geophysics 22, No. 3, pp. 523-552

Noble, D. C., McKee, E. H.; 1977: Spatial distribution of earthquakes and subduction of the Nazca plate beneath South America: Comment, Geology 5, pp. 576-577

Norabuena E. O., Dixon T. H., Stein S., Harrison C. G. A.; 1999: Decelerating Nazca-South America and Nazca-Pacific Plate Motions, Geophys. Res. Lett. 26, pp. 3405-3408

Nur, A., Ben-Avraham, Z.; 1981: Volcanic gaps and the consumption of aseismic ridges in South America, in: Kulm, L. D., Dymond, J., Dasch, E. J., Hussong, D. M. (eds.): Nazca Plate Crustal Formation and Andean Convergence, Geol. Soc. Am. Mem. 154, pp. 729-740

Ocola, L. C., Luetgert, J. H., Aldrich, L. T., Meyer, R. P., Helsey, C. E.; 1995: Velocity structure of the coastal region of southern Peru from seismic refraction / wide-angle reflection data, J. Geodynamics 20, No. 1, pp. 1-30

Okal, E. A., Newman, A. V.; 2001: Tsunami earthquakes: the quest for a regional signal, Physics of the Earth and Planetary Interiors 124, pp. 45-70

Okubo, Y., Makino, M., Kasuga, S.; 1991: Magnetic model of the subduction zone in the northeast Japan Arc, Tectonophysics 192, pp. 103-115

Pardo-Casas, F., Molnar, P.; 1987: Relative motion of the Nazca (Farallon) and South American plates since Late Cretaceous time, Tectonics 6, pp. 233-248

Pariso, J. E., Johnson, H. P.; 1993a: Do lower crustal rocks record reversals of the Earths magnetic field? Magnetic petrology of oceanic gabbros from Ocean Drilling Program Hole 735B, J. Geophys. Res. 98, B9, pp. 16013-16032

Pariso, J. E., Johnson, H. P.; 1993b: Do Layer 3 Rocks Make a Significant Contribution to Marine Magnetic Anomalies? In Situ Magnetization of Gabbros at Ocean Drilling Program Hole 735B, J. Geophys. Res. 98, B9, pp. 16033-16052

Pilger, R. H.; 1981: Plate reconstructions, aseismic ridges, and low-angle subduction beneath the Andes, Geol. Soc. Am. Bull. 92, pp. 448-456

Pilger, R. H.; 1984: Cenozoic plate kinematics, subduction and magmatism: South American Andes, Journal of the Geological Society of London 141, pp. 793-802

Pilger, R. H., Handschumacher, D. W.; 1981: The Fixed Hotspot Hypothesis and the Origin of the Easter-Sala y Gomez-Nazca Trace, Bull. Geol. Soc. Am. 92, pp. 437-446

Prince, R. A., Kulm, L. D.; 1975: Crustal rupture and initiation of imbricate thrusting in the Peru-Chile Trench, Geol. Soc. Am. Bull. 86, pp. 1639-1653

Rangarajan, G. K.; 1989: Indices of magnetic activity, in: Jacobs, I. A.: Geomagnetism, Academic, San Diego

Resig, J. M.; 1990: Benthic foraminiferal stratigraphy and paleoenvironments off Peru, Leg 112; in: Suess, E., von Huene, R., et al.: Proc. Ocean Drilling Program (ODP), Sci. Results 112, College Station, TX, pp. 263–296

Roeder, D.; 1988: Andean-age structure of Eastern Cordillera (Province of La Paz, Bolivia), Tectonics 7, pp. 23-39

Roeser, H. A.; 2000: Die Interpretation seemagnetischer Messungen, Mitteilungen - Deutsche Geophysikalische Gesellschaft, Sonderband 1, pp. 25-36

Rosa, J. W. C., Molnar, P.; 1988: Uncertainties in reconstructions of the Pacific, Farallon, Vancouver, and Kula plates and constraints on the rigidity of the Pacific and Farallon (and Vancouver) plates between 72 and 35 Ma, J. Geophys. Res. 93, pp. 2997-3008

Russo, R. M., Silver, P. G.; 1994: Trench-parallel flow beneath the Nazca plate from seismic anisotropy, Science 263, pp. 1105-1111

Rutland, R. W. R.; 1971: Andean orogeny and ocean sea floor spreading, Nature 223, pp. 252-255

Sacks, I. S.; 1983: The subduction of young lithosphere, J. Geophys. Res. 88, B4, pp. 3355-3366

Sandwell, D. T.; 1992: Antarctic marine gravity field from high-density satellite altimetry, Geophys. J. Int. 109, pp. 437-438

Sandwell, D. T., Smith, W. H. F.; 1997a: Marine gravity anomaly from Geosat and ERS 1 satellite altimetry, J. Geophys. Res. 102, No. B5, p. 10039

Sandwell, D. T., Smith, W. H. F.; 1997b: Exploring the ocean basins with satellite altimeter data, http://topex.ucsd.edu/marine_grav/explore_grav.html

Sandwell, D. T., Smith, W. H. F., Smith, S. M., Small, C.; 1997: Measured and Estimated Seafloor Topography, http://topex.ucsd.edu/marine_topo/mar_topo.html

Satake, K., Tanioka, Y.; 1999: Sources of tsunami and tsunamigenic earthquakes in subduction zones, Pure Appl. Geophys. 154, pp. 467-483

Shepherd, G. L., Moberly, R.; 1981: Coastal structure of the continental margin, northwest Peru and southeast Equador, Geological Society of America Memoir 154, pp. 351-392

Scheuber, E., Bogdanic, T., Jensen, A., Reutter, K.-J.; 1994: Tectonic development of the north Chilean Andes in relation to plate convergence and magmatism since the Jurassic, in: Reutter, K.-J., Scheuber, E., Wigger, P. J. (eds.): tectonics of the Southern Central Andes, Springer, Berlin, Heidelber, New York, pp. 121-139

Schmitz, M., Lessel, K., Giese, P., Wigger, P., Araneda, M., Bribach, J., Graeber, F., Grunewald, S., Haberland, C., Lüth, S., Röwer, P., Ryberg, T. Schulze, A.; 1999: The crustal structure beneath the Central Andean forearc and magmatic arc as derived from seismic studies - the PISCO 94 experiment in northern Chile (21-23˚S), Journal of South American Earth Sciences 12, pp. 237-260

Scholl, D. W., Christensen, M. N., von Huene, R., Marlow, M. S.; 1970: Peru-Chile trench sediments and sea-floor spreading, Geol. Soc. Am. Bull. 81, pp. 1339-1360

Schreckenberger, B.; 1998: Magnetic modelling, Bundesanstalt für Geowissenschaften und Rohstoffe Hannover, Archiv-Nr. BGR 117 613, pp. 147-162

Schweller, W. J., Kulm, L. D., Prince, R. A.; 1981: Tectonics, structure, and sedimentary framework of the Peru-Chile trench. In Kulm, L. D., Dymond, J., Dasch, E. J., Hussong, D. M., Roderick, R. (eds.): Nazca Plate: Crustal Formation and Andean Convergence, Mem. Geol. Soc. Am. 154, pp. 232-349

Sheffels, B.; 1990: Lower bound on the amount of crustal shortening in the central Bolivian Andes, Geology 18, pp. 812-815

Silver, P. G., Russo, R. M., Lithgow-Bertelloni, C.; 1998: Coupling of Southern American and African plate motion and plate deformation, Science 279, pp. 60-63

Somoza, R.; 1998: Updated Nazca (Farallon)-South America relative motions during the last 40 My: implications for mountain building in the central Andean region, J. South Am. Earth Sci. 11, pp. 211-215

Sosson, M., Bourgois, J., Mercier de Lépinay, B.; 1994: SeaBeam and deep-sea submersible Nautile surveys in the Chiclayo canyon off Peru (7˚S): subsidence and subduction - erosion of an Andean-type convergent margin since Pliocene times, Marine Geology 118, pp. 237-256

Spence, W., Mendoza, C., Engdahl, E. R, Choy, G. L., Norabuena, E.; 1999: Seismic subduction of the Nazca Ridge as shown by the 1996-97 Peru earthquakes, Pure Appl. Geophys. 154, pp. 753-776

Suess, E., Kulm, L. D., Killingley, J. S.; 1987: Coastal upwelling and a history of organic-rich mudstone deposition off Peru, in: Brooks, J., Fleet, A. J. (eds.), Marine Petroleum Source Rocks, Geol. Soc. London Spec. Publ. 24, pp. 181-197

Suess E., von Huene, R., Leg 112 Shipboard Scientists; 1988: Introduction, objectives, and principal results, Leg 112, Peru continental margin, Proc. Ocean Drilling Program (ODP), Init. Reports 112, College Station, TX, pp. 5-23

Swenson, J. L., Beck, S. L.; 1999: Source Characteristics of the 12 November 1996 Mw 7.7 Peru Subduction Zone Earthquake, Pure Appl. Geophys. 154, pp. 731-751

Telford, W. M., Geldart, L. P., Sheriff, R. E.; 1990: Applied Geophysics, Second Edition, Cambridge University Press, p. 74

Thornburg, T. M.; 1985: Seismic stratigraphy of Peru forearc basins, in: Hussong, D. M., Dang, S. P., Kulm, L. D., Couch, R. W., Hilde, T. W. C. (eds.): Atlas of the Ocean Margin Program, Peru Continental Margin, Region VI: Woods Hole (Marine Science International) 16

Thornburg, T. M., Kulm, L. D.; 1981: Sedimentary basins of the Peru continental margin: structure, stratigraphy, and Cenozoic tectonics from 6˚S to 16˚S latitude, in: Kulm, L. D., Dymond, J., Dasch, E. J., Hussong, D. M. (eds.): Nazca Plate Crustal Formation and Andean Convergence, Geol. Soc. Am. Mem. 154, pp. 469-508

Thorpe, R. S., Francis, P. W., Hammill, M., Baker, M. C. W.; 1982: The Andes, in Thorpe, R. S. (ed.): Andesites: Orogenic Andesites and Related Rocks, John Wiley and Sons, Chichester, U.K., pp. 187-206

Uyeda, S.; 1982: Subduction zones: an introduction to comparative subductology, Tectonophysics 81, pp. 133-159

Vine, F. J., Matthews, D. H.; 1963: Magnetic anomalies over oceanic ridges, Nature 199, pp. 947-949

Wagner, M., Hübscher, Ch., Greinert, J., Kukowski, N., Pecher, I., Bialas, J.; 2001: BSR und Bright Spot Verteilung im Yaquina Forearc Becken vor Peru, 61. Jahrestagung der DGG, Frankfurt am Main, Marine Geophysik

Warsi, W. E. K., Hilde, T. W. C., Searle, R. C.; 1983: Convergence structures of the peru Trench between 10°S and 14°S, in: Hilde, T. W. C., Uyeda, S. (eds.): Convergence and Subduction, Tectonophysics 99, pp. 313-329

Watts, A. B., Lamb, S. H., Fairhead, J. D. Dewey, J. F.; 1995: Lithospheric flexure and bending of the Central Andes, Earth and Planetary Science Letters 134, pp. 9-21

Wessel, P., Smith, W. H. F.; 2001: GMT - The Generic Mapping Tools, http://gmt.soest.hawaii.edu

Williams, T., Louvel, V., Lauer-Leredde, C.; 2002: Magnetic Polarity Stratigraphy from Downhole Logs, West Antarctic Peninsula, ODP Leg 178, in: Barker, P.F., Camerlenghi, A., Acton, G. D., Ramsay, A. T. S. (eds.): Proc. ODP, Sci. Results 178 (Online), http://odp.pangaea.de:8000/publications/178_SR/chap_31/c31_.htm

Wilson, M.; 1989: Igneous Petrogenesis: A Global Tectonic Approach, Unwin Hyman

Worm, H. U., Böhm, V., Bosum, W.; 1996: 24. Implications for the Sources of Marine Magnetic Anomalies derived from Magnetic Logging in Holes 504B and 896A, Proceedings of the Ocean Drilling Program, Scientific Results 148, pp. 331-338

Yamano, M., Uyeda, S.; 1990: Heat-Flow Studies in the Peru Trench Subduction Zone, Proceedings of the Ocean Drilling Program, Scientific Results 112, pp. 653-661

Yañez, G. A., Ranero, C. R., von Huene, R., Diaz, J.; 2001: Magnetic anomaly interpretation across the southern central Andes (32°-34°S): The role of the Juan Fernandez Ridge in the late Tertiary evolution of the margin, J. Geophys. Res. 106, B4, pp. 6325-6345

Data Resources

Magnetic storm data from:
Danish Meteorological Institute, Solar-Terrestrial Physics Division
World Data Center for Geomagnetism, Copenhagen,
http://web.dmi.dk/fsweb/cgi-bin/webin_wdcget.sh

Geomagnetic indices downloaded at:
ftp://ftp.ngdc.noaa.gov/STP/GEOMAGNETIC_DATA/INDICES/
http://www.gfz-potsdam.de/pb2/pb23/GeoMag/niemegk/kp_index/quietdst/

Declination and inclination calculated at:
World Data Center for Solid Earth Geophysics - A, maintained by the National Oceanic and Atmospheric Administration (NOAA)
http://www.ngdc.noaa.gov/cgi-bin/seg/gmag/fldsnth1.pl

Magnetic time scales:
http://deeptow.whoi.edu/gpts.html

Magnetic lineation and fracture zone data from:
National Geophysical Data Center (NOAA): Global Relief Data CD-ROM, 1993

Seismology:
http://neic.usgs.gov/neis/epic/epic_rect.html

Volcanism:
http://www.volcano.si.edu/gvp/volcdata/index.htm

Satellite topography and gravity data:
http://topex.ucsd.edu/cgi-bin/get_data.cgi

Ocean floor age data:
ftp://beryl.es.su.oz.au/pub/agegrid/
age_1.6.grd (2001)

Tectonic plate reconstructions:
http://www.odsn.de

Data from the Deep Sea Drilling Project (DSDP):
ftp://ftp.ngdc.noaa.gov/MGG/geology/dsdp/data/34/321/holeinfo.html

GEODAS data base:
Geodas marine geological and geophysical data from U.S. Department of Commerce NOAA and NGDC, CDROM, 1992

Appendix

In the following a detailed comparison of the conversions from seismic p-wave velocities to densities for the different three-dimensional models is provided.

Table 7: The Velocity-Density Conversions of the Nazca Ridge Model

Layer	x-axis [km]	p-wave velocities [km/s] top-bottom	average p-wave velocity [km/s]	Nafe & Drake density [g/cm^3]	average Nafe & Drake density [g/cm^3]	Carlson & Raskin density [g/cm^3]	average Carlson & Raskin density [g/cm^3]
Water	0.000	1.5-1.5	1.5				
	176.791	1.5-1.5	1.5				
Sediments 1	0.000	1.6-1.8	1.7	1.44-2.05	1.73		
	176.791	1.6-1.8	1.7	1.44-2.05	1.73		
Sediments 2	108.965	1.80-1.80	1.80	1.54-2.13	1.80		
	109.385	1.90-1.90	1.90	1.62-2.18	1.86		
	109.805	2.00-2.00	2.00	1.68-2.20	1.92		
	110.638	2.10-2.10	2.10	1.73-2.22	1.98		
	110.917	2.20-2.20	2.20	1.79-2.24	2.01		
	111.196	2.30-2.30	2.30	1.83-2.27	2.03		
	111.474	2.40-2.40	2.40	1.87-2.29	2.06		
	111.753	2.50-2.50	2.50	1.92-2.31	2.09		
	112.032	2.50-2.55	2.53	1.93-2.32	2.10		
	112.311	2.50-2.55	2.53	1.93-2.32	2.10		
	112.590	2.50-2.60	2.55	1.94-2.32	2.10		
	112.868	2.50-2.65	2.58	1.95-2.32	2.11		
	113.147	2.50-2.70	2.60	1.96-2.33	2.11		
	113.426	2.50-2.75	2.63	1.97-2.33	2.12		
	113.705	2.50-2.80	2.65	1.98-2.34	2.12		
	113.983	2.50-2.85	2.68	1.99-2.34	2.13		
	114.262	2.50-2.90	2.70	2.00-2.34	2.13		
	114.541	2.50-2.95	2.73	2.01-2.34	2.14		
	115.027	2.50-3.00	2.75	2.02-2.35	2.14		
	176.791	2.50-3.00	2.75	2.02-2.35	2.14		

Table 7: The Velocity-Density Conversions of the Nazca Ridge Model

Layer	x-axis [km]	p-wave velocities [km/s] top-bottom	average p-wave velocity [km/s]	Nafe & Drake density [g/cm^3]	average Nafe & Drake density [g/cm^3]	Carlson & Raskin density [g/cm^3]	average Carlson & Raskin density [g/cm^3]
Sediments 3	108.965	1.80-1.80	1.80	1.54-2.13	1.80		
	110.027	2.00-2.00	2.00	1.68-2.20	1.92		
	111.089	2.20-2.20	2.20	1.79-2.24	2.01		
	111.620	2.40-2.40	2.40	1.87-2.29	2.06		
	112.150	2.60-2.60	2.60	1.96-2.33	2.11		
	112.681	3.00-3.05	3.03	2.09-2.39	2.22		
	112.947	3.30-3.30	3.30	2.13-2.42	2.26		
	113.212	3.50-3.50	3.50	2.16-2.46	2.30		
	113.743	3.50-3.50	3.50	2.16-2.46	2.30		
	114.008	3.50-3.55	3.53	2.17-2.47	2.31		
	114.539	3.50-3.55	3.53	2.17-2.47	2.31		
	114.805	3.50-3.60	3.55	2.17-2.48	2.31		
	115.070	3.50-3.60	3.55	2.17-2.48	2.31		
	115.336	3.50-3.65	3.58	2.18-2.49	2.32		
	115.866	3.50-3.70	3.60	2.18-2.50	2.32		
	116.397	3.50-3.75	3.63	2.18-2.51	2.33		
	116.928	3.50-3.80	3.65	2.19-2.51	2.33		
	117.459	3.50-3.90	3.70	2.19-2.52	2.34		
	117.945	3.50-3.90	3.70	2.19-2.52	2.34		
	118.431	3.50-4.00	3.75	2.20-2.53	2.35		
	150.706	3.50-4.00	3.75	2.20-2.53	2.35		
	151.210	4.00-4.00	4.00	2.24-2.60	2.39		
	176.791	4.00-4.00	4.00	2.24-2.60	2.39		
Continental Crust 1	118.431	4.00-4.00	4.00	2.24-2.60	2.39		
	120.377	4.00-4.00	4.00	2.24-2.60	2.39		
	121.349	4.10-4.10	4.10	2.26-2.62	2.41		
	121.836	4.10-4.15	4.13	2.26-2.62	2.42		
	122.322	4.20-4.30	4.15	2.27-2.63	2.42		
	122.808	4.20-4.35	4.28	2.28-2.64	2.44		
	123.295	4.20-4.40	4.30	2.29-2.65	2.44		
	123.781	4.20-4.45	4.33	2.30-2.66	2.45		
	124.267	4.20-4.50	4.35	2.30-2.66	2.45		
	176.791	4.20-4.50	4.35	2.30-2.66	2.45		

Table 7: The Velocity-Density Conversions of the Nazca Ridge Model

Layer	x-axis [km]	p-wave velocities [km/s] top-bottom	average p-wave velocity [km/s]	Nafe & Drake density [g/cm^3]	average Nafe & Drake density [g/cm^3]	Carlson & Raskin density [g/cm^3]	average Carlson & Raskin density [g/cm^3]
Continental Crust 2	122.322	4.30-4.30	4.30	2.29-2.65	2.44		
	123.295	4.40-4.40	4.40	2.31-2.67	2.46		
	124.754	4.45-4.45	4.45	2.32-2.68	2.47		
	126.213	4.50-4.50	4.50	2.32-2.69	2.48		
	126.942	4.65-4.65	4.65	2.34-2.71	2.51		
	127.671	4.80-4.80	4.80	2.35-2.72	2.53		
	129.130	4.80-4.85	4.83	2.35-2.72	2.54		
	130.103	4.80-4.90	4.85	2.35-2.73	2.54		
	132.048	4.80-4.90	4.85	2.35-2.73	2.54		
	133.021	4.80-5.00	4.90	2.35-2.73	2.55		
	135.921	4.80-5.00	4.90	2.35-2.73	2.55		
	136.843	4.80-5.10	4.95	2.36-2.74	2.56		
	139.830	4.80-5.10	4.95	2.36-2.74	2.56		
	140.803	4.80-5.20	5.00	2.36-2.74	2.57		
	145.666	4.80-5.20	5.00	2.36-2.74	2.57		
	146.674	4.80-5.30	5.05	2.36-2.74	2.58		
	150.706	4.80-5.30	5.05	2.36-2.74	2.58		
	151.714	4.80-5.40	5.10	2.36-2.74	2.59		
	154.576	4.80-5.40	5.10	2.36-2.74	2.59		
	155.421	4.80-5.50	5.15	2.37-2.75	2.60		
	176.791	4.80-5.50	5.15	2.37-2.75	2.60		

Table 7: The Velocity-Density Conversions of the Nazca Ridge Model

Layer	x-axis [km]	p-wave velocities [km/s] top-bottom	average p-wave velocity [km/s]	Nafe & Drake density [g/cm^3]	average Nafe & Drake density [g/cm^3]	Carlson & Raskin density [g/cm^3]	average Carlson & Raskin density [g/cm^3]
2A	0.000	3.50-3.90	3.70	2.19-2.52	2.34	2.25-2.70	2.48
	96.699	3.50-3.90	3.70	2.19-2.52	2.34	2.25-2.70	2.48
	98.929	3.50-3.85	3.70	2.19-2.52	2.34	2.25-2.70	2.48
	101.159	3.50-3.85	3.70	2.19-2.52	2.34	2.25-2.70	2.48
	103.390	3.50-3.90	3.70	2.19-2.52	2.34	2.25-2.70	2.48
	105.620	3.55-3.95	3.75	2.20-2.53	2.35	2.26-2.72	2.49
	106.735	3.55-3.95	3.75	2.20-2.53	2.35	2.26-2.72	2.49
	107.850	3.60-4.00	3.80	2.21-2.54	2.36	2.28-2.73	2.51
	114.534	3.60-4.00	3.80	2.21-2.54	2.36	2.28-2.73	2.51
	115.514	3.70-4.10	3.90	2.23-2.58	2.38	2.30-2.75	2.53
	116.486	3.80-4.10	3.95	2.24-2.59	2.39	2.32-2.77	2.54
	117.459	3.90-4.20	4.05	2.25-2.61	2.40	2.34-2.79	2.57
	118.431	3.90-4.20	4.05	2.25-2.61	2.40	2.34-2.79	2.57
	119.404	4.00-4.20	4.10	2.26-2.62	2.41	2.35-2.80	2.58
	120.372	4.00-4.20	4.10	2.26-2.62	2.41	2.35-2.80	2.58
	121.349	4.10-4.30	4.20	2.27-2.63	2.43	2.37-2.82	2.60
	122.322	4.30-4.50	4.40	2.31-2.67	2.46	2.42-2.86	2.64
	123.295	4.40-4.60	4.50	2.32-2.69	2.48	2.44-2.88	2.66
	124.267	4.40-4.60	4.50	2.32-2.69	2.48	2.44-2.88	2.66
	125.423	4.50-4.70	4.60	2.33-2.70	2.50	2.45-2.90	2.68
	126.580	4.60-4.80	4.70	2.34-2.71	2.52	2.47-2.91	2.70
	127.369	4.70-4.90	4.80	2.35-2.72	2.53	2.49-2.93	2.71
	128.158	4.80-5.00	4.90	2.35-2.73	2.55	2.51-2.95	2.73
	129.130	4.85-5.05	4.95	2.36-2.74	2.56	2.51-2.95	2.74
	130.103	4.90-5.10	5.00	2.36-2.74	2.57	2.52-2.96	2.74
	132.048	4.90-5.10	5.00	2.36-2.74	2.57	2.52-2.96	2.74
	133.021	5.00-5.20	5.10	2.36-2.74	2.59	2.54-2.98	2.76
	135.939	5.00-5.20	5.10	2.36-2.74	2.59	2.54-2.98	2.76
	136.912	5.10-5.30	5.20	2.37-2.75	2.61	2.55-2.99	2.77
	140.672	5.10-5.30	5.20	2.37-2.75	2.61	2.55-2.99	2.77
	141.514	5.20-5.40	5.30	2.37-2.76	2.62	2.57-3.00	2.79
	145.666	5.20-5.40	5.30	2.37-2.76	2.62	2.57-3.00	2.79
	146.663	5.30-5.50	5.40	2.38-2.77	2.64	2.58-3.02	2.80
	150.701	5.30-5.50	5.40	2.38-2.77	2.64	2.58-3.02	2.80
	151.714	5.40-5.60	5.50	2.39-2.78	2.66	2.59-3.03	2.81
	154.576	5.40-5.60	5.50	2.39-2.78	2.66	2.59-3.03	2.81
	155.421	5.50-5.70	5.60	2.40-2.79	2.68	2.61-3.04	2.83
	176.791	5.50-5.70	5.60	2.40-2.79	2.68	2.61-3.04	2.83

Table 7: The Velocity-Density Conversions of the Nazca Ridge Model

Layer	x-axis [km]	p-wave velocities [km/s] top-bottom	average p-wave velocity [km/s]	Nafe & Drake density [g/cm^3]	average Nafe & Drake density [g/cm^3]	Carlson & Raskin density [g/cm^3]	average Carlson & Raskin density [g/cm^3]
2B	0.000	4.50-5.00	4.75	2.35-2.72	2.53	2.48-2.92	2.70
	110.081	4.50-5.00	4.75	2.35-2.72	2.53	2.48-2.92	2.70
	112.311	4.60-5.00	4.80	2.35-2.72	2.53	2.49-2.93	2.71
	116.486	4.60-5.00	4.80	2.35-2.72	2.53	2.49-2.93	2.71
	118.431	4.65-5.00	4.83	2.35-2.72	2.53	2.49-2.94	2.72
	120.377	4.65-5.00	4.83	2.35-2.72	2.53	2.49-2.94	2.72
	122.322	4.70-5.10	4.90	2.35-2.73	2.55	2.51-2.95	2.73
	123.569	4.70-5.10	4.90	2.35-2.73	2.55	2.51-2.95	2.73
	124.815	4.80-5.10	4.95	2.36-2.74	2.56	2.51-2.95	2.74
	126.062	4.90-5.20	5.05	2.36-2.74	2.58	2.53-2.97	2.75
	127.309	5.00-5.30	5.15	2.37-2.75	2.60	2.54-2.98	2.77
	128.555	5.10-5.30	5.20	2.37-2.75	2.61	2.55-2.99	2.77
	129.802	5.20-5.40	5.30	2.37-2.76	2.62	2.57-3.00	2.79
	132.295	5.20-5.40	5.30	2.37-2.76	2.62	2.57-3.00	2.79
	134.323	5.30-5.50	5.40	2.38-2.77	2.64	2.58-3.02	2.80
	136.351	5.40-5.60	5.50	2.39-2.78	2.66	2.59-3.03	2.81
	140.408	5.40-5.60	5.50	2.39-2.78	2.66	2.59-3.03	2.81
	141.637	5.50-5.70	5.60	2.40-2.79	2.68	2.61-3.04	2.83
	145.324	5.50-5.70	5.60	2.40-2.79	2.68	2.61-3.04	2.83
	146.553	5.60-5.80	5.70	2.41-2.80	2.70	2.62-3.05	2.84
	150.241	5.60-5.80	5.70	2.41-2.80	2.70	2.62-3.05	2.84
	152.761	5.70-5.90	5.80	2.42-2.82	2.72	2.63-3.06	2.85
	154.021	5.70-5.90	5.80	2.42-2.82	2.72	2.63-3.06	2.85
	155.281	5.80-6.00	5.90	2.43-2.86	2.74	2.64-3.07	2.86
	176.791	5.80-6.00	5.90	2.43-2.86	2.74	2.64-3.07	2.86
2C	0.000	5.20-5.70	5.45	2.39-2.78	2.65	2.59-3.02	2.81
	105.620	5.20-5.70	5.45	2.39-2.78	2.65	2.59-3.02	2.81
	107.850	5.30-5.80	5.55	2.40-2.79	2.67	2.60-3.04	2.82
	116.176	5.30-5.80	5.55	2.40-2.79	2.67	2.60-3.04	2.82
	117.812	5.35-5.85	5.60	2.40-2.79	2.68	2.61-3.04	2.83
	119.447	5.35-5.85	5.60	2.40-2.79	2.68	2.61-3.04	2.83
	121.083	5.35-5.90	5.63	2.40-2.79	2.69	2.61-3.04	2.83
	122.718	5.40-5.90	5.65	2.41-2.80	2.69	2.61-3.05	2.83
	124.353	5.40-5.90	5.65	2.41-2.80	2.69	2.61-3.05	2.83
	125.989	5.50-5.90	5.70	2.41-2.80	2.70	2.62-3.05	2.84
	128.439	5.50-5.90	5.70	2.41-2.80	2.70	2.62-3.05	2.84
	129.253	5.60-6.00	5.80	2.42-2.82	2.72	2.63-3.06	2.85
	134.139	5.60-6.00	5.80	2.42-2.82	2.72	2.63-3.06	2.85
	135.768	5.70-6.10	5.90	2.43-2.86	2.74	2.64-3.07	2.86
	140.653	5.70-6.10	5.90	2.43-2.86	2.74	2.64-3.07	2.86
	142.282	5.80-6.20	6.00	2.44-2.88	2.77	2.65-3.09	2.87
	143.911	5.80-6.20	6.00	2.44-2.88	2.77	2.65-3.09	2.87
	145.539	5.90-6.20	6.05	2.47-2.89	2.79	2.66-3.09	2.88
	150.425	5.90-6.20	6.05	2.47-2.89	2.79	2.66-3.09	2.88
	152.054	6.00-6.30	6.15	2.51-2.92	2.82	2.67-3.10	2.89
	153.683	6.00-6.30	6.15	2.51-2.92	2.82	2.67-3.10	2.89
	155.219	6.10-6.40	6.25	2.53-2.95	2.84	2.68-3.11	2.90
	176.791	6.10-6.40	6.25	2.53-2.95	2.84	2.68-3.11	2.90

Table 7: The Velocity-Density Conversions of the Nazca Ridge Model

Layer	x-axis [km]	p-wave velocities [km/s] top-bottom	average p-wave velocity [km/s]	Nafe & Drake density [g/cm^3]	average Nafe & Drake density [g/cm^3]	Carlson & Raskin density [g/cm^3]	average Carlson & Raskin density [g/cm^3]
3A	0.000	6.20-6.60	6.40	2.58-2.99	2.87	2.69-3.12	2.91
	98.929	6.20-6.60	6.40	2.58-2.99	2.87	2.69-3.12	2.91
	101.074	6.25-6.65	6.45	2.61-3.04	2.89	2.70-3.13	2.91
	103.390	6.25-6.65	6.45	2.61-3.04	2.89	2.70-3.13	2.91
	105.620	6.30-6.70	6.50	2.61-3.04	2.90	2.70-3.13	2.92
	116.176	6.30-6.70	6.50	2.61-3.04	2.90	2.70-3.13	2.92
	117.812	6.35-6.75	6.55	2.63-3.06	2.92	2.71-3.14	2.92
	121.083	6.35-6.75	6.55	2.63-3.06	2.92	2.71-3.14	2.92
	124.353	6.40-6.80	6.60	2.64-3.08	2.93	2.71-3.14	2.93
	145.539	6.40-6.80	6.60	2.64-3.08	2.93	2.71-3.14	2.93
	147.168	6.45-6.85	6.65	2.65-3.10	2.94	2.87-2.95	2.93
	150.425	6.45-6.85	6.65	2.65-3.10	2.94	2.87-2.95	2.93
	153.683	6.50-6.90	6.70	2.66-3.11	2.95	2.88-2.95	2.92
	176.791	6.50-6.90	6.70	2.66-3.11	2.95	2.88-2.95	2.92
3B	0.000	6.70-7.50	7.10	2.80-3.24	3.07	2.93-3.00	2.97
	98.929	6.70-7.50	7.10	2.80-3.24	3.07	2.93-3.00	2.97
	101.159	6.75-7.55	7.15	2.85-3.26	3.09	2.94-3.01	2.98
	103.390	6.75-7.55	7.15	2.85-3.26	3.09	2.94-3.01	2.98
	105.620	6.80-7.60	7.20	2.90-3.28	3.10	2.94-3.01	2.98
	116.176	6.80-7.60	7.20	2.90-3.28	3.10	2.94-3.01	2.98
	117.812	6.85-7.65	7.25	2.94-3.30	3.12	2.95-3.02	2.99
	121.083	6.85-7.65	7.25	2.94-3.30	3.12	2.95-3.02	2.99
	124.353	6.90-7.70	7.30	2.97-3.32	3.13	2.95-3.02	2.99
	143.911	6.90-7.70	7.30	2.97-3.32	3.13	2.95-3.02	2.99
	147.168	6.95-7.75	7.35	3.00-3.34	3.15	2.96-3.03	3.00
	150.425	6.95-7.75	7.35	3.00-3.34	3.15	2.96-3.03	3.00
	153.683	7.00-7.80	7.40	3.02-3.35	3.16	2.97-3.04	3.01
	176.791	7.00-7.80	7.40	3.02-3.35	3.16	2.97-3.04	3.01
Mantle	0.000	7.90-8.00	7.95	3.13-3.40	3.33		
	130.103	7.90-8.00	7.95	3.13-3.40	3.33		
	134.331	7.95-8.05	8.00	3.13-3.40	3.34		
	138.559	7.95-8.05	8.00	3.13-3.40	3.34		
	142.787	8.00-8.10	8.05	3.14-3.40	3.36		
	176.791	8.00-8.10	8.05	3.14-3.40	3.36		

Table 8: The Velocity-Density Conversions of the Lima Area Model

Layer	x-axis [km]	p-wave velocities [km/s] top-bottom	average p-wave velocity [km/s]	Nafe & Drake density [g/cm^3]	average Nafe & Drake density [g/cm^3]	Carlson & Raskin density [g/cm^3]	average Carlson & Raskin density [g/cm^3]
Water	0.000	1.50-1.50	1.50		1.04		
	230.000	1.50-1.50	1.50		1.04		

Table 8: The Velocity-Density Conversions of the Lima Area Model

Layer	x-axis [km]	p-wave velocities [km/s] top-bottom	average p-wave velocity [km/s]	Nafe & Drake density [g/cm^3]	average Nafe & Drake density [g/cm^3]	Carlson & Raskin density [g/cm^3]	average Carlson & Raskin density [g/cm^3]
Sediments 1	0.000	1.70-2.00	1.85	1.58-2.16	1.83		
	53.910	1.70-2.00	1.85	1.58-2.16	1.83		
	55.700	1.60-2.00	1.80	1.54-2.13	1.80		
	57.500	1.70-2.00	1.85	1.58-2.16	1.83		
	76.540	1.70-2.00	1.85	1.58-2.16	1.83		
	78.970	1.70-1.90	1.80	1.54-2.13	1.80		
	87.660	1.70-1.90	1.80	1.54-2.13	1.80		
	89.060	1.60-1.90	1.75	1.54-2.13	1.77		
	90.470	1.60-1.80	1.70	1.44-2.05	1.73		
	93.570	1.60-1.80	1.70	1.44-2.05	1.73		
	95.270	1.70-1.90	1.80	1.54-2.13	1.80		
	230.000	1.70-1.90	1.80	1.54-2.13	1.80		
Sediments 2	86.250	2.10-3.50	2.80	2.04-2.35	2.15		
	87.660	2.00-2.10	2.05	1.73-2.22	1.95		
	89.060	2.00-2.10	2.05	1.73-2.22	1.95		
	90.470	1.90-2.00	1.95	1.68-2.20	1.89		
	95.270	1.90-2.00	1.95	1.68-2.20	1.89		
	97.350	2.00-2.30	2.15	1.76-2.23	2.00		
	99.750	2.00-2.60	2.30	1.83-2.27	2.03		
	102.140	2.10-2.60	2.35	1.87-2.29	2.05		
	110.970	2.10-2.60	2.35	1.87-2.29	2.05		
	115.000	2.10-3.50	2.30	1.83-2.27	2.03		
	117.091	2.10-3.00	2.55	1.94-2.32	2.10		
	119.060	2.10-2.50	2.30	1.83-2.27	2.03		
	120.955	2.10-2.40	2.25	1.83-2.27	2.02		
	122.850	2.10-2.30	2.20	1.79-2.24	2.01		
	130.895	2.10-2.30	2.20	1.79-2.24	2.01		
	135.150	2.15-2.25	2.20	1.79-2.24	2.01		
	137.262	2.15-2.25	2.20	1.79-2.24	2.01		
	139.400	2.15-2.35	2.25	1.83-2.27	2.02		
	143.650	2.18-2.30	2.24	1.79-2.24	2.02		
	150.860	2.18-2.30	2.24	1.79-2.24	2.02		
	158.070	2.18-2.35	2.27	1.83-2.27	2.02		
	165.290	2.20-2.40	2.30	1.83-2.27	2.03		
	172.500	2.20-2.40	2.30	1.83-2.27	2.03		
	179.690	2.20-2.30	2.25	1.83-2.27	2.02		
	186.880	2.20-2.30	2.25	1.83-2.27	2.02		
	194.060	2.29-2.35	2.32	1.83-2.27	2.04		
	201.220	2.25-2.32	2.29	1.83-2.27	2.03		
	204.840	2.30-2.40	2.35	1.87-2.29	2.05		
	208.440	2.50-2.60	2.55	1.94-2.32	2.10		
	215.620	2.30-2.40	2.35	1.87-2.29	2.05		
	230.000	2.30-2.40	2.35	1.87-2.29	2.05		

Table 8: The Velocity-Density Conversions of the Lima Area Model

Layer	x-axis [km]	p-wave velocities [km/s] top-bottom	average p-wave velocity [km/s]	Nafe & Drake density [g/cm^3]	average Nafe & Drake density [g/cm^3]	Carlson & Raskin density [g/cm^3]	average Carlson & Raskin density [g/cm^3]
Sediments 3	87.660	2.20-2.30	2.25	1.83-2.27	2.02		
	89.060	2.10-2.20	2.15	1.79-2.24	2.00		
	93.570	2.10-2.20	2.15	1.79-2.24	2.00		
	95.270	2.20-2.50	2.35	1.87-2.29	2.05		
	97.350	2.20-2.00	2.10	1.73-2.22	1.98		
	99.750	2.50-3.00	2.75	2.02-2.35	2.14		
	102.660	3.80-4.00	3.90	2.23-2.58	2.38		
	104.880	4.10-4.50	4.30	2.29-2.65	2.44		
	107.100	4.30-4.60	4.45	2.32-2.68	2.47		
	111.420	4.30-4.70	4.50	2.32-2.69	2.48		
	120.400	4.30-4.70	4.50	2.32-2.69	2.48		
	124.890	4.20-4.60	4.40	2.31-2.67	2.46		
	129.970	3.00-3.30	3.15	2.12-2.41	2.24		
	136.550	3.00-3.30	3.15	2.12-2.41	2.24		
	140.330	2.90-3.20	3.05	2.10-2.40	2.22		
	144.230	3.00-3.70	3.35	2.14-2.44	2.27		
	147.680	3.35-3.80	3.58	2.18-2.50	2.32		
	149.410	3.35-3.80	3.58	2.18-2.50	2.32		
	151.170	3.40-3.90	3.65	2.19-2.51	2.33		
	154.640	3.65-4.10	3.88	2.23-2.58	2.38		
	158.110	4.20-4.70	4.45	2.32-2.68	2.47		
	161.885	4.30-4.80	4.55	2.33-2.70	2.49		
	165.660	4.40-4.90	4.65	2.34-2.71	2.51		
	169.305	4.40-4.90	4.65	2.34-2.71	2.51		
	172.950	4.50-4.90	4.70	2.34-2.71	2.52		
	179.150	4.52-4.61	4.57	2.33-2.70	2.49		
	185.480	4.50-4.60	4.55	2.33-2.70	2.49		
	192.770	4.90-5.10	5.00	2.36-2.74	2.57		
	200.610	4.62-4.75	4.69	2.34-2.71	2.52		
	204.800	5.20-5.22	5.21	2.37-2.75	2.61		
	208.600	5.35-5.50	5.43	2.38-2.77	2.65		
	215.620	5.35-5.50	5.43	2.38-2.77	2.65		
	222.810	5.30-5.60	5.45	2.39-2.78	2.65		
	230.000	5.35-5.60	5.48	2.39-2.78	2.65		

Table 8: The Velocity-Density Conversions of the Lima Area Model

Layer	x-axis [km]	p-wave velocities [km/s] top-bottom	average p-wave velocity [km/s]	Nafe & Drake density [g/cm^3]	average Nafe & Drake density [g/cm^3]	Carlson & Raskin density [g/cm^3]	average Carlson & Raskin density [g/cm^3]
Continental Crust 1	102.855	4.55-4.60	4.58	2.33-2.70	2.49		
	105.090	4.70-4.80	4.75	2.35-2.72	2.53		
	109.560	4.80-5.00	4.90	2.35-2.73	2.55		
	112.280	4.80-5.00	4.90	2.35-2.73	2.55		
	115.000	4.90-5.00	4.95	2.36-2.74	2.56		
	118.595	5.00-5.10	5.05	2.36-2.74	2.58		
	122.190	5.00-5.10	5.05	2.36-2.74	2.58		
	126.260	5.00-5.40	5.20	2.37-2.75	2.61		
	130.350	5.00-5.40	5.20	2.37-2.75	2.61		
	134.249	5.00-5.30	5.15	2.37-2.75	2.60		
	142.150	5.00-5.30	5.15	2.37-2.75	2.60		
	146.210	4.90-5.20	5.05	2.36-2.74	2.58		
	152.740	5.10-5.30	5.20	2.37-2.75	2.61		
	158.490	5.30-5.60	5.45	2.39-2.78	2.65		
	163.610	5.40-5.50	5.45	2.39-2.78	2.65		
	171.670	5.30-5.50	5.40	2.38-2.77	2.64		
	202.300	5.30-5.50	5.40	2.38-2.77	2.64		
	206.140	5.55-5.60	5.58	2.40-2.79	2.67		
	213.430	5.55-5.60	5.58	2.40-2.79	2.67		
	216.890	5.65-5.75	5.70	2.41-2.80	2.70		
	230.000	5.65-5.75	5.70	2.41-2.80	2.70		
Continental Crust 2	86.250	4.80-4.90	4.85	2.35-2.73	2.54		
	97.700	4.80-4.90	4.85	2.35-2.73	2.54		
	100.620	4.60-4.60	4.60	2.33-2.70	2.50		
	102.855	4.60-4.60	4.60	2.33-2.70	2.50		
	105.068	4.85-4.90	4.88	2.35-2.73	2.54		
	109.560	5.05-5.10	5.08	2.36-2.74	2.58		
	112.280	5.05-5.10	5.08	2.36-2.74	2.58		
	115.000	5.10-5.20	5.15	2.37-2.75	2.60		
	118.595	5.20-5.40	5.30	2.37-2.76	2.62		
	122.190	5.50-5.60	5.55	2.40-2.79	2.67		
	138.090	5.50-5.60	5.55	2.40-2.79	2.67		
Continental Crust 3	146.210	5.50-5.80	5.65	2.41-2.80	2.69		
	152.740	5.70-6.00	5.85	2.43-2.86	2.73		
	158.175	5.70-6.10	5.90	2.43-2.86	2.74		
	163.610	5.70-6.10	5.90	2.43-2.86	2.74		
	179.090	5.50-6.10	5.80	2.42-2.82	2.72		
	192.590	5.60-6.10	5.85	2.43-2.86	2.73		
	202.300	6.00-6.10	6.05	2.47-2.89	2.79		
	216.890	5.90-6.10	6.00	2.44-2.88	2.77		
	230.000	5.90-6.10	6.00	2.44-2.88	2.77		

Table 8: The Velocity-Density Conversions of the Lima Area Model

Layer	x-axis [km]	p-wave velocities [km/s] top-bottom	average p-wave velocity [km/s]	Nafe & Drake density [g/cm^3]	average Nafe & Drake density [g/cm^3]	Carlson & Raskin density [g/cm^3]	average Carlson & Raskin density [g/cm^3]
Pillow Lava	0.000	4.70-6.00	5.35	2.38-2.77	2.63	2.57-3.01	2.79
	72.600	4.70-6.00	5.35	2.38-2.77	2.63	2.57-3.01	2.79
	75.860	4.80-6.20	5.50	2.39-2.78	2.66	2.59-3.03	2.81
	82.680	4.80-6.20	5.50	2.39-2.78	2.66	2.59-3.03	2.81
	86.250	5.00-6.20	5.60	2.40-2.79	2.68	2.61-3.04	2.83
	88.920	5.30-6.20	5.75	2.42-2.82	2.71	2.62-3.06	2.84
	91.590	5.30-6.40	5.85	2.43-2.86	2.73	2.64-3.07	2.85
	94.275	5.30-6.30	5.80	2.42-2.82	2.72	2.63-3.06	2.85
	96.960	5.30-6.30	5.80	2.42-2.82	2.72	2.63-3.06	2.85
	100.865	5.30-6.20	5.75	2.42-2.82	2.71	2.62-3.06	2.84
	104.770	5.30-6.20	5.75	2.42-2.82	2.71	2.62-3.06	2.84
	107.580	5.50-6.20	5.85	2.43-2.86	2.73	2.64-3.07	2.85
	117.240	5.50-6.20	5.85	2.43-2.86	2.73	2.64-3.07	2.85
	120.630	5.70-6.20	5.95	2.44-2.88	2.76	2.65-3.08	2.86
	125.870	5.70-6.20	5.95	2.44-2.88	2.76	2.65-3.08	2.86
	132.010	5.70-6.30	6.00	2.44-2.88	2.77	2.65-3.09	2.87
	139.430	5.70-6.30	6.00	2.44-2.88	2.77	2.65-3.09	2.87
	151.460	6.35-6.45	6.40	2.58-2.99	2.87	2.69-3.12	2.91
	172.440	6.45-6.50	6.48	2.61-3.04	2.89	2.70-3.13	2.91
	195.460	6.55-6.57	6.56	2.64-3.08	2.92	2.71-3.14	2.92
	204.030	6.55-6.58	6.57	2.64-3.08	2.92	2.71-3.14	2.92
	208.320	6.55-6.59	6.57	2.64-3.08	2.92	2.71-3.14	2.92
	212.600	6.55-6.60	6.58	2.64-3.08	2.92	2.71-3.14	2.92
	230.000	6.55-6.60	6.58	2.64-3.08	2.92	2.71-3.14	2.92
Sheeted Dykes	0.000	4.70-6.00	5.35	2.38-2.77	2.63	2.57-3.01	2.79
	72.600	4.70-6.00	5.35	2.38-2.77	2.63	2.57-3.01	2.79
	75.860	4.80-6.20	5.50	2.39-2.78	2.66	2.59-3.03	2.81
	82.680	4.80-6.20	5.50	2.39-2.78	2.66	2.59-3.03	2.81
	86.250	5.00-6.20	5.60	2.40-2.79	2.68	2.61-3.04	2.83
	88.920	5.30-6.20	5.75	2.42-2.82	2.71	2.62-3.06	2.84
	91.590	5.30-6.40	5.85	2.43-2.86	2.73	2.64-3.07	2.85
	94.275	5.30-6.30	5.80	2.42-2.82	2.72	2.63-3.06	2.85
	96.960	5.30-6.30	5.80	2.42-2.82	2.72	2.63-3.06	2.85
	100.865	5.30-6.20	5.75	2.42-2.82	2.71	2.62-3.06	2.84
	104.770	5.30-6.20	5.75	2.42-2.82	2.71	2.62-3.06	2.84
	107.580	5.50-6.20	5.85	2.43-2.86	2.73	2.64-3.07	2.85
	117.240	5.50-6.20	5.85	2.43-2.86	2.73	2.64-3.07	2.85
	120.630	5.70-6.20	5.95	2.44-2.88	2.76	2.65-3.08	2.86
	125.870	5.70-6.20	5.95	2.44-2.88	2.76	2.65-3.08	2.86
	132.010	5.70-6.30	6.00	2.44-2.88	2.77	2.65-3.09	2.87
	139.430	5.70-6.30	6.00	2.44-2.88	2.77	2.65-3.09	2.87
	151.460	6.35-6.45	6.40	2.58-2.99	2.87	2.69-3.12	2.91
	172.440	6.45-6.50	6.48	2.61-3.04	2.89	2.70-3.13	2.91
	195.460	6.55-6.57	6.56	2.64-3.08	2.92	2.71-3.14	2.92
	204.030	6.55-6.58	6.57	2.64-3.08	2.92	2.71-3.14	2.92
	208.320	6.55-6.59	6.57	2.64-3.08	2.92	2.71-3.14	2.92
	212.600	6.55-6.60	6.58	2.64-3.08	2.92	2.71-3.14	2.92
	230.000	6.55-6.60	6.58	2.64-3.08	2.92	2.71-3.14	2.92

Table 8: The Velocity-Density Conversions of the Lima Area Model

Layer	x-axis [km]	p-wave velocities [km/s] top-bottom	average p-wave velocity [km/s]	Nafe & Drake density [g/cm^3]	average Nafe & Drake density [g/cm^3]	Carlson & Raskin density [g/cm^3]	average Carlson & Raskin density [g/cm^3]
Gabbros	0.000	6.50-7.20	6.85	2.71-3.19	2.99	2.90-2.97	2.94
	12.410	6.50-7.20	6.85	2.71-3.19	2.99	2.90-2.97	2.94
	24.820	6.70-7.20	6.95	2.73-3.21	3.03	2.91-2.98	2.95
	37.220	6.70-7.20	6.95	2.73-3.21	3.03	2.91-2.98	2.95
	43.430	6.70-7.30	7.00	2.73-3.21	3.04	2.92-2.99	2.95
	49.630	6.80-7.30	7.05	2.80-3.24	3.06	2.92-3.00	2.96
	54.270	6.80-7.20	7.00	2.73-3.21	3.04	2.92-2.99	2.95
	58.910	6.80-7.20	7.00	2.73-3.21	3.04	2.92-2.99	2.95
	62.380	6.70-7.20	6.95	2.73-3.21	3.03	2.91-2.98	2.95
	65.850	6.70-7.20	6.95	2.73-3.21	3.03	2.91-2.98	2.95
	72.790	6.50-7.20	6.85	2.71-3.19	2.99	2.90-2.97	2.94
	86.220	6.50-7.20	6.85	2.71-3.19	2.99	2.90-2.97	2.94
	93.845	6.70-7.20	6.95	2.73-3.21	3.03	2.91-2.98	2.95
	100.800	6.50-6.90	6.70	2.66-3.11	2.95	2.88-2.95	2.92
	112.180	6.50-6.90	6.70	2.66-3.11	2.95	2.88-2.95	2.92
	117.880	6.50-7.00	6.75	2.69-3.16	2.97	2.89-2.96	2.92
	129.580	6.50-7.00	6.75	2.69-3.16	2.97	2.89-2.96	2.92
	135.600	6.60-7.00	6.80	2.69-3.16	2.98	2.89-2.97	2.93
	141.610	6.70-7.00	6.85	2.71-3.19	2.99	2.90-2.97	2.94
	147.620	6.70-7.05	6.88	2.71-3.19	3.00	2.90-2.98	2.94
	184.984	6.70-7.05	6.88	2.71-3.19	3.00	2.90-2.98	2.94
	190.150	6.72-7.05	6.89	2.71-3.19	3.00	2.90-2.98	2.94
	195.316	6.75-7.05	6.90	2.71-3.19	3.01	2.91-2.98	2.94
	230.000	6.75-7.05	6.90	2.71-3.19	3.01	2.91-2.98	2.94
Mantle	0.000	8.05-8.15	8.10	3.14-3.40	3.38		
	31.340	8.05-8.15	8.10	3.14-3.40	3.38		
	41.760	7.95-8.10	8.03	3.13-3.40	3.35		
	52.190	7.95-8.05	8.00	3.13-3.40	3.34		
	64.740	7.95-8.05	8.00	3.13-3.40	3.34		
	75.500	7.85-7.95	7.90	3.13-3.40	3.31		
	86.250	7.85-7.90	7.88	3.13-3.40	3.30		
	230.000	7.85-7.90	7.88	3.13-3.40	3.30		

Table 9: The Velocity-Density Conversions of the Yaquina Area Model

Layer	x-axis [km]	p-wave velocities [km/s] top-bottom	average p-wave velocity [km/s]	Nafe & Drake density [g/cm^3]	average Nafe & Drake density [g/cm^3]	Carlson & Raskin density [g/cm^3]	average Carlson & Raskin density [g/cm^3]
Water	103.576	1.50-1.50	1.50		1.04		
	298.576	1.50-1.50	1.50		1.04		

Table 9: The Velocity-Density Conversions of the Yaquina Area Model

Layer	x-axis [km]	p-wave velocities [km/s] top-bottom	average p-wave velocity [km/s]	Nafe & Drake density [g/cm^3]	average Nafe & Drake density [g/cm^3]	Carlson & Raskin density [g/cm^3]	average Carlson & Raskin density [g/cm^3]
Sediments	103.576	1.70-2.00	1.85	1.58-2.16	1.83		
	196.506	1.70-2.00	1.85	1.58-2.16	1.83		
	198.029	1.70-1.90	1.80	1.54-2.13	1.80		
	213.264	1.70-1.90	1.80	1.54-2.13	1.80		
	216.310	1.70-2.10	1.90	1.62-2.18	1.86		
	222.378	1.70-2.10	1.90	1.62-2.18	1.86		
	225.399	1.70-2.00	1.85	1.58-2.16	1.83		
	237.638	1.70-2.00	1.85	1.58-2.16	1.83		
	240.685	1.75-2.00	1.88	1.62-2.18	1.85		
	251.512	1.75-2.00	1.88	1.62-2.18	1.85		
	255.920	1.70-2.00	1.85	1.58-2.16	1.83		
	298.576	1.70-2.00	1.85	1.58-2.16	1.83		
Continental Crust 1	186.389	4.00-4.50	4.25	2.29-2.65	2.44		
	194.982	4.20-4.50	4.35	2.31-2.67	2.45		
	197.003	2.10-2.30	2.20	1.79-2.24	2.01		
	198.013	2.10-2.30	2.20	1.79-2.24	2.01		
	199.024	2.00-2.30	2.15	1.76-2.23	2.00		
	208.357	2.00-2.30	2.15	1.76-2.23	2.00		
	211.468	2.10-2.70	2.40	1.87-2.29	2.06		
	214.564	2.60-3.00	2.80	2.04-2.35	2.15		
	217.660	2.80-3.50	3.15	2.12-2.41	2.24		
	227.023	2.80-3.50	3.15	2.12-2.41	2.24		
	230.134	2.80-3.20	3.00	2.09-2.38	2.21		
	233.245	2.70-3.20	2.95	2.09-2.38	2.20		
	236.356	2.80-3.20	3.00	2.09-2.38	2.21		
	239.467	2.80-3.20	3.00	2.09-2.38	2.21		
	242.578	2.70-3.20	2.95	2.09-2.38	2.20		
	248.800	2.70-3.00	2.85	2.08-2.37	2.17		
	251.893	2.70-3.00	2.85	2.08-2.37	2.17		
	254.987	2.69-3.00	2.85	2.08-2.37	2.17		
	257.576	2.70-3.00	2.85	2.08-2.37	2.17		
	261.244	2.70-3.05	2.88	2.08-2.37	2.17		
	264.355	2.60-2.90	2.75	2.02-2.35	2.14		
	267.466	2.60-2.85	2.73	2.01-2.34	2.14		
	273.688	2.60-2.85	2.73	2.01-2.34	2.14		
	279.910	2.60-2.80	2.70	2.00-2.34	2.13		
	283.021	2.60-2.65	2.63	1.97-2.33	2.12		
	298.576	2.60-2.65	2.63	1.97-2.33	2.12		

Table 9: The Velocity-Density Conversions of the Yaquina Area Model

Layer	x-axis [km]	p-wave velocities [km/s] top-bottom	average p-wave velocity [km/s]	Nafe & Drake density [g/cm^3]	average Nafe & Drake density [g/cm^3]	Carlson & Raskin density [g/cm^3]	average Carlson & Raskin density [g/cm^3]
Continental Crust 2	186.389	4.70-4.70	4.70	2.34-2.71	2.52		
	194.982	4.70-4.70	4.70	2.34-2.71	2.52		
	199.024	3.50-4.30	3.90	2.23-2.58	2.38		
	202.135	3.50-4.30	3.90	2.23-2.58	2.38		
	205.246	3.70-4.00	3.85	2.23-2.58	2.37		
	208.357	4.00-4.50	4.25	2.29-2.65	2.44		
	211.468	4.30-5.00	4.65	2.34-2.71	2.51		
	214.579	4.50-5.40	4.95	2.36-2.74	2.56		
	217.690	4.50-5.40	4.95	2.36-2.74	2.56		
	220.801	4.50-5.10	4.80	2.35-2.72	2.53		
	223.912	4.50-5.10	4.80	2.35-2.72	2.53		
	226.972	4.70-5.20	4.95	2.36-2.74	2.56		
	239.467	4.70-5.20	4.95	2.36-2.74	2.56		
	242.578	4.50-5.00	4.75	2.35-2.72	2.53		
	248.669	4.50-5.00	4.75	2.35-2.72	2.53		
	251.828	4.60-5.20	4.90	2.35-2.73	2.55		
	258.115	4.60-5.20	4.90	2.35-2.73	2.55		
	261.244	4.50-5.20	4.85	2.35-2.73	2.54		
	267.466	4.50-5.10	4.80	2.35-2.72	2.53		
	270.577	4.50-5.10	4.80	2.35-2.72	2.53		
	273.688	4.00-4.80	4.40	2.31-2.67	2.46		
	276.778	4.00-4.80	4.40	2.31-2.67	2.46		
	279.868	3.50-4.50	4.00	2.24-2.60	2.39		
	282.946	3.50-3.80	3.65	2.19-2.51	2.33		
	286.048	3.30-3.80	3.55	2.17-2.48	2.31		
	292.312	3.30-4.00	3.65	2.19-2.51	2.33		
	298.576	3.30-4.00	3.65	2.19-2.51	2.33		
Continental Crust 3	186.389	4.70-4.70	4.70	2.34-2.71	2.52		
	194.982	4.70-4.70	4.70	2.34-2.71	2.52		
	199.024	5.10-5.20	5.15	2.37-2.75	2.60		
	205.246	5.10-5.20	5.15	2.37-2.75	2.60		
	208.319	5.00-5.20	5.10	2.36-2.74	2.59		
	211.468	5.20-5.45	5.33	2.37-2.76	2.63		
	214.579	5.40-5.45	5.43	2.38-2.77	2.65		
	217.690	5.45-5.60	5.53	2.39-2.78	2.67		
	226.972	5.45-5.60	5.53	2.39-2.78	2.67		
	230.032	5.50-5.70	5.60	2.40-2.79	2.68		
	248.669	5.50-5.70	5.60	2.40-2.79	2.68		
	251.828	5.60-5.90	5.75	2.42-2.82	2.71		
Continental Crust 4	254.987	5.80-6.00	5.90	2.43-2.86	2.74		
	258.115	5.90-6.00	5.95	2.44-2.88	2.76		
	261.244	5.90-6.00	5.95	2.44-2.88	2.76		
	264.355	5.80-6.00	5.90	2.43-2.86	2.74		
	279.868	5.80-6.00	5.90	2.43-2.86	2.74		
	282.946	5.80-6.20	6.00	2.44-2.88	2.77		
	298.576	5.80-6.20	6.00	2.44-2.88	2.77		

Table 9: The Velocity-Density Conversions of the Yaquina Area Model

Layer	x-axis [km]	p-wave velocities [km/s] top-bottom	average p-wave velocity [km/s]	Nafe & Drake density [g/cm^3]	average Nafe & Drake density [g/cm^3]	Carlson & Raskin density [g/cm^3]	average Carlson & Raskin density [g/cm^3]
Pillow Lava	103.576	4.70-6.00	5.35	2.38-2.77	2.63	2.57-3.01	2.79
	106.623	4.70-6.00	5.35	2.38-2.77	2.63	2.57-3.01	2.79
	108.146	4.69-6.00	5.35	2.38-2.77	2.63	2.57-3.01	2.79
	109.670	4.70-6.00	5.35	2.38-2.77	2.63	2.57-3.01	2.79
	152.326	4.70-6.00	5.35	2.38-2.77	2.63	2.57-3.01	2.79
	158.420	4.75-6.05	5.40	2.38-2.77	2.64	2.58-3.02	2.80
	164.514	4.75-6.05	5.40	2.38-2.77	2.64	2.58-3.02	2.80
	170.607	4.70-6.00	5.35	2.38-2.77	2.63	2.57-3.01	2.79
	191.444	4.70-6.00	5.35	2.38-2.77	2.63	2.57-3.01	2.79
	194.982	5.00-6.00	5.50	2.39-2.78	2.66	2.59-3.03	2.81
	199.024	5.50-6.00	5.75	2.42-2.82	2.71	2.62-3.06	2.84
	202.135	5.50-6.00	5.75	2.42-2.82	2.71	2.62-3.06	2.84
	205.246	5.50-6.10	5.80	2.42-2.82	2.72	2.63-3.06	2.85
	208.268	5.70-6.10	5.90	2.43-2.86	2.74	2.64-3.07	2.86
	211.468	5.70-6.10	5.90	2.43-2.86	2.74	2.64-3.07	2.86
	214.579	5.70-6.20	5.95	2.44-2.88	2.76	2.65-3.08	2.86
	217.690	5.70-6.00	5.85	2.43-2.86	2.73	2.64-3.07	2.85
	226.972	5.70-6.00	5.85	2.43-2.86	2.73	2.64-3.07	2.85
	230.032	5.75-6.00	5.88	2.43-2.86	2.73	2.64-3.07	2.86
	236.356	5.75-6.00	5.88	2.43-2.86	2.73	2.64-3.07	2.86
	239.467	5.80-6.10	5.95	2.44-2.88	2.76	2.65-3.08	2.86
	242.578	5.90-6.35	6.13	2.50-2.90	2.81	2.67-3.10	2.88
	245.623	6.00-6.35	6.18	2.52-2.93	2.82	2.67-3.10	2.89
	248.669	6.00-6.45	6.23	2.52-2.93	2.84	2.68-3.11	2.89
	251.828	6.00-6.45	6.23	2.52-2.93	2.84	2.68-3.11	2.89
	254.987	6.10-6.45	6.28	2.54-2.97	2.84	2.68-3.11	2.90
	258.115	6.10-6.45	6.28	2.54-2.97	2.84	2.68-3.11	2.90
	261.244	6.20-6.50	6.35	2.58-2.99	2.86	2.69-3.12	2.90
	267.466	6.30-6.60	6.45	2.61-3.04	2.89	2.70-3.13	2.91
	276.778	6.30-6.60	6.45	2.61-3.04	2.89	2.70-3.13	2.91
	279.868	6.40-6.60	6.50	2.61-3.04	2.90	2.70-3.13	2.92
	282.946	6.50-6.70	6.60	2.64-3.08	2.93	2.71-3.14	2.93
	298.576	6.50-6.70	6.60	2.64-3.08	2.93	2.71-3.14	2.93

Table 9: The Velocity-Density Conversions of the Yaquina Area Model

Layer	x-axis [km]	p-wave velocities [km/s] top-bottom	average p-wave velocity [km/s]	Nafe & Drake density [g/cm^3]	average Nafe & Drake density [g/cm^3]	Carlson & Raskin density [g/cm^3]	average Carlson & Raskin density [g/cm^3]
Sheeted Dykes	103.576	4.70-6.00	5.35	2.38-2.77	2.63	2.57-3.01	2.79
	106.623	4.70-6.00	5.35	2.38-2.77	2.63	2.57-3.01	2.79
	108.146	4.69-6.00	5.35	2.38-2.77	2.63	2.57-3.01	2.79
	109.670	4.70-6.00	5.35	2.38-2.77	2.63	2.57-3.01	2.79
	152.326	4.70-6.00	5.35	2.38-2.77	2.63	2.57-3.01	2.79
	158.420	4.75-6.05	5.40	2.38-2.77	2.64	2.58-3.02	2.80
	164.514	4.75-6.05	5.40	2.38-2.77	2.64	2.58-3.02	2.80
	170.607	4.70-6.00	5.35	2.38-2.77	2.63	2.57-3.01	2.79
	191.444	4.70-6.00	5.35	2.38-2.77	2.63	2.57-3.01	2.79
	194.982	5.00-6.00	5.50	2.39-2.78	2.66	2.59-3.03	2.81
	199.024	5.50-6.00	5.75	2.42-2.82	2.71	2.62-3.06	2.84
	202.135	5.50-6.00	5.75	2.42-2.82	2.71	2.62-3.06	2.84
	205.246	5.50-6.10	5.80	2.42-2.82	2.72	2.63-3.06	2.85
	208.268	5.70-6.10	5.90	2.43-2.86	2.74	2.64-3.07	2.86
	211.468	5.70-6.10	5.90	2.43-2.86	2.74	2.64-3.07	2.86
	214.579	5.70-6.20	5.95	2.44-2.88	2.76	2.65-3.08	2.86
	217.690	5.70-6.00	5.85	2.43-2.86	2.73	2.64-3.07	2.85
	226.972	5.70-6.00	5.85	2.43-2.86	2.73	2.64-3.07	2.85
	230.032	5.75-6.00	5.88	2.43-2.86	2.73	2.64-3.07	2.86
	236.356	5.75-6.00	5.88	2.43-2.86	2.73	2.64-3.07	2.86
	239.467	5.80-6.10	5.95	2.44-2.88	2.76	2.65-3.08	2.86
	242.578	5.90-6.35	6.13	2.50-2.90	2.81	2.67-3.10	2.88
	245.623	6.00-6.35	6.18	2.52-2.93	2.82	2.67-3.10	2.89
	248.669	6.00-6.45	6.23	2.52-2.93	2.84	2.68-3.11	2.89
	251.828	6.00-6.45	6.23	2.52-2.93	2.84	2.68-3.11	2.89
	254.987	6.10-6.45	6.28	2.54-2.97	2.84	2.68-3.11	2.90
	258.115	6.10-6.45	6.28	2.54-2.97	2.84	2.68-3.11	2.90
	261.244	6.20-6.50	6.35	2.58-2.99	2.86	2.69-3.12	2.90
	267.466	6.30-6.60	6.45	2.61-3.04	2.89	2.70-3.13	2.91
	276.778	6.30-6.60	6.45	2.61-3.04	2.89	2.70-3.13	2.91
	279.868	6.40-6.60	6.50	2.61-3.04	2.90	2.70-3.13	2.92
	282.946	6.50-6.70	6.60	2.64-3.08	2.93	2.71-3.14	2.93
	298.576	6.50-6.70	6.60	2.64-3.08	2.93	2.71-3.14	2.93

Table 9: The Velocity-Density Conversions of the Yaquina Area Model

Layer	x-axis [km]	p-wave velocities [km/s] top-bottom	average p-wave velocity [km/s]	Nafe & Drake density [g/cm^3]	average Nafe & Drake density [g/cm^3]	Carlson & Raskin density [g/cm^3]	average Carlson & Raskin density [g/cm^3]
Gabbros	103.576	6.50-7.20	6.85	2.71-3.19	2.99	2.90-2.97	2.94
	124.865	6.50-7.20	6.85	2.71-3.19	2.99	2.90-2.97	2.94
	127.899	6.40-7.20	6.80	2.69-3.16	2.98	2.89-2.97	2.93
	140.099	6.40-7.20	6.80	2.69-3.16	2.98	2.89-2.97	2.93
	146.232	6.30-7.20	6.75	2.69-3.16	2.97	2.89-2.96	2.92
	152.326	6.40-7.10	6.75	2.69-3.16	2.97	2.89-2.96	2.92
	164.514	6.40-7.10	6.75	2.69-3.16	2.97	2.89-2.96	2.92
	170.607	6.30-7.10	6.70	2.66-3.11	2.95	2.88-2.95	2.92
	182.795	6.30-7.10	6.70	2.66-3.11	2.95	2.88-2.95	2.92
	188.073	6.30-7.30	6.80	2.69-3.16	2.98	2.89-2.97	2.93
	204.182	6.30-7.30	6.80	2.69-3.16	2.98	2.89-2.97	2.93
	207.289	6.30-7.10	6.70	2.66-3.11	2.95	2.88-2.95	2.92
	213.501	6.30-7.10	6.70	2.66-3.11	2.95	2.88-2.95	2.92
	219.450	6.40-7.10	6.75	2.69-3.16	2.97	2.89-2.96	2.92
	231.519	6.40-7.10	6.75	2.69-3.16	2.97	2.89-2.96	2.92
	234.579	6.30-7.10	6.70	2.66-3.11	2.95	2.88-2.95	2.92
	237.638	6.30-7.10	6.70	2.66-3.11	2.95	2.88-2.95	2.92
	243.732	6.50-7.10	6.80	2.69-3.16	2.98	2.89-2.97	2.93
	255.920	6.50-7.10	6.80	2.69-3.16	2.98	2.89-2.97	2.93
	262.014	6.60-7.20	6.90	2.71-3.19	3.01	2.91-2.98	2.94
	268.107	6.70-7.20	6.95	2.73-3.21	3.03	2.91-2.98	2.95
	274.201	6.70-7.20	6.95	2.73-3.21	3.03	2.91-2.98	2.95
	280.295	6.80-7.20	7.00	2.73-3.21	3.04	2.92-2.99	2.95
	298.576	6.80-7.20	7.00	2.73-3.21	3.04	2.92-2.99	2.95
Mantle	103.576	7.95-8.15	8.05	3.14-3.40	3.36		
	164.514	7.95-8.15	8.05	3.14-3.40	3.36		
	176.701	8.00-8.15	8.08	3.14-3.40	3.37		
	243.732	8.00-8.15	8.08	3.14-3.40	3.37		
	249.826	8.05-8.15	8.10	3.14-3.40	3.38		
	298.576	8.05-8.15	8.10	3.14-3.40	3.38		